

DTIC FILE COPY

AD-A225 659

WRDC-TR-90-2031



ANALYSIS OF TRANSIENT AND START-UP BEHAVIOR OF HEAT PIPES AND AN ENERGY STORAGE MODULE

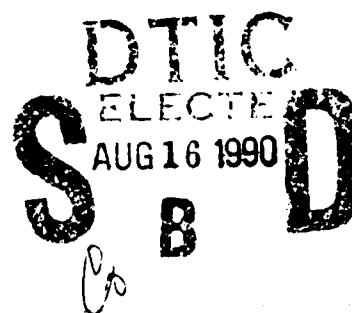
Amir Faghri, Ph.D.
Brage Golding Distinguished Professor

DEPARTMENT OF MECHANICAL AND MATERIALS ENGINEERING
WRIGHT STATE UNIVERSITY
DAYTON, OH 45435

JUNE 1990

INTERIM REPORT FOR PERIOD JANUARY 1989 - DECEMBER 1989

Approved for public release; distribution unlimited



AERO PROPULSION AND POWER LABORATORY
WRIGHT RESEARCH AND DEVELOPMENT CENTER
AIR FORCE SYSTEMS COMMAND
WRIGHT-PATTERSON AIR FORCE BASE, OHIO 45433-6563

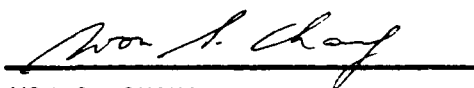
90 08 74 128

NOTICE

WHEN GOVERNMENT DRAWINGS, SPECIFICATIONS, OR OTHER DATA ARE USED FOR ANY PURPOSE OTHER THAN IN CONNECTION WITH A DEFINITELY GOVERNMENT-RELATED PROCUREMENT, THE UNITED STATES GOVERNMENT INCURS NO RESPONSIBILITY OR ANY OBLIGATION WHATSOEVER. THE FACT THAT THE GOVERNMENT MAY HAVE FORMULATED OR IN ANY WAY SUPPLIED THE SAID DRAWINGS, SPECIFICATIONS, OR OTHER DATA, IS NOT TO BE REGARDED BY IMPLICATION, OR OTHERWISE IN ANY MANNER CONSTRUED, AS LICENSING THE HOLDER, OR ANY OTHER PERSON OR CORPORATION; OR AS CONVEYING ANY RIGHTS OR PERMISSION TO MANUFACTURE, USE, OR SELL ANY PATENTED INVENTION THAT MAY IN ANY WAY BE RELATED THERETO.

THIS REPORT HAS BEEN REVIEWED BY THE OFFICE OF PUBLIC AFFAIRS (ASD/PA) AND IS RELEASABLE TO THE NATIONAL TECHNICAL INFORMATION SERVICE (NTIS). AT NTIS IT WILL BE AVAILABLE TO THE GENERAL PUBLIC INCLUDING FOREIGN NATIONS.

THIS TECHNICAL REPORT HAS BEEN REVIEWED AND IS APPROVED FOR PUBLICATION.

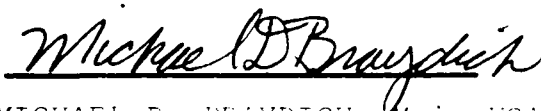


WON S. CHANG
Project Engineer

FOR THE COMMANDER



JERRY E. BEAM, TAM
Power Technology Branch
Aerospace Power Division
Aero Propulsion and Power Laboratory



MICHAEL D. BRAYDICH, Maj, USAF
Actg Chief, Aerospace Power Division
Aero Propulsion & Power Laboratory

IF YOUR ADDRESS HAS CHANGED, IF YOU WISH TO BE REMOVED FROM OUR MAILING LIST, OR IF THE ADDRESSEE IS NO LONGER EMPLOYED BY YOUR ORGANIZATION PLEASE NOTIFY WRDC/POOS-3, WRIGHT-PATTERSON AFB, OH 45433-6563 TO HELP MAINTAIN A CURRENT MAILING LIST.

COPIES OF THIS REPORT SHOULD NOT BE RETURNED UNLESS RETURN IS REQUIRED BY SECURITY CONSIDERATIONS, CONTRACTUAL OBLIGATIONS, OR NOTICE ON A SPECIFIC DOCUMENT.

REPORT DOCUMENTATION PAGE

Form Approved
OMB No. 0704-0188

1a. REPORT SECURITY CLASSIFICATION Unclassified			1b. RESTRICTIVE MARKINGS N/A		
2a. SECURITY CLASSIFICATION AUTHORITY N/A			3. DISTRIBUTION/AVAILABILITY OF REPORT Approved for public release; distribution is unlimited.		
2b. DECLASSIFICATION/DOWNGRADING SCHEDULE N/A					
4. PERFORMING ORGANIZATION REPORT NUMBER(S) WSU-TR-88-001			5. MONITORING ORGANIZATION REPORT NUMBER(S) WRDC-TR-90-2031		
6a. NAME OF PERFORMING ORGANIZATION Wright State University		6b. OFFICE SYMBOL (if applicable)	7a. NAME OF MONITORING ORGANIZATION Aero Propulsion & Power Laboratory (WRDC/POOS) Wright Research and Development Center		
6c. ADDRESS (City, State, and ZIP Code) Department of Mechanical & Materials Engineering Wright State University, Dayton, OH 45435			7b. ADDRESS (City, State, and ZIP Code) Wright-Patterson Afb, OH 45433-6563		
8a. NAME OF FUNDING/SPONSORING ORGANIZATION		8b. OFFICE SYMBOL (if applicable)	9. PROCUREMENT INSTRUMENT IDENTIFICATION NUMBER F33615-88-C-2820		
8c. ADDRESS (City, State, and ZIP Code)			10. SOURCE OF FUNDING NUMBERS		
			PROGRAM ELEMENT NO. 62203F	PROJECT NO. 3145	TASK NO. 20
11. TITLE (Include Security Classification) Analysis of Transient and Start-Up Behavior of Heat Pipes and an Energy Storage Module					
12. PERSONAL AUTHOR(S) Amir Faghri					
13a. TYPE OF REPORT Interim Report		13b. TIME COVERED FROM Jan 89 TO Dec 89		14. DATE OF REPORT (Year, Month, Day) 1990 June	
15. PAGE COUNT 237					
16. SUPPLEMENTARY NOTATION					
17. COSATI CODES			18. SUBJECT TERMS (Continue on reverse if necessary and identify by block number)		
FIELD	GROUP	SUB-GROUP	Heat Pipes; Phase Change; Frozen Start-Up; Start-Up Mathematical Model; Transient Analysis		
19. ABSTRACT (Continue on reverse if necessary and identify by block number) The objective of this report is to examine the steady, transient, and start-up behavior of heat pipes as well as a transient analysis related to a thermal energy storage module. A detailed experimental and numerical analysis of low temperature heat pipes with multiple heat sources is also performed. The performance of a thermal energy module is simulated numerically. The change of phase of the phase-change material (PCM) and transient forced convective heat transfer for the transfer fluid with a low Prandtl number are solved simultaneously as a conjugate problem. The start-up process of a frozen heat pipe is described and a complete model for the start-up of the frozen heat pipe is developed based on the existing experimental data, which is simplified and solved numerically. Finally, a unique and efficient transient two-dimensional compressible analysis of high temperature heat pipes with a pulsed heat input is given.					
20. DISTRIBUTION/AVAILABILITY OF ABSTRACT <input checked="" type="checkbox"/> UNCLASSIFIED/UNLIMITED <input type="checkbox"/> SAME AS RPT. <input type="checkbox"/> DTIC USERS			21. ABSTRACT SECURITY CLASSIFICATION Unclassified		
22a. NAME OF RESPONSIBLE INDIVIDUAL Won S. Chang			22b. TELEPHONE (Include Area Code) (513) 255-2922		22c. OFFICE SYMBOL WRDC/POOS

FOREWORD

The information in this report was assembled for contract #F33615-88-C-2820 with the Aero Propulsion and Power Laboratory, Wright Research and Development Center and NASA Lewis Research Center as the sponsoring agencies. The work was carried out at the Department of Mechanical and Materials Engineering at Wright State University.

During FY 1989, seven tasks were performed as outlined in the table of contents. The various tasks dealt with performance characteristics of steady, transient and start-up behavior of heat pipes as well as an analysis related to a thermal energy storage module. Seven journal publications were produced from the present work. My co-workers in the preparation of this report are Mr. Yiding Cao, Mr. Matt Buchko, Dr. Jong Hoon Jang and Mr. Scott Thomas. Support from Dr. Tom Mahefkey, Dr. Jerry Beam, and Dr. Won Chang from Wright Research and Development Center and Mr. Al Juhasz from NASA Lewis Research Center is appreciated.

Accession For	
NTIS GRA&I	<input checked="checked" type="checkbox"/>
DTIC TAB	<input type="checkbox"/>
Unannounced	<input type="checkbox"/>
Justification	
By _____	
Distribution/	
Availability Codes	
Dist	Avail and/or Special
A-1	



TABLE OF CONTENTS

Section	Page
I. EXPERIMENTAL AND NUMERICAL ANALYSIS OF LOW TEMPERATURE HEAT PIPES WITH MULTIPLE HEAT SOURCES.....	1
1.1 Summary.....	1
1.2 Introduction.....	2
1.3 Mathematical Modeling and Numerical Analysis.....	5
1.4 Experimental Apparatus and Procedure.....	14
1.5 Results and Discussion.....	19
1.6 Conclusions.....	30
II. HEAT TRANSFER IN LIQUID METALS BY NATURAL CONVECTION.....	31
2.1 Summary.....	31
2.2 Introduction.....	32
2.3 Formulation and Numerical Method.....	33
2.4 Results and Discussion.....	37
2.4.1 Partial Heating with Constant Heat Flux.....	37
2.4.2 Natural Convection in a Horizontal Rigid Cavity with Specified Boundary Temperature.....	43
2.5 Conclusions.....	44
III. PERFORMANCE CHARACTERISTICS OF A THERMAL ENERGY STORAGE MODULE: A TRANSIENT PCM/FORCED CONVECTION CONJUGATE ANALYSIS.....	47
3.1 Summary.....	47
3.2 Introduction.....	48
3.3 Mathematical Modeling.....	51
3.4 Numerical Procedure.....	57
3.5 Numerical Results and Discussion.....	58
3.6 Conclusions.....	71
IV. MATHEMATICAL MODELING AND ANALYSIS OF HEAT PIPE START-UP FROM THE FROZEN STATE.....	72
4.1 Summary.....	72
4.2 Introduction.....	73
4.3 Description of Heat Pipe Start-up.....	76
4.4 Mathematical Formulation.....	79
4.4.1 Heat Pipe Wall.....	79
4.4.2 Wick Structure Region.....	81
4.4.3 Vapor Flow Dynamics.....	86
4.5 Simplification of the Model.....	91
4.6 Numerical Procedures.....	95
4.7 Results and Discussion.....	99
4.7.1 Simulation of the Heat Pipe Start-up in the Initial Stages.....	100
4.7.2 Transient Heat Pipe Operation.....	109
4.8 Conclusions.....	117

Table of Contents (continued)

Section	Page
V. A TEMPERATURE TRANSFORMING MODEL FOR PHASE-CHANGE PROBLEMS INCLUDING NATURAL CONVECTION.....	118
5.1 Summary.....	118
5.2 Introduction.....	119
5.3 Numerical Formulation and Modeling.....	123
5.4 Numerical Scheme for the Energy Equation.....	128
5.5 Numerical Results and Discussion.....	133
5.5.1 Phase Change without Convection.....	133
5.5.2 Phase Change with Natural Convection.....	140
5.6 Conclusions.....	145
VI. A TRANSIENT TWO-DIMENSIONAL COMPRESSIBLE ANALYSIS FOR HIGH TEMPERATURE HEAT PIPES WITH A PULSED HEAT INPUT.....	149
6.1 Summary.....	149
6.2 Introduction.....	150
6.3 Mathematical Formulation and Modeling.....	151
6.3.1 Governing Equations.....	151
6.3.2 Analysis of the Vapor-Liquid Interface.....	153
6.3.3 Boundary Conditions.....	160
6.4 Numerical Procedure.....	163
6.5 Numerical Results and Discussion.....	165
6.5.1 Compressible Vapor Flow in a Simulated Heat Pipe..	165
6.5.2 Transient Response of the Heat Pipe to a Pulsed Heat Input.....	168
6.6 Conclusions.....	180
VII. ANALYSIS OF THE TRANSIENT COMPRESSIBLE VAPOR FLOW IN HEAT PIPES.	181
7.1 Summary.....	181
7.2 Introduction.....	182
7.3 Mathematical Modeling.....	184
7.4 Friction Coefficients.....	188
7.5 Numerical Formulation.....	190
7.6 Results and Discussion.....	192
7.6.1 Comparison with the Simulated Heat Pipe Vapor Flow.....	192
7.6.1.1 Transient Results.....	194
7.6.1.2 Steady State Results.....	196
7.6.2 Comparison with Actual Vapor Flow in Cylindrical Heat Pipes.....	202
7.7 Conclusions.....	206
REFERENCES.....	209

LIST OF FIGURES

Figure	Page
1.1a. The multiple evaporator heat pipe and coordinate system.....	6
1.1b. Low temperature heat pipe with multiple heat source thermocouple locations.....	6
1.2. Low temperature heat pipe with multiple heat sources experimental test setup.....	18
1.3. $\Delta T_{\text{wall-vapor}}$ versus heat input for different single evaporator operations.....	20
1.4. Heat pipe wall and vapor temperatures versus axial location for Case 1.....	23
1.5. Heat pipe wall and vapor temperatures versus axial location for Case 5.....	24
1.6. Heat pipe wall and vapor temperatures versus axial location for Case 6.....	25
1.7. Heat pipe wall and vapor temperatures versus axial location for Case 7.....	26
1.8. $\Delta T_{\text{wall-vapor}}$ versus heat input to evaporator 3 with heat input to evaporator 1 held constant at 100 watts for Case 11.....	28
1.9. $\Delta T_{\text{wall-vapor}}$ versus heat input to evaporator 2 with heat input to evaporator 1 held constant at 100 watts for Case 12.....	29
2.1. Two-dimensional horizontal liquid metal layer with localized heating from below.....	34
2.2. Comparison between the numerical solution and the experimental data.....	38
2.3. Calculated temperature contours.....	40
2.4. Calculated stream function contours.....	41
2.5. Temperature distributions for different heat flux q	42
2.6. Comparison of eqn. (2.6) and the present numerical solutions.....	45
3.1. The schematic of the latent heat storage system.....	49
3.2. Interface position along the diagonal with prescribed boundary temperature.....	59

List of Figures (continued)

3.3.	Axial velocity distribution of transfer fluid at $X = 6$ for different time periods.....	61
3.4.	Radial temperature distribution at $X = 6$ for different time periods.....	62
3.5.	Melting fronts along axial direction for different time periods..	63
3.6.	Melting fronts along axial direction for different Prandtl numbers at $\tau = 1000$	65
3.7.	Melting fronts along axial direction for different Reynolds numbers.....	66
3.8.	Melting fronts along axial direction for different thermal conductivities of the wall at $\tau = 1000$	67
3.9.	System optimization analysis for different L/D at $\tau = 1000$	69
3.10.	System optimization analysis for different r_o/D at $\tau = 1000$	70
4.1.	Schematic diagram and coordinate configuration of the heat pipe..	80
4.2.	Temperature distribution at the outer wall surface and liquid-vapor interface of the heat pipe wall with time for case 1.....	104
4.3.	Temperature distribution at the outer wall surface of the heat pipe wall with different times for case 1.....	105
4.4.	Temperature distribution at the outer wall surface and liquid-vapor interface of the heat pipe wall with time for case 2.....	107
4.5.	Temperature distribution at the outer wall surface of the heat pipe wall with different times for case 2.....	108
4.6.	Temperature distribution at the outer wall surface and liquid-vapor interface of the heat pipe wall with time for case 3.....	110
4.7.	Temperature distribution at the outer wall surface of the heat pipe wall with different times for case 3.....	111
4.8.	Temperature distributions at the outer wall surface and liquid-vapor interface, and saturation temperature for time of 0.3 second.....	114
4.9.	Comparison of new heat flux with old heat flux at the interface for time of 0.3 second during transient continuum flow.....	115
4.10.	Axial variations of temperature, pressure, density and velocity for time of 0.3 second during transient continuum flow.....	116

List of Figures (continued)

5.1.	Approximation of equivalent specific heat for melting/for solidification problem.....	121
5.2.	Relation between T^0 and E with phase-change temperature range....	125
5.3.	Control volume for the two-dimensional situation.....	131
5.4.	The exact and numerical solutions of the melting front in a half-space.....	135
5.5.	Description of the geometry and boundary conditions for the two-dimensional freezing problem.....	136
5.6.	Interface position along the diagonal with prescribed boundary temperature.....	138
5.7.	Temperature profiles along an adiabatic line for different values of δT^* and grid sizes.....	139
5.8.	The thermal cavity configuration.....	141
5.9.	Comparison of the locations of the melting front.....	144
5.10.	Calculated temperature contours.....	146
5.11.	Calculated stream function contours.....	147
6.1.	The heat pipe configuration and coordinate system.....	152
6.2.	Vapor-liquid interface control volume.....	154
6.3.	Temperature distribution in the wick.....	157
6.4.	The axial pressure profile along the centerline of the simulated heat pipe for steady state.....	166
6.5.	The axial Mach number profile along the centerline of the simulated heat pipe for steady state.....	167
6.6.	The vapor temperature along the centerline for different time periods with the convective boundary condition.....	170
6.7.	The vapor temperature along the centerline for different time periods with the radiative boundary condition.....	171
6.8.	The outer wall temperature T_w of the heat pipe for different time periods with the radiative boundary condition.....	172

List of Figures (continued)

6.9.	The axial pressure profile along the centerline of the heat pipe for different time periods.....	174
6.10.	The vapor density along the centerline of the heat pipe for different time periods.....	175
6.11.	The axial velocity profile along the centerline for different time periods.....	176
6.12.	Axial velocity distributions in the radial direction at different axial locations and times.....	177
6.13.	Radial temperature distribution at different axial locations and times.....	178
7.1.	Schematic diagram of model for air flow in the porous pipe.....	193
7.2.	Comparison of the present numerical results with Bowman's 2-D model for pressure variations with time at three locations of the porous pipe: Case B.1.....	195
7.3.	Comparison of the present numerical results with the experimental pressure variations (Bowman, 1987) in the porous pipe.....	198
7.4.	Axial variations of temperature, pressure, velocity and density for case B.4.....	200
7.5.	Axial variations of temperature, pressure, velocity and density for case B.5.....	201
7.6.	Schematic diagram of model for the sodium vapor flow in the heat pipe.....	203
7.7.	Axial variations of temperature, pressure, velocity and density of the sodium heat pipe at steady state.....	205
7.8.	Comparison of the temperature variations with and without viscous dissipation for actual vapor flow.....	207

LIST OF TABLES

Table	Page
1.1 Design summary of the low temperature heat pipe with multiple heat sources.....	15
1.2 Low temperature heat pipe with multiple heat sources text matrix...	21
4.1 Boundary specifications at the outer surface of the heat pipe wall.....	103

NOMENCLATURE

- A area, m
- a inner radius of vapor space, m (Section I)
- a coefficient in the discretization equation (6.9) or coefficient in eqn. (5.19)
- B term in eqn. (5.12)
- B^{*} term in eqn. (5.15)
- b inner radius of heat pipe, m (Section I)
- b term in eqn. (5.19)
- b source term in eqn. (6.9)
- B₁ W/H
- B₂ L/H
- C C^0/c_ℓ
- C⁰ coefficient in eqns. (3.5 and 5.9), J/(kg - K)
- C_{sℓ} c_s/c_ℓ
- c specific heat, J/(kg-K)
- c outer radius of heat pipe, m (Section I)
- c_m specific heat of mushy phase, $1/2(c_s + c_\ell)$, J/(kg - K)
- c_p specific heat at constant pressure, J/(kg-K)
- c_p^{*} equivalent specific heat, J/(kg - K)
- c_v specific heat at constant volume, J/kg-K
- D inside diameter of the circular pipe, or diagonal distance, m (Section III)
- D diameter of the vapor space, m (Section IV)
- D diagonal distance, m, also used as dimensionless conductances in eqn. (5.19) (Section V)
- D_v diameter of the vapor space, m

Nomenclature (continued)

E	total energy of the vapor per unit volume, $\rho [c_v T_v + 1/2 (U_v^2 + v_v^2)]$ (Section IV)
E	enthalpy, J/kg (Section V)
E _t	total energy of the vapor per unit volume, $\rho(C_v T + 1/2 U^2)$
erf	error function
F	dimensionless flow rate through a control-volume face
f	friction coefficient at the wall, $\tau/\rho U^2$
f _e	friction coefficient at the exit of the evaporator
f _t	friction coefficient for the fully developed turbulent flow
g	gravitational acceleration, m/s ²
g _ℓ	integral in eqn. (3.18)
g _t	integral in eqn. (3.19)
H	height of thermal cavities or height of the liquid level, m (Section II)
H	latent heat, J/kg (Section III)
H	height of the vertical wall, m (Section V)
H _{sℓ}	latent heat of melting per unit volume, J/m ³
h	enthalpy, J/kg
h _c	heat transfer coefficient, W/m ² - K
h _{fg}	latent heat of evaporation, J/kg
K	permeability, m ²
K	dimensionless thermal conductivity, k/k _ℓ (Sections III and V)
K _n	Knudsen number
K _{sℓ}	k _s /k _ℓ
k	thermal conductivity, W/(m-K)

Nomenclature (continued)

L	half width of the heating element, m (Section II)
L	length of the pipe, m (Section III)
L	length of the heat pipe, m (Sections IV, VI, and VII)
L	latent heat, J/kg (Section V)
L_a	length of the adiabatic section, m
L_c	length of the condenser, m
L_e	length of the evaporator, m
ℓ	reference length in Figs. 3.2 and 5.5, m
M	Mach number, $U/\sqrt{\gamma RT}$
M	molecular weight, kg/Kmol (Section IV)
Ma	Mach number, $w/\sqrt{\gamma p/\rho_v}$
m	total mass of the PCM, kg
\dot{m}	mass flux, $\text{kg}/\text{m}^2\text{-s}$
\dot{m}_i	mass flux at the liquid-vapor interface, $\text{kg}/(\text{m}^2\text{-s})$
\dot{m}_0	rate of evaporation or condensation per unit area, $\text{kg}/\text{m}^2\text{-s}$
Nu	Nusselt number, $qH/k(T_h - T_c)$
n	unit outward normal direction (Section IV)
n	normal direction of the liquid-vapor interface (Section VI)
n	time step (Section VII)
P	$(p + \rho_0 gy) H^2/\rho a^2$ (Section II)
P	dimensionless pressure, $(p-p_0)/\rho_f U_0^2$ (Section III)
P	$(p + \rho gy) H^2/\rho a_\ell^2$ (Section V)
P_c	reference pressure for the Clausius-Clapeyron equation, N/m^2
P_{cr}	reference pressure for the Clausius-Clapeyron relationship, N/m^2
P_e	pressure at the evaporator end cap, N/m^2

Nomenclature (continued)

P_{sk}	sink pressure, N/m^2
P_{so}	source pressure, N/m^2
Pr	Prandtl number, ν/a
p	pressure, N/m^2
p^*	modified pressure
p'	pressure correction
p_o	inlet pressure, N/m^2 (Section III)
p_o	centerline pressure at the end cap of the evaporator, or reference pressure, N/m^2 (Section VI)
Q	heat energy, J (Section III)
Q	total heat input rate at the outer pipe wall at the evaporator, W (Section VI)
Q	heat input, W (Section VII)
$Q_{c,max}$	maximum capillary heat transport rate, W
$(Q_L)_{c,max}$	heat transport factor, W-m
Q_ℓ	total latent energy stored, J
Q_m	energy storage density, J/kg
Q_t	total energy stored, J
q	heat flux, W/m^2
q'	new heat flux, W/m^2
q''	new guessed heat flux, W/m^2
q_L	latent heat flux, W/m^2
q_s	heat source, W/m^3
R	gas constant, J/kg-K
R_o	outer pipe wall radius, m

Nomenclature (continued)

R_u	universal gas constant, KJ/Kmol-K
R_v	vapor space radius, m
R_w	wick-wall interface radius, m
Ra	Raleigh number, $g\beta H^3(T_h - T_c)/\nu a$ (Section II)
Ra	Raleigh number, $g\beta H^3(T_h^0 - T_c^0)/\nu_\ell a_\ell$ (Section V)
Ra_1	Raleigh number, $g\beta H^3 T_c/\nu a$
Re	axial Reynolds number, $\rho U D_v/\mu$
Re_f	fluid Reynolds number, $U_o D/\nu_f$
Re_o	radial Reynolds number at the wall, $\rho V_o D_v/\mu$
r	radial coordinate, m
r_c	effective capillary radius, m
r_p	radius of curvature of the meniscus, m
S	$S^0/c_\ell (T_{in}^0 - T_m^0)$ (Section III)
S	$S^0/c_\ell (T_h^0 - T_c^0)$ (Section V)
\vec{S}	interface position in vector, m
S^0	term in eqns. (3.5 and 5.9), J/kg
St	Stefan number, $c_\ell(T_{in}^0 - T_m^0)/H$ (Section III)
St	Stefan number, $c_\ell(T_h^0 - T_c^0)/L$ (Section V)
s	interface position along the diagonal, m
T	temperature, K
T	dimensionless temperature, $(T^0 - T_m^0)/(T_h^0 - T_c^0)$ (Section V)
T	dimensionless temperature, $(T^0 - T_m^0)/(T_{in}^0 - T_m^0)$ (Section III)
T^*	transition temperature, K (Section IV)
T^*	scaled temperature, $T^0 - T_m^0$, K (Sections III and V)

Nomenclature (continued)

T^0	temperature, K
T_a	environment temperature, K
T_c	reference temperature for convection, K (Section IV)
T_c	reference temperature for the Clausius-Clapeyron equation, K (Section VII)
T_c	cold surface temperature, $^{\circ}\text{C}$ (Section II)
T_c	dimensionless cold surface temperature, $(T_c^0 - T_m^0)/(T_h^0 - T_c^0)$ (Section V)
T_c^0	cold surface temperature, K
T_{cr}	reference temperature for the Clausius-Clapeyron relationship, K
T_h	hot surface temperature, $^{\circ}\text{C}$ (Section II)
T_h	dimensionless hot surface temperature, $(T_h^0 - T_m^0)/(T_h^0 - T_c^0)$ (Section V)
T_h^0	hot surface temperature, K
T_i	initial dimensionless temperature, $(T_i^0 - T_m^0)/(T_h^0 - T_c^0)$
T_i^0	initial temperature, K
T_{iw}	temperature at the wick-wall interface, K
T_{j-1}	temperature at node j-1 in the radial direction in the wick region, K
T_j	temperature at last node near liquid-vapor interface in the radial direction in the wick region, K
T_m	melting temperature, K
T_m^0	melting (or freezing) temperature, K
T_o	reference temperature, K
T_0	initial temperature, K (Section IV)
T_0	reference temperature, $^{\circ}\text{C}$ (Section II)
T_r	reference temperature for radiation, K

Nomenclature (continued)

T_s	saturation temperature, K (Section IV)
T_s	saturation temperature, °C (Section II)
T_s^0, T_ℓ^0	the temperatures defined in Fig. 5.2, K
T_w	outer wall surface temperature, K (Section VI)
T_w	temperature of heating surface in the case of the constant heat flux, °C (Section II)
T_w	dimensionless wall temperature, $(T_w^0 - T_m^0)/(T_h^0 - T_c^0)$ (Section V)
T_w^0	wall temperature, K
t	time, s
U	axial velocity m/s (Sections IV and VII)
U_0	inlet velocity, m/s
U, V	dimensionless velocities, uH/a , vH/a (Section II)
U, V	dimensionless velocities, u/U_0 , v/U_0 (Section III)
U, V, W	dimensionless velocities, uH/a_ℓ , vH/a_ℓ , wH/a_ℓ (Section V)
u, v	velocities, m/s (Sections II and III)
u, v, w	velocities, m/s (Section V)
\vec{V}	net velocity vector, m/s
V	radial velocity, m/s (Section IV)
V_0	radial velocity at the wall, m/s
v	radial velocity, m/s (Section VI)
v_i	radial vapor velocity at the interface, m/s
v^*	radial velocity based on the guessed pressure p^* , m/s
W	width of the thermal cavities, m (Section II)
w	axial velocity, m/s (Section VI)

Nomenclature (continued)

- w^* axial velocity based on the guessed pressure, p^* , m/s
 X, R dimensionless coordinate directions, x/D , r/D (Section III)
 X, Y dimensionless coordinate directions, x/H , y/H (Section II)
 X, Y, Z dimensionless coordinate directions, x/H , y/H , z/H (Section V)
 x, y, z coordinate directions (Section V)
 x, r coordinate directions (Section III)
 x, y coordinate directions (Section II)
 x coordinate in the axial direction (Sections IV and VII)
 $x_{t,i}$ initial location of the transition region, m
 \bar{x} dimensionless location of the transition region, $(x - x_{t,i})/\Omega$
 z axial coordinate, m (Section VI)

Greek Symbols

- a thermal diffusivity, m^2/s
 α relaxation factor (Section IV)
 β coefficient of volumetric thermal expansion, $^{\circ}C^{-1}$
 γ ratio of specific heats, c_p/c_v
 Γ fraction of transition to turbulent flow
 δ wall or liquid-wick thickness, m
 δt time increment, s
 δx distance between nodes, m
 $2\delta T^0$ phase-change temperature range, or mushy phase range, K (Section III)
 $2\delta T^0$ phase-change temperature range, $(T_{\ell}^0 - T_s^0)$, K (Section V)

Nomenclature (continued)

- δT^* $\delta T^0 / (T_{in}^0 - T_m^0)$ (Section III)
- δT^* $\delta T^0 / (T_h^0 - T_c^0)$ (Section V)
- $\delta(T - T_m)$ Dirac function
- Δr radial distance between nodes, m
- ΔT small finite temperature interval around T_m to define mushy zone, K
- ϵ porosity (Sections I and IV)
- ϵ emissivity (Section VI)
- θ dimensionless temperature, $(T - T_c) / (T_h - T_c)$ or $(T - T_c) / T_c$ (Section II)
- θ contact angle of the liquid, deg (Section IV)
- θ_o $(T_i^0 - T_w^0) / (T_m^0 - T_w^0)$
- λ length of mean free path, m (Section IV)
- λ parameter in eqn. 5.20
- μ dynamic viscosity, kg/(m·s)
- ν kinematic viscosity, m²/s
- ξ emissivity
- ρ density, kg/m³
- ρ_o reference density, kg/m³
- ρ_i vapor density at the liquid-vapor interface, kg/m³
- ρ' density correction
- ρ^* guessed vapor density
- ρ^* modified density (Section I)
- σ Stefan-Boltzmann constant, W/(m²·K⁴)
- τ shear stress (Sections IV and VII)
- τ dimensionless time, $U_o t / D$ (Section III)

Nomenclature (continued)

- τ dimensionless time, $a_\ell t/H^2$ (Section V)
- ϕ general variable in the discretization eqn. (6.9)
- Φ viscous dissipation term in eqn. (6.14)
- ω surface tension, N/m (Section IV)
- ω porosity (Section VI)
- Ω $x_\Gamma = 3/4$ - $x_\Gamma = 1/4$

Subscripts

- a adiabatic
- B "bottom" neighbor of grid P
- b control-volume face between P and B
- c condenser
- cond conduction
- conv convection
- E "east" neighbor of grid P
- e control-volume face between P and E (Section V)
- e evaporator or control-volume face between grid P and E (Section VI)
- eff effective
- f transfer fluid
- $f\ell$ working substance in the liquid state in the wick
- fs working substance in the solid state in the wick
- i initial condition, or inside radius of the pipe (Section III)
- i initial condition (Section V)
- i vapor-liquid interface (Section VI)
- in inlet

Nomenclature (continued)

inf	melting interface
L	latent heat
ℓ	liquid PCM or latent heat (Section III)
ℓ	liquid where there is liquid motion in the wick (Section IV)
ℓ	liquid phase (Section V)
ℓ	liquid or liquid-wick (Sections I and VI)
ℓe	wick region where the working substance is in the liquid state
m	mass or mushy phase (Section III)
m	mushy phase (Section V)
m	wick structure material (Section VI)
me	wick region where the working substance is in the mushy state
N	"north" neighbor of grid p
n	control-volume face between P and N
o	outer surface of the PCM module (Section III)
o	properties at the liquid-vapor interface (Sections I and IV)
o	properties of the injected or extracted fluid at the wall (Section VII)
P	grid point
p	PCM
S	"south" neighbor of grid P
s	solid PCM (Section III)
s	wick structure material (Section IV)
s	control-volume face between P and S, or solid phase (Section V)
s	saturation (Section VI)
se	wick region where the working substance is in the solid state

Nomenclature (continued)

T	"top" neighbor of grid P
t	control-volume face between P and T
v	vapor
W	"west" neighbor of grid P
w	control-volume face between P and W (Section V)
w	wall
x	derivative with respect to x

Section I

EXPERIMENTAL AND NUMERICAL ANALYSIS OF LOW TEMPERATURE HEAT PIPES WITH MULTIPLE HEAT SOURCES

1.1 SUMMARY

A numerical analysis and experimental verification of the effects of heat load distribution on the vapor temperature, evaporation and condensation rates, and the heat transport capacity for heat pipes with multiple heat sources is presented. The elliptic conjugate mass, momentum and energy equations in conjunction with the thermodynamic equilibrium relations and appropriate boundary conditions for the vapor region, wick structure, and the heat pipe wall are given. A numerical solution of these coupled equations as a conjugate problem was required for the performance prediction of heat pipes with multiple heat sources. The experimental testing of a copper-water heat pipe with multiple heat sources was also made which shows excellent agreement with the numerical results. An optimization of the heat distribution for such heat pipes was performed and it was concluded that by redistribution of the heat load, the heat capacity of heat pipes can be increased.

1.2 INTRODUCTION

Since the invention of the heat pipe by Grover et al. (1964), many investigations have been performed concerning heat pipe operation, factors limiting heat pipe performance, heat pipe applications and design modifications for the improvement of heat pipe performance. Because of the simplicity of design and ease of manufacture and maintenance, heat pipes have found applications in a wide variety of areas (Chi, 1976; Dunn and Reay, 1982), including energy conversion systems, cooling of nuclear and isotope reactors, cooling of electronic equipment and high performance space applications. The performance of a heat pipe often is critical and is judged in part by the amount of heat a unit length of the heat pipe can transport under a uniform heat load.

Advanced spacecraft electronic cooling systems will require heat transport loops and heat pipes which have multiple heat sources in series along the heat flow path separated by uniform and nonuniform distances. In addition, advanced spacecraft and hypersonic thermal management requirements also motivate the analysis and performance evaluation of heat pipes with multiple heat sources. In general, the analytical and experimental analyses developed for single evaporator heat pipes cannot be applied to multiple evaporator heat pipes with nonuniform heat loads. Military applications of such heat pipes are the cooling of leading edges and nose cones of re-entry vehicles and cooling rail guns and laser mirrors. Future hypersonic vehicle structures will also require high performance heat pipes with multiple evaporators for regions subjected to high intensity heating where large quantities of heat must be absorbed and the heating distribution is not uniform.

The axial heat flux in heat pipes is governed in principal by vapor flow and liquid return flow limitations. If the liquid return flow can be guaranteed by the appropriate wick structure design, then the axial heat flux is limited only by the vapor flow effects. The vapor flow is limited by: the choking phenomenon, where the vapor velocity approaches the sonic velocity; the viscous phenomenon, in which the vapor pressure approaches zero; and the entrainment phenomenon, where liquid droplets are entrained into the vapor flow.

The interruption of the liquid return flow can be caused by insufficient capillary pressure (wicking limit) or by the formation of bubbles in the wick (boiling limit). It should be noted that the capillary limitation on the heat transport rate $Q_{c,max}$ for conventional heat pipes can be derived from the heat transport factor $(Q_L)_{c,max}$ if the heat flow distribution along the pipe is known. In conventional heat pipe analysis (Chi, 1976), the heat flux distribution is assumed uniform for simplicity and because there is no information available for nonuniform heat loading.

Many investigators have examined the problem of vapor flow in circular and annular heat pipes under uniform heating loads using numerical and analytical methods. The majority of these investigators neglected the effect of the wick and the heat conduction in the pipe wall. Compressible vapor flow analysis is also needed for the sonic conditions. A recent detailed literature survey concerning the thermal modelling of heat pipes is given by Chen and Faghri (1989). The review covers both analytical and numerical methods, transient and steady conditions as well as one- or two-dimensional modeling. Some of the most recent investigations are by

Busse (1987), Faghri and Parvani (1988), Issacci et al. (1988), Bowman and Hitchcock (1988), Cao et al. (1989b), Faghri and Thomas (1989), Faghri (1989), Chen and Faghri (1989), Faghri and Chen (1989), Jang et al. (1989a), and Jang et al. (1989b).

Gernert (1986) attempted the analysis of heat pipes with multiple heat sources with the use of superposition and the extension of the existing theories for a single evaporator heat pipe. It is clear that one cannot use superposition for fluid flow analysis due to the nonlinearity of the momentum equations. Furthermore, axial conduction is neglected which can play an important role with multiple heat sources. The objective of this paper was to achieve the following:

- 1- The formulation of a detailed mathematical model with numerical results for predicting the performance of heat pipes with multiple evaporators. This was accomplished by solving numerically the complete mass, momentum and energy equations in the vapor region, wick structure and the heat pipe wall for heat pipes with multiple heat sources as a conjugate problem. This new model includes the effect of liquid flow in the wick which is important for low temperature heat pipes rather than assuming pure conduction through the wick as was done by Chen and Faghri (1989).
- 2- The experimental testing of a copper-water heat pipe with multiple evaporators using various heat loads in each evaporator for model verification as well as optimization of the heat distribution for such heat pipes.

1.3 MATHEMATICAL MODELING AND NUMERICAL ANALYSIS

Fluid mechanics and heat transfer problems in heat pipes are categorized in the four basic types: vapor flow in the core region; liquid flow in the wick; heat conduction in the heat pipe wall; and the interaction between the liquid and vapor flows. Most of the analytical and numerical studies on heat pipes have been done on the vapor region for the case of uniform heating and cooling with one evaporator section.

The physical problem under consideration is a conventional heat pipe with multiple heat sources as shown in Fig. 1.1a, which is divided into three regions, namely, the vapor flow region, the liquid-wick, and the solid wall. It is assumed that the vapor flow in all segments of the heat pipe, i.e., the evaporator, adiabatic and the condenser sections, is operating under laminar, subsonic and steady conditions. Nonuniform radial inflow and outflow boundary conditions are needed to model evaporation and condensation. Since the heat pipe is closed at both ends, it is required that the vapor which flows out of the evaporator segment enters into the condenser section. The conservation of mass, momentum, and energy equations for the compressible vapor flow region including viscous dissipation are:

$$\frac{\partial}{\partial z}(\rho_v w_v) + \frac{1}{r} \frac{\partial}{\partial r}(\rho_v r v_v) = 0 \quad (1.1)$$

$$\rho_v \left(w_v \frac{\partial w_v}{\partial z} + v_v \frac{\partial w_v}{\partial r} \right) = - \frac{\partial p_v}{\partial z} + \mu_v \left[\frac{4}{3} \frac{\partial^2 w_v}{\partial z^2} + \frac{1}{r} \frac{\partial}{\partial r} \left(r \frac{\partial w_v}{\partial r} \right) + \frac{1}{r} \frac{\partial}{\partial r} \left(r \frac{\partial v_v}{\partial z} \right) - \frac{2}{3} \frac{\partial}{\partial z} \left(\frac{1}{r} \frac{\partial}{\partial r} (r v_v) \right) \right] \quad (1.2)$$

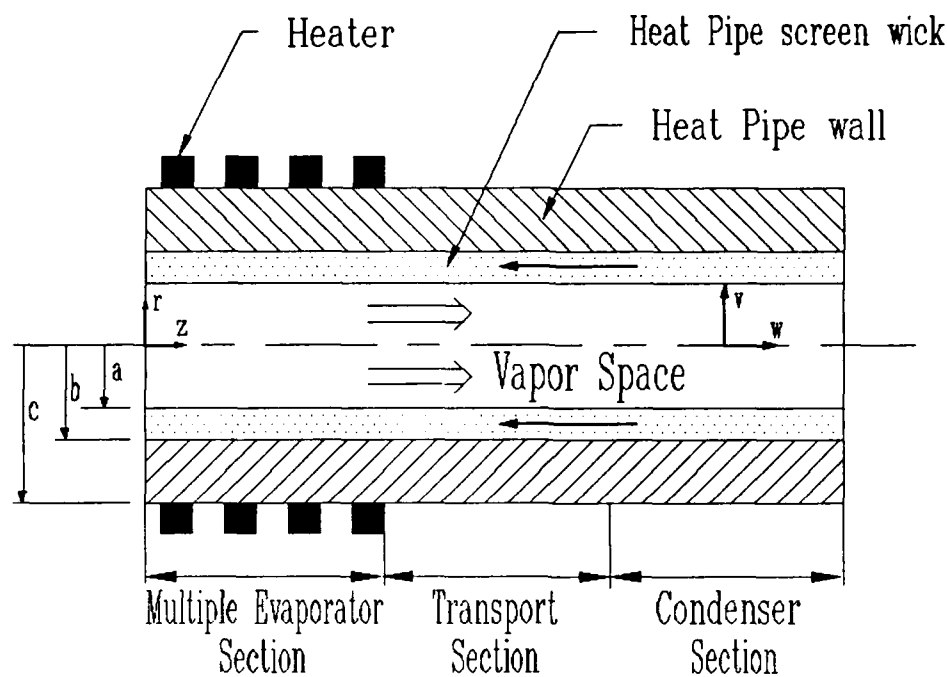
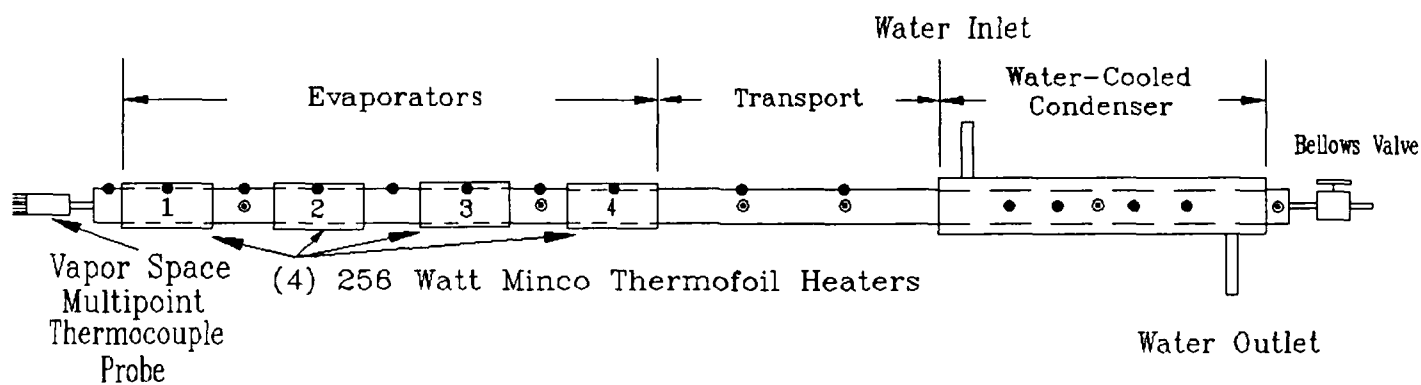


Figure 1.1a. The Multiple Evaporator Heat Pipe and Coordinate System



Evaporator Length --(4) 6.35cm Heaters with 7.53cm adiabatic separation = 50cm total

Transport Length ----- 18cm

Condenser Length ----- 30cm

- Vapor-space Thermocouple
- Wall Thermocouple

Figure 1.1b. Low Temperature Heat Pipe with Multiple Heat Source Thermocouple locations

$$\rho_v \left(w_v \frac{\partial v_v}{\partial z} + v_v \frac{\partial v_v}{\partial r} \right) = - \frac{\partial p_v}{\partial r} + \mu_v \left[\frac{\partial^2 v_v}{\partial z^2} + \frac{4}{3r} \frac{\partial}{\partial r} \left(r \frac{\partial v_v}{\partial r} \right) - \frac{4}{3} \frac{v_v}{r^2} + \frac{1}{3} \frac{\partial^2 w_v}{\partial z \partial r} \right] \quad (1.3)$$

$$\rho_v c_{p,v} \left(w_v \frac{\partial T_v}{\partial z} + v_v \frac{\partial T_v}{\partial r} \right) = - \frac{k_v}{r} \left[\frac{\partial}{\partial r} \left(r \frac{\partial T_v}{\partial r} \right) + r \frac{\partial^2 T_v}{\partial z^2} \right] + v_v \frac{\partial p_v}{\partial r} + w_v \frac{\partial p_v}{\partial z} + \mu_v \phi \quad (1.4)$$

$$\text{where } \phi = 2 \left[\left(\frac{\partial v_v}{\partial r} \right)^2 + \left(\frac{v_v}{r} \right)^2 + \left(\frac{\partial w_v}{\partial z} \right)^2 + \frac{1}{2} \left(\frac{\partial v_v}{\partial z} + \frac{\partial w_v}{\partial r} \right)^2 - \frac{1}{3} (\nabla \cdot v_v)^2 \right]$$

$$\nabla \cdot v_v = \frac{1}{r} \frac{\partial}{\partial r} (r v_v) + \frac{\partial w_v}{\partial z}$$

It should be noted that the perfect gas law is employed to account for the compressibility of the vapor.

The use of liquid capillary action is the unique feature of the heat pipe. From a fundamental viewpoint, the liquid capillary flow in heat pipes with screen wicks should be modeled as a flow through a porous media. It is assumed that wicking material is isotropic and of constant thickness. In addition, the wick is saturated and the vapor condenses or the liquid evaporates at the vapor-liquid interface.

The averaging technique was applied by many investigators to obtain the general governing equation which describes the conservation of momentum in a porous structure. Since the development of Darcy's semi-empirical equation, which characterizes the fluid motion under certain conditions, many scientists have tried to develop and extend Darcy's law in order to

see the effect of the inertia terms. In this respect, those who have tried to model the flow with the Navier-Stokes equation were the most successful.

The general equations of motion and energy for steady state laminar incompressible liquid flow in porous media in terms of the volume-averaged velocities (Bachmat and Bear, 1986) are:

$$\rho_{\ell}^v \frac{\partial w_{\ell}}{\partial r} + \rho_{\ell}^w \frac{\partial w_{\ell}}{\partial z} = - \frac{\partial p_{\ell}}{\partial z} + \mu_{\ell} \left[\frac{1}{r} \frac{\partial}{\partial r} \left(r \frac{\partial w_{\ell}}{\partial r} \right) + \frac{\partial^2 w_{\ell}}{\partial z^2} \right] - \frac{\mu_{\ell} \epsilon_z w_{\ell}}{K_z} \quad (1.5)$$

$$\rho_{\ell}^v \frac{\partial v_{\ell}}{\partial r} + \rho_{\ell}^w \frac{\partial v_{\ell}}{\partial z} = - \frac{\partial p_{\ell}}{\partial r} + \mu_{\ell} \left[\frac{\partial}{\partial r} \left(\frac{1}{r} \frac{\partial (v_{\ell} r)}{\partial r} \right) + \frac{\partial^2 v_{\ell}}{\partial z^2} \right] - \frac{\mu_{\ell} \epsilon_r v_{\ell}}{K_r} \quad (1.6)$$

$$\rho_{\ell}^{c_{p,\ell}} \left(v_{\ell} \frac{\partial T_{\ell}}{\partial r} + w_{\ell} \frac{\partial T_{\ell}}{\partial z} \right) = k_{\text{eff}} \left[\frac{1}{r} \frac{\partial}{\partial r} \left(r \frac{\partial T_{\ell}}{\partial r} \right) + \frac{\partial^2 T_{\ell}}{\partial z^2} \right] \quad (1.7)$$

For only a capillary jacket when the pores in the isotropic wicking material are completely filled with liquid,

$$\begin{aligned} \epsilon_r &= \epsilon_z = \epsilon \\ K_r &= K_z = K \end{aligned} \quad (1.8)$$

The above assumption was made in all the numerical results presented in this paper. The method of calculating the effective thermal conductivity of the wick, k_{eff} , from the thermal conductivity of the solid and liquid phases are given by Chi (1976),

$$k_{\text{eff}} = \frac{k_{\ell} [(k_{\ell} + k_s) - (1 - \epsilon) (k_{\ell} - k_s)]}{[k_{\ell} + k_s) + (1 - \epsilon) (k_{\ell} - k_s)]} \quad (1.9)$$

The steady state energy equation that describes the temperature in the heat pipe wall is:

$$\frac{\partial}{\partial z} \left[k_w \frac{\partial T_w}{\partial z} \right] + \frac{1}{r} \frac{\partial}{\partial r} \left[k_w r \frac{\partial T_w}{\partial r} \right] = 0 \quad (1.10)$$

where k_w is the local thermal conductivity of the heat pipe wall. The boundary conditions are:

$$w(0,r) = v(0,r) = 0 \quad (1.11)$$

$$w(LT,r) = v(LT,r) = 0 \quad (1.12)$$

$$w(z,a) = 0 \quad (1.13)$$

$$w(z,b) = 0 \quad (1.14)$$

$$v(z,a) = \frac{-k_{\text{eff}} \frac{\partial T_{\ell}}{\partial r} \Big|_{r=a} + k_v \frac{\partial T_v}{\partial r} \Big|_{r=a}}{\rho_v h_{fg}} \quad (1.15)$$

$$v(z,b) = 0 \quad (1.16)$$

$$\frac{\partial T}{\partial z} (0,r) = \frac{\partial T}{\partial z} (LT,r) = 0 \quad (1.17)$$

$$T(z,a) = \frac{1}{\frac{1}{T_0} - \frac{R}{h_{fg}} \ln \frac{p_v}{p_0}} \quad (1.18)$$

$$k_w \frac{dT_w}{dr} (z,c) = \frac{Q}{A} (z) \quad (1.19)$$

In boundary condition (1.19), the heat flux was constant under the active evaporators and zero in all adiabatic and transport sections and the inactive evaporators. In the condenser section, the heat flux was assumed to be uniform based on the total heat input through the evaporators. The temperature along the vapor-liquid interface is taken as the equilibrium saturation temperature corresponding to its equilibrium pressure condition. By the above procedure, the effect of energy conduction in the heat pipe wall and the liquid flow in the wick is taken into account.

For simplicity and generality, the problem should be solved using conjugate heat transfer analysis as a single domain problem. To achieve this, one should generalize the conservation equations for mass, momentum and energy such that each conservation equation should have the same source term for the energy equation in terms of temperature as a dependent variable for the three regions (i.e., wall, wick and vapor). In addition, the continuity of temperature, heat flux and mass flux should be satisfied at each of the interfaces as well as some special boundary conditions like the no-slip condition, thermodynamic equilibrium, etc. The following approach is not only very beneficial for those who develop their own computer program to solve this heat pipe problem, but also for those who wish to use the existing commercial codes to set up this problem.

The energy equation can be written in terms of temperature as

$$\rho \frac{DT}{Dt} = \frac{k}{c_p} \nabla^2 T + \frac{S}{c_p} \quad (1.20)$$

Here S is the source term which includes viscous dissipation and pressure work. It should be noted that solving the problem in terms of enthalpy does not preserve the condition of temperature continuity at an interface when harmonic averaging is employed and leads to an incorrect calculation of diffusion.

For the vapor region, the energy equation is

$$\rho_v \frac{DT}{Dt} = \frac{k_v}{c_{p,v}} \nabla^2 T + \frac{S}{c_{p,v}} \quad (1.21)$$

Multiplying both sides of the energy equation for the liquid-wick region by $c_{p,\ell}/c_{p,v}$ results in

$$\rho_\ell \frac{c_{p,\ell}}{c_{p,v}} \frac{DT}{Dt} = \frac{k_\ell}{c_{p,v}} \nabla^2 T + \frac{S}{c_{p,v}} \quad (1.22)$$

Similarly, the energy equation for the heat pipe wall is

$$\rho_w \frac{c_{p,w}}{c_{p,v}} \frac{DT}{Dt} = \frac{k_w}{c_{p,v}} \nabla^2 T + \frac{S}{c_{p,v}} \quad (1.23)$$

From this transformation, we observe the following:

- 1) The source term for the energy equation is divided by $c_{p,v}$ for all three regions.
- 2) One needs to set up the density equal to the modified density ρ^* for different regions, i.e., ρ_v for vapor, $\rho_\ell c_{p,\ell}/c_{p,v}$ for liquid and $\rho_w c_{p,w}/c_{p,v}$ for solid.
- 3) The diffusion coefficients contain only one c_p , namely, $c_{p,v}$. The transformation makes possible an exact representation of diffusion across an interface when the harmonic average is used for the diffusion coefficient at the interfaces.

The momentum equation for the vapor flow does not need any special treatment since $\rho^* = \rho_v$ in the vapor region. In the wick region, the momentum equation can be transformed in the same manner.

$$\rho^* \frac{D\vec{V}}{Dt} = -\nabla p^* + \nu_\ell \rho^* \nabla^2 \vec{V} - \frac{\nu_\ell \rho^* \epsilon \vec{V}}{K} \quad (1.24)$$

We observe the following:

- 1) A source term should be added in the momentum equation for the porosity effect in the wick region.
- 2) The pressure solved for is the modified pressure p^* , which is proportional to the actual pressure. The actual pressure drop between two points in the flow fluid can be calculated as $\Delta p = c_{p,v}/c_{p,\ell} \Delta p^*$

The transformed continuity equation can be written as

$$\nabla \cdot (\rho^* \vec{V}) = 0 \quad (1.25)$$

The finite-difference iteration method of solution developed by Spalding (1980) is employed in the solution of the elliptic governing equations (1.1-1.10) subjected to the boundary conditions (1.11-1.19). In this methodology, finite-domain equations are derived by integration of the differential equations over a control volume surrounding a grid node. The source terms due to viscous dissipation and pressure work in the energy equation, and the source term due to the porous matrix in the momentum equation are linearized, and the "SIMPLEST" practice (Spalding, 1980) was employed for the momentum equations. The solution procedure is based on a line-by-line iteration method in the axial direction and the Jacobi point-by-point procedure in the radial direction.

The energy equation is not continuous at the vapor-liquid interface due to the latent heat of evaporation and condensation. The term $\dot{m} h_{fg}$ must be added as a source term in the energy equation at the vapor-liquid interface. For the first few iterations, it was assumed the heat flux at the liquid-vapor interface is equal to the outer wall heat flux. An exact energy balance given by eqn. (1.15) is satisfied after these initial iterations.

The computation proceeded until the sum of the absolute volumetric errors over the whole field was negligibly small ($\leq 10^{-6}$). The numerical results were also tested for grid independence by systematically varying the number of grids in both the r- and z-directions. For the numerical

results presented here, the final grid sizes for all of the cases presented were chosen as follows: $100 \times (20 + 5 + 10) = (\text{axial}) \times [(\text{radial vapor}) + (\text{radial liquid-wick}) + (\text{radial solid wall})]$.

1.4 EXPERIMENTAL APPARATUS AND PROCEDURE

The objective of this project was to determine the operating characteristics and performance of a low temperature heat pipe with multiple heat sources. The low temperature heat pipe was a copper-water heat pipe designed to operate at a vapor temperature of 60-100°C. The compatibility and efficiency of the copper-water heat pipe is well-documented in heat pipe literature.

The low temperature heat pipe shell and end caps were fabricated from standard composition copper (UNS-C12200). The heat pipe shell is 1000 mm in length with an outside diameter of 25.4 mm, and a wall thickness of 1.7 mm. The ends of the heat pipe shell were machined so that the end caps fit snugly. A simple circumferential screen wick consisting of two wraps of 50 per inch mesh copper screen was installed to provide a liquid return path to the evaporators. A summary of the design specifications for the heat pipe is given in Table 1.1.

All of the heat pipe parts were carefully fitted, cleaned, and deoxidized using standard procedures (Chi, 1976), and the end caps were brazed to the heat pipe shell using Harris 15 filler rod. The interior of the heat pipe was protected from oxidation during brazing with a cover layer of hydrogen. A bellows type valve was attached to the heat pipe fill tube to facilitate sealing, purging, and charging of the fluid inventory

TABLE 1.1
DESIGN SUMMARY OF THE LOW TEMPERATURE HEAT PIPE
WITH MULTIPLE HEAT SOURCES

Container material	copper
Wick material	copper
End cap material	copper
Length	1000 mm
Container O.D.	25.4 mm
Container I.D.	22.0 mm
End cap thickness	3.175 mm
Screen mesh number	$1.97 \times 10^3 \text{ m}^{-1}$ (50 mesh)
Screen wire diameter	.178 mm
Screen wick thickness	.712 mm
Vapor core diameter	20.5 mm
Working fluid	distilled water
Fluid charge	40 cm ³
Evaporator length [*]	(4) @ 63.5 mm
Transport length	180 mm
Condenser length ^{**}	300 mm

* Evaporators separated by 75.3 mm adiabatic sections, with a 20 mm adiabatic section between the evaporator end cap and evaporator 1.

** 20 mm adiabatic section between the condenser and the condenser end cap.

inside the heat pipe.

The heat pipe has four independently controlled evaporators in the evaporator section. Each evaporator consists of a 63.5 mm long 257 watt Minco Thermofoil heater clamped to the heat pipe (Fig. 1.1b). Power input for each heater was supplied by a 120 volt variable ac transformer and measured with a Fluke 77 multimeter which has an accuracy of approximately $\pm 2\%$ of the reading. Heat was removed from the condenser section by a 300 mm long copper water-cooled manifold calorimeter mounted to the heat pipe. Thermocouples in the calorimeter inlet and outlet and mass flow measurements were used to calculate the power output from the calorimeter, which was compared to the electrical input power so that accurate heat pipe power levels were obtained.

All heat pipe vapor and wall temperatures were measured with standard Type K thermocouples, which have an accuracy of $\pm 2.2^{\circ}\text{C}$ or 0.75% of the reading, whichever is greater. There were thirteen wall thermocouples and six vapor space thermocouples (Fig. 1.1b). Wall temperatures in the adiabatic sections were measured with beaded thermocouples clamped to the heat pipe shell. Four sheathed thermocouples were soft-soldered to the heat pipe wall within the calorimeter. These thermocouples exit the calorimeter through shallow grooves machined in the heat pipe wall. Wall temperatures at the axial center of each evaporator were measured with sheathed thermocouples soft-soldered to the heat pipe shell. These thermocouples exit the evaporator sections through a shallow groove in the heat pipe wall. The heat pipe was evacuated to a pressure of 10^{-7} torr prior to wall thermocouple soldering to prevent interior oxidation. Vapor

temperatures were measured with a 4.7 mm diameter type 316 stainless steel sheathed multipoint thermocouple mounted axially within the heat pipe vapor space. The multipoint thermocouple exits the heat pipe through a tube in the evaporator end cap and was swaged in place to provide a leak-tight seal.

After the installation of all thermocouples and heaters, the heat pipe was processed in a specially built heat pipe filling station. The heat pipe was evacuated to a pressure of 10^{-7} torr and filled with 40 cm³ of degassed, distilled water.

A schematic of the test setup is shown in Fig. 1.2. The heat pipe was mounted horizontally on an optical bench. The optical bench was equipped with adjustable base plates to allow for precise leveling of the heat pipe assembly. The thermocouples were read by a Fluke 2285B Data Logger. Cooling water was supplied to the calorimeter by a centrifugal pump connected to a constant head reservoir in order to maintain a steady coolant flow. A coolant pre-heater was located prior to the calorimeter inlet to allow greater flexibility in the heat pipe operating temperature. The entire length of the heat pipe assembly was insulated with 2 inches of Fiberfrax ceramic fiber insulation.

Tests were performed to establish the maximum heat transport capacity of the heat pipe with variable heat input rates and locations when the heat pipe was horizontal. The operating vapor temperature was held between 65°C and 85°C. Energy balances between the heat input by the heaters and the heat removed by the calorimeter were monitored to ensure an energy balance

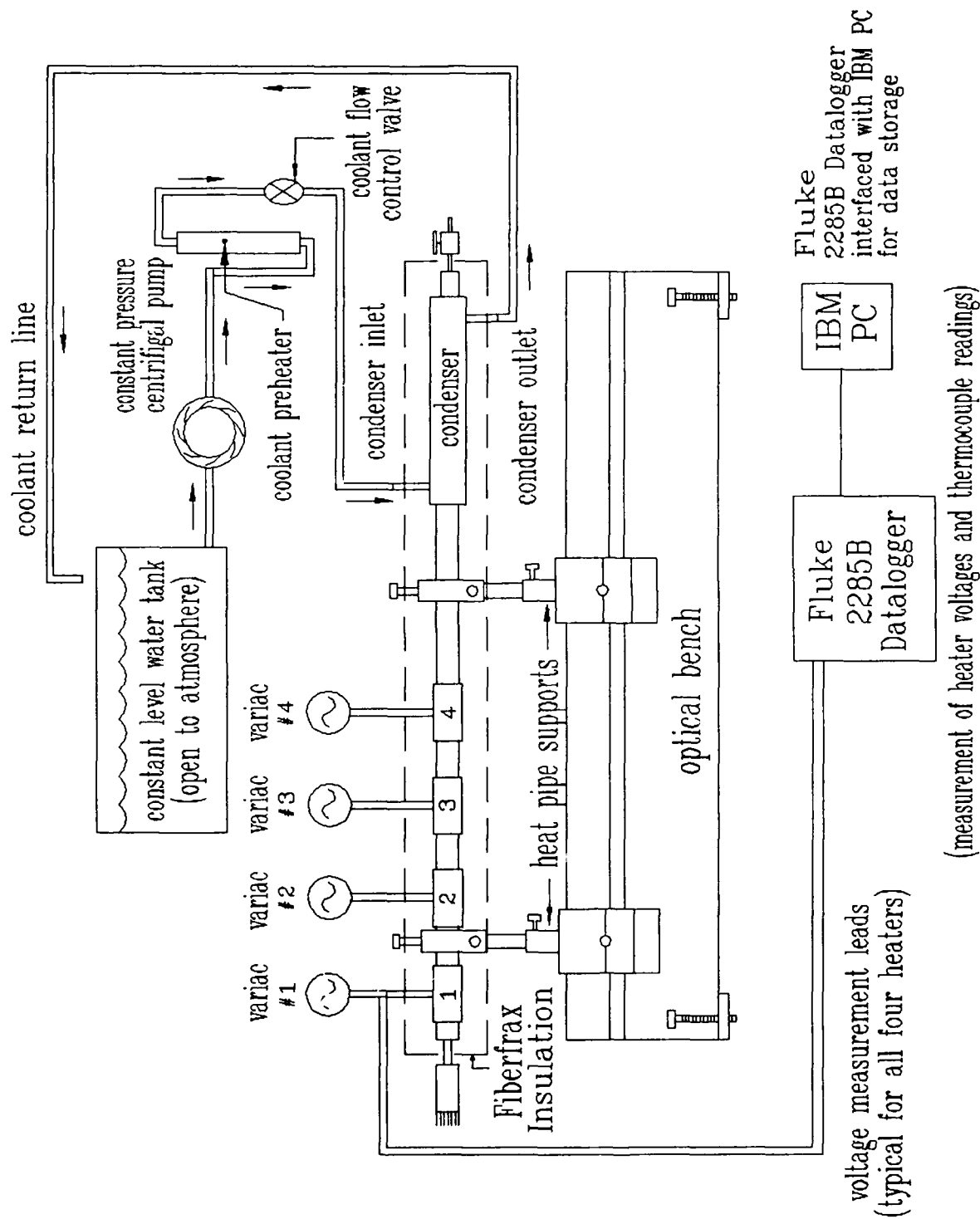


Figure 1.2 Low Temperature Heat Pipe with Multiple Heat Sources Experimental Test Setup

of at least 90% during steady state operation.

The primary interest in these tests was to determine the capillary limit of the heat pipe in multiple evaporator operation. Because the evaporator located farthest from the condenser will experience dry-out first, all multiple evaporator tests were performed with some combination of evaporator 1 and the other evaporators. The maximum heat transport capacity, or capillary limit, of the heat pipe was defined as a sudden, rapid, and continuous increase in the wall temperature of evaporator 1.

1.5 RESULTS AND DISCUSSION

The heat pipe was first operated in the single evaporator mode in order to establish the capillary limits of the heat pipe at all four heat input locations. The capillary limit for the evaporator farthest from the condenser, evaporator 1, was found to be 181 watts. Limits for evaporators 2, 3, and 4 were greater than the maximum power levels that the heaters could deliver, which was 250 watts. Figure 1.3 shows the difference between the evaporator wall temperature and the vapor temperature ($\Delta T_{\text{wall-vapor}}$) versus the power input for each single evaporator test. The single evaporator tests show that the $\Delta T_{\text{wall-vapor}}$ increases linearly with increasing power, and that the heat pipe can successfully operate with a high $\Delta T_{\text{wall-vapor}}$.

The test matrix, Table 1.2, shows the experimentally determined capillary limits for the heat pipe in the single and multiple evaporator operating modes. All of the multiple evaporator tests were performed with evaporator 1 in combination with the other evaporators, since the single

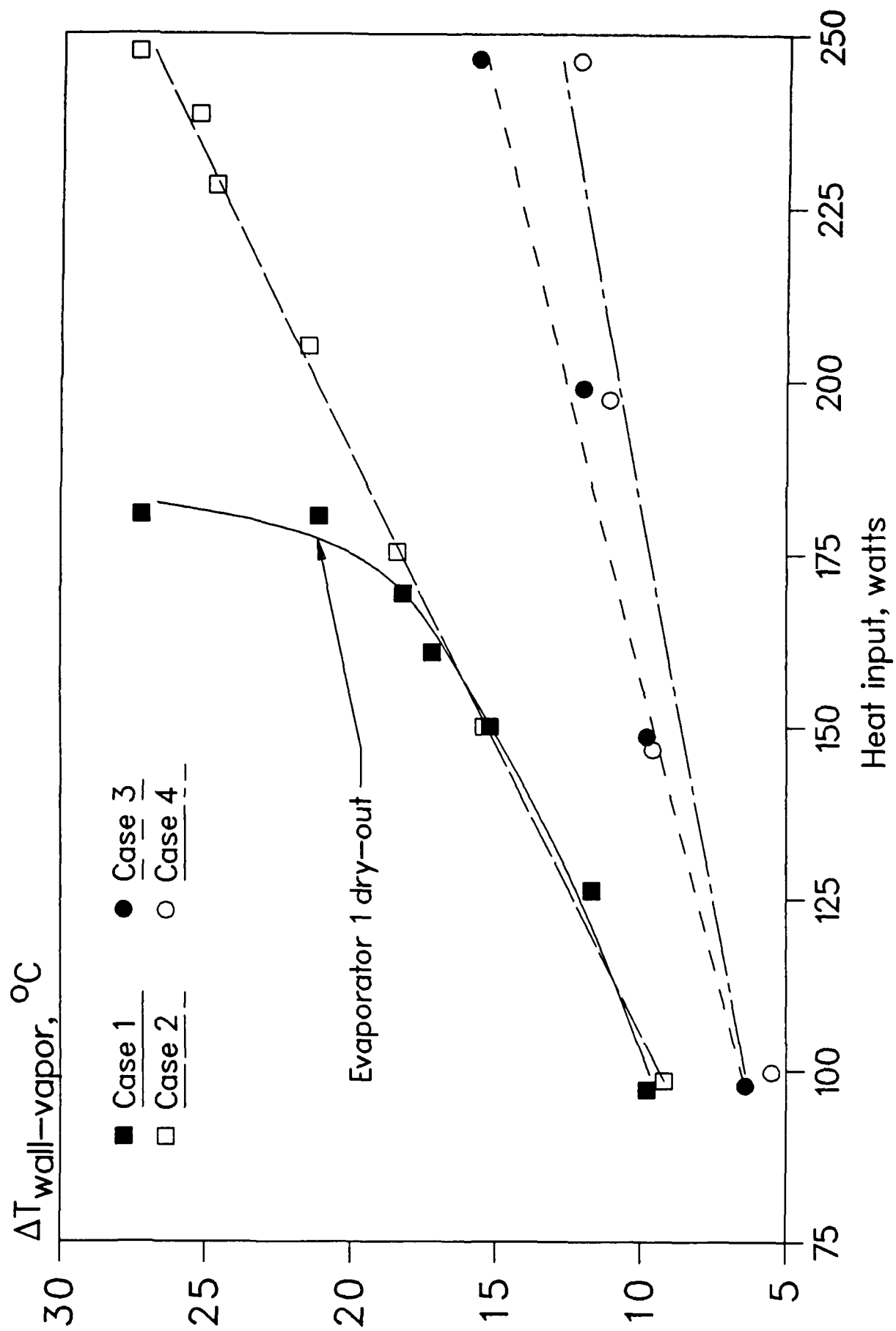


Figure 1.3. $\Delta T_{\text{wall-vapor}}$ versus heat input for different single evaporator operations

TABLE 1.2
LOW TEMPERATURE HEAT PIPE WITH MULTIPLE
HEAT SOURCES TEST MATRIX

Power listed is experimental capillary limit⁺⁺

Power in Evaporator (watts)

Case	1	2	3	4	Total Power
1	181	-	-	-	181
2	-	>247 *	-	-	>247 *
3	-	-	>246 *	-	>246 *
4	-	-	-	>246 *	>246 *
5	119	118	-	-	237
6	112	112	110	-	334
7	97	98	99	98	392
8	161	-	160	-	321
9	150	-	-	149	299
10	97 **	-	-	>245 *	>342 *
11	100 **	-	250	-	350
12	102 **	182	-	-	284

⁺⁺ The capillary limit for multiple evaporator operation was defined as a sudden, rapid and continuous increase in the wall temperature in evaporator 1.

*

The capillary limit was not reached in cases 2, 3, 4, and 10 due to the maximum power level limitations of the heaters.

** In cases 10, 11, and 12 evaporator 1 was held constant at 100 watts (nominal).

evaporator tests indicated that the evaporator located farthest from the condenser had the lowest capillary limit. Figures 1.4 - 1.7 show typical plots of wall and vapor temperatures versus axial location for the heat pipe in multiple evaporator operation for cases 1, 5, 6, and 7, respectively, at power loads significantly less than the capillary limit. The numerical results based on the mathematical modeling presented in this paper are also shown in Figures 1.4-1.7 which show good agreement with experimental data for the wall and vapor temperatures along the heat pipe. In the condenser section, it can be seen that the experimental and numerical values of the outer wall temperature do not coincide. This is due to the assumption of a constant heat flux along the condenser section at the outer wall, which is not precisely correct in this particular design, and the fact that the thermocouples mounted on the condenser wall may be affected by the cooling water circulating in the calorimeter. Near the evaporator end cap, the outer wall temperature can be seen to decrease from the center of evaporator 1 to the end cap. The reason for this is the 20 mm unheated length between the evaporator end cap and evaporator 1. It should be noted, however, that even though the outer pipe wall is adiabatic in the unheated lengths, these sections still act as evaporators due to axial conduction.

In Figs. 4.5-4.7, the experimental wall temperatures in the center of the active evaporators decrease closer to the condenser, but the numerical model predicts that these peak temperatures are all nearly the same. Again, this is due to the assumption of a constant heat flux at the outer wall in the condenser section. Since the heat pipe is a closed system, the downstream boundary conditions can affect the temperature, velocity, and

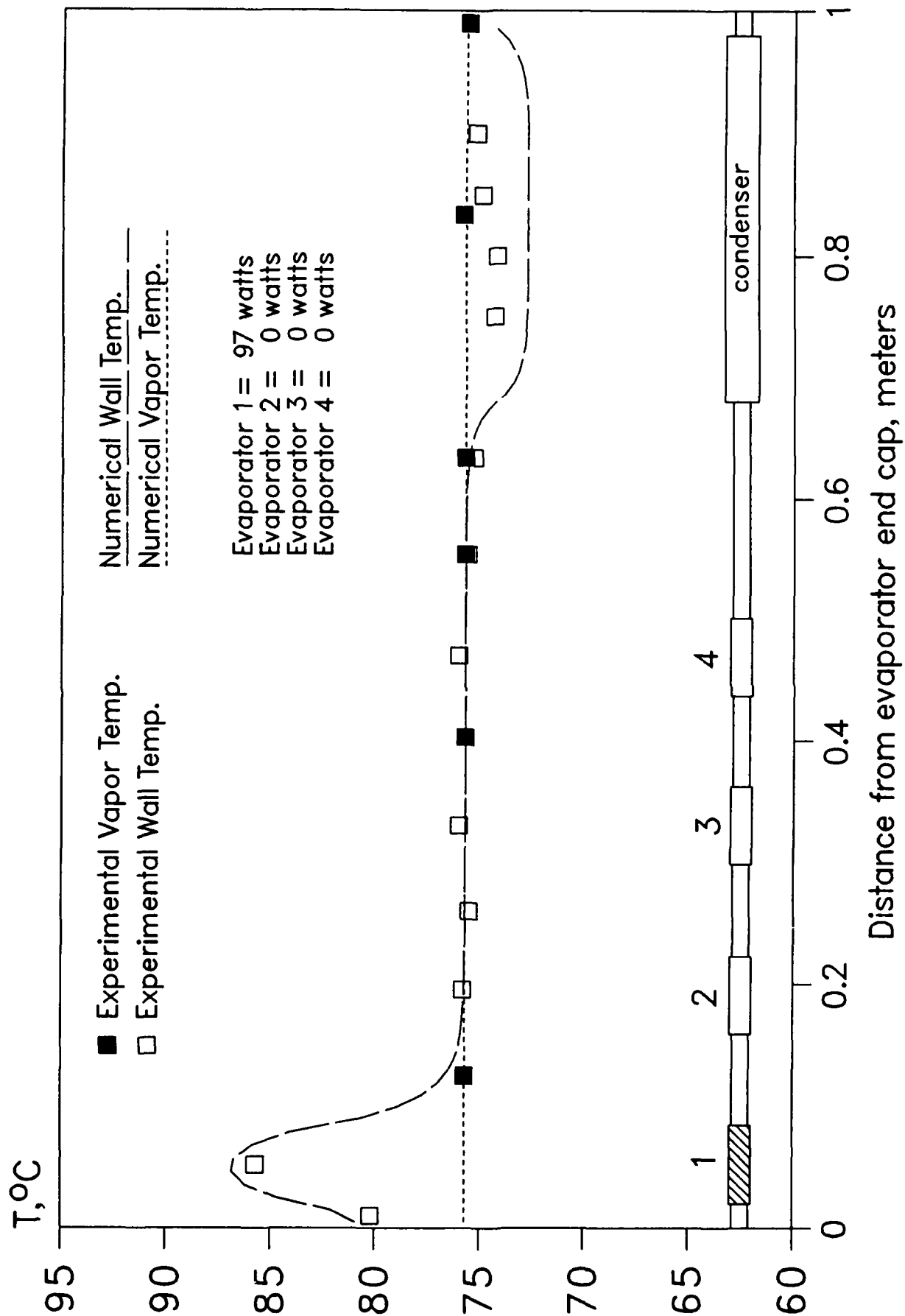


Figure 1.4. Heat pipe wall and vapor temperatures versus axial location for Case 1

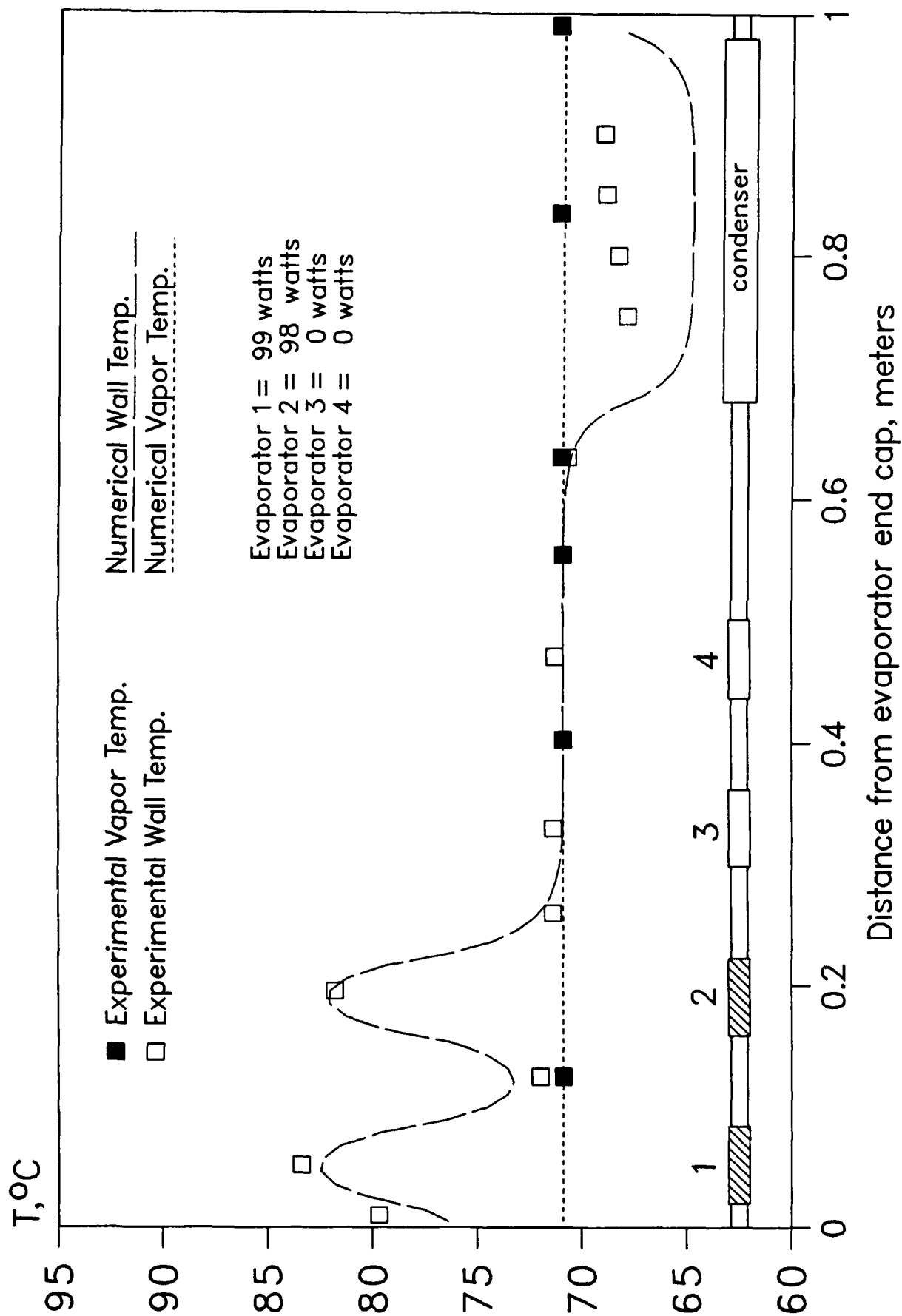


Figure 1.5. Heat pipe wall and vapor temperatures versus axial location for Case 5

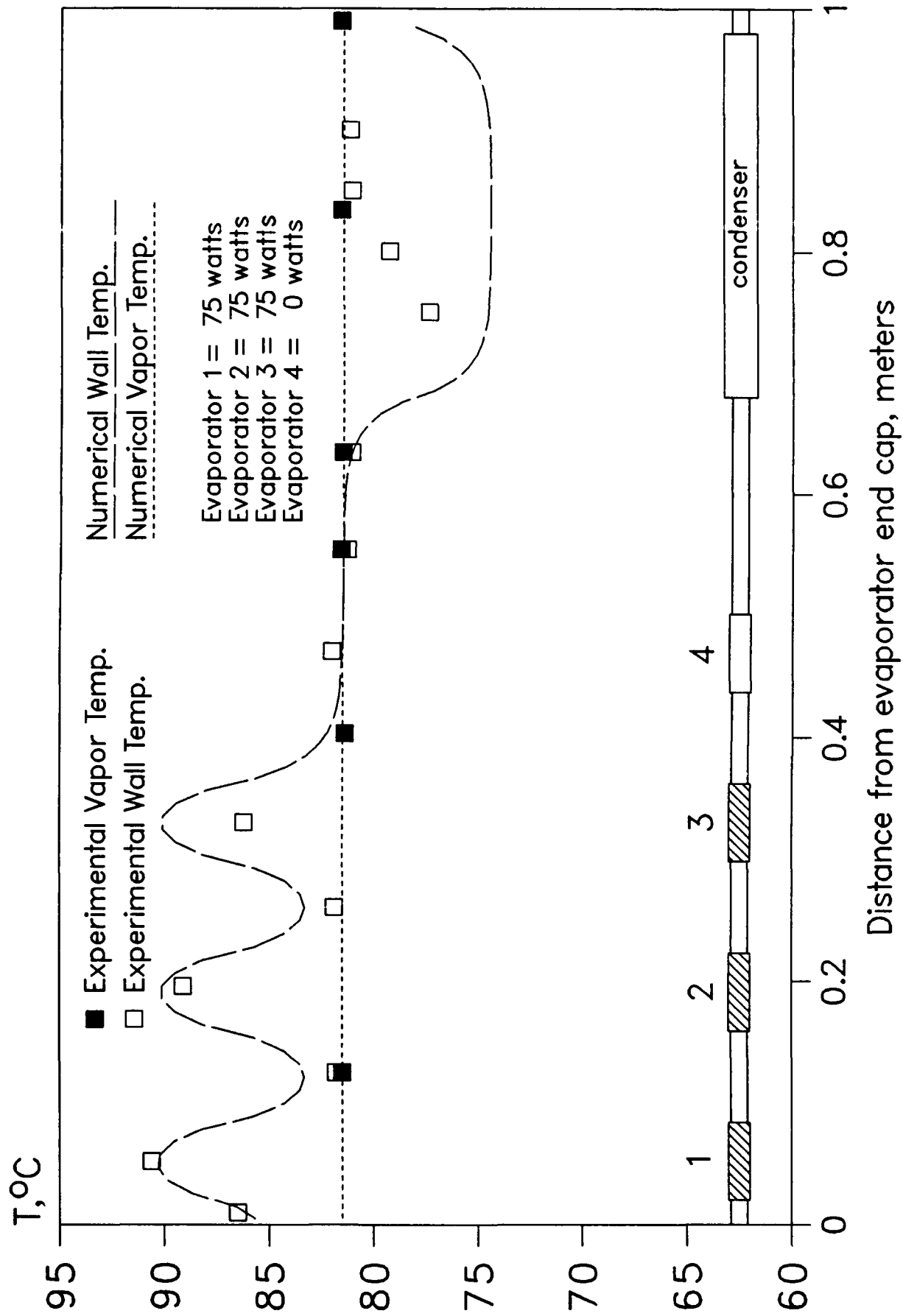


Figure 1.6. Heat pipe wall and vapor temperatures versus axial location for Case 6

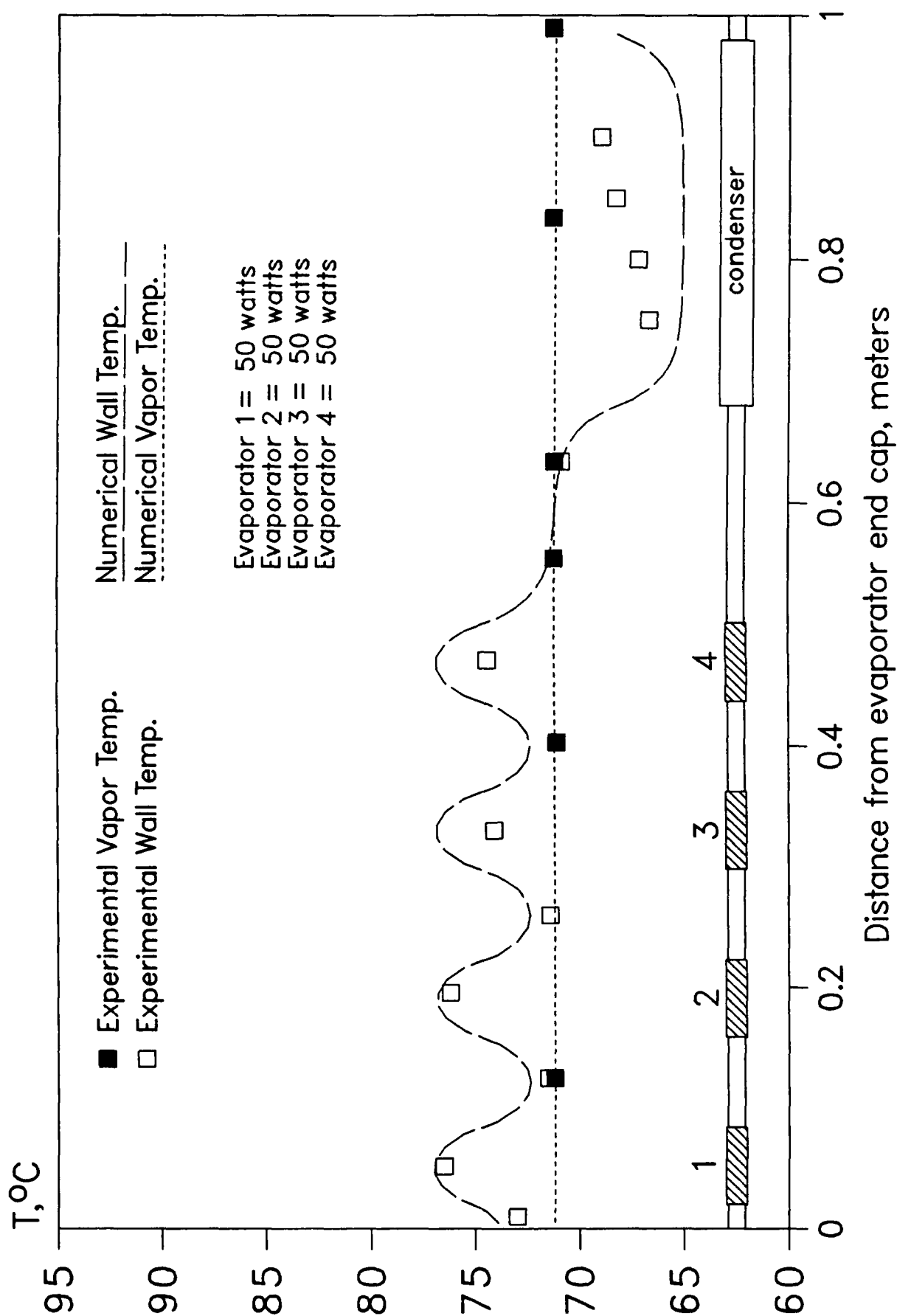


Figure 1.7. Heat pipe wall and vapor temperatures versus axial location for Case 7

density upstream.

In cases 5-9 the heat pipe was operated with uniformly increasing power to each evaporator until dry-out occurred in evaporator 1. Cases 5, 6, and 7 indicate that the total heat load on the heat pipe can be significantly increased by adding evaporators, although the maximum heat flux for evaporator 1 decreases as evaporators are added downstream (i.e., toward the condenser section).

In cases 10-12 the power input to evaporator 1 was held at a constant 100 watts, while the power input to evaporators 2, 3 or 4 was increased uniformly. Figures 1.8 and 1.9 show that $\Delta T_{\text{wall-vapor}}$ in evaporator 1 remains relatively constant as the total heat load on the heat pipe is increased for cases 11 and 12, respectively, then evaporator 1 suddenly dries out when a specific downstream power level is reached. This maximum downstream power level decreases as the second evaporator moves farther away from the condenser.

Bienert et al. (1977) demonstrated a jet pump-assisted arterial heat pipe in which a venturi located in the vapor space maximized capillary pumping by providing a low pressure source to the evaporator end of the heat pipe artery. Similarly, the addition of one or more evaporators near the condenser of a heat pipe will provide a pressure drop in the wick and increase the liquid mass flow rate, while the loss of capillary pressure in the wick due to the additional evaporators is minimal given their proximity to the condenser. This argument can be applied to cases 8 and 9 that show the addition of one downstream evaporator increases the heat capacity of

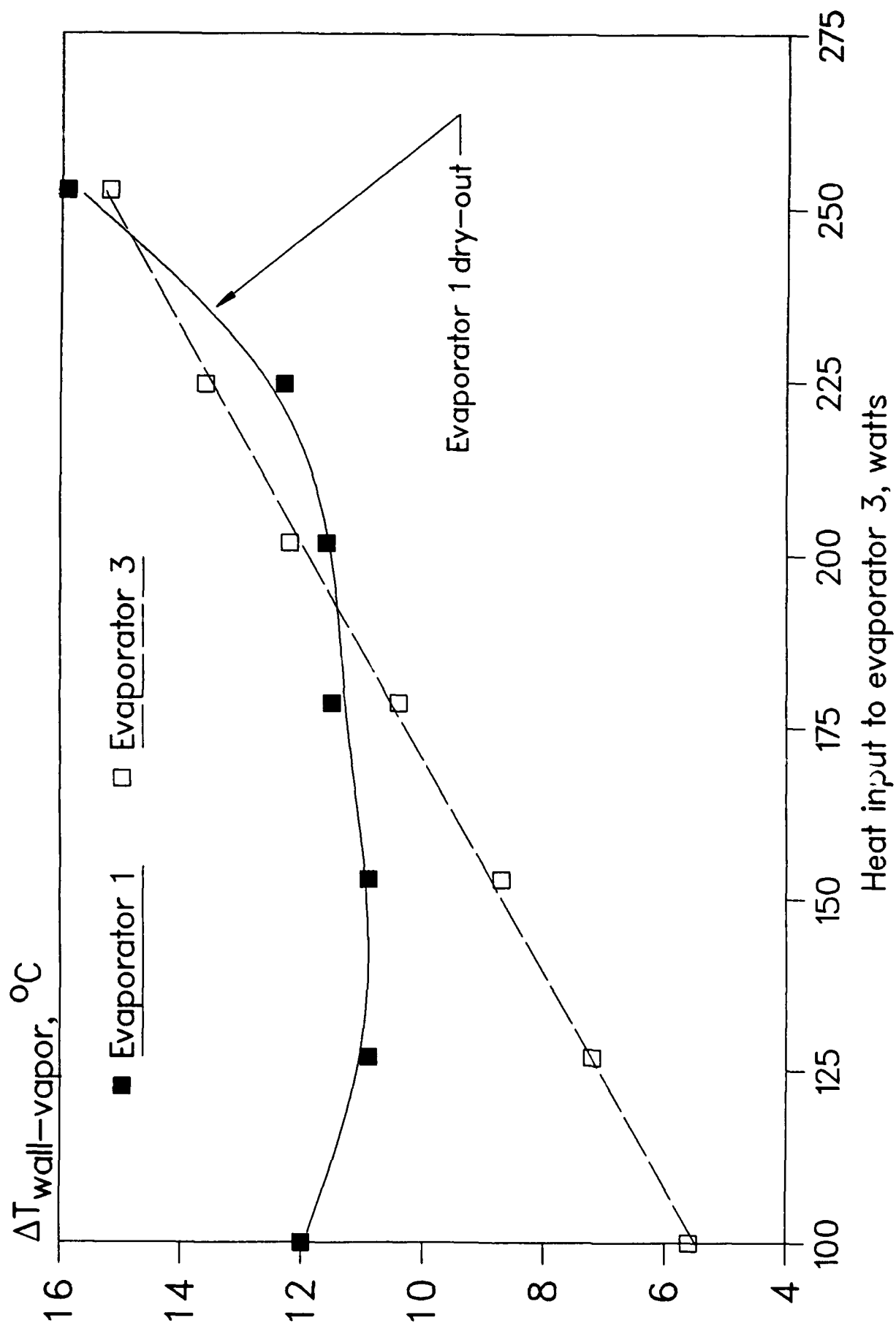


Figure 1.8. $\Delta T_{\text{wall-vapor}}$ versus heat input to evaporator 3 with heat input to evaporator 1 held constant at 100 watts for Case 11

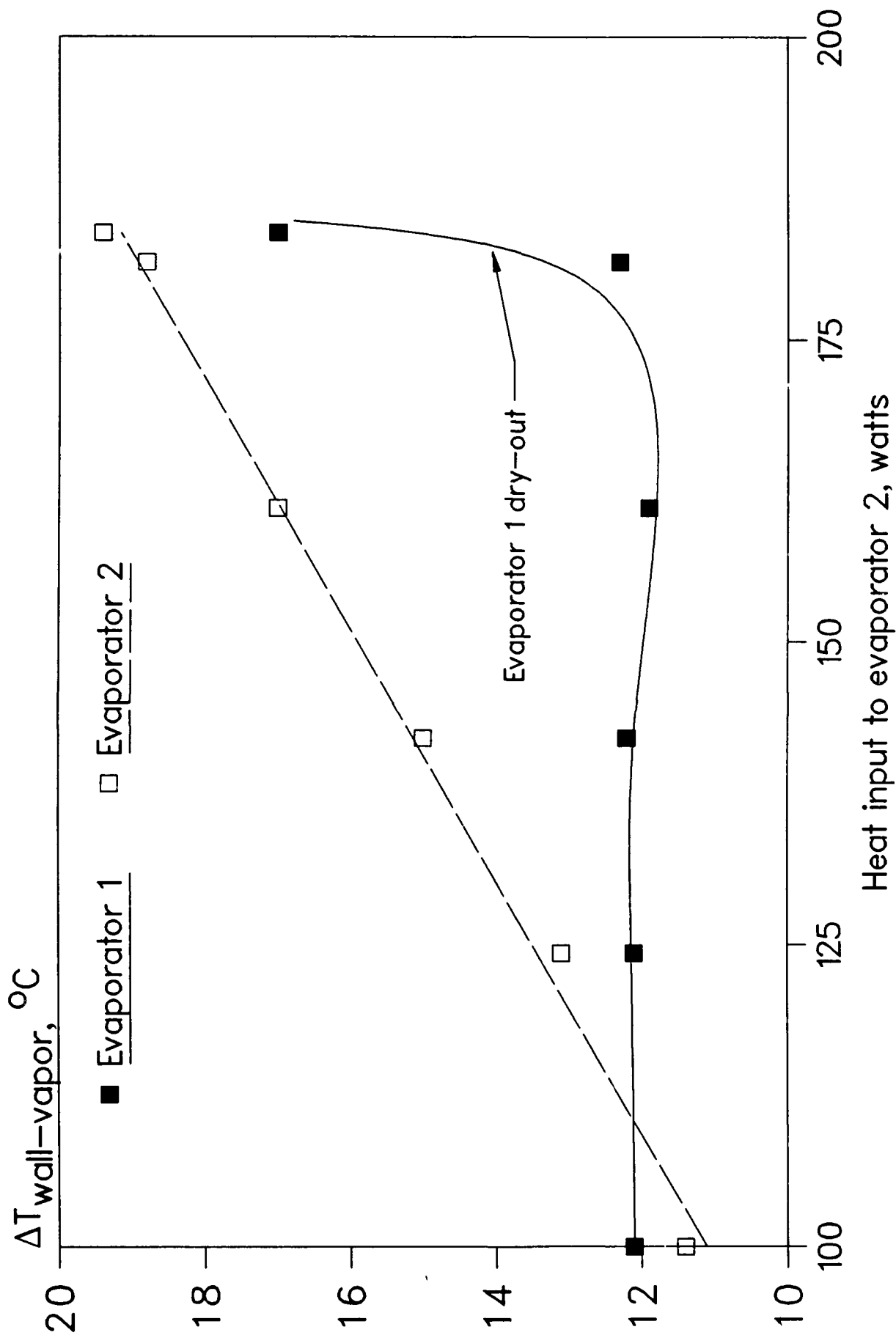


Figure 1.9. $\Delta T_{\text{wall-vapor}}$ versus heat input to evaporator 2 with heat input to evaporator 1 held constant at 100 watts for Case 12

the heat pipe by 40% over the single evaporator case 1. It is also true that in the case of multiple heat sources, one is reducing the effective length of the heat pipe and therefore increasing the total heat capacity.

1.6 CONCLUSIONS

A complete two-dimensional numerical modelling of heat pipes with multiple heat sources including the heat conduction in the wall, fluid flow is a porous media for the screen wick as well as compressible vapor flow as a conjugate problem is given. This methodology can be easily extended to predict the performance of capillary pumped loops as well.

A simple circumferential screen-wick copper-water heat pipe with multiple heat sources has also been fabricated and successfully tested. These tests show that the maximum total heat load on the heat pipe varies greatly with the location of the local heat fluxes. Significant heat loads can be carried by evaporators close to the condenser without affecting the operation of upstream evaporators, but adding additional evaporators to the heat pipe lowers the maximum heat flux capacity of the evaporator located farthest from the condenser. The evaporator wall-vapor temperature difference seems to be mainly a function of the local heat flux, and cannot be used to predict the maximum heat capacity of the heat pipe operating in the multiple evaporator mode. The numerical results agree with the experimental results for wall and vapor temperatures along the heat pipe for cases with different heat distributions along the evaporator section.

Section II

HEAT TRANSFER IN LIQUID METALS BY NATURAL CONVECTION

2.1 SUMMARY

A numerical study of the natural convection in low Prandtl number fluids which are heated from below has been performed. Because of the limitations of experiments, a numerical study is needed to obtain temperature distributions prior to boiling and to study mechanisms of boiling incipience on the wall for fluids with very low Prandtl numbers. The finite-difference scheme SIMPLER was used to solve the steady two-dimensional governing equations with the Boussinesq approximation. The numerical results were compared to previous experimental results with an excellent agreement.

2.2 INTRODUCTION

Natural convection in horizontal enclosures with heating from below has been the subject of many numerical studies in recent years. However, little attention has been paid to the fluids having very low Prandtl numbers such as liquid metals (McDonough and Catton, 1982; Raithby and Hollands, 1985; Yang, 1987; Reed, 1987). McDonough and Catton (1982) studied natural convection using a mixed finite difference - Galerkin procedure in a horizontal square box which was heated from below, cooled from above and the side walls were insulated. They found that the numerical results with lower Pr did not converge as quickly as those with higher Pr, and the convergence is not monotonic. They believed that this is due to the increasing nonlinearity as the Prandtl number decreases. In the numerical results presented by McDonough and Catton (1982), the Prandtl numbers were not lower than $Pr = 0.71$. Obviously, further numerical studies in the low Prandtl number range are needed, which is one of the objectives of this paper.

For pool boiling and two-phase flow heat transfer, the temperature distribution in liquid metals is crucial to the operation and boiling incipience. In a gravitational environment, heat transfer in liquid metals prior to boiling incipience is a problem of natural convection combined with conduction, even for liquid metal layers with a thickness on the order of 10 mm. Because of the limitations of experiments, a numerical study is needed to obtain temperature distributions prior to boiling and to study mechanisms of boiling incipience on the wall for very low Prandtl numbers. This is another motivation of the present numerical study.

Many pool boiling and evaporation test sections for liquid metal layers can be modeled as a two-dimensional partial heating configuration as shown in Fig. 2.1, with the dimension perpendicular to the paper being infinitely long. A uniform heat flux along the heating element is specified. The upper liquid surface is kept at the saturation temperature $T_s = T_c$, corresponding to the system pressure, and is considered as a free surface in contrast with the rigid lower surface. The container wall except the heating element is insulated to prevent heat loss to the environment. Another alternative boundary condition for this problem is to specify a constant temperature $T_h > T_s$ at the lower surface, which has been used more often in the previous numerical studies.

In this paper, the natural convection of fluids having very low Prandtl numbers down to $Pr = 0.00125$ in enclosures with partial or full heating from below will be studied numerically, and the numerical results will be compared with the existing experimental data (Takenaka et al., 1983) and the empirical heat transfer equation (Raithby and Hollands, 1985), respectively.

2.3 FORMULATION AND NUMERICAL METHOD

The dimensionless governing equations for steady two-dimensional laminar flow of a Newtonian fluid with no dissipation under Boussinesq approximation can be written as follows:

$$\frac{\partial U}{\partial X} + \frac{\partial V}{\partial Y} = 0 \quad (2.1)$$

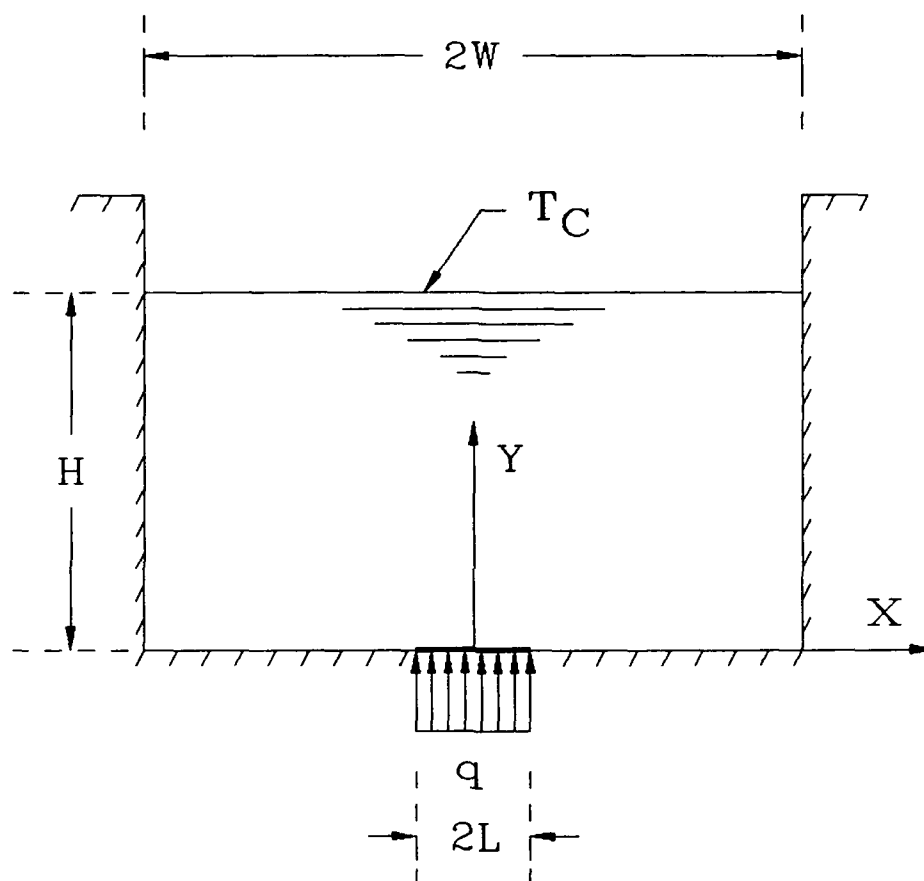


Fig. 2.1 Two-dimensional horizontal liquid metal layer with localized heating from below

$$\frac{\partial(U^2)}{\partial X} + \frac{\partial(UV)}{\partial Y} = - \frac{\partial P}{\partial X} + \text{Pr} \left(\frac{\partial^2 U}{\partial X^2} + \frac{\partial^2 U}{\partial Y^2} \right) \quad (2.2)$$

$$\frac{\partial(UV)}{\partial X} + \frac{\partial(V^2)}{\partial Y} = - \frac{\partial P}{\partial Y} + \text{Ra}_1 \text{Pr} \theta + \text{Pr} \left(\frac{\partial^2 V}{\partial X^2} + \frac{\partial^2 V}{\partial Y^2} \right) \quad (2.3)$$

$$\frac{\partial(U\theta)}{\partial X} + \frac{\partial(V\theta)}{\partial Y} = \frac{\partial^2 \theta}{\partial X^2} + \frac{\partial^2 \theta}{\partial Y^2} \quad (2.4)$$

with the following dimensionless variables:

$$X = \frac{x}{H} ; Y = \frac{y}{H} ; U = u \frac{H}{a} ; V = v \frac{H}{a} ; \theta = \frac{T - T_c}{T_c} ;$$

$$P = (p + \rho_0 g y) H^2 / \rho a^2 ; \text{Pr} = \nu / a ; \text{Ra}_1 = g \beta H^3 T_c / a \nu$$

where

$$\beta = - \frac{1}{\rho_0} (\rho - \rho_0) / (T - T_0)$$

For the partial heating from below, two geometrical parameters are needed:

$$B_1 = W/H, \text{ and } B_2 = L/H.$$

The boundary conditions for the constant heat flux and free upper surface shown in Fig. 2.1 are

$$V = 0, \quad \frac{\partial U}{\partial Y} = 0, \quad \theta = 0 \quad Y = 1, \quad -B_1 \leq X \leq B_1 \quad (2.5a)$$

$$V = U = 0, \quad \frac{\partial \theta}{\partial X} = 0 \quad 0 \leq Y \leq 1, \quad X = -B_1 \quad (2.5b)$$

$$V = U = 0, \quad \frac{\partial \theta}{\partial X} = 0 \quad 0 \leq Y \leq 1, \quad X = B_1 \quad (2.5c)$$

For the rigid lower boundary condition ($Y = 0$)

$$V = U = 0 \quad -B_1 \leq X \leq B_1 \quad (2.5d)$$

$$\frac{\partial \theta}{\partial Y} = -\frac{q H}{T_c k} \quad -B_2 \leq X \leq B_2 \quad (2.5e)$$

$$\frac{\partial \theta}{\partial Y} = 0 \quad -B_1 \leq X < -B_2 \quad \text{and} \quad B_2 < X \leq B_1 \quad (2.5f)$$

For the case of a constant temperature T_h at the lower surface, the dimensionless numbers θ and Ra_1 need to be changed as

$$\theta = \frac{T - T_c}{T_h - T_c} \quad \text{and} \quad Ra = \frac{g H^3 (T_h - T_c)}{\alpha \nu} \quad (2.5g)$$

The corresponding boundary condition (2.5e) is replaced by

$$\theta = 1 \quad -B_2 \leq X \leq B_2 \quad (2.5h)$$

The problem is specified mathematically by eqns. (2.1-2.5). The

solution procedure used for solving these equations is the finite-difference method SIMPLER, which has been described in detail by Patankar (1980, 1988). The power-law scheme is used for the convection-diffusion terms and the discretization equations are solved by using the tridiagonal matrix algorithm (TDMA or Thomas algorithm). Under-relaxation parameters are used to control the advancement of the solutions and to ensure convergence. The computer program was tested with different grid sizes for the same problem, and the solutions proved to be essentially independent of the grid sizes.

2.4 RESULTS AND DISCUSSION

2.4.1 Partial heating with constant heat flux

The numerical calculations were conducted with the configuration in Fig. 2.1, and the results of the temperature distribution at $x = 0$ were compared with the experimental data from Takenaka et al. (1983). The experiment was made with a horizontal potassium layer heated from below. The test vessel had a rectangular cross section of $140 \times 96 \text{ mm}^2$. The effective heating area in the center of the vessel is $100 \times 20 \text{ mm}^2$. The vertical liquid temperature distribution was measured by sliding thermocouples along the central line of the vessel. Since the length of the heating element is much larger than its width, the heat transfer can be modeled as two-dimensional natural convection within the configuration as shown in Fig. 2.1, with $B_1 = 1.70$, $B_2 = 0.360$, $q = 10^5 \text{ W/m}^2$ and $T_c = T_s = 527^\circ\text{C}$. The reference temperature T_0 is chosen as T_s and the relevant properties are given by Subbotin et al. (1972), thus giving $Pr = 0.004$ and $Ra_1 = 3.0 \times 10^6$. Figure 2.2 shows the comparison of the numerical temperature distribution at $x = 0$ and the experimental data of $H = 28 \text{ mm}$

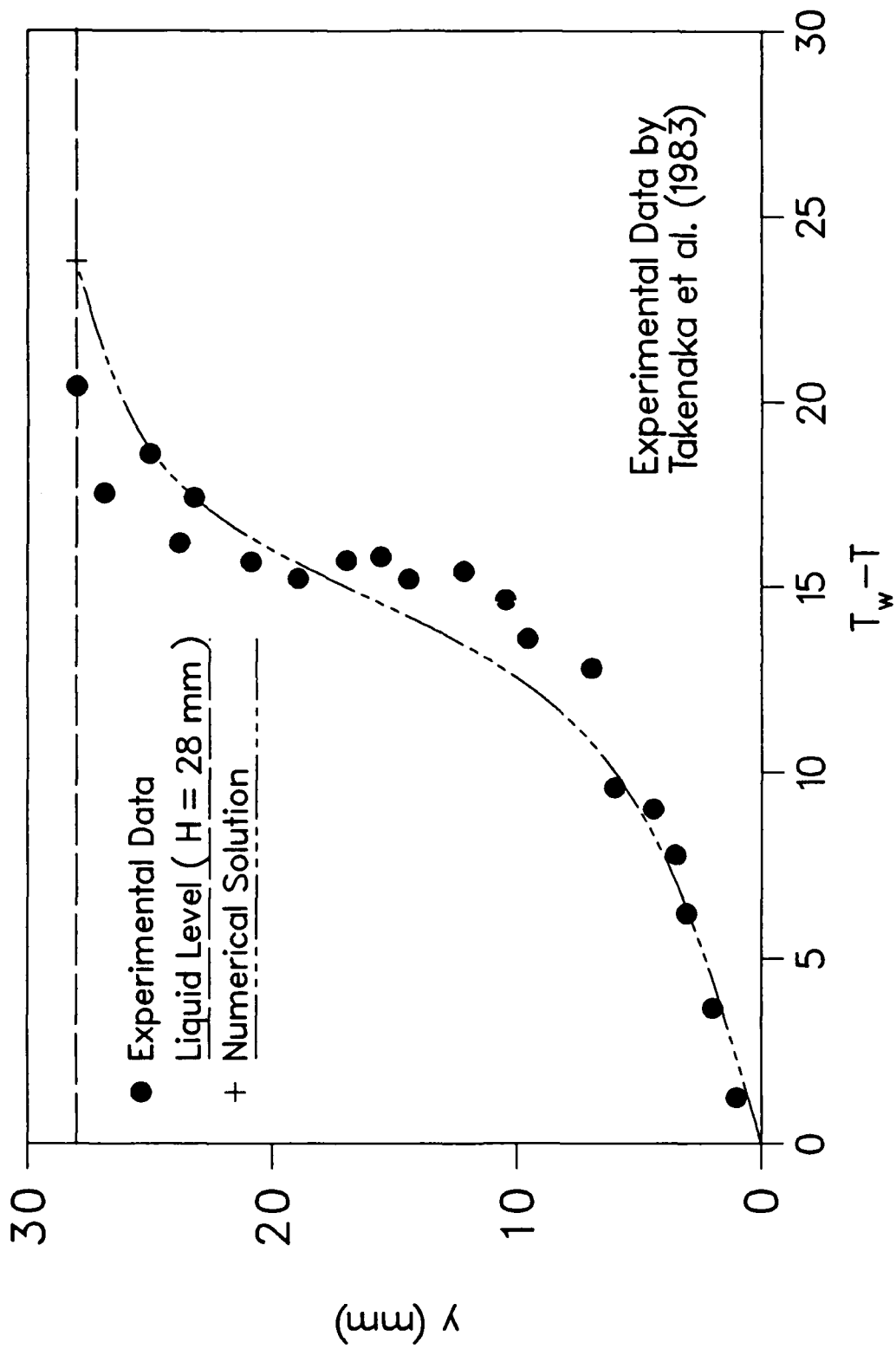


Figure 2.2. Comparison between the numerical solution and the experimental data

from Takenaka et al. (1983). It can be seen that the agreement is generally good and is excellent near the lower surface. The grid size used in the numerical calculation is 33×20 . The temperature distribution consists of the boundary region near the heating surface and the bulk region. The boundary thickness is relatively larger compared with those of ordinary fluids. Figures 2.3 and 2.4 show the corresponding temperature contours and dimensionless stream function contours, respectively. The isotherms and streamlines indicate that a plumelike flow is generated above the heated region, which is the normal case for natural convection in a liquid heated from below with a rigid or free upper surface (Prasad and Kulacki, 1987; Boehm and Kamyab, 1977).

Figure 2.5 shows the temperature distributions for sodium with different values of the heat flux q . Since the temperature of the upper free surface is fixed at T_c , higher values of the heat flux results in a higher T_w . For example, the T_w of the case with $q = 30 \text{ W/cm}^2$ is almost 50°C higher than that of the case with $q = 5 \text{ W/cm}^2$. Also, for the low heat flux the temperature field shifts towards the conduction regime with an almost linear temperature distribution.

In the numerical calculations, it was found that the convergence speed is much slower with lower values of the Prandtl number, as indicated by McDonough and Catton (1982) and Catton et al. (1974). Considering this fact, the calculations proceeded from higher to lower Prandtl numbers with the solutions of the higher Pr as the starting values for the lower Pr. Also, under-relaxation was needed to ensure convergent solutions. The

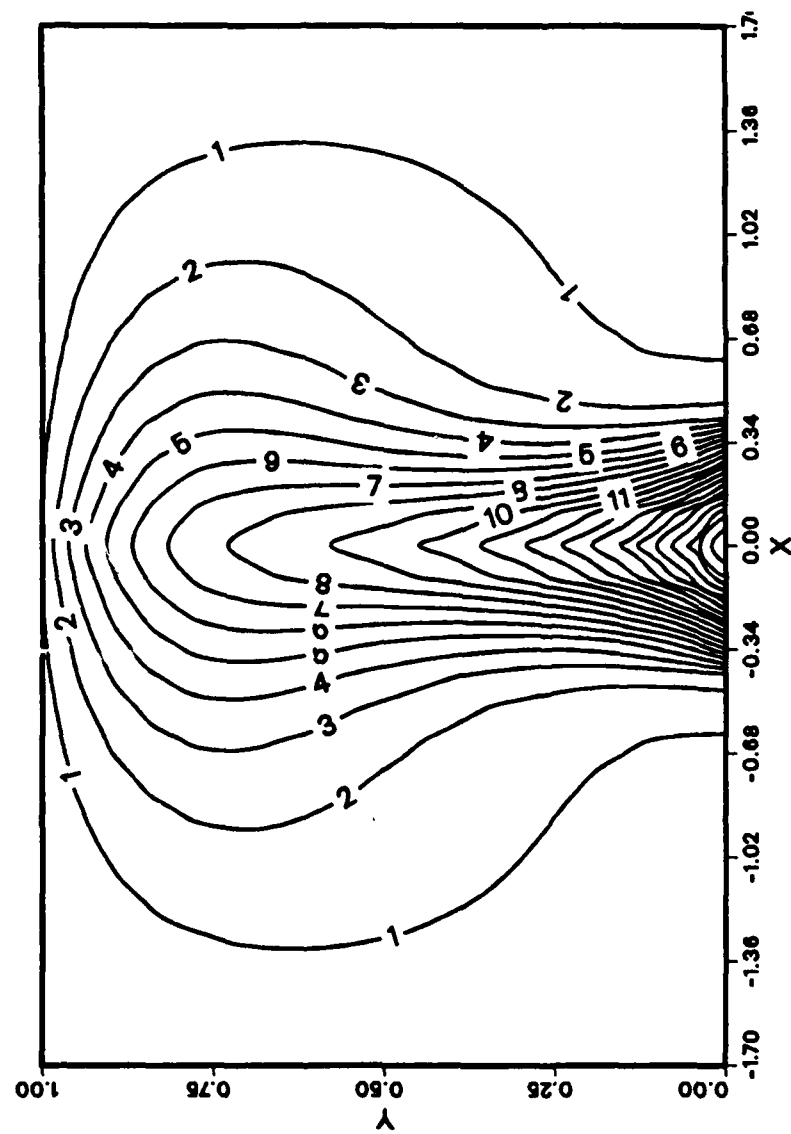


Figure 2.3. Calculated temperature contours

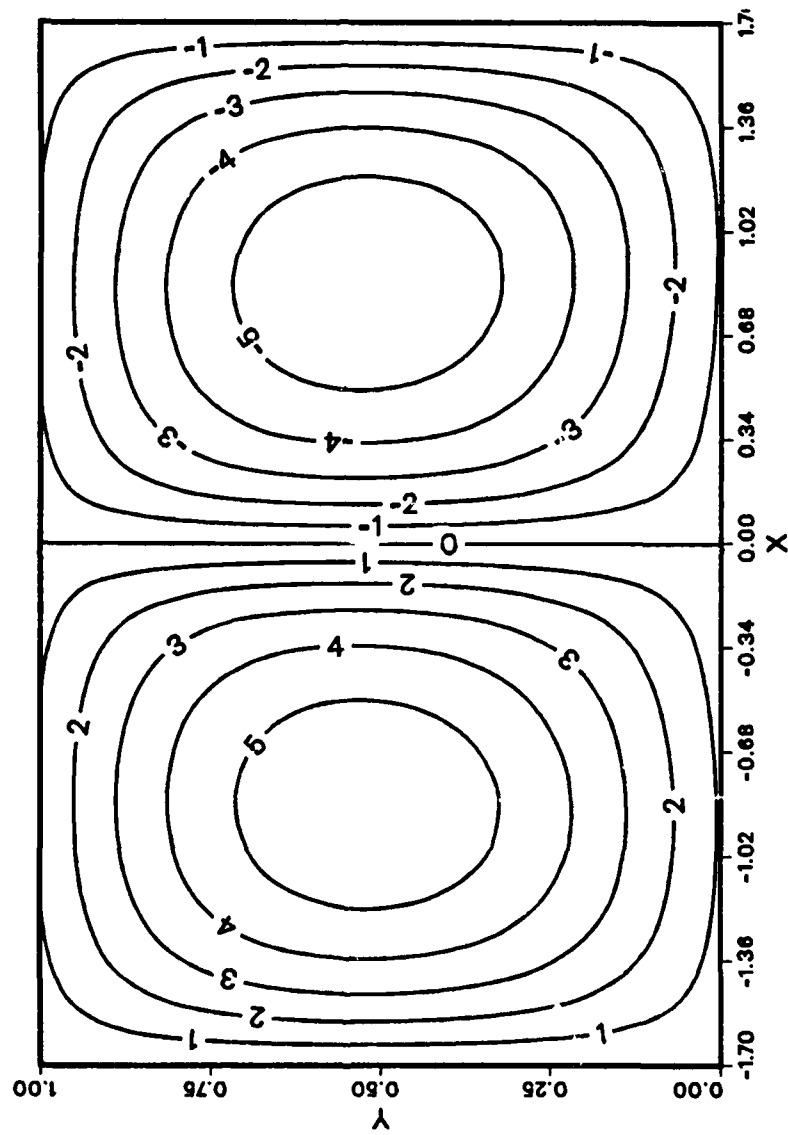


Figure 2.4 Calculated stream function contours

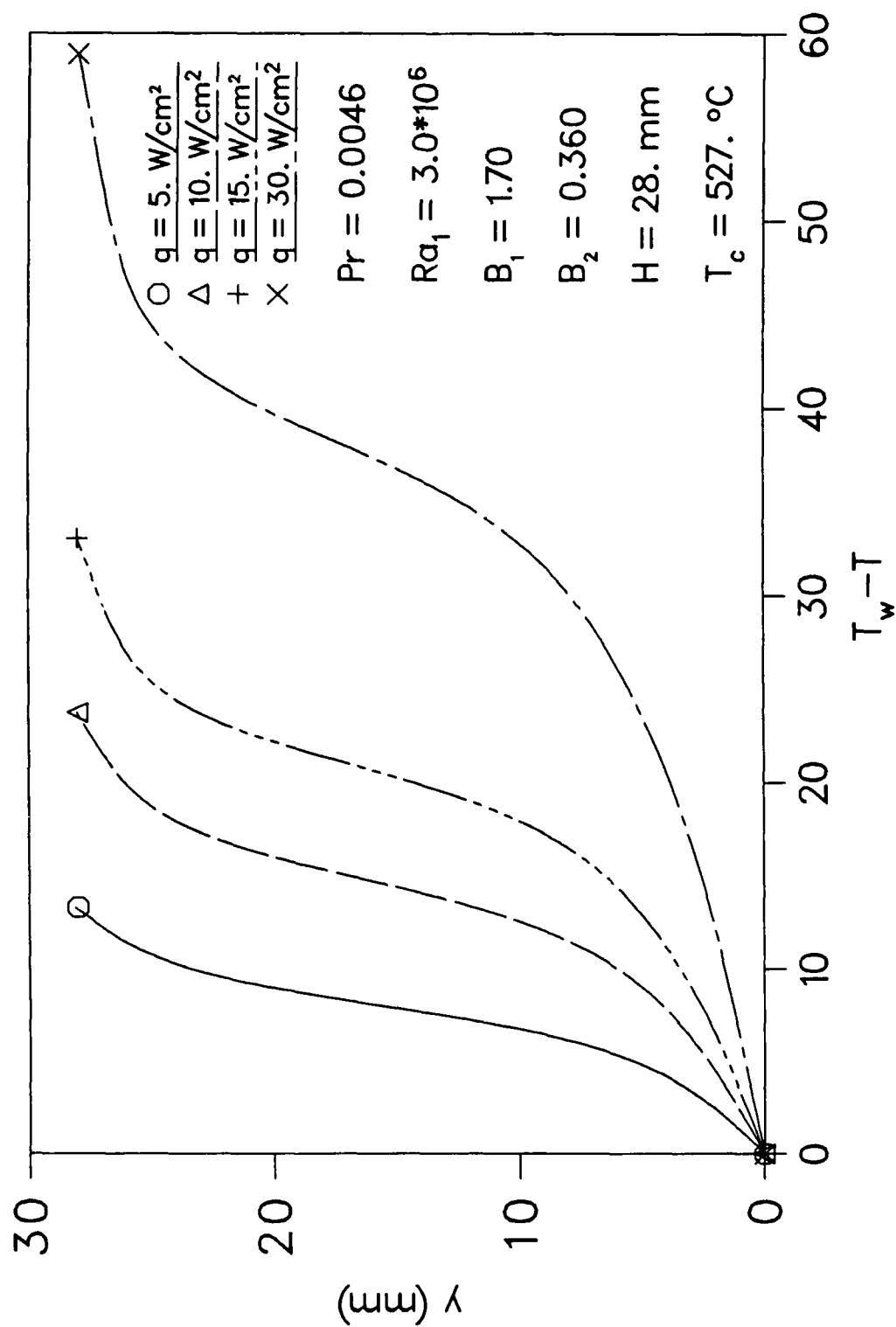


Figure 2.5. Temperature distributions for different heat flux q

under-relaxation parameter used in the above calculations is 0.1.

2.4.2 Natural convection in a horizontal rigid cavity with specified boundary temperature

The problem of natural convection in a rigid cavity with specified boundary temperatures will now be examined. The boundary conditions with reference to Fig. 2.1 in this case are changed to the following:

$$\begin{array}{lll}
 V = U = 0, & \theta = 0 & Y = 1, \quad -B_1 \leq X \leq B_1 \\
 V = U = 0, & \theta = 1 & Y = 0, \quad -B_1 \leq X \leq B_1 \\
 V = U = 0, & \frac{\partial \theta}{\partial X} = 0 & 0 \leq Y \leq 1, \quad X = -B_1 \\
 V = U = 0, & \frac{\partial \theta}{\partial X} = 0 & 0 \leq Y \leq 1, \quad X = B_1
 \end{array}$$

The dimensionless temperature and Raleigh numbers are $\theta = (T - T_c)/(T_h - T_c)$ and $Ra = g\beta H^3(T_h - T_c)/\alpha\nu$, respectively.

Raithby and Hollands (1985) have proposed an empirical equation for the natural convection heat transfer in horizontal cavities nonextensive in the horizontal direction, which is

$$\begin{aligned}
 Nu = 1 + [1 - Ra_c/Ra]^* [k_1 + 2(Ra^{1/3}/k_2)^{1 - \ln(Ra^{1/3}/k_2)}] \\
 + [(\frac{Ra}{5380})^{1/3} - 1]^* (1 - \exp\{-0.95[(Ra/Ra_c)^{1/3} - 1]^*\}) \quad (2.6)
 \end{aligned}$$

where Ra_c is the critical Raleigh number, k_1 and k_2 are both functions of Pr , and are given as follows:

$$k_1 = 1.44/(1 + 0.018/Pr + 0.00136/Pr^2) \quad (2.7)$$

$$k_2 = 75 \exp(1.5 Pr^{-1/2}) \quad (2.8)$$

The square brackets with the asterisk, $[]^*$, indicate that only positive values of the argument are to be taken, i.e.,

$$[X]^* = (|X| + X)/2 \quad (2.9)$$

The above equation has been tested against experimental data for gases and liquids of various Prandtl numbers except liquid metals, with a maximum difference of 25 percent.

It is of interest to compare the present numerical solutions with eqn. (2.6) and to fill the gap in the low Prandtl number range. The calculations were carried out with $B_1 = 0.5$ (i.e., a square box) and the results are presented in Fig. 2.6. It can be seen that the agreement between the numerical solutions and eqn. (2.6) is generally good. The maximum difference within the range of comparison is less than 20 percent. A grid size of 25 x 25 was used in the numerical calculations, and the solutions were obtained from higher Pr to lower Pr with the solutions of the higher Pr as the initial guesses for the lower Pr. The number of iterations for convergence ranges from 700 - 1000.

2.5 CONCLUSIONS

A numerical study has been reported for natural convection in horizontal liquid metal layers with localized heating from below. The

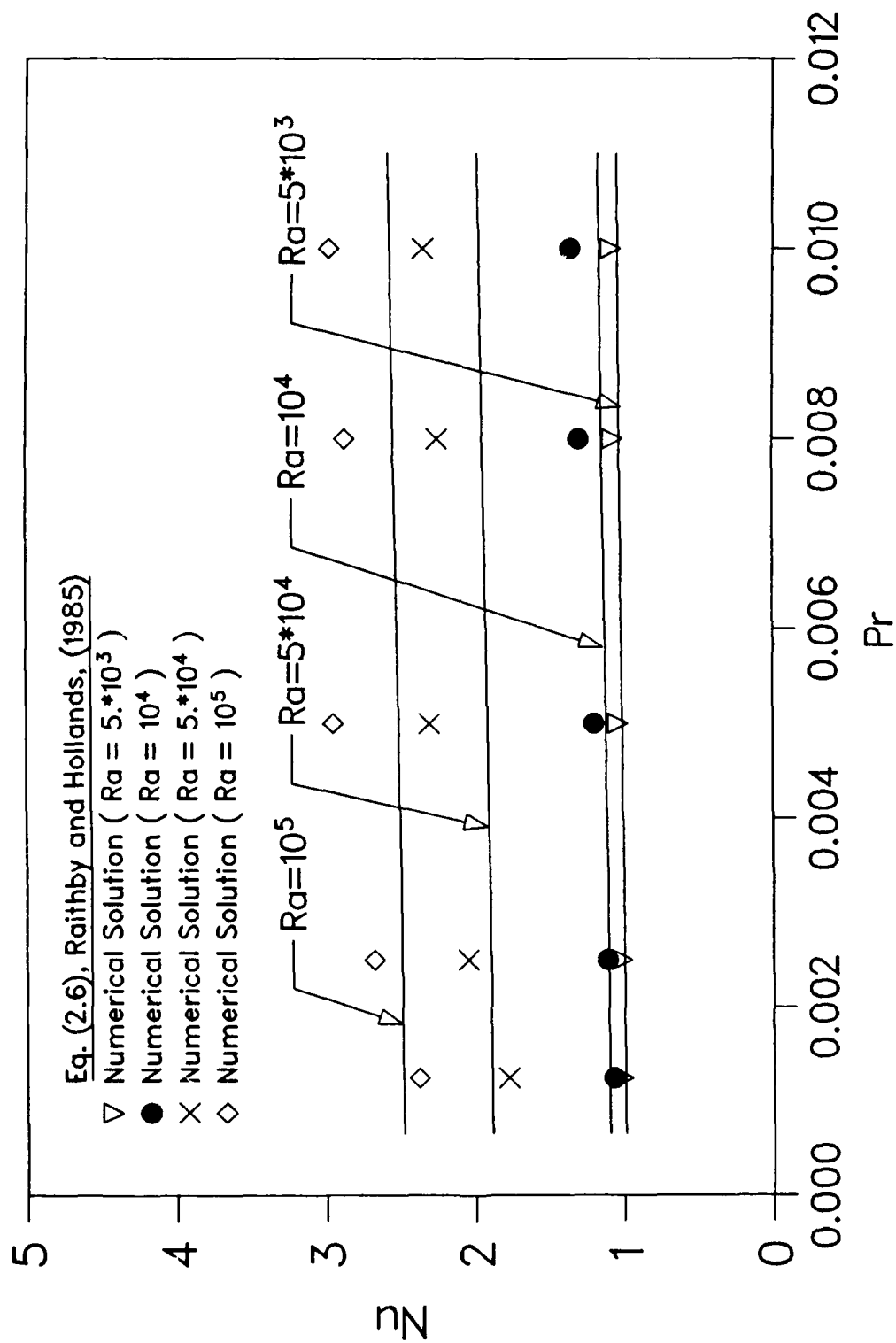


Figure 2.6. Comparison of Eq. (2.6) and the present numerical solutions

temperature distribution of the numerical results at $x = 0$ agrees well with the corresponding experimental data for a potassium layer. The isotherms and streamlines indicate that a plumelike flow is generated above the heated region. The numerical results based on a rigid square box with insulated side walls, T_h on the bottom, and T_c on the top generally agree with eqn. (2.6) of Raithby and Hollands (1985), within the Raleigh number range of $5 \times 10^3 - 10^5$, and the Prandtl number range of 0.00125 - 0.01.

Section III

PERFORMANCE CHARACTERISTICS OF A THERMAL ENERGY STORAGE MODULE: A TRANSIENT PCM/FORCED CONVECTION CONJUGATE ANALYSIS

3.1 SUMMARY

The performance of a thermal energy storage module is simulated numerically. The change of phase of the phase-change material (PCM) and the transient forced convective heat transfer for the transfer fluid with low Prandtl numbers are solved simultaneously as a conjugate problem. A parametric study and a system optimization are conducted. The numerical results show that module geometry is crucial to the design of a space-based thermal energy storage system.

3.2 INTRODUCTION

Recently, the study of phase-change thermal energy storage systems is active due to applications to space-based power plants and the utilization of solar energy. Phase-change materials (PCM) have a large latent heat, so it is an efficient way to absorb the heat energy during the time period when the materials are subject to heat input and to release it to space over a long period of time. A basic latent heat thermal storage geometry is shown schematically in Fig. 3.1. The PCM surrounds a pipe, through which the heat transfer fluid is passed. The problem by nature is a time-dependent phase-change heat transfer problem combined with conjugate forced convection.

Heat transfer involving melting and solidification is a fertile area for research because of its great importance in many applications. Since problems of this type are inherently nonlinear due to the existence of a moving interface whose position is not known *a priori*, there are relatively few analytical solutions to these so-called Stefan problems. A large number of numerical techniques have been developed, but most of the numerical studies have focused on diffusion-controlled phase-change problems or phase-change problems including natural convection (Shamsundar and Sparrow, 1975; Voller and Cross, 1981; Sparrow and Ohkuho, 1986; Voller and Prakash, 1987; Cao et al., 1989a; Cao and Faghri, 1989, 1990).

The use of a hollow cylinder of PCM similar to that in Fig. 3.1 for a solar latent energy storage system was modeled by Solomon et al. (1986). A finite difference formulation with the Kirchhoff temperature was used to calculate the internal energy, temperature, and the position of the

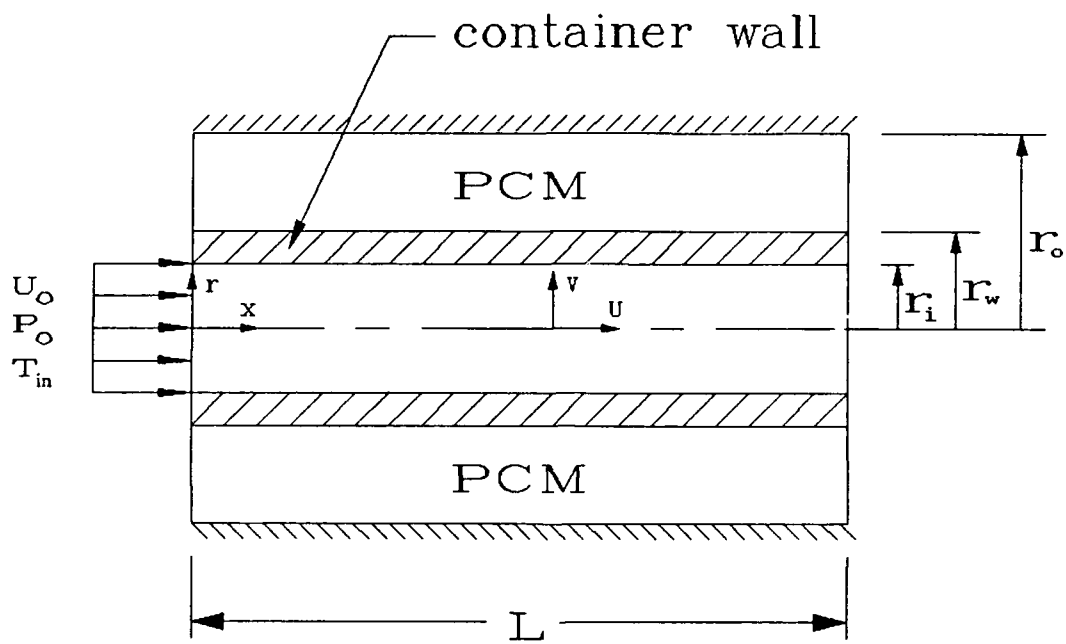


Figure 3.1 The schematic of the latent heat storage system

phase-change front. Stovall and Arimilli (1988) studied a thermal energy storage system consisting of a cylindrical tube filled with a phase-change material having a high melting temperature. The tube is surrounded by an annular region containing the liquid metal heat transfer fluid for pulsed power load applications. The emphasis of both of the above studies is on the diffusion-controlled heat transfer in the PCM. The heat transfer between the transfer fluid and the PCM is calculated using empirical correlations instead of solving the flow and temperature fields of the transfer fluid numerically as a conjugate problem. Also, the container wall shown in Fig. 3.1 was ignored. It should be pointed out that most of the empirical correlations are based on limited experimental or numerical data and the fully-developed conditions; the use of correlations may increase the uncertainty of the numerical modeling. Furthermore, the change of phase is by nature a transient problem. The boundary temperature of the transfer fluid changes as the phase-change interface progresses, therefore the temperature field of the transfer fluid may never reach the fully-developed state. This is especially important for PCM storage systems with liquid metals as the transfer fluid. With relatively shorter cylinders and lower fluid velocities, the laminar combined hydrodynamic and thermal entry region may dominate the flow along the entire length of the cylinder.

In this paper, a PCM energy storage system with the configuration in Fig. 3.1 is modeled numerically. The two-dimensional change of phase for the PCM and the two-dimensional transient forced convection entrance region for the transfer fluid with low Prandtl numbers is solved simultaneously. Also, the influence of the container wall is included in the numerical

analysis, and an optimization of the configuration is conducted. To the authors' knowledge, this work is the first PCM/forced convection conjugate problem reported in the literature.

3.3 Mathematical Modeling

The continuity, momentum, and energy equations governing two-dimensional transient incompressible laminar flows with no viscous dissipation in a pipe are (Ganic et al., 1985)

$$\frac{1}{r} \frac{\partial}{\partial r} (rv) + \frac{\partial u}{\partial x} = 0 \quad (3.1)$$

$$\frac{\partial v}{\partial t} + v \frac{\partial v}{\partial r} + u \frac{\partial v}{\partial x} = -\frac{1}{\rho_f} \frac{\partial p}{\partial r} + \nu_f \left[\frac{1}{r} \frac{\partial}{\partial r} \left(r \frac{\partial v}{\partial r} \right) - \frac{v}{r^2} + \frac{\partial^2 v}{\partial x^2} \right] \quad (3.2)$$

$$\frac{\partial u}{\partial t} + v \frac{\partial u}{\partial r} + u \frac{\partial u}{\partial x} = -\frac{1}{\rho_f} \frac{\partial p}{\partial x} + \nu_f \left[\frac{1}{r} \frac{\partial}{\partial r} \left(r \frac{\partial u}{\partial r} \right) + \frac{\partial^2 u}{\partial x^2} \right] \quad (3.3)$$

$$\rho_f c_f \left(\frac{\partial T^0}{\partial t} + v \frac{\partial T^0}{\partial r} + u \frac{\partial T^0}{\partial x} \right) = k_f \left[\frac{1}{r} \frac{\partial}{\partial r} \left(r \frac{\partial T^0}{\partial r} \right) + \frac{\partial^2 T^0}{\partial x^2} \right] \quad (3.4)$$

For the PCM, the temperature transforming model (Cao and Faghri, 1989) is used. The energy equation is written as

$$\frac{\partial(\rho C^0 T^*)}{\partial t} = \frac{1}{r} \frac{\partial}{\partial r} \left(kr \frac{\partial T^*}{\partial r} \right) + \frac{\partial}{\partial x} \left(k \frac{\partial T^*}{\partial x} \right) - \frac{\partial(\rho S^0)}{\partial t} \quad (3.5)$$

where $T^* = T^0 - T_m^0$

$$C^0 = C^0(T^*) = \begin{cases} c_s & (T^* < -\delta T^0) & \text{(solid phase)} \\ c_m + \frac{H}{2\delta T^0} & (-\delta T^0 \leq T^* \leq \delta T^0) & \text{(mushy phase)} \\ c_\ell & (T^* > \delta T^0) & \text{(liquid phase)} \end{cases} \quad (3.6)$$

$$S^0 = S^0(T^*) = \begin{cases} c_s \delta T^0 & (T^* < -\delta T^0) & \text{(solid phase)} \\ c_m \delta T^0 + \frac{H}{2} & (-\delta T^0 \leq T^* \leq \delta T^0) & \text{(mushy phase)} \\ c_s \delta T^0 + H & (T^* > \delta T^0) & \text{(liquid phase)} \end{cases} \quad (3.7)$$

$$k(T^*) = \begin{cases} k_s & (T^* < -\delta T^0) & \text{(solid phase)} \\ k_s + (k_\ell - k_s)(T^* + \delta T^0)/2\delta T^0 & (-\delta T^0 \leq T^* \leq \delta T^0) & \text{(mushy phase)} \\ k_\ell & (T^* > \delta T^0) & \text{(liquid phase)} \end{cases} \quad (3.8)$$

For the pipe wall, the energy equation is

$$\rho_w c_w \frac{\partial T^0}{\partial t} = k_w \left[\frac{1}{r} \frac{\partial}{\partial r} \left(r \frac{\partial T^0}{\partial r} \right) + \frac{\partial^2 T^0}{\partial x^2} \right] \quad (3.9)$$

The initial and boundary conditions for the case of uniform inlet conditions are defined as follows:

Initial conditions: $t = 0$

Entire domain: $0 \leq x \leq L, \quad 0 < r \leq r_0$

$$T^0 = T_i^0, \quad u = v = 0$$

Boundary conditions: $t > 0$

Inlet plane: $x = 0$

$$0 < r < r_i: \quad u = U_o, \quad T^o = T_{in}^o, \quad v = 0$$

$$r_i < r < r_o: \quad \frac{\partial T^o}{\partial x} = 0$$

Outer wall: $0 < x < L, \quad r = r_o$

$$\left. \frac{\partial T^o}{\partial r} \right|_{r = r_o} = 0$$

PCM-wall interface: $0 < x < L, \quad r = r_w$

$$k_p \left. \frac{\partial T^o}{\partial r} \right|_{r = r_w^+} = k_w \left. \frac{\partial T^o}{\partial r} \right|_{r = r_w^-}$$

Wall-fluid interface: $0 < x < L, \quad r = r_i$

$$k_w \left. \frac{\partial T^o}{\partial r} \right|_{r = r_i^+} = k_f \left. \frac{\partial T^o}{\partial r} \right|_{r = r_i^-}$$

Outlet plane: $x = L$

$$0 < r < r_o: \quad \frac{\partial T^o}{\partial x} = 0$$

$$0 < r < r_i: \quad \frac{\partial u}{\partial x} = 0$$

The use of the temperature transforming model (Cao and Faghri, 1989) has two advantages. First, equations (3.5 - 3.8) form a set of closed-group equations, so an explicit treatment of the phase-change interface is not

needed. Secondly, The time step and grid size limitations are eliminated, which are normally encountered for other fixed-grid methods. It should be pointed out that due to the space application the natural convection in the liquid PCM has been ignored.

The following non-dimensional variables are introduced

$$\begin{aligned} R &= r/D, \quad X = \frac{x}{D}, \quad U = \frac{u}{U_0}, \quad V = \frac{v}{U_0}, \quad Re_f = \frac{U_0 D}{\nu_f}, \quad T = \frac{T^0 - T_m^0}{T_{in}^0 - T_m^0}, \quad \tau = \frac{U_0}{D} t, \\ P &= \frac{P - P_0}{\rho_f U_0^2}, \quad C = \frac{C^0}{c_\ell}, \quad K = \frac{k}{k_\ell}, \quad S = S^0 / c_\ell (T_{in}^0 - T_m^0), \quad St = c_\ell (T_{in}^0 - T_m^0) / H, \\ \delta T^* &= \delta T^0 / (T_{in}^0 - T_m^0) \end{aligned}$$

The dimensionless continuity, momentum and energy equations for the transfer fluid are as follows:

$$\frac{1}{R} \frac{\partial}{\partial R} (RV) + \frac{\partial U}{\partial X} = 0 \quad (3.10)$$

$$\frac{\partial U}{\partial \tau} + V \frac{\partial U}{\partial R} + U \frac{\partial U}{\partial X} = -\frac{\partial P}{\partial X} + \frac{1}{Re_f} \left[\frac{1}{R} \frac{\partial}{\partial R} (R \frac{\partial U}{\partial R}) + \frac{\partial^2 U}{\partial X^2} \right] \quad (3.11)$$

$$\frac{\partial V}{\partial \tau} + V \frac{\partial V}{\partial R} + U \frac{\partial V}{\partial X} = -\frac{\partial P}{\partial R} + \frac{1}{Re_f} \left[\frac{1}{R} \frac{\partial}{\partial R} (R \frac{\partial V}{\partial R}) + \frac{\partial^2 V}{\partial X^2} - \frac{V}{R^2} \right] \quad (3.12)$$

$$\frac{\partial T}{\partial \tau} + V \frac{\partial T}{\partial R} + U \frac{\partial T}{\partial X} = -\frac{\partial P}{\partial R} + \frac{1}{Re_f Pr_f} \left[\frac{1}{R} \frac{\partial}{\partial R} (R \frac{\partial T}{\partial R}) + \frac{\partial^2 T}{\partial X^2} \right] \quad (3.13)$$

The dimensionless energy equation for the PCM is

$$\frac{\partial(CT)}{\partial\tau} = \frac{1}{Re_f Pr_f} \frac{a_f}{a_f} \left[\frac{1}{R} \frac{\partial}{\partial R} (KR \frac{\partial T}{\partial R}) + \frac{\partial}{\partial X} (K \frac{\partial T}{\partial X}) \right] - \frac{\partial S}{\partial\tau} \quad (3.14)$$

where

$$C(T) = \begin{cases} C_{sl} & (T < -\delta T^*) \\ \frac{1}{2} (1+C_{sl}) + \frac{1}{2St\delta T^*} & (-\delta T^* \leq T \leq \delta T^*) \\ 1 & (T > \delta T^*) \end{cases}$$

$$S(T) = \begin{cases} C_{sl} \delta T^* & (T < -\delta T^*) \\ \frac{1}{2} \delta T^* (1+C_{sl}) + \frac{1}{2St} & (-\delta T^* \leq T \leq \delta T^*) \\ C_{sl} \delta T^* + \frac{1}{St} & (T > \delta T^*) \end{cases}$$

$$K(T) = \begin{cases} K_{sl} & (T < -\delta T^*) \\ K_{sl} + (1-K_{sl}) (T + \delta T^*) / 2\delta T^* & (-\delta T^* \leq T \leq \delta T^*) \\ 1 & (T > \delta T^*) \end{cases}$$

The dimensionless energy equation for the container wall is

$$\frac{\partial T}{\partial\tau} = \frac{1}{Re_f Pr_f} \frac{a_w}{a_f} \left[\frac{1}{R} \frac{\partial}{\partial R} (R \frac{\partial T}{\partial R}) + \frac{\partial^2 T}{\partial X^2} \right] \quad (3.15)$$

The initial and boundary conditions are nondimensionalized as follows:

Initial conditions: $\tau = 0$

Entire domain: $0 \leq X \leq L/D, \quad 0 \leq R \leq R_0$

$$T = T_i, \quad U = V = 0 \quad (3.16a)$$

Boundary conditions: $\tau > 0$

Inlet plane: $X = 0$

$$0 < R < 0.5 : \quad U = 1, \quad T = 1, \quad V = 0 \quad (3.16b)$$

$$0.5 < R < R_0 : \quad \frac{\partial T}{\partial X} = 0$$

Outer wall: $0 < X < L/D, \quad R = R_0$

$$\left. \frac{\partial T}{\partial R} \right|_{R = R_0} = 0 \quad (3.16c)$$

PCM-wall interface: $0 < X < L/D, \quad R = R_w$

$$\frac{k_p}{k_w} \left. \frac{\partial T}{\partial R} \right|_{R = R_w^+} = \left. \frac{\partial T}{\partial R} \right|_{R = R_w^-} \quad (3.16d)$$

Wall-fluid interface: $0 < X < L/D, \quad R = 0.5$

$$\left. \frac{\partial T}{\partial R} \right|_{R = 0.5^+} = \frac{k_f}{k_w} \left. \frac{\partial T}{\partial R} \right|_{R = 0.5^-} \quad (3.16e)$$

Outer plane: $X = L/D$

$$0 < R < R_0 : \quad \frac{\partial T}{\partial X} = 0 \quad (3.16f)$$

$$0 < R < 0.5 : \quad \frac{\partial U}{\partial X} = 0$$

It can be seen that the temperature field can be expressed as

$$T = T(\tau, R, X, Re_f, Pr_f, a_\ell/a_f, a_w/a_f, St, C_{s\ell}, \delta T^*, K_{s\ell}, k_f/k_w, k_p/k_w, r_w/D, r_o/D, L/D) \quad (3.17)$$

3.4 Numerical Procedure

The problem has been specified mathematically by eqns. (3.10 - 3.16). The solution procedure used for solving these equations is the control-volume finite-difference approach described by Patankar (1980, 1988). In this methodology, the discretization equations are obtained by applying the conservation laws over a finite size control volume surrounding the grid node and integrating the equation over the control volume. The velocities and pressure are solved by using the SIMPLE scheme (Patankar, 1980). At the PCM-wall and the wall-fluid interfaces, the harmonic mean of the thermal conductivity is used.

$$k_p \left. \frac{\partial T^0}{\partial r} \right|_{r=r_w^+} = k_w \left. \frac{\partial T^0}{\partial r} \right|_{r=r_w^-} = \frac{2k_p k_w}{k_p + k_w} \left. \frac{\partial T^0}{\partial r} \right|_{r=r_w}$$

$$k_w \left. \frac{\partial T^0}{\partial r} \right|_{r=r_i^+} = k_f \left. \frac{\partial T^0}{\partial r} \right|_{r=r_i^-} = \frac{2k_w k_f}{k_w + k_f} \left. \frac{\partial T^0}{\partial r} \right|_{r=r_i}$$

The discretization equations are solved by using the tridiagonal matrix algorithm (TDMA or Thomas algorithm). During each time step, iterations are needed. The converged results were assumed to be reached when the maximum relative change of all variables between consecutive iterations was less than 0.1%. The residual of the continuity equation was also checked. The iteration was continued until the sum of the residuals was less 10^{-5} . Different grid sizes for the same problem have been tested

and it proves that both the PCM model and the numerical scheme used for the transfer fluid are essentially independent of grid sizes for the numerical results in the next section. The space and time grid specifications are given in the next section for the cases presented.

3.5 NUMERICAL RESULTS AND DISCUSSION

Before presenting the numerical results for the phase-change system, the phase-change model (eqn. 3.5) was checked against other numerical results for a two-dimensional freezing problem. Consider a liquid initially at T_i^0 in a infinitely long prism with a uniform cross section (Hsiao and Chung, 1984). At $t > 0$, the surface is kept at a temperature $T_w^0 < T_m^0$ and freezing takes place immediately. Because of the symmetry of the geometry, only a quarter of the prism is considered. Figure 3.2 shows the interface position as a function of ta_s/ℓ^2 along the diagonal. Also included in this figure are solutions by Hsiao and Chung (1984), and by Cao et al. (1989). It can be seen that the present model agrees well with the results of these studies.

The numerical calculations for the thermal energy storage system were then conducted with the configuration as shown in Fig. 3.1. The system is initially at a temperature $T_i < 0$ (less than the melting temperature of the PCM). The hotter fluid enters into the circular channel and heats the system, which absorbs the energy from the fluid and stores it as both latent and sensible heat. The grid size used for the calculation was 70 (axial) x 20 (radial transfer fluid) x 5 (container wall) x 15 (PCM) and a dimensionless time step of $\Delta\tau = 10$. In order to simulate the phase-change at a single temperature using eqn. (3.14), the dimensionless phase-change

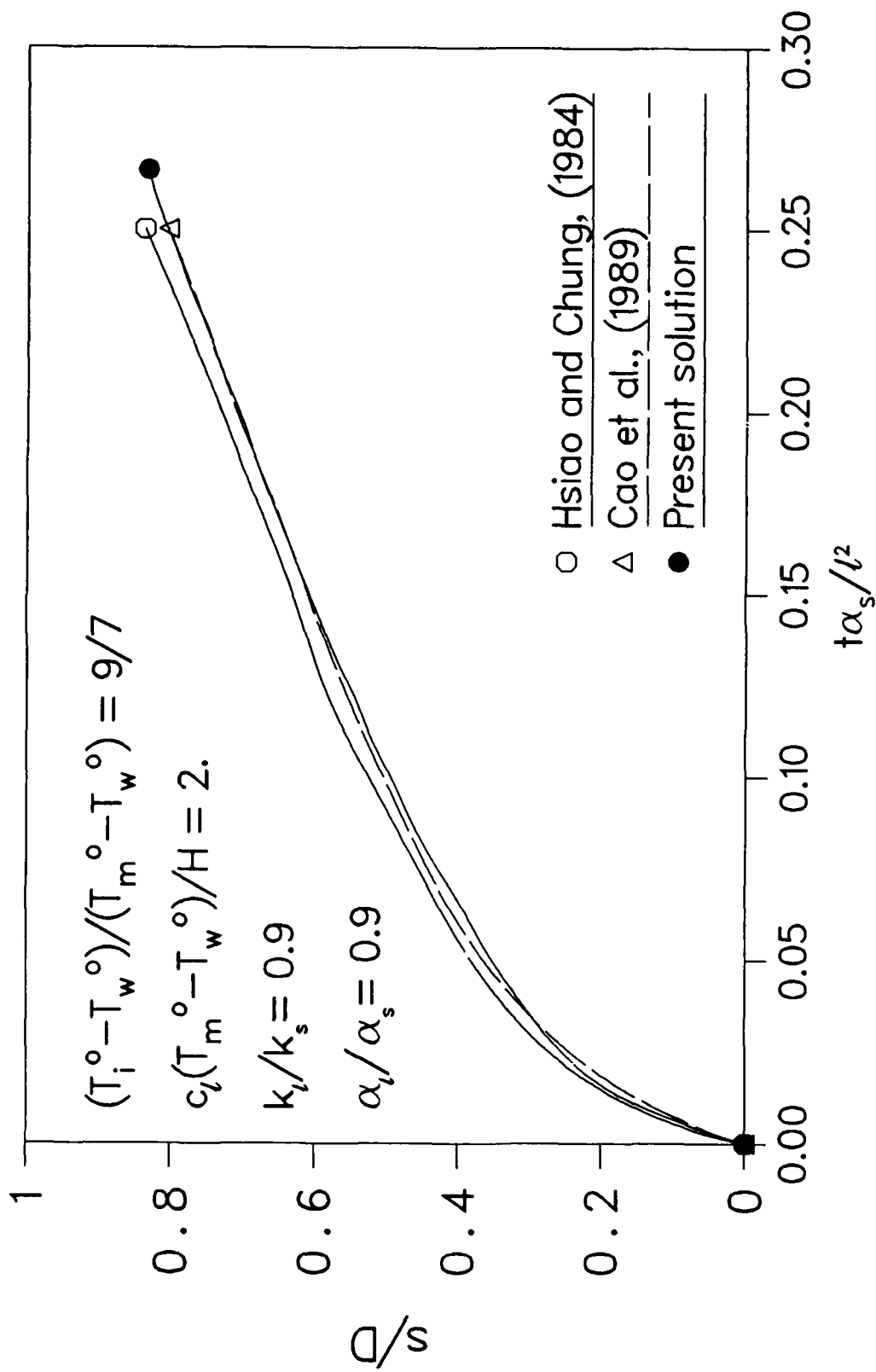


Figure 3.2. Interface position along the diagonal with prescribed boundary temperature

temperature range δT^* is taken to be 0.01.

Figure 3.3 shows the axial velocity distribution in the radial direction at $X = 6$ at different times. It can be seen that the velocity reaches the steady state quickly. After $\tau = 45$, the velocity profile remains unchanged. This does not mean the velocity profile has reached the fully developed condition along the pipe. Since the pipe is comparatively short and the Prandtl number is small, the developing velocity region is dominant along the whole pipe length. The temperature profile, however, is different. Figure 3.4 shows the radial temperature distribution at $X = 6$ for different time periods. The three regions in the radial direction (transfer fluid, container wall, and the PCM) are also indicated in the figure. The melting interfaces at different times are the intersections of $T = 0$ and the corresponding temperature curves. It can be seen that as the melting interface progresses, the temperature curve moves upward accordingly. Although the velocity field of the transfer fluid reaches the steady state quickly, its temperature counterpart cannot reach the steady state before the PCM is totally melted. This clearly demonstrates that the use of steady fully-developed empirical heat-transfer correlations for the transfer fluid may result in a significant error for the evaluation of the system performance.

Figure 3.5 shows the melting interface along the axial direction at different times. At $\tau = 1000$, the melting interface has reached the outer surface ($r = r_0$) for $X < 6$, while some PCM remains unmelted for $X > 6$. The reason is that since the Prandtl number of the transfer fluid is very small (the thermal conductivity is very large) a large amount of heat is

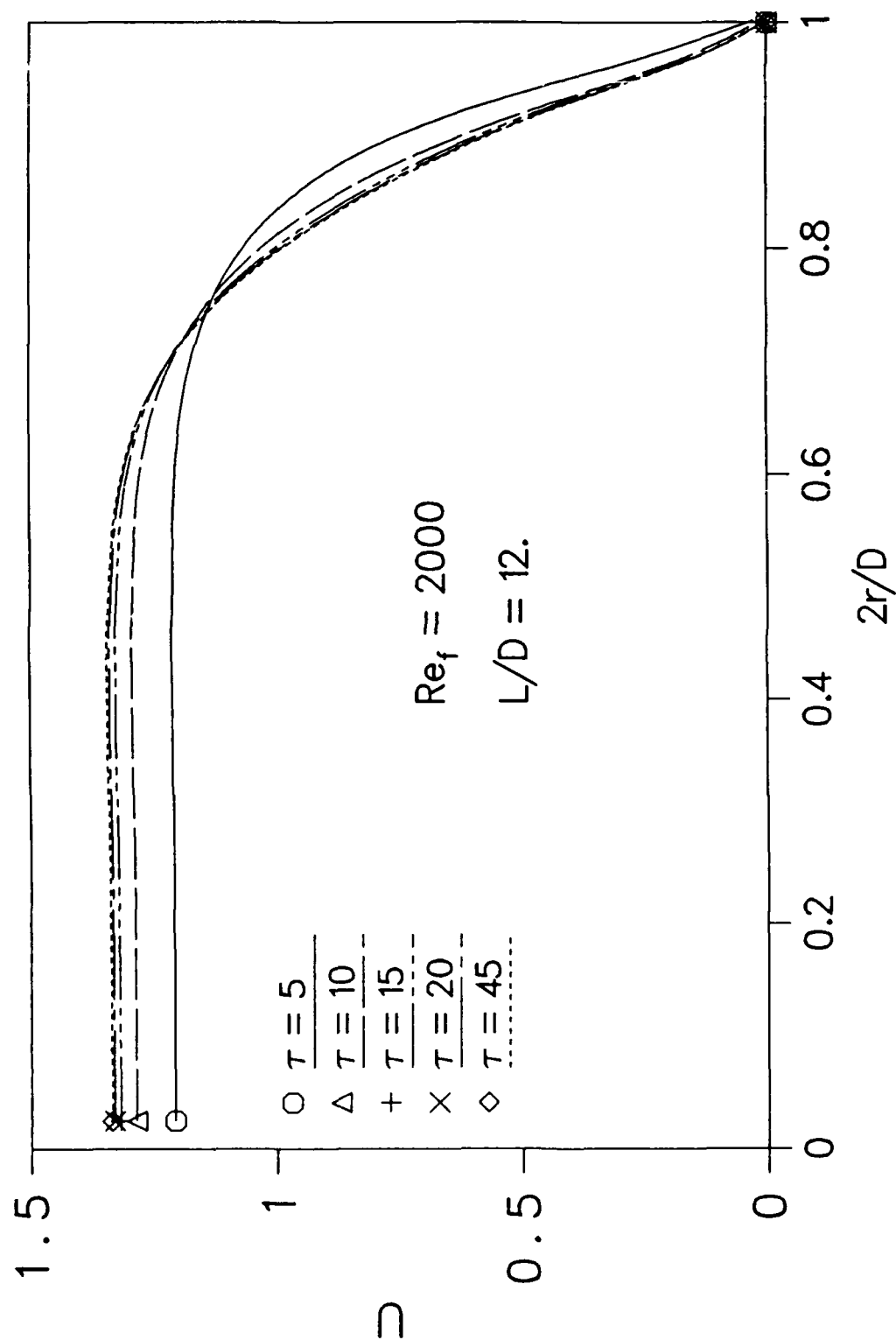


Figure 3.3. Axial velocity distribution of transfer fluid at $X=6$ for different time periods

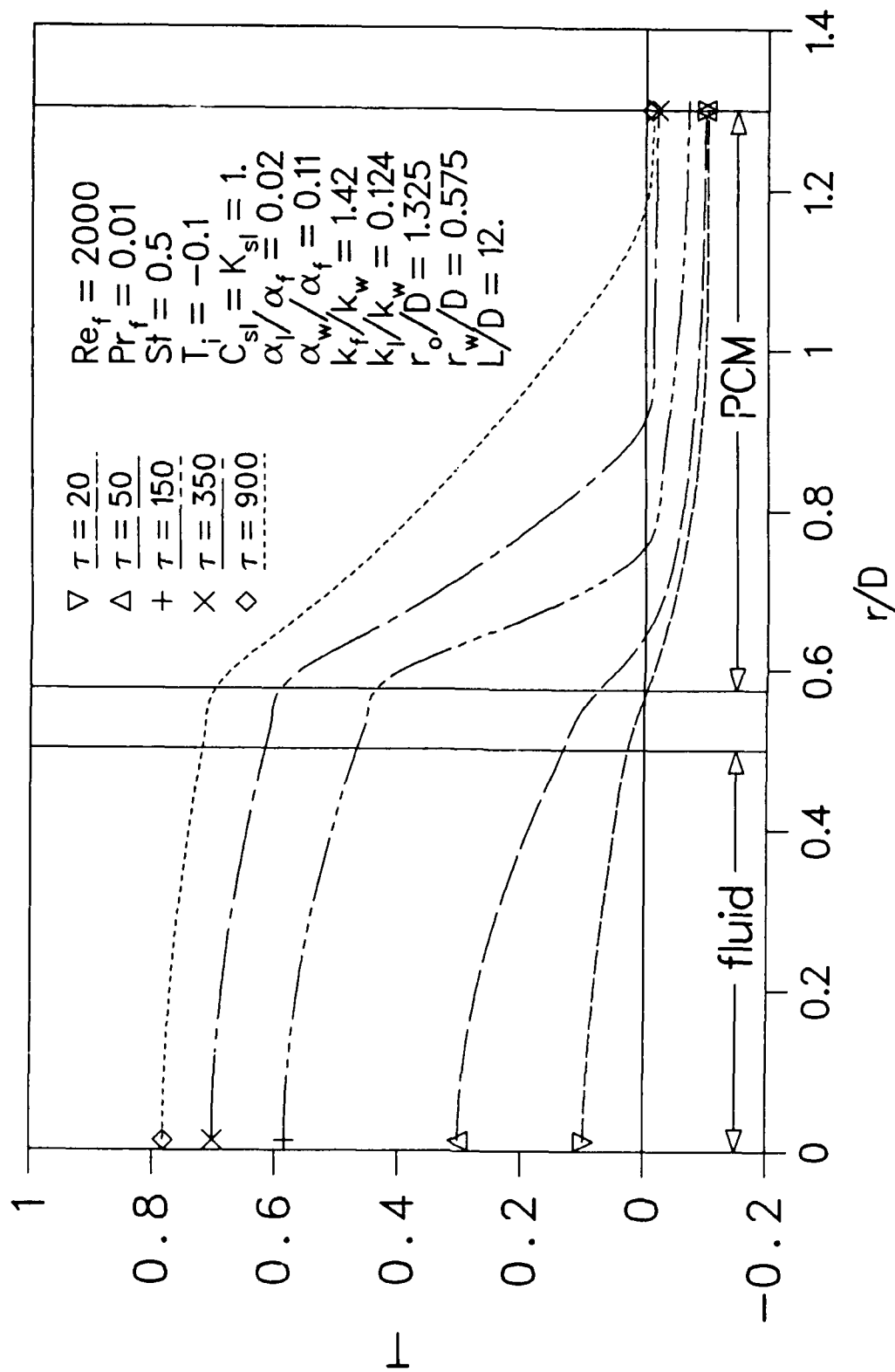


Figure 3.4. Radial temperature distribution at $X=6$ for different time periods

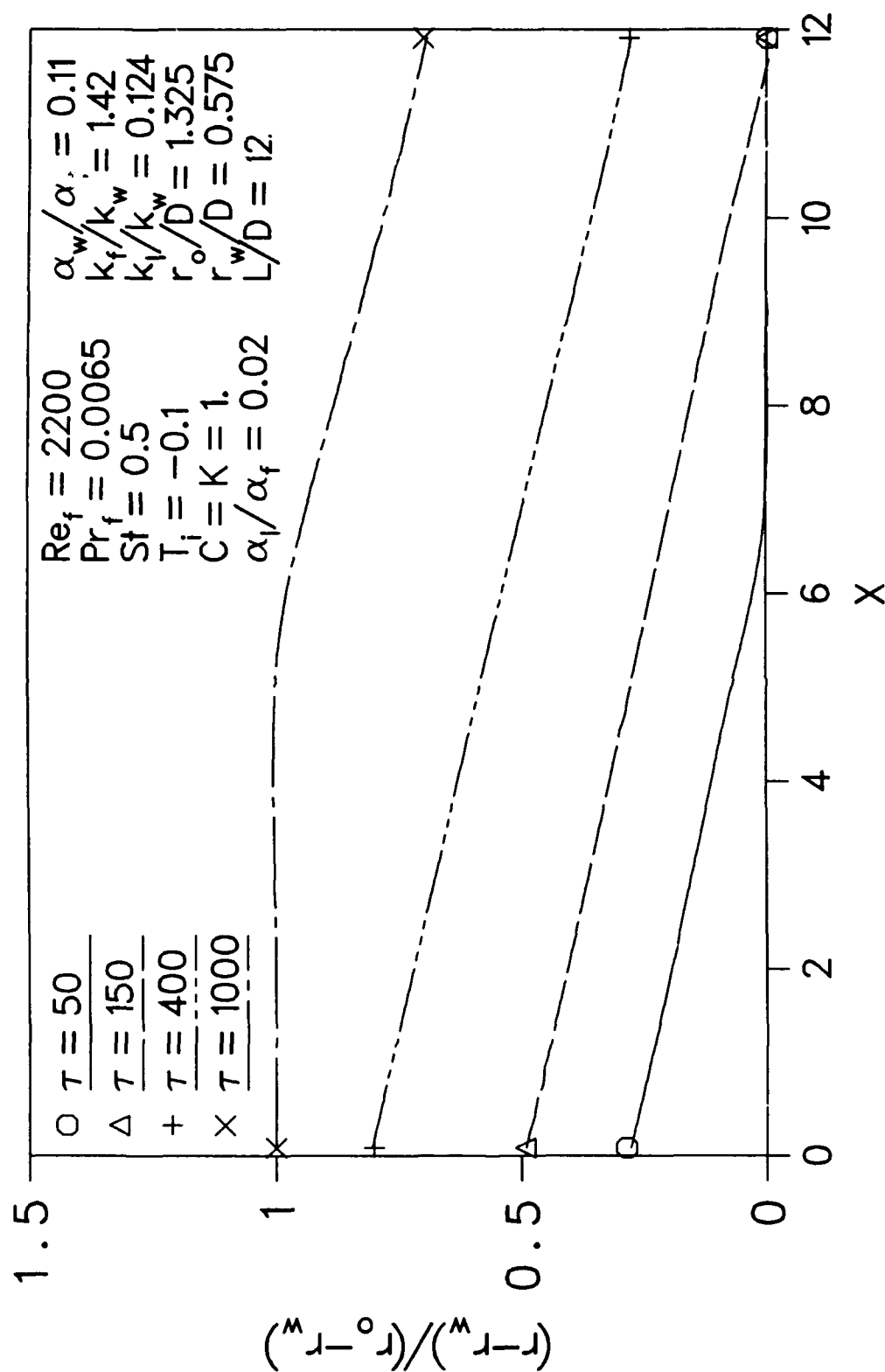


Figure 3.5. Melting fronts along axial direction for different time periods

transferred directly to the PCM upstream while a relatively small amount of heat is carried downstream. Figure 3.6 shows the melting interfaces along the axial direction for the transfer fluids with different Prandtl numbers. With a smaller Prandtl number, heat transfer to the PCM is much faster as indicated in the figure.

As in normal forced convective heat transfer, the Reynolds number has a significant influence on the system performance. This is illustrated in Fig. 3.7 with the same Prandtl number and different Reynolds numbers. Since the dimensionless time τ contains the inlet velocity U_0 , the comparison has been made at a dimensional time t . The dimensionless time for the case of $Re_f = 2200$ was taken as $\tau = 1000$, the corresponding dimensionless times for $Re_f = 1700$ and $Re_f = 1200$ were 773 and 545, respectively, with the assumption of the same D and ν_f for the three cases.

Since the transfer fluid is a liquid metal, the thermal conductivity has the same order of magnitude as that of the container wall. The influence of the thermal conductivity of the wall on the system performance may not be as important as those using gases as transfer fluids, as illustrated in Fig. 3.8.

It is very important to evaluate the overall performance of the system and to optimize the geometry of the system with given flow parameters and thermal properties. The important system parameters used to evaluate a thermal energy storage system are the energy storage capacity or total energy stored, Q_t (J), the energy storage density $Q_m = Q_t/m$ (J/kg), the total latent energy stored Q_ℓ (J) and the ratio of the latent to the total

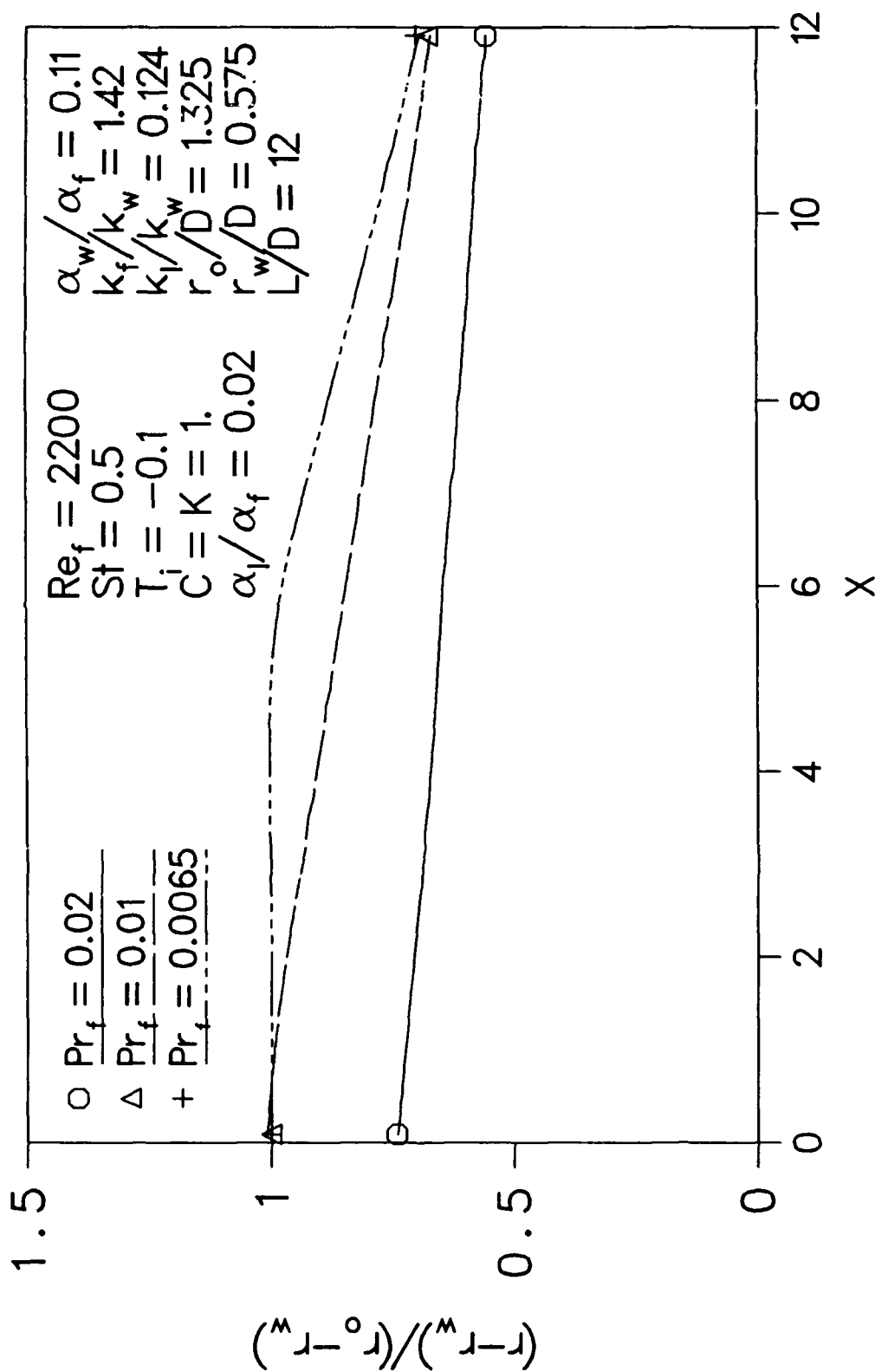


Figure 3.6. Melting fronts along axial direction for different Prandtl numbers at $\tau=1000$.

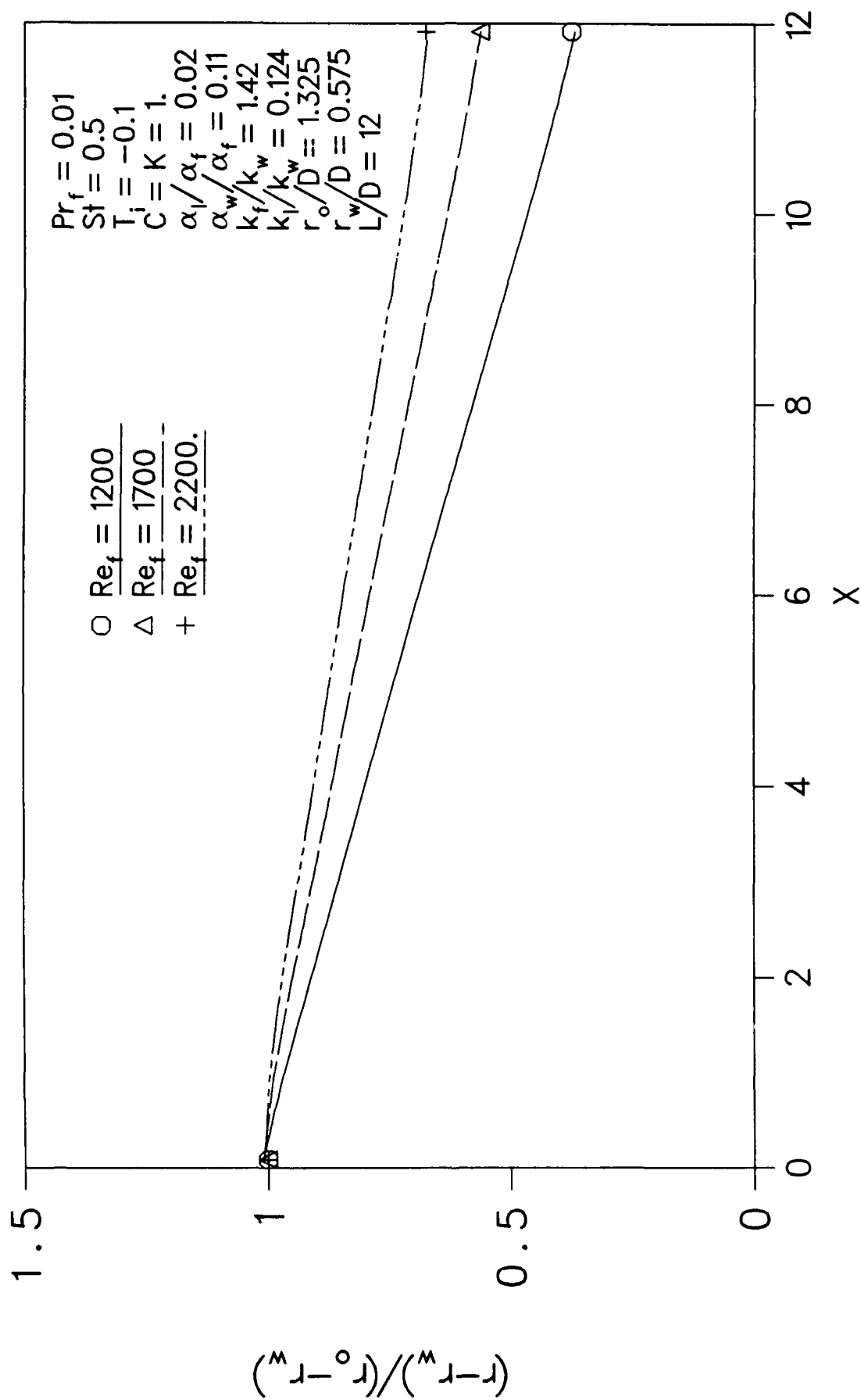


Figure 3.7. Melting fronts along axial direction for different Reynolds numbers

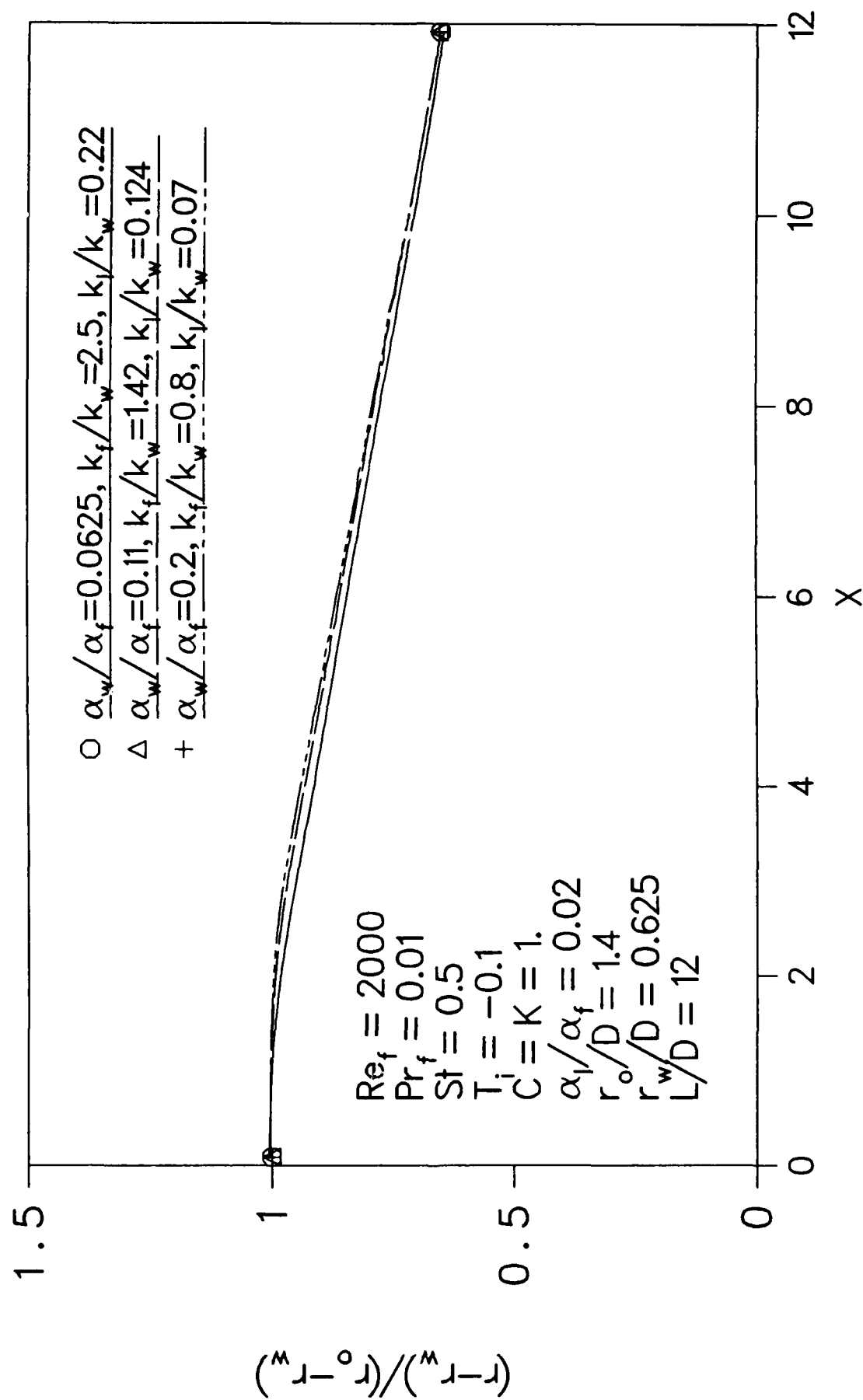


Figure 3.8. Melting fronts along axial direction for different thermal conductivities of the wall at $\tau=1000$

energy stored Q_ℓ/Q_t . The first two parameters, Q_t and Q_m , are most important to an energy storage system. In many cases, the energy storage capacity is the primary parameter one would be concerned with, while for a space application the energy storage density is equally important because the weight of the system is critical. With reference to the geometry shown in Fig. 3.1, they can be expressed as

$$Q_\ell = D^3 \rho_p H \pi \int_0^{L/D} (R_{\text{inf}}^2(X) - R_w^2) dX = D^3 \rho_p H \pi g_\ell \quad (3.18)$$

where $R_{\text{inf}}(X)$ is the radial location of the melting interface along the x direction, and

$$g_\ell = \int_0^{L/D} (R_{\text{inf}}^2(X) - R_w^2) dX$$

$$\begin{aligned} Q_t &= Q_\ell + 2 \pi D^3 c_p \rho_p (T_{\text{in}}^0 - T_m^0) \int_{R_w}^{R_o} \int_0^{L/D} (T - T_i) R dR dX \\ &= Q_\ell + 2 \pi D^3 c_p \rho_p (T_{\text{in}}^0 - T_m^0) g_t \end{aligned} \quad (3.19)$$

$$\text{where } g_t = \int_{R_w}^{R_o} \int_0^{L/D} (T - T_i) R dR dX$$

$$Q_t/Q_\ell = 1 + 2St g_t/g_\ell \quad (3.20)$$

$$Q_m = Q_t/m = H g_\ell / (R_o^2 - R_w^2) \frac{L}{D} + 2(T_{\text{in}}^0 - T_m^0) c_p g_t / (R_o^2 - R_w^2) \frac{L}{D} \quad (3.21)$$

Figures 3.9 and 3.10 present the numerical results for the system

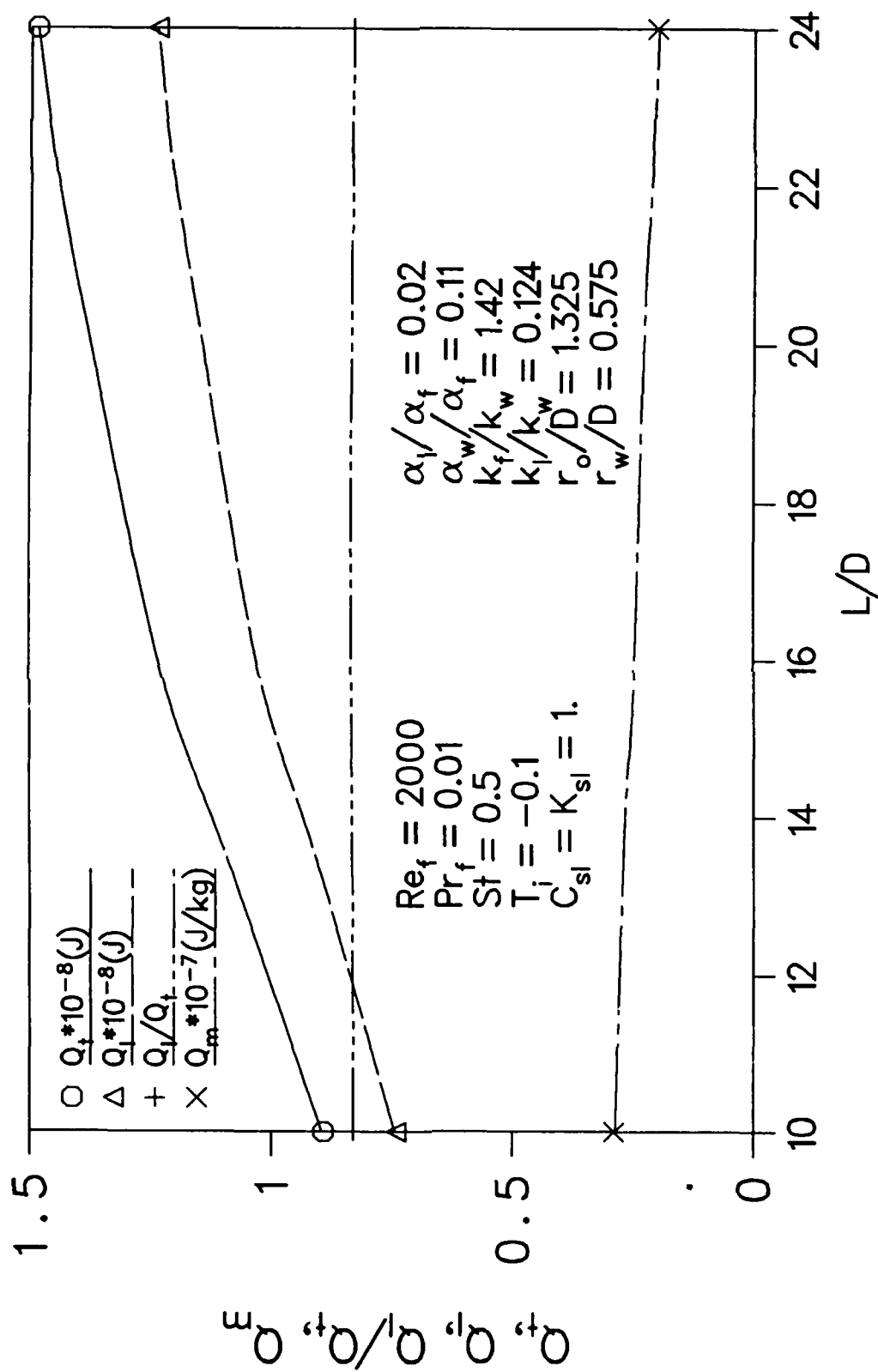


Figure 3.9. System optimization analysis for different L/D at $\tau=1000$

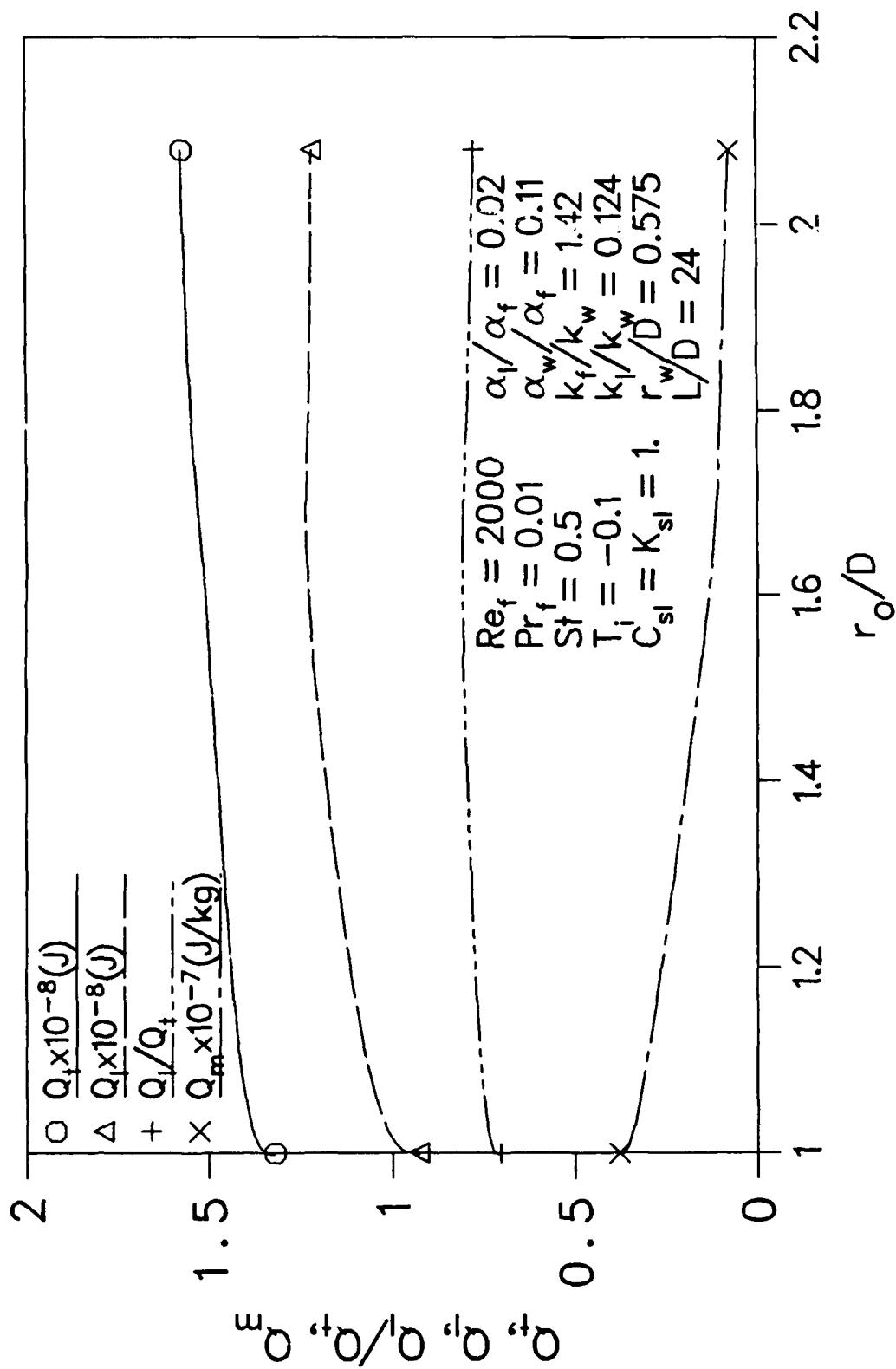


Figure 3.10. System optimization analysis for different r_o/D at $\tau=1000$

optimization analysis for different L/D and r_o/D . The dimensional parameters needed in eqns. (3.18 - 3.21) are $H = 2.9 \times 10^6$ J/kg, $\rho_p = 690$ kg/m³, $c_p = 7420$ J/(kg - K), $T_{in}^o - T_m^o = 195.4$ K and $D = 0.1$ m. Both Q_t and Q_ℓ follow the trend of increasing with larger L/D and r_o/D , while Q_ℓ/Q_t remains almost constant. The high proportion of latent heat storage in the PCM is largely attributable to the small difference between the initial system temperature and the PCM melt temperature ($T_i = -0.1$). The trend of the energy storage density is opposite to that of Q_t and Q_ℓ . The energy storage density Q_m drops sharply with the increase in L/D and r_o/D . In this situation, a trade-off needs to be reached when selecting the design parameters.

3.6 CONCLUSIONS

A energy storage system with the configuration in Fig. 3.1 has been studied numerically. Numerical results show that the fluid velocity inside the pipe reaches the steady state quickly, while the temperature field continues to change as the melting interface progresses. It is very important to treat the phase change and the fluid flow as a conjugate problem and solve them simultaneously. The numerical results for the parametric study and geometry optimization provide guidelines for the design of a space-based thermal energy storage system.

Section IV

MATHEMATICAL MODELING AND ANALYSIS OF HEAT PIPE START-UP FROM THE FROZEN STATE

4.1 SUMMARY

The start-up process of a frozen heat pipe is described and a complete mathematical model for the start-up of the frozen heat pipe is developed based on the existing experimental data, which is simplified and solved numerically. The two-dimensional transient model for the wall and wick is coupled with the one-dimensional transient model for the vapor flow when vaporization and condensation occur at the interface. A parametric study is performed to examine the effect of the boundary specification at the surface of the outer wall on the successful start-up from the frozen state. For successful start-up, the boundary specification at the outer wall surface must melt the working substance in the condenser before dry-out takes place in the evaporator.

4.2 INTRODUCTION

The heat pipe transports a large amount of energy between a source and a sink by using the latent heat of vaporization of the working substance and operates passively in the closed system at various temperatures depending on the working substance. The demand for an effective thermal management device for high temperature applications such as cooling the leading edges of reentry vehicles and hypersonic aircraft, and a space-based power station stimulates the study of the start-up of frozen liquid-metal heat pipes. Also, the start-up of frozen low temperature heat pipes is important in applications such as heat pipe heat exchangers, cooling electronic equipment, and melting the snow and ice on roads and bridges.

Neal (1967) and Shlosinger (1968) performed the first experimental tests to study the start-up performance of low temperature heat pipes with the water initially frozen. Deverall et al. (1970) also made a series of tests with water and liquid metal heat pipes. Successful start-up from the frozen state was possible but was highly dependent on the heat rejection rate at the condenser, which should be low enough to enable the heat to melt the working substance in the condenser and allow liquid to return to the evaporator. Tolubinsky et al. (1978) investigated the start-up characteristics of sodium and potassium heat pipes. The characteristics of the start-up are described based on the experimental results. Camarda (1977) investigated the performance of a sodium heat pipe cooling a leading edge. The heat input was step-wise increased with time and the distribution of heat was non-uniform to simulate aerodynamic heating. Heat rejection was accomplished by radiation. Start-up and shut-down of a 4 m long lithium heat pipe was studied experimentally by Merrigan et al.

(1985, 1986), in which the heat input was increased with time. A temperature history of a typical point on the condenser showed the progress of the effective heat pipe length with time. Ivanovskii et al. (1982) presented the vapor temperature distribution along the length of a sodium heat pipe during the start-up period. The vapor temperature was measured by using a movable microthermocouple placed in the vapor channel. Three flow regimes in the condenser are described based on the vapor temperature: free molecular flow, intermediate, and continuum vapor flow. Unfortunately, the existing experimental data for the start-up period are in general not represented in the archival literature and lack sufficient information for comparison with numerical simulations. The surface temperature distribution along the heat pipe length at different times are required in addition to the vapor temperature to accurately analyse the start-up behavior of heat pipes.

Colwell et al. (1987) and Jang (1988) developed a simple mathematical model to predict the start-up behavior of a sodium heat pipe with a rectangular cross section from the frozen state. In the wall and wick structure, energy transport is described by the transient, two-dimensional heat conduction equation, and the phase change of the working substance is taken into account. In the vapor region, free molecular, choked and continuum flows are considered and one-dimensional, compressible quasi-steady state laminar flow is assumed. The lengths of the evaporator and condenser are not fixed and a variable heat flux and radiation boundary condition are simultaneously applied to the outer surface. The numerical results obtained by using the finite element method are in agreement with experimental results given by Camarda (1977).

The liquid metal heat pipe operates not only at high temperatures but

also the initial temperature may be ambient temperature. All of the experimental results mentioned above show that the temperature near the evaporator increases rapidly up to a certain temperature and then remains constant while the temperature in the rest of the heat pipe is unchanged. Thus, a large temperature gradient exists between these two regions and the location of this gradient moves toward the cooled end of the heat pipe as time increases until the temperature at the end of the condenser reaches the evaporator temperature. In this temperature range, the working substance may be in the solid state as well as the liquid and vapor states. In the vapor space, free molecular flow, continuum flow, sonic and supersonic flow may be encountered due to the extremely small density during the start-up of the heat pipe. These conditions may cause the failure of operation of the heat pipe and limit the performance of the heat pipe. Understanding the start-up behavior and transient performance of the high temperature heat pipe is therefore important and an efficient mathematical model is needed to predict this behavior.

The first part of this paper presents a complete mathematical model to describe the start-up behavior of the heat pipe from the frozen state. This model is then simplified to obtain numerical results. The transient two-dimensional energy equation is solved numerically for the heat pipe wall and wick structure saturated with the working substance and the phase change of the working substance is considered. The transient one-dimensional compressible model is used for the vapor flow dynamics to facilitate coupling the governing equations of the vapor with that of the wall and wick. To the authors' knowledge, the analysis presented here is the only model that includes the effect of the transient vapor flow in the analysis of the start-up of a heat pipe from the frozen state. After the

mathematical models are tested separately, the models are used for a parametric study of the start-up of frozen heat pipes.

4.3 DESCRIPTION OF HEAT PIPE START-UP

Previous experimental observations suggest the following sequence of events during heat pipe start-up from the frozen state. Initially, the working substance is in the solid state and the vapor density is extremely low, so that free molecular flow conditions prevail throughout the vapor space. The input heat flux over the evaporator increases the temperature and starts to melt the frozen substance in this region. Meanwhile, the heat transport from the heated zone to the adjacent pipe proceeds quite slowly via axial conduction through the heat pipe wall, working substance, and wick structure, while the heat transfer in the vapor is almost negligible. Thus, a large temperature gradient exists between the evaporator and condenser.

When energy is continuously added to the evaporator, the frozen working substance in the evaporator is melted, so that evaporation can take place at the liquid-vapor interface and the vapor density in this region is increased. The molecular mean free path in the heated region then becomes small compared to the diameter of the vapor passage and the continuum flow regime is established, while in the cooled zone the vapor is still in free molecular flow. In the continuum flow region, the vapor flows into the condenser section due to the large pressure gradient. During this stage, energy is mainly transferred as latent heat owing to vaporization in the heated zone, and condensation in the cooled zone in the vapor space where continuum flow is established. The temperature near the evaporator remains constant and the location of the temperature gradient moves toward the end

of the condenser until continuum flow is established in the entire vapor space. Cotter (1967) also described this frontal start-up mode when the vapor density is so low and non-condensable gas does not exist in the vapor space.

In heat pipes with metallic working substances, the vapor densities are very small during the start-up even in the continuum flow region. Thus, even for relatively low values of heat input, sonic vapor velocities can be reached. Also, the vapor flow in the heat pipe is quite similar to the flow in a converging-diverging nozzle due to the vapor addition in the evaporator and the vapor removal in the condenser (Dunn and Reay, 1982). Thus, the heat transfer through the vapor space may be limited by the choked flow condition, and supersonic vapor flow and a shock front may occur in the continuum flow region in the condenser. The maximum rate of heat transfer is limited by the sonic limit so that a high heat input in the evaporator causes the various types of start-up failure.

This process continues until the frozen working substance is completely melted and the continuum flow regime reaches the end of the heat pipe, at which time liquid returning to the evaporator is sufficient for normal transient operation. Eventually, the heat pipe may reach a steady state condition. The start-up process of the liquid metal heat pipe from a frozen state may be divided into several distinct periods for convenience of analysis based on the status of the working substance and the behavior of the vapor flow.

1. In the first period, no phase change takes place in the entire region but the temperature near the heated region increases. The vapor flow is in the free molecular condition.
2. The working substance in the evaporator is in the liquid state, but

evaporation does not occur at the liquid-vapor interface.

3. The liquid and solid states of the working substance exist simultaneously in the wick structure and vaporization of the working substance takes place at the liquid-vapor interface. In the vapor space, a region of continuum flow is established in the heated region and a continuum flow front moves toward the cooled end of the heat pipe. The vapor flow may be choked at the beginning of the condenser.
4. The working substance is completely melted but free molecular flow still exists in part of the vapor space.
5. Continuum flow exists over the entire heat pipe length in the vapor region but the heat pipe does not reach the steady state condition.
6. The heat pipe then reaches the steady state operation.

For low temperature heat pipes, the experimental results of the successful start-up from the frozen state are very rare. Deverall et al. (1970) successfully started a water heat pipe from the frozen state (208 K). The wall temperature distribution obtained is similar to that of high temperature heat pipes. The vapor temperature was not obtained, but the vapor density is relatively high even around the melting temperature. This means that the vapor velocity is very low so that choked flow and supersonic vapor velocities may not be encountered during start-up. Unlike high temperature heat pipes, experimental results show that the heat pipe becomes immediately active where the ice is melted, but there still is a large temperature gradient in the axial direction. The heat input at the evaporator should be low enough to return sufficient water into the evaporator for the successful start-up.

4.4 MATHEMATICAL FORMULATION

Consideration is given to the heat pipe wall, the wick structure with the working substance initially subcooled at a uniform temperature, and the vapor region. The external surface of the heat pipe wall in the evaporator and condenser can be exposed to heat flux, convection, and radiation based on the application of the heat pipe. The heat pipe is insulated at both ends of the pipe. A schematic diagram of the physical model is shown in Fig. 4.1.

4.4.1 Heat Pipe Wall

In this region, the progress can be modeled by the heat conduction equation in a hollow cylinder. The temperature and heat flux are continuous at the interface between the wall and the wick structure. The governing equation and boundary conditions are expressed as follows:

$$(\rho c_p)_w \frac{\partial T_w}{\partial t} = \frac{1}{r} \frac{\partial}{\partial r} \left[r k_w \frac{\partial T_w}{\partial r} \right] + \frac{\partial}{\partial x} \left[k_w \frac{\partial T_w}{\partial x} \right] \quad (4.1)$$

The initial condition is

$$T_w(r, x, 0) = T_0 \quad (4.2)$$

The applicable boundary conditions at the outer surfaces of the evaporator and condenser of the heat pipe are given by

$$k_w \frac{\partial T_w}{\partial r} = q(x, t) + h_c (T_c - T_w) + \sigma \xi (T_r^4 - T_w^4) \quad (4.3)$$

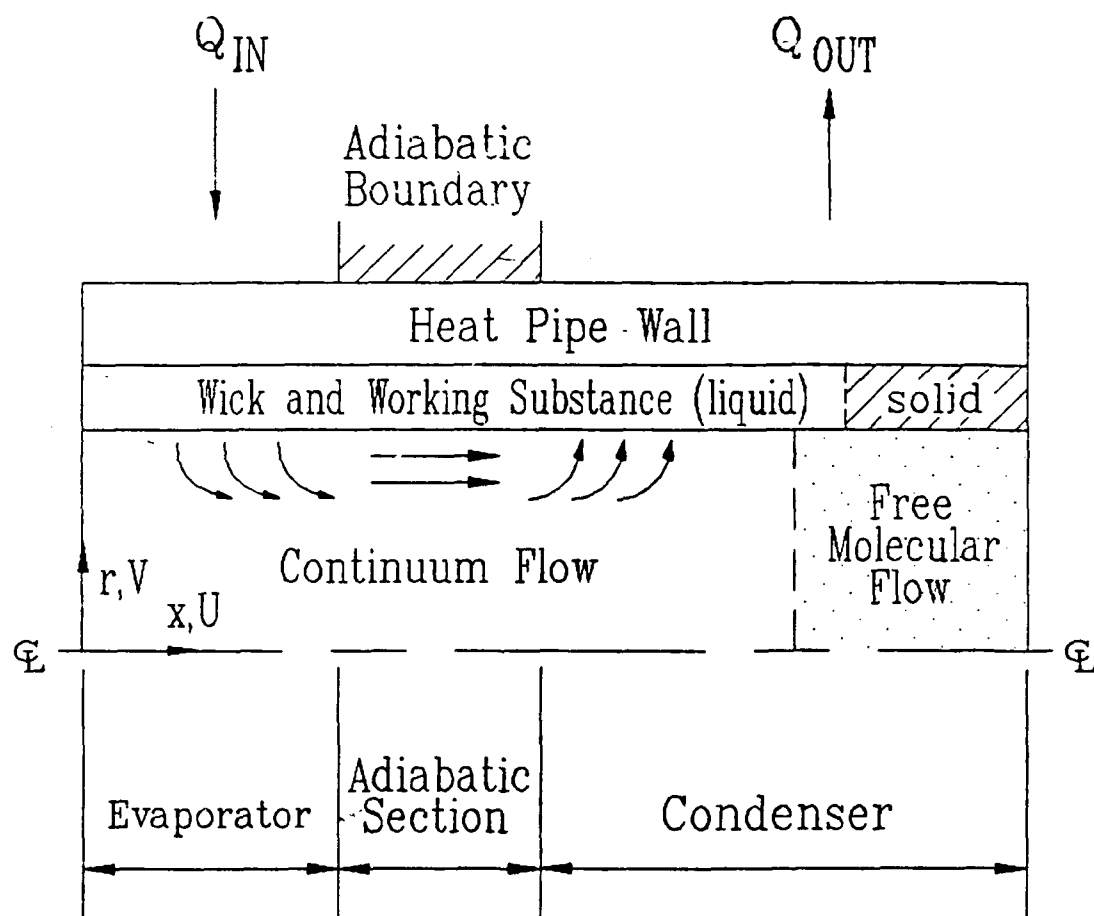


Figure 4.1. Schematic diagram and coordinate configuration of the heat pipe

The applicable boundary conditions at the ends of the heat pipe are

$$\frac{\partial T_w}{\partial x} = 0 \quad (4.4)$$

4.4.2 Wick Structure Region

Initially, the working substance is in the solid state and the vapor flow in the vapor space is negligible so that the adiabatic condition is valid at the liquid-vapor interface. When heat is added to the evaporator, the frozen working substance in the heated region is melted so that the liquid and solid states of the working substance exist in the wick. Fluid motion in the liquid region may then occur due to vaporization and condensation of the working substance. The liquid flow in the wick is considered to be unsteady two-dimensional incompressible laminar flow with negligible body forces. The fluid and wick structure are assumed to be in local equilibrium and the velocities in the axial and radial directions are the local area-averaged velocities over a cross section of a finite element of the wick region instead of the pore velocity or actual velocity. Also, the wick is assumed to be isotropic and homogeneous. The governing equations for the wick region are formulated by using the principles of the conservation of mass, momentum, and energy. The continuity and momentum equations are only effective when fluid motion exists in the wick. The viscous dissipation terms in the energy equation are neglected.

The continuity, momentum and energy equations are

$$\frac{1}{r} \frac{\partial}{\partial r} (r v_\ell) + \frac{\partial u_\ell}{\partial x} = 0 \quad (4.5)$$

$$\frac{1}{\epsilon} \frac{\partial v_\ell}{\partial t} + \frac{1}{\epsilon^2} \left[v_\ell \frac{\partial v_\ell}{\partial r} + U_\ell \frac{\partial v_\ell}{\partial x} \right] = - \frac{1}{\rho_\ell} \frac{\partial p_\ell}{\partial r} - \frac{\nu_\ell v_\ell}{K} + \frac{\nu_\ell}{\epsilon} \left[\frac{1}{r} \frac{\partial}{\partial r} \left[r \frac{\partial v_\ell}{\partial r} \right] - \frac{v_\ell}{r^2} + \frac{\partial^2 v_\ell}{\partial x^2} \right] \quad (4.6)$$

$$\frac{1}{\epsilon} \frac{\partial U_\ell}{\partial t} + \frac{1}{\epsilon^2} \left[v_\ell \frac{\partial U_\ell}{\partial r} + U_\ell \frac{\partial U_\ell}{\partial x} \right] = - \frac{1}{\rho_\ell} \frac{\partial p_\ell}{\partial x} - \frac{\nu_\ell U_\ell}{K} + \frac{\nu_\ell}{\epsilon} \left[\frac{1}{r} \frac{\partial}{\partial r} \left[r \frac{\partial U_\ell}{\partial r} \right] + \frac{\partial^2 U_\ell}{\partial x^2} \right] \quad (4.7)$$

$$(\rho c_p)_i \frac{\partial T_i}{\partial t} + v_\ell \frac{\partial T_i}{\partial r} + U_\ell \frac{\partial T_i}{\partial x} = \frac{1}{r} \frac{\partial}{\partial r} \left[r k_i \frac{\partial T_i}{\partial r} \right] + \frac{\partial}{\partial x} \left[k_i \frac{\partial T_i}{\partial x} \right] \quad (4.8)$$

$$i = \begin{cases} \text{se} & \text{for solid region} \\ \text{me} & \text{for mushy region} \\ \text{le} & \text{for liquid region} \end{cases}$$

$$(\rho c_p)_i = \begin{cases} \epsilon (\rho c_p)_{fs} + (1 - \epsilon) (\rho c_p)_s & \text{for solid region} \\ \epsilon H_{sl} \delta(T - T_m) + (1 - \epsilon) (\rho c_p)_s & \text{for mushy region} \\ \epsilon (\rho c_p)_{fl} + (1 - \epsilon) (\rho c_p)_s & \text{for liquid region} \end{cases} \quad (4.9)$$

where K is the permeability of the wick structure, ϵ is the porosity, and k_i is the effective thermal conductivity. The porosity is between 0 and 1 depending on the porous material. When the porosity approaches unity (no wick structure exists), the permeability approaches infinity. Therefore, eqns. (4.5-4.8) can be reduced to the Navier-Stokes equation for unsteady two-dimensional incompressible laminar flow. For the steady state, eqns. (4.5-4.8) also approach a special case given by Hong et al. (1985). The expressions for the porosity and the effective thermal conductivity of

the screen wicks are given by Chang (1987).

The status of the working substance during start-up is described during six distinct periods mentioned in the previous section. The governing equations (4.5-4.8), however, are not always applicable. For example, during the second period the liquid state of the working substance exists in the wick but evaporation of the working substance at the interface is negligible. Also, the liquid layer is so thin that the effect of natural convection in the liquid region is neglected. Thus, there is no fluid motion in the liquid region so that only eqn. (4.8) without the second and third terms is applicable and eqns. (4.5-4.7) are useful after the second period when there is liquid motion in the wick.

In addition to eqns. (4.5-4.8), coupling conditions at the liquid-solid interface are needed:

$$T_{se} = T_{le} = T_m \quad (4.10)$$

$$k_{se} \frac{\partial T_{se}}{\partial n} - k_{le} \frac{\partial T_{le}}{\partial n} = \epsilon H_{sl} \frac{dS}{dt} \quad (4.11)$$

The boundary conditions at the ends of the heat pipe are

$$\frac{\partial T_i}{\partial x} = 0 \quad (4.12)$$

Based on the continuity of the heat flux and temperature between the heat pipe wall and the wick structure, the boundary conditions are

$$T_i = T_w \quad (4.13)$$

$$k_i \frac{\partial T_i}{\partial r} = k_w \frac{\partial T_w}{\partial r} \quad (4.14)$$

The boundary conditions at the liquid-vapor interface change during the start-up process. In the first and second periods, free molecular flow is prevalent in the vapor space so that the boundary condition at the liquid-vapor interface is

$$\frac{\partial T_i}{\partial r} = 0 \quad (4.15)$$

In the third period, the temperature of part of the liquid-vapor interface is greater than the transition temperature from free molecular flow to continuum flow, T^* , and the vaporization and condensation of the working substance occurs. New boundary conditions are then required to take into account the phase change of the working substance at the interface. This period will be terminated when the frozen working substance is completely melted. The new boundary conditions at the liquid-vapor interface are given as

$$k_{\ell e} \frac{\partial T_{\ell e}}{\partial r} - k_v \frac{\partial T_v}{\partial r} = h_{fg} \dot{m}_o \quad \text{for } T_{\ell e} \geq T^* \quad (4.16)$$

$$\frac{\partial T_i}{\partial r} = 0 \quad \text{for } T_i < T^* \quad (4.17)$$

In the fourth and fifth periods, the working substance is completely

melted so that boundary condition (4.16) is still valid at the interface where continuum flow is established and boundary condition (4.17) is expressed as follows:

$$\frac{\partial T_{\ell e}}{\partial r} = 0 \quad (4.18)$$

When there is fluid motion in the liquid region, additional boundary conditions are required for the liquid flow field. Boundary conditions (4.13 and 4.14) at the wall-liquid interface are still effective and in addition new boundary conditions resulting from the no-slip and impermeable conditions are given by

$$U_{\ell}(R_w, x, t) = 0 \quad (4.19)$$

$$V_{\ell}(R_w, x, t) = 0 \quad (4.20)$$

In addition to boundary conditions (4.16 and 4.17), the boundary conditions for the velocity components at the liquid-vapor interface where the temperature is greater than the transition temperature are

$$U_{\ell}(R_v, x, t) = U_v(R_v, x, t) \quad (4.21)$$

$$\mu_{\ell} \frac{\partial U_{\ell}}{\partial r} = \mu_v \frac{\partial U_v}{\partial r} \quad (4.22)$$

$$V_{\ell}(R_v, x, t) = - \frac{\dot{Bm}_0}{\rho_{\ell}} = V_v(R_v, x, t) \frac{\rho_v}{\rho_{\ell}} \quad (4.23)$$

where B is equal to 1 for evaporation, -1 for condensation and zero for the adiabatic section. The additional boundary conditions at both ends of the heat pipe are needed along with boundary condition (4.12) as follows:

$$U_{\ell}(r, 0, t) = 0 \quad \text{and} \quad U_{\ell}(r, L, t) = 0 \quad (4.24)$$

$$V_{\ell}(r, 0, t) = 0 \quad \text{and} \quad V_{\ell}(r, L, t) = 0 \quad (4.25)$$

4.4.3 Vapor flow dynamics

Initially, the entire working substance is in the solid state so that the vapor space may be nearly evacuated. As the temperature at the interface increases, the vapor density also increases. Continuum flow in the vapor space is considered to be established when the mean free path, λ , is substantially less than the minimum dimensions of the vapor flow passage (Holman, 1981), e.g.,

$$K_n \equiv \frac{\lambda}{D} \leq 0.01 \quad (4.26)$$

The transition temperature, T^* , of the vapor corresponding to the given dimension of the vapor space is expressed by using the kinetic theory of gases as follows (Jang, 1988):

$$T^* \geq \frac{\pi}{2 \times 10^{-4}} \frac{M}{R_u} \left[\frac{\mu_v}{\rho_v D} \right]^2 \quad (4.27)$$

Iterations are required to obtain a value of T^* due to the temperature dependence of the properties. When the vapor temperature is greater than that calculated by eqn. (4.27), continuum flow is assumed to be established in the vapor space.

When continuum flow is established in the vapor space during the start-up from the frozen state, complex flow phenomena are encountered in the continuum flow region due to the extremely small density of the vapor. The vapor pressure is low and the temperature and pressure gradients are large in the axial direction, so the vapor velocity may reach the sonic velocity, and supersonic vapor flow and a shock front may occur in the condenser. Thus, the effects of compressibility, friction at the liquid-vapor interface and dissipation in the vapor should be considered in the mathematical model. The vapor flow may be considered to be axisymmetric, compressible, unsteady laminar flow and the governing equations for this flow are formulated with negligible body forces and heat sources as follows. In cylindrical coordinates, the continuity, momentum and energy equations are:

$$\frac{\partial \rho_v}{\partial t} + \frac{1}{r} \frac{\partial}{\partial r} (r \rho_v v_v) + \frac{\partial (\rho_v U_v)}{\partial x} = 0 \quad (4.28)$$

$$\begin{aligned} \frac{\partial}{\partial t} (\rho_v v_v) + \frac{1}{r} \frac{\partial}{\partial r} (r \rho_v v_v^2) + \frac{\partial}{\partial x} (\rho_v v_v U_v) = - \frac{\partial p_v}{\partial r} + \frac{1}{r} \frac{\partial}{\partial r} (r \tau_{rr}) \\ + \frac{\partial \tau_{rx}}{\partial x} - \frac{\tau_{\theta\theta}}{r} \end{aligned} \quad (4.29)$$

$$\begin{aligned} \frac{\partial}{\partial t}(\rho_v U_v) + \frac{1}{r} \frac{\partial}{\partial r} (r \rho_v V_v U_v) + \frac{\partial}{\partial x} (\rho_v U_v^2) = - \frac{\partial p_v}{\partial x} + \frac{1}{r} \frac{\partial}{\partial r} (r \tau_{rx}) \\ + \frac{\partial \tau_{xx}}{\partial x} \end{aligned} \quad (4.30)$$

$$\begin{aligned} \frac{\partial E_v}{\partial t} + \frac{1}{r} \frac{\partial}{\partial r} \left\{ r [V_v (E_v - \tau_{rr}) - U_v \tau_{rx}] \right\} + \frac{\partial}{\partial x} [U_v (E_v - \tau_{xx}) - V_v \tau_{xr}] \\ = - \frac{1}{r} \frac{\partial}{\partial r} \left[r (p_v V_v - k_v \frac{\partial T_v}{\partial r}) \right] - \frac{\partial}{\partial x} (p_v U_v - k_v \frac{\partial T_v}{\partial x}) \end{aligned} \quad (4.31)$$

where

$$\begin{aligned} \tau_{rr} &= 2\mu_v \frac{\partial V_v}{\partial r} + \mu'_v \left[\frac{1}{r} \frac{\partial}{\partial r} (r V_v) + \frac{\partial U_v}{\partial x} \right] \\ \tau_{xx} &= 2\mu_v \frac{\partial U_v}{\partial x} + \mu'_v \left[\frac{1}{r} \frac{\partial}{\partial r} (r V_v) + \frac{\partial U_v}{\partial x} \right] \\ \tau_{\theta\theta} &= 2\mu_v \frac{V_v}{r} + \mu'_v \left[\frac{1}{r} \frac{\partial}{\partial r} (r V_v) + \frac{\partial U_v}{\partial x} \right] \\ \tau_{xr} &= \tau_{rx} = \mu_v \left[\frac{\partial V_v}{\partial x} + \frac{\partial U_v}{\partial r} \right] \end{aligned}$$

μ'_v is the second coefficient of viscosity and E_v is the total energy per unit volume. The numerical and analytical solutions of the above equations under steady state conditions for annular and conventional heat pipes were given by Faghri (1986) and Faghri and Parvani (1988). Transient results are needed for the start-up from the frozen condition.

While part of the vapor space is in the continuum flow regime, free molecular flow also exists in the rest of the vapor space. Even though the heat transfer through the free molecular flow region may be negligible, the boundary conditions at the border of the two regions are needed to solve the governing equations for the continuum flow region. Since a large temperature gradient exists in the continuum flow region in the condenser

during start-up, most of the vapor may be condensed at the interface. Thus, the vapor penetration in the free molecular flow region may be minimal or penetration may occur in the immediate vicinity of the interface between the continuum flow region and the free molecular flow region. Also, the temperature in the region of free molecular flow remains unchanged except in the vicinity of the continuum flow region due to the near vacuum. Therefore, an imaginary plane, which is adiabatic and normal to the axial direction, is assumed to divide the two vapor flow regions at the point of the transition temperature. The dividing plane moves towards the cooled end of the heat pipe as the location of the transition temperature at the liquid-vapor interface moves.

From the physical conditions at the boundary such as the no-slip condition and the adiabatic condition at both ends of the heat pipe, both the axial and radial velocity components can be assumed to be

$$U_v(r,0,t) = U_v(r,L,t) = V_v(r,0,t) = V_v(r,L,t) = 0 \quad (4.32)$$

and the derivatives of the temperature are expressed as:

$$\frac{\partial T_v}{\partial x}(r,0,t) = \frac{\partial T_v}{\partial x}(r,L,t) = 0 \quad (4.33)$$

Also, at the liquid-vapor interface of the heat pipe the boundary conditions (4.21 - 4.23) are effective.

Since the pressure and density at both ends of the heat pipe are unknown, the axial pressure and density gradients are used to specify the

boundary conditions as follows:

$$\frac{\partial p_v}{\partial x} (r,0,t) = \frac{\partial p_v}{\partial x} (r,L,t) = 0 \quad (4.34)$$

$$\frac{\partial \rho_v}{\partial x} (r,0,t) = \frac{\partial \rho_v}{\partial x} (r,L,t) = 0 \quad (4.35)$$

These conditions are realistic because the vapor velocity near the ends of the heat pipe is so low that the variation of the vapor pressure is very small.

Another boundary condition is induced from the action of the surface tension at the liquid-vapor interface. The radius of curvature of the meniscus is assumed to be characterized by one radius of curvature at the same axial distance. Then, the pressure difference at the interface can be given by using the Laplace and Young equation.

$$p_v - p_\ell = \frac{2\omega}{r_p} = \frac{2\omega}{r_c} \cos \theta \quad (4.36)$$

Boundary condition (4.36) couples the liquid and vapor momentum equations at the liquid-vapor interface. The unknown contact angle of the liquid may be evaluated from the conservation of the liquid mass in the capillary structure. Since evaporation and condensation of the vapor occurs at the interface, the vapor temperature at the interface is the saturation temperature. The Clausius-Clapeyron relationship is used to obtain the

saturation temperature of the vapor from the pressure as given by

$$T_s = \frac{1}{\frac{1}{T_{cr}} - \frac{R_u}{Mh_{fg}} \ln \frac{p}{p_{cr}}} \quad (4.37)$$

The axisymmetric condition along the centerline of the heat pipe specifies the following conditions:

$$\frac{\partial \rho_v}{\partial r} = \frac{\partial U_v}{\partial r} = \frac{\partial E_v}{\partial r} = \frac{\partial p_v}{\partial r} = 0 \quad (4.38)$$

$$V_v(0, x, t) = 0 \quad (4.39)$$

4.5 SIMPLIFICATION OF THE MODEL

The mathematical model, eqns. (4.1-4.39), for the start-up behavior of the liquid metal heat pipe described in the previous section includes most of the physical phenomena which may occur in the heat pipe. Therefore, this model is very complex to solve numerically. The effect of some physical phenomena may be negligible, so a simplified model is derived to predict the performance of the heat pipe during the start-up period. For this purpose, assumptions are made based on the characteristics of the heat pipe and previous studies.

The density of the liquid state of the working substance is much greater than that of the vapor state, so the velocity of the working substance in the wick structure is small. The thermal conductivity of the

liquid metal is large and the thickness of the wick region is very thin. It is then assumed that the effect of the liquid flow in the wick structure is negligible and the wick structure is saturated by the working substance. Thus, the heat transport through the wick structure and working substance is by conduction only but the phase change of the working substance is considered. Under these assumptions, the same governing equation is also applicable to the heat pipe wall and the wick structure by using the proper properties for each region. The governing equation is given as follows:

$$(\rho c_p)_i \frac{\partial T_i}{\partial t} = \frac{1}{r} \frac{\partial}{\partial r} \left[r k_i \frac{\partial T_i}{\partial r} \right] + \frac{\partial}{\partial x} \left[k_i \frac{\partial T_i}{\partial x} \right] \quad (4.40)$$

$$i = \begin{cases} w & \text{for wall region} \\ se & \text{for solid region} \\ me & \text{for mushy region} \\ le & \text{for liquid region} \end{cases}$$

The expression of $(\rho c_p)_i$ for each region is given as follows:

$$(\rho c_p)_i = \begin{cases} (\rho c_p)_w & \text{for wall region} \\ \epsilon (\rho c_p)_{fs} + (1 - \epsilon) (\rho c_p)_s & \text{for solid region in the wick} \\ \epsilon H_{sl} \delta(T - T_m) + (1 - \epsilon) (\rho c_p)_s & \text{for mushy region in the wick} \\ \epsilon (\rho c_p)_{fl} + (1 - \epsilon) (\rho c_p)_s & \text{for liquid region in the wick} \end{cases} \quad (4.41)$$

The thermal conductivity, k_i , can be the thermal conductivity of the wall

material for the wall region. When the effective thermal conductivity for the wick region is calculated by using the expression given by Chang (1987), the thermal conductivity for the working substance is substituted by the solid conductivity, liquid conductivity, or the average value of the solid and liquid conductivity of the working substance corresponding to the solid, liquid, or mushy region, respectively.

The initial condition is

$$T_i(r, x, 0) = T_0 \quad (4.42)$$

The vapor flow is also simplified further from the two-dimensional model to a one-dimensional model since a previous study (Jang et al., 1989) shows that the one-dimensional transient compressible model described the vapor flow dynamics as well as the two-dimensional model for simulated heat pipe vapor flow. The transient compressible one-dimensional continuity, momentum and energy equation are written as follows:

$$\frac{\partial}{\partial t} (\rho_v) + \frac{\partial}{\partial x} (\rho U_v) = \frac{4\rho_o V_o(x)}{D} \quad (4.43)$$

$$\frac{\partial}{\partial t} (\rho_v U_v) + \frac{\partial}{\partial x} (\rho_v U_v U_v) + \frac{\partial}{\partial x} \left[p_v - \frac{4}{3} \mu_v \frac{\partial U_v}{\partial x} \right] = - \frac{2\rho_v U_v^2 f}{D} \quad (4.44)$$

$$\begin{aligned} \frac{\partial E_v}{\partial t} + \frac{\partial}{\partial x} \left[U_v (E_v + p_v) - \frac{4}{3} \mu_v \frac{\partial U_v}{\partial x} U_v - k_v \frac{\partial T_v}{\partial x} \right] &= \frac{4\rho_o V_o(x)}{D} \left[h_o(x) \right. \\ &\left. + \frac{V_o^2(x)}{2} \right] + \frac{2\rho_v U_v^2 f}{D} U_v \end{aligned} \quad (4.45)$$

Since the governing equations are simplified, the corresponding boundary

conditions are also modified to match the governing equations. The applicable boundary conditions at the outer surfaces of the evaporator and condenser of the heat pipe are the same as eqn. (4.3). The boundary conditions at the ends of the heat pipe are

$$\frac{\partial T_i}{\partial x} = 0 \quad (4.46)$$

The boundary condition at the liquid-vapor interface where continuum flow is not established is

$$\frac{\partial T_i}{\partial r} = 0 \quad \text{for} \quad T_i < T^* \quad (4.47)$$

Since the one-dimensional model is used for the vapor flow, boundary condition (4.16) at the liquid-vapor interface is not valid. The heat fluxes, $q(x)$, at the liquid-vapor interface are calculated by using the temperature distribution of the wick structure in the radial direction and then these heat fluxes are applied to the one-dimensional model of the vapor flow as the heat source and sink expressed by

$$q(x) = \rho_o V_o(x) \left[h_o(x) + \frac{V_o^2(x)}{2} \right] \quad (4.48)$$

The other boundary conditions for the temperature, velocity, pressure, and density at both ends of the pipe for the one-dimensional vapor flow are described by Jang et al. (1989).

4.6 NUMERICAL PROCEDURES

The governing equation (4.40) is applicable to the heat pipe wall and the wick structure and the governing equations (4.43-4.45) describe the vapor flow dynamics. For the first and second periods, there is no vapor flow in the vapor space so that only eqn. (4.40) is effective with the adiabatic boundary condition at the liquid-vapor interface. For the third period, continuum flow is established in part of the vapor space so that governing eqns. (4.43-4.45) are also solved and then coupled with the results for the heat pipe wall and wick by using eqn. (4.48) at the liquid-vapor interface. Thus, the governing equations are separately solved for each region. When the coupling is implemented at the interface, iterations are needed. To reduce the amount of computer time, non-iterative schemes are employed for each region.

The well-known alternating direction implicit (ADI) method is used for the heat pipe wall and wick, and the phase change of the working substance during start-up is modeled by using the equivalent heat capacity method (Hsiao, 1985). This method approximates the rapid change of the heat capacity over the phase change temperature range, which is an artificially defined finite temperature range, ΔT , instead of using the Dirac function. Thus, eqn. (4.41) can be expressed as follows:

$$(\rho c_p)_i = \begin{cases} (\rho c_p)_w & \text{for wall region} \\ \epsilon(\rho c_p)_{fs} + (1-\epsilon)(\rho c_p)_s & \text{for solid region} \\ \epsilon \left[\frac{(\rho c_p)_{fs} + (\rho c_p)_{fl}}{2} + \frac{H_{sl}}{2\Delta T} \right] + (1-\epsilon)(\rho c_p)_s & \text{for mushy region} \\ \epsilon(\rho c_p)_{fl} + (1-\epsilon)(\rho c_p)_s & \text{for liquid region} \end{cases} \quad (4.49)$$

In the numerical calculation, this property is evaluated based on the nodal temperatures.

The implicit Beam-Warming method is used for the vapor flow dynamics. This scheme is a non-iterative implicit method and is similar to ADI for multi-dimensional flow problems by using factorization. The spatial derivatives are approximated by using the three-point second-order accurate central difference approximation for the interior points and the one-sided second-order accurate difference approximation for the boundary nodes. The time difference formula is second-order accurate. This system of equations is solved using the conventional methods for solving block tridiagonal systems of equations. The detailed numerical method for the vapor flow in the heat pipe is described by Jang et al. (1989).

After continuum flow exists in the vapor space, eqn. (4.40) should be coupled with eqns. (4.43-4.45) by using the same boundary conditions at the interface. The same amount of heat flux is applicable to the governing equations for the wick structure and vapor space at the liquid-vapor interface. Evaporation and condensation occurs at this interface so that the temperature at the interface is the same as the saturation temperature of the vapor. Therefore, the coupling of the governing equations for the vapor region to those for the wall and wick regions would be achieved by using the heat flux and the saturation temperature at the interface. However, the heat flux at this interface and the saturation temperature are initially unknown, so that these boundary conditions should be assumed and iterations are needed for each time step until the coupling conditions are satisfied along the interface.

Initially, the heat flux at the liquid-vapor interface is unknown when continuum flow exists. Therefore, the governing equations for the wall and

wick regions are solved and then the heat fluxes at each node of the interface are calculated based on the temperature variation in the radial direction in the wick region. These heat fluxes are used as the assumed boundary conditions at the interface for the following time step. After the governing equations are solved for the wall, wick and vapor regions, new heat fluxes are calculated based on the saturation temperature and the temperature in the wick region. The numerical procedure used for coupling is as follows:

1. It is assumed that the liquid-vapor interface temperature is the initial temperature for the first time step.
2. Solve for the temperatures in the wall and wick regions.
3. Calculate the heat fluxes, q , at each node of the liquid-vapor interface by using the temperatures (T_{j-1} and T_j) in the wick region.

$$q = k_{le} \frac{(T_{j-1} - T_j)}{\Delta r} \quad (4.50)$$

4. These heat fluxes are used as the boundary conditions at the interface to solve for temperatures in the wall and wick regions.
5. Use the same heat fluxes to solve the vapor temperature and pressure for the same period at the wall and wick regions. Obtain the saturation temperature, T_s , by using the Clausius-Clapeyron relationship.
6. Calculate the new heat fluxes, q' , at the interface by using the saturation temperature, T_s , in the wick.

$$q' = k_{le} \frac{(T_{j-1} - T_s)}{1.5\Delta r} \quad (4.51)$$

7. Compare the new heat fluxes, q' , with the old heat fluxes, q , at each node of the interface.
8. If the difference between the new heat flux and old heat flux is within an acceptable range, repeat steps 4 to 7 for the next time step.
9. If the difference between the new heat flux and the old heat flux is not within the acceptable range, assume new guessed heat fluxes, q'' , by using the relaxation method and repeat steps 4 to 7 until the comparison of the results is acceptable.

$$q'' = q + a (q' - q) \quad (4.52)$$

10. Repeat steps 4 to 9 until the temperatures reach the steady state.

When the coupling of the governing equations is attempted, some physical characteristics of the two regions are considered. Since the density of the vapor is much smaller than that of the liquid, the volumetric specific heat ρc_p ($= 8.8 \text{ J/m}^3\text{K}$) for the vapor is much smaller than that ($= 1040.1 \text{ KJ/m}^3\text{K}$) for the liquid. Therefore, a difference between the transient response times of the vapor region, and the wall and wick regions exists. The time step for the vapor space should then be much smaller than that for the wall and wick regions. The governing equations for the wall and wick regions are solved for one time step by using the heat flux assumed at the interface, and then the governing equations for the vapor space are solved by using the same heat flux at the interface and smaller time steps for the same period as the wall and wick regions. Also, unlike the steady state case, the heat input to the vapor space in the evaporator is not equal to the heat output in the condenser. During one

time step of the numerical procedure, the unbalanced heat fluxes are fixed at the interface. The vapor temperature and pressure are very sensitive to the heat flux due to the small density of the vapor. Thus, the saturation temperature of the vapor can be greater or smaller than the wick temperature along the axial length depending on the difference of the net heat fluxes at the evaporator and condenser. However, the saturation temperature is physically less than the wick temperature in the evaporator and is greater than the wick temperature in the condenser.

The temperatures at the border between the evaporator and condenser change abruptly due to the sudden change of the boundary conditions at the external surface and interface. However, the saturation temperature changes gradually along the axial distance. When the saturation temperature is forced to become the interface temperature, a large difference between the saturation temperature and the wick temperature at the interface exists at the region separating the evaporator and condenser. When new heat fluxes at the interface are calculated by using eqn. (4.51), the new heat fluxes, q' , for small temperature differences are much greater than the old heat fluxes, q , due to the small distance (1.2×10^{-4} m) between nodes in the radial direction. This may cause the numerical procedures to become unstable and leads to the use of small relaxation factors and many iterations.

4.7 RESULTS AND DISCUSSION

The governing equations for the wall and wick regions and the vapor flow are separately solved, and then are coupled at the liquid-vapor interface by using eqn. (4.48). Therefore, the numerical methods and algorithms can be separately tested and compared to the available data.

Since the working substance changes phase from the solid state to the liquid state during the start-up period from the frozen state, this effect should be incorporated into the numerical model. The solidification of sodium in a square region is chosen to verify the numerical model and algorithm for governing eqn. (4.40). An initial temperature of 393 K is used, which is greater than the melting temperature of 371 K. A constant boundary temperature of 293 K is suddenly imposed on the two surfaces and the adiabatic boundary condition is applied to the other two surfaces. A time step of 1 second and a uniform grid (45 x 45) is used for the numerical calculation. The locations of the interface between the liquid and solid for the time of 50 seconds are calculated by interpolating the nodal temperatures and the results are in agreement with available data (Rathjen and Jiji, 1971). The transient one-dimensional model for the vapor flow dynamics in the heat pipe has already been verified by Jang et al. (1989). The combined model is used to predict the performance of the liquid-metal heat pipe.

4.7.1 Simulation of the heat pipe start-up in the initial stages

Since the numerical scheme and algorithm are verified for the phase change problem, the governing equations which described the start-up behavior of a cylindrical heat pipe during the first and second periods are solved numerically for the wall and wick regions. Initially, the working substance (sodium) is in the solid state at the ambient temperature. The liquid-vapor interface is assumed to be adiabatic due to the free molecular flow in the vapor space during these initial two periods. Thus, the heat transfer mainly takes place through the wall and wick regions by conduction only. The physical model for the present investigation has evaporator,

adiabatic, and condenser section lengths of 0.2, 0.1 and 0.2 m, respectively. The radius of the vapor space and the inner and outer radii of the heat pipe wall are 0.00685, 0.008, and 0.01 m, respectively. The material for the heat pipe wall and wick structure is stainless steel.

Previous experimental results (Deverall et al., 1970) show that successful start-up of the frozen heat pipe greatly depends on the boundary condition at the outer surface of the evaporator and condenser. The working substance in the evaporator where heat is added is melted but that in the condenser where heat is rejected is still in the solid state. Since vapor flow is negligible during the initial stage of the start-up, a large temperature gradient is developed between the evaporator and condenser. Also, the rate of heat transfer in the axial direction is so slow that the working substance in the condenser may not be melted before available liquid is vaporized in the evaporator. Thus, additional heat input in the evaporator easily causes dry-out of the wick while heat extraction at the condenser prevents raising the temperature of the condenser above the melting temperature. Deverall et al. (1970) made successful start-ups of the frozen heat pipe by using a radiation boundary condition at the condenser. Since the radiation boundary automatically controls the heat rejection rate depending on the temperature at the condenser, the temperature of the condenser is allowed to rise. Camarda (1977) used not only a radiation boundary but also a small amount of heat was added on the entire heat pipe surface. Also, the heat input was gradually increased as time goes on. Unlike the transient behavior of the conventional heat pipe, start-up from the frozen state is highly dependent on the state of the working substance in the wick. For successful start-up from the frozen state, the heat input and output should melt the working substance in the

condenser and allow sufficient liquid to return to the evaporator. Also, optimizing the start-up period is very important to reduce possible start-up failure and to perform the original objective.

In light of the previous experimental results, the boundary conditions on the outer surface of the condenser plays an important role in successful start-up. All of the previous experimental results show the wall surface temperatures, so that even for successful start-up the status of the working substance with time is unknown. Numerical simulations are performed to examine the effect of the boundary conditions and to recommend the optimum boundary condition. For this purpose, three different boundary condition cases are chosen for the outer surface of the heat pipe as shown in Table 4.1. A uniform input heat flux of 50 kW/m^2 and radiative heat output are used on the evaporator for all three cases. An emissivity of 0.9 and a radiation reference temperature of 293 K are employed. The boundary conditions at the condenser and adiabatic sections are changed while that at the evaporator remains the same for all three cases. Sodium is used as the working substance. The melting temperature of sodium is 371 K and the transition temperature of 680 K is obtained by using eqn. (27) for the radius of the vapor space (0.00685 m) by iteration. For the numerical calculation, 20 nodes are used at the wall and wick regions in the radial direction and 100 nodes are used in the axial direction. A time step of 1 second is used.

For case 1, radiation is used in the condenser to reject heat. Figure 4.2 shows the temperature distributions at the heat pipe outer wall surface and the liquid-vapor interface. Figure 4.3 shows the surface temperature distributions at different times. As heat is added in the evaporator, the temperature in the evaporator increases and at 20 seconds the working

Table 4.1 Boundary specifications at the outer surface of the heat pipe wall

Case No.	Evaporator		Adiabatic Section	Condenser	
	$Q(\text{kW/m}^2)$	Radiation		$Q(\text{kW/m}^2)$	Radiation
1	50.0	YES	YES	0.0	YES
2	50.0	YES	YES	10.0	YES
3	50.0	YES	NO	10.0	YES

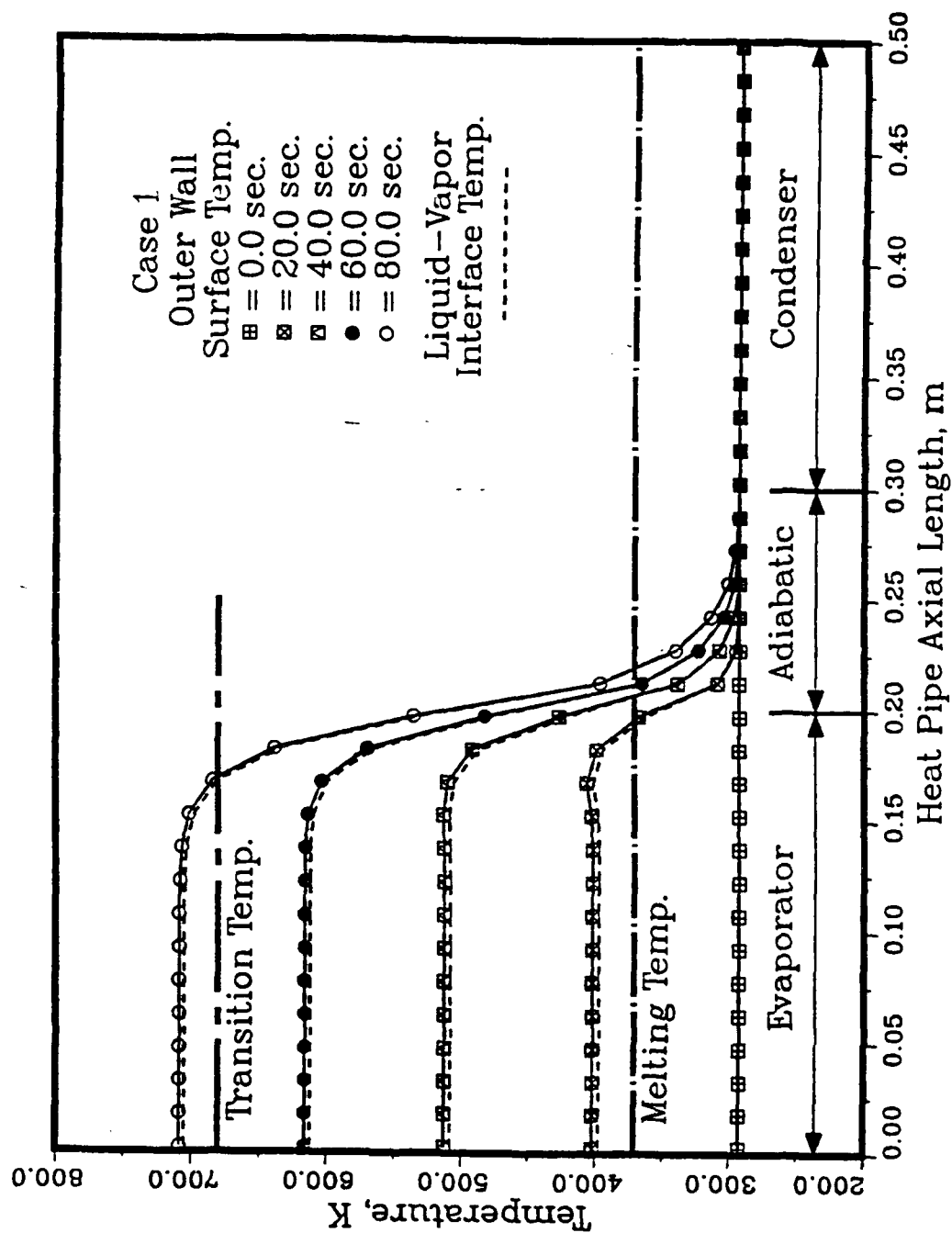


Figure 4.2. Temperature distribution at the outer wall surface and liquid-vapor interface of the heat pipe wall with time for case 1

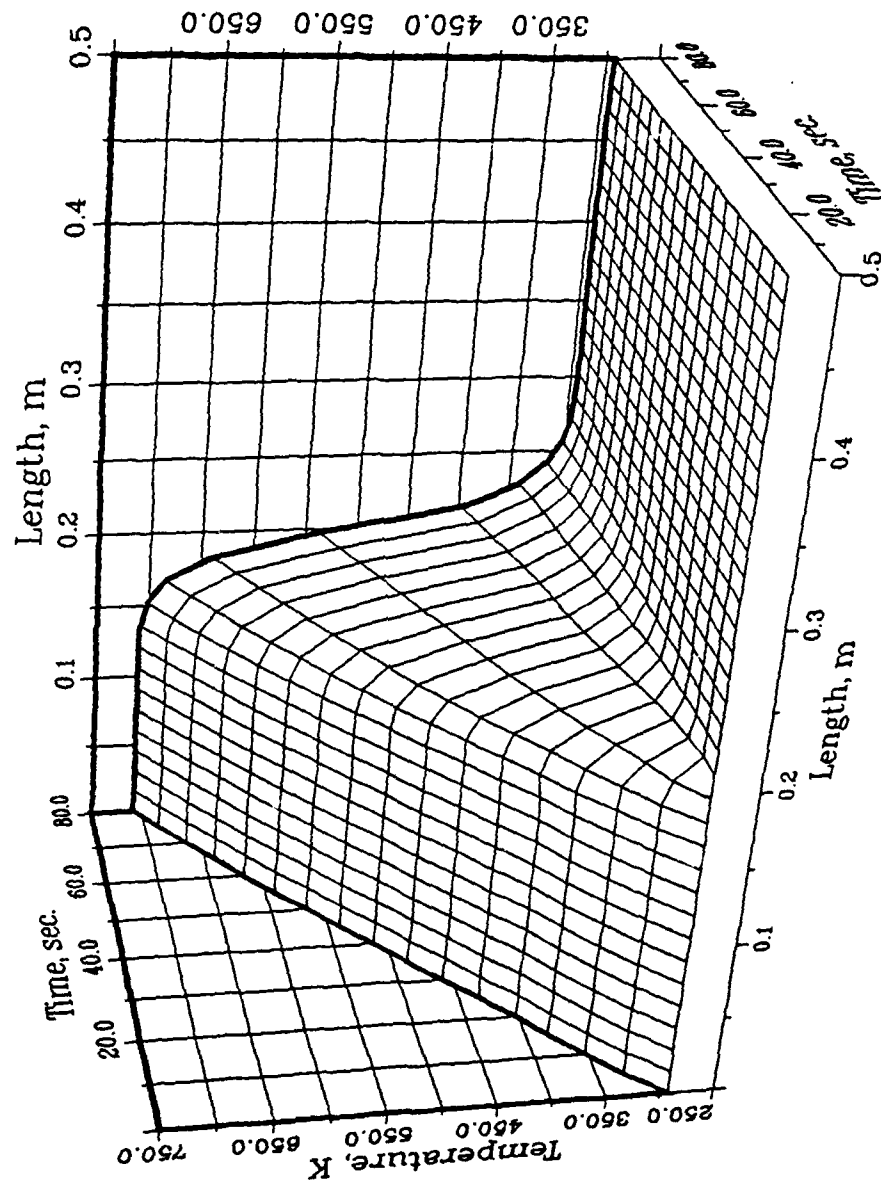


Figure 4.3. Temperature distribution at the outer wall surface of the heat pipe wall with different times for case 1

substance in the evaporator is in the liquid state. However, the temperature in the condenser is not changed from the initial temperature and in the adiabatic section the temperature in the region adjacent to the evaporator increases due to axial conduction. Additional heat input in the evaporator increases the temperature above the transition temperature in the evaporator, but the temperature in the condenser is still not changed so that a large temperature gradient exists. In the adiabatic section, part of the working substance (sodium) is in the liquid state. When the heat input is continued at the evaporator, vaporization occurs at the interface in the evaporator. However, the working substance in most of the adiabatic section and condenser is in the solid state. Therefore, the heat input in the evaporator should be small to prevent dry-out of the wick structure while the working substance in the solid state is melted. Even though successful start-up may be possible for this case, the start-up progresses very slowly.

For case 2, 10 kW/m^2 is added in the condenser in addition to the radiative boundary condition to assist in the start-up of the frozen heat pipe. Figure 4.4 shows the temperature distributions at the outer wall surface and liquid-vapor interface. Figure 4.5 also shows the surface temperature variation for different times. Since a small amount of heat is added in the condenser, the temperature in the condenser is raised above the melting temperature. However the temperature in the adiabatic section is still below the melting temperature. Thus, liquid in the condenser cannot flow to evaporator until the working substance in the adiabatic section liquefies. The temperature in the adiabatic section increases relatively faster than that for case 1 due to heat transfer at both ends of the adiabatic section. The start-up period may be shorter than that for

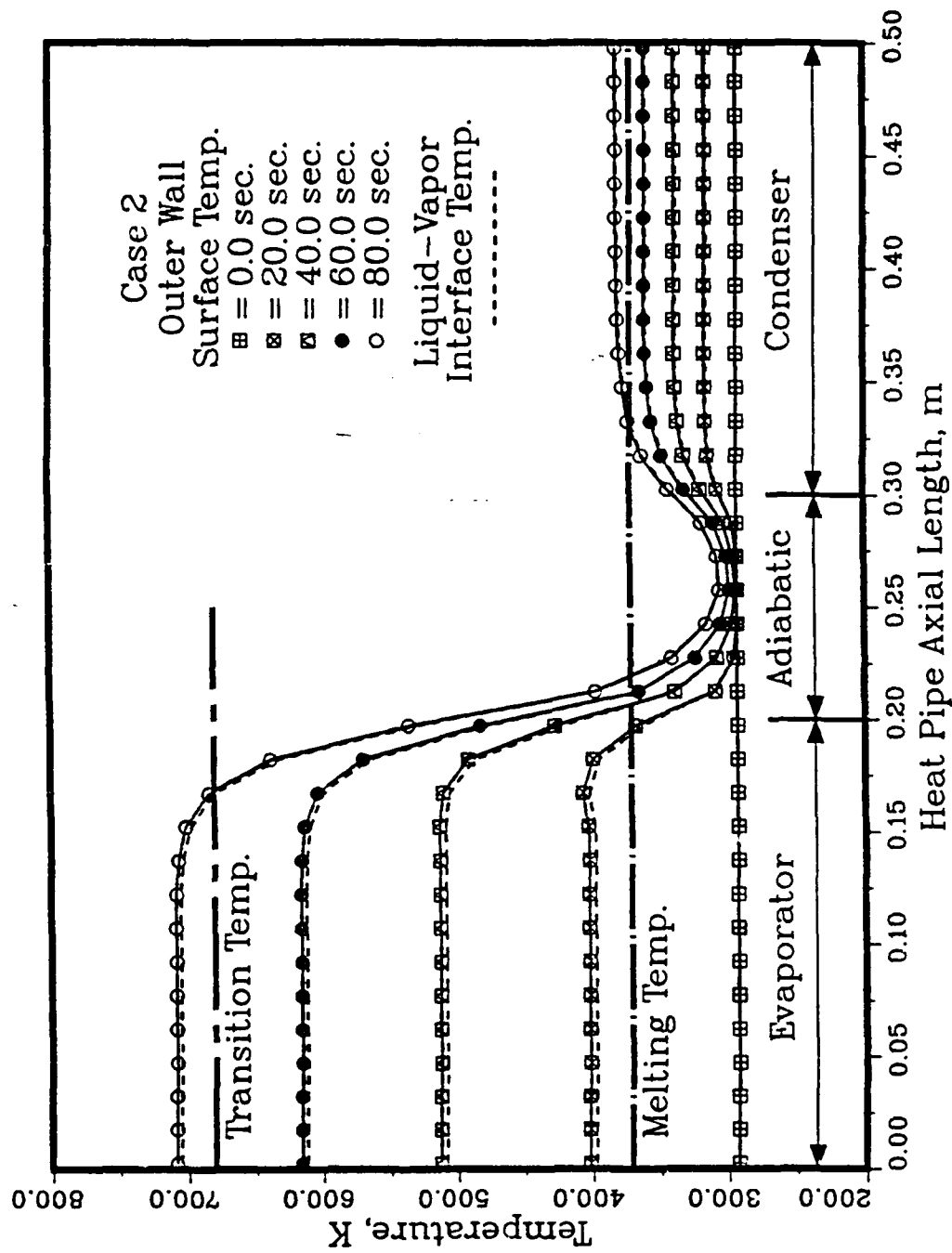


Figure 4.4. Temperature distribution at the outer wall surface and liquid-vapor interface of the heat pipe wall with time for case 2

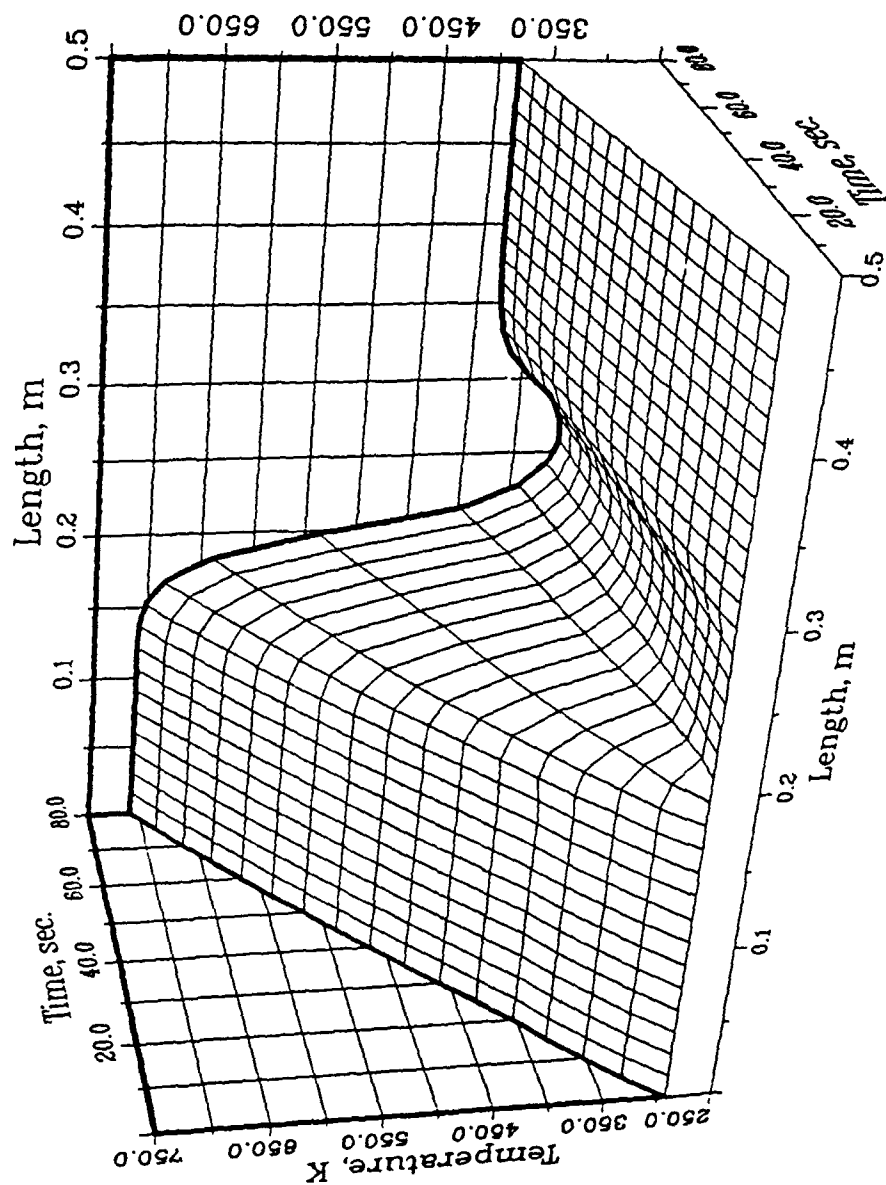


Figure 4.5. Temperature distribution at the outer wall surface of the heat pipe wall with different times for case 2

case 1.

Finally, the adiabatic section is used as part of the condenser and 10 kW/m^2 of heat is input in the condenser section. Figure 4.6 shows the temperature distributions at the heat pipe surface and the liquid-vapor interface and Fig. 4.7 shows the surface temperature at different times. Even though a large temperature gradient still exists along the axial direction, the working substance is completely melted in the entire heat pipe in 80 seconds. When vaporization occurs in the evaporator, the working substance can flow from the condenser to the evaporator to prevent dry-out of the wick structure in the evaporator. Thus, a relatively large amount heat can be added at the evaporator without dry-out so that the start-up period is expected to be much less than those of cases 1 and 2.

Based on the numerical results for three different cases, the boundary conditions for the evaporator and condenser should be chosen such that prior to vaporization occurring in the evaporator, the working substance in most of the wick structure is melted to be able to provide liquid. Therefore, a small amount of heat input at the condenser is recommended to improve the start-up characteristics and a high heat extraction at the condenser which prevents an increase in the condenser temperature should be avoided. The presence of the adiabatic section also retards the progress of start-up.

4.7.2 Transient heat pipe operation

During the initial stages of start-up, the vapor space is nearly evacuated, so that heat transfer in the vapor space is neglected. Only the two-dimensional transient governing equation for the wall and wick regions are solved with an adiabatic boundary condition at the liquid-vapor

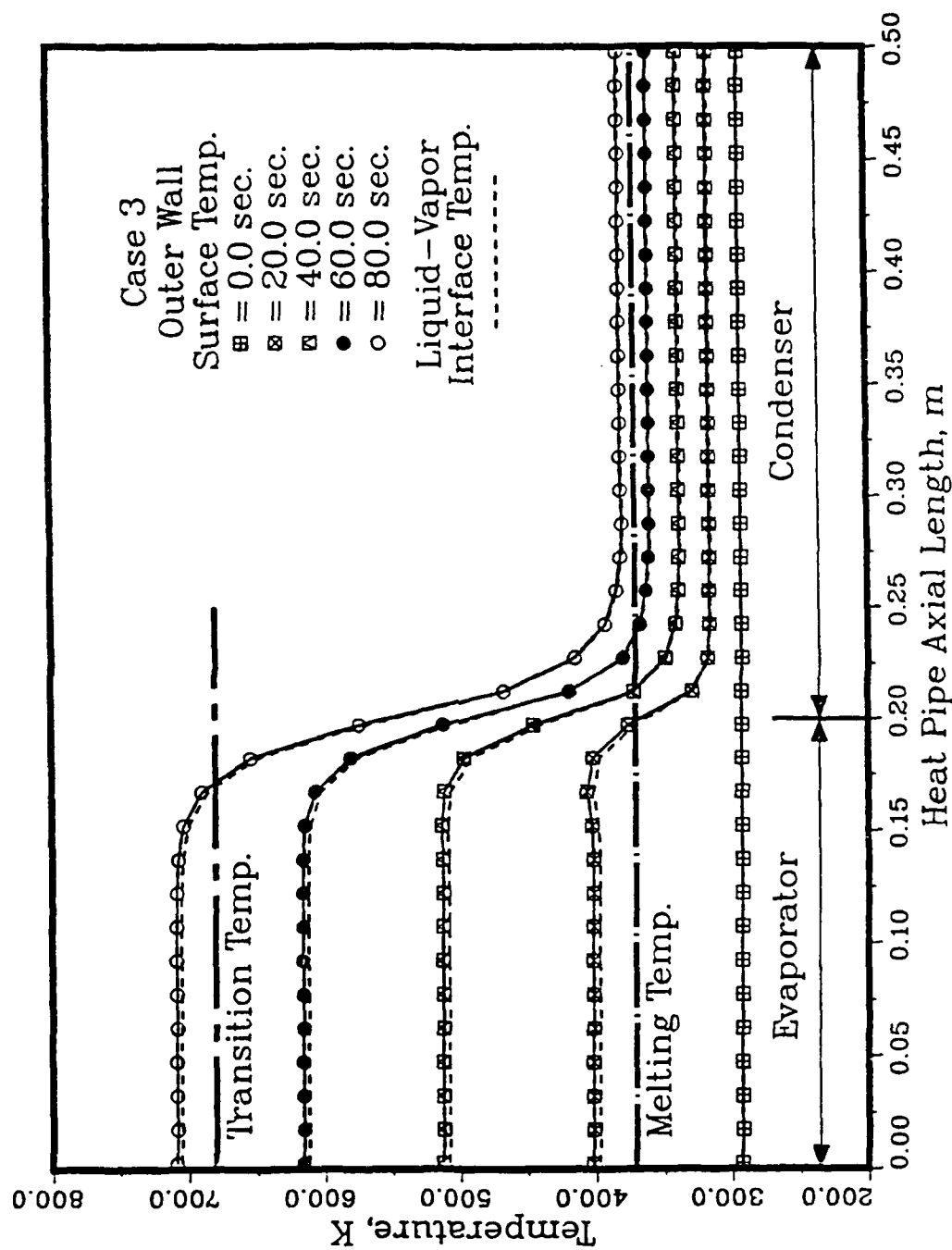


Figure 4.6. Temperature distribution at the outer wall surface and liquid-vapor interface of the heat pipe wall with time for case 3

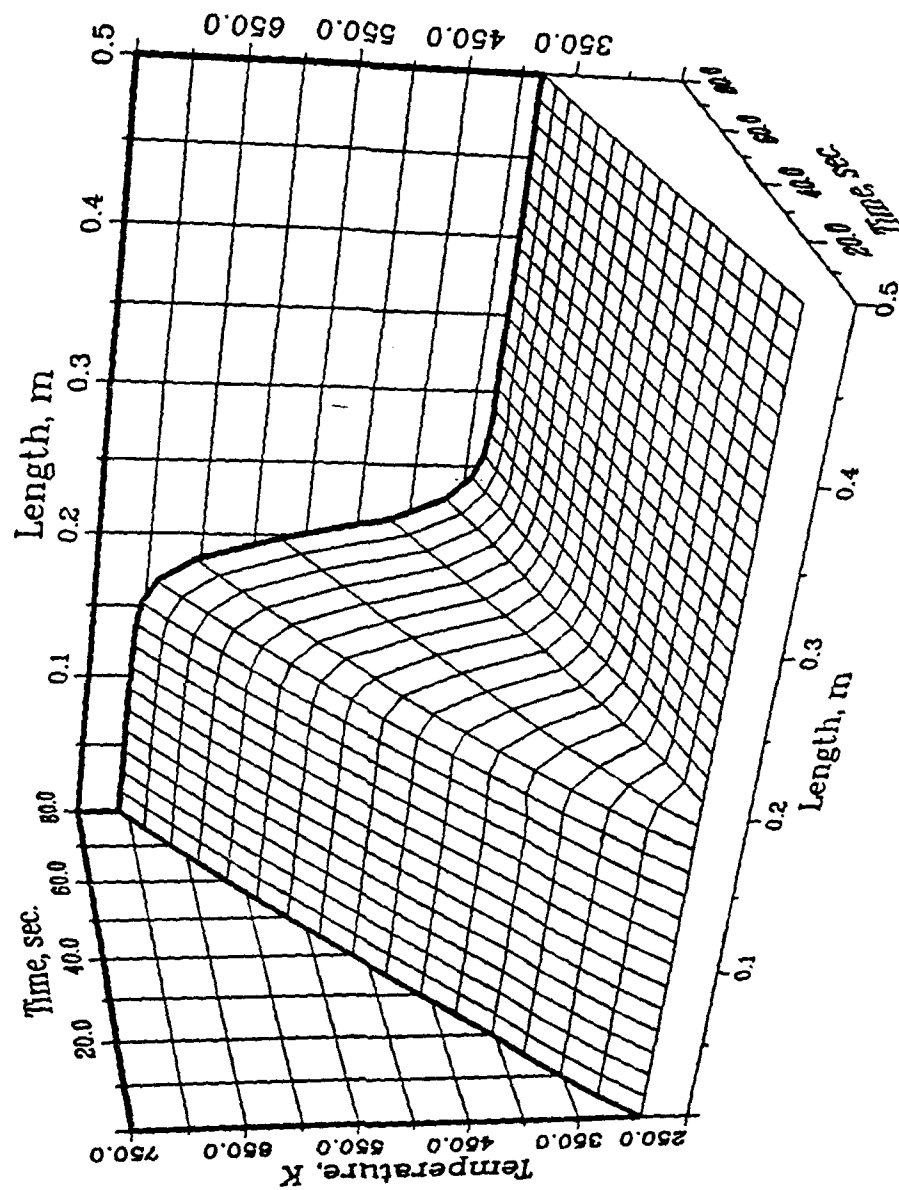


Figure 4.7. Temperature distribution at the outer wall surface of the heat pipe wall with different times for case 3

interface. When continuum flow is developed in the vapor space, heat transfer mainly occurs through the vapor space by using the latent heat of vaporization and condensation at the interface. Thus, the one-dimensional transient governing equation for the vapor flow should be solved and coupled with the results for the wall and wick regions at the interface. However, the difference between the densities of the liquid and vapor is so large that the volumetric specific heat of the vapor is much less than that of the liquid. This difference leads to the use of a different time step for the transient governing equations for the vapor flow. Also, the vapor flow is very sensitive to the heat input and output at the interface. During one time step of the numerical procedure, the heat input to the vapor space is not equal to the heat output due to the transient operation of the heat pipe. Thus, these factors make the coupling procedure difficult and slow.

To simulate the coupling of the governing equation for the wall and wick to that for the vapor flow, the same physical heat pipe model is used except that the adiabatic section is eliminated. Sodium is employed as the working substance. In order to concentrate on the coupling problem, it is assumed that continuum flow is established in the entire vapor space and the working substance is in the liquid state. To yield these conditions, a uniform initial temperature of 800 K, which is greater than the transition temperature (680 K), is used for the wall, wick, and vapor regions. The external surfaces of the heat pipe wall at the evaporator and condenser are exposed to a uniform heat flux of 50000 W/m^2 and a convective boundary condition, respectively. A reference temperature of 300 K and a heat transfer coefficient of $100 \text{ W/m}^2\text{K}$ are used for the convective boundary condition at the condenser section. The time step for the vapor space

should be much smaller than that for the wall and wick regions, so a time step of 0.1 second is employed for the wall and wick regions and time step of 0.1×10^{-3} second is used for the vapor flow. 20 nodes in the radial direction and 160 nodes in the axial direction are used at the wall and wick regions. Also, 160 nodes are employed along the vapor space. A relaxation factor of $\alpha = 0.00003$ is used to obtain the new guessed heat flux.

Figure 4.8 shows the temperature distributions at the outer wall surface, liquid-vapor interface, and the saturation temperature for a time of 0.3 second. The temperature distribution at the outer wall surface is uniform within each section and near the border between the evaporator and condenser, the surface temperature abruptly changes corresponding to the boundary conditions at the surface. The interface temperature matches well with the saturation temperature which is evaluated by using the Clausius-Clapeyron relationship with the vapor pressure. The saturation temperature decreases gradually. Figure 4.9 shows the heat flux distribution at the interface. The new heat flux calculated is converged to the old heat flux. The maximum difference between the two heat fluxes is about 10%. Even though the heat flux at the surface is relatively uniform, the heat flux at the interface is not uniform. Also, the heat flux at the interface is much less than that at the surface. This implies that most of the energy is used to raise the wall and wick temperature at this moment. Figure 4.10 shows the vapor temperature, pressure, velocity, and density distributions. The variation of the vapor temperature, pressure, and density is small. Also, a Mach number of $M = 0.027$ is obtained at the exit of the evaporator.

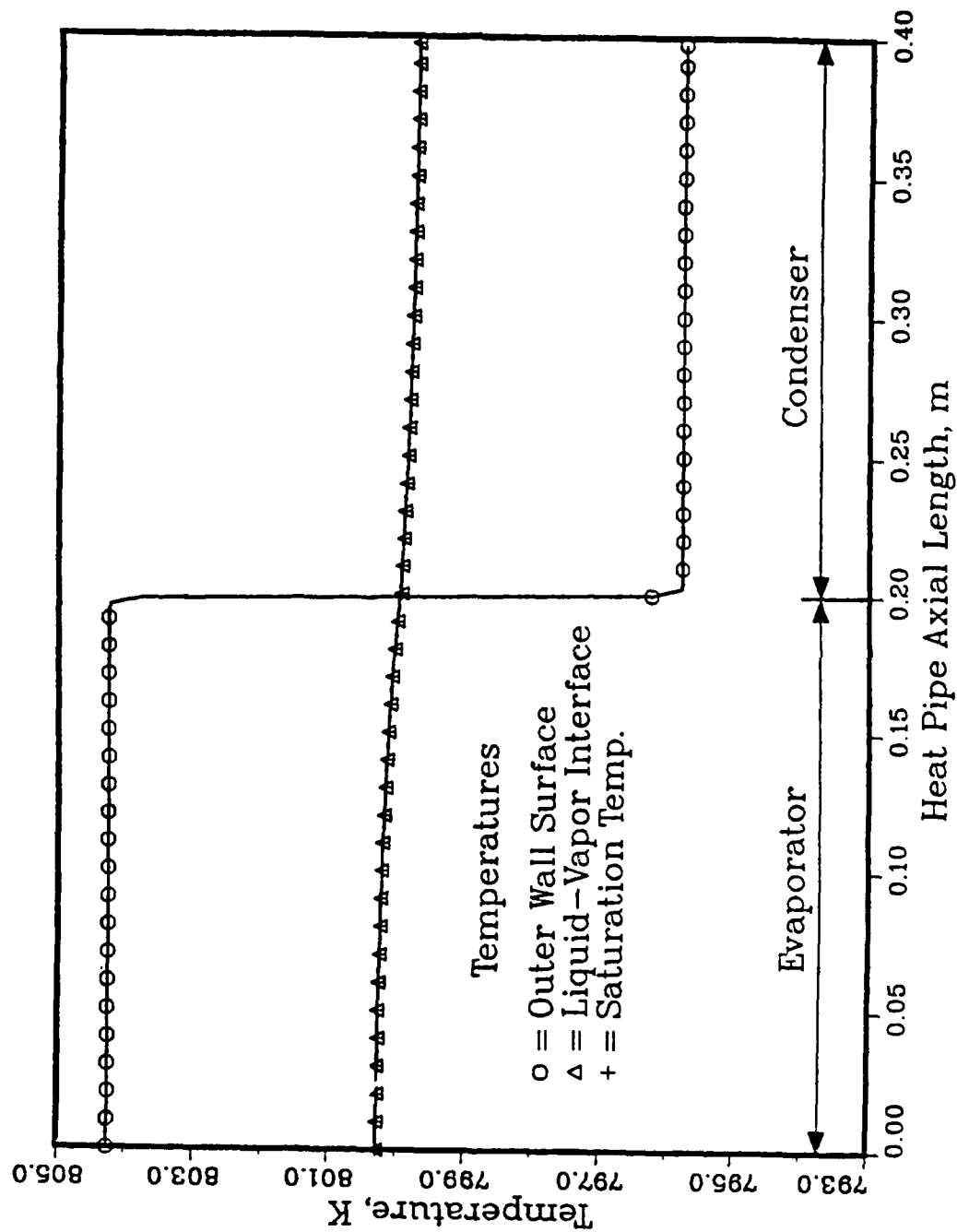


Figure 4.8. Temperature distributions at the outer wall surface and liquid-vapor interface, and saturation temperature for time of 0.3 second

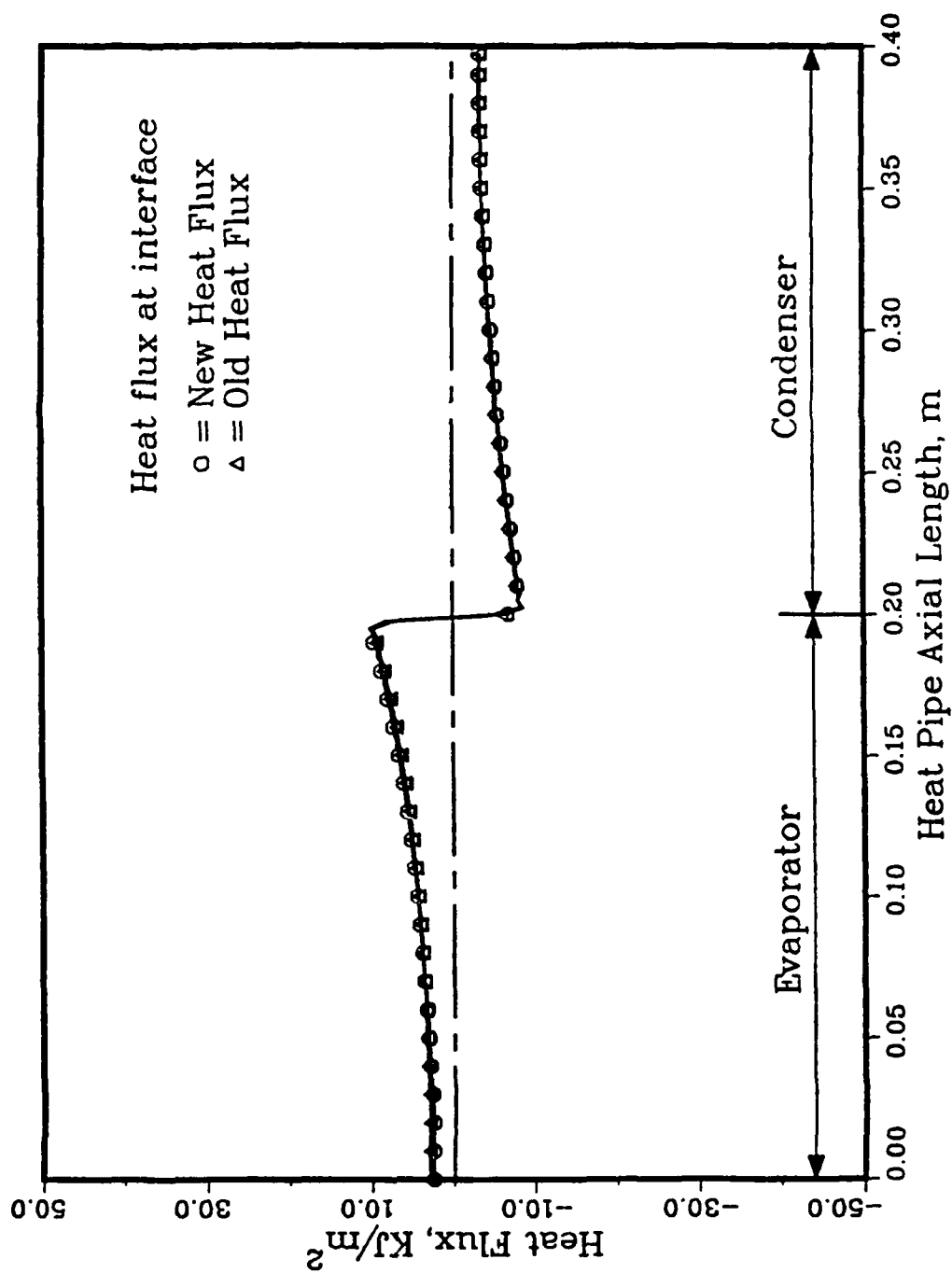


Figure 4.9. Comparison of new heat flux with old heat flux at the interface for time of 0.3 second during transient continuum flow

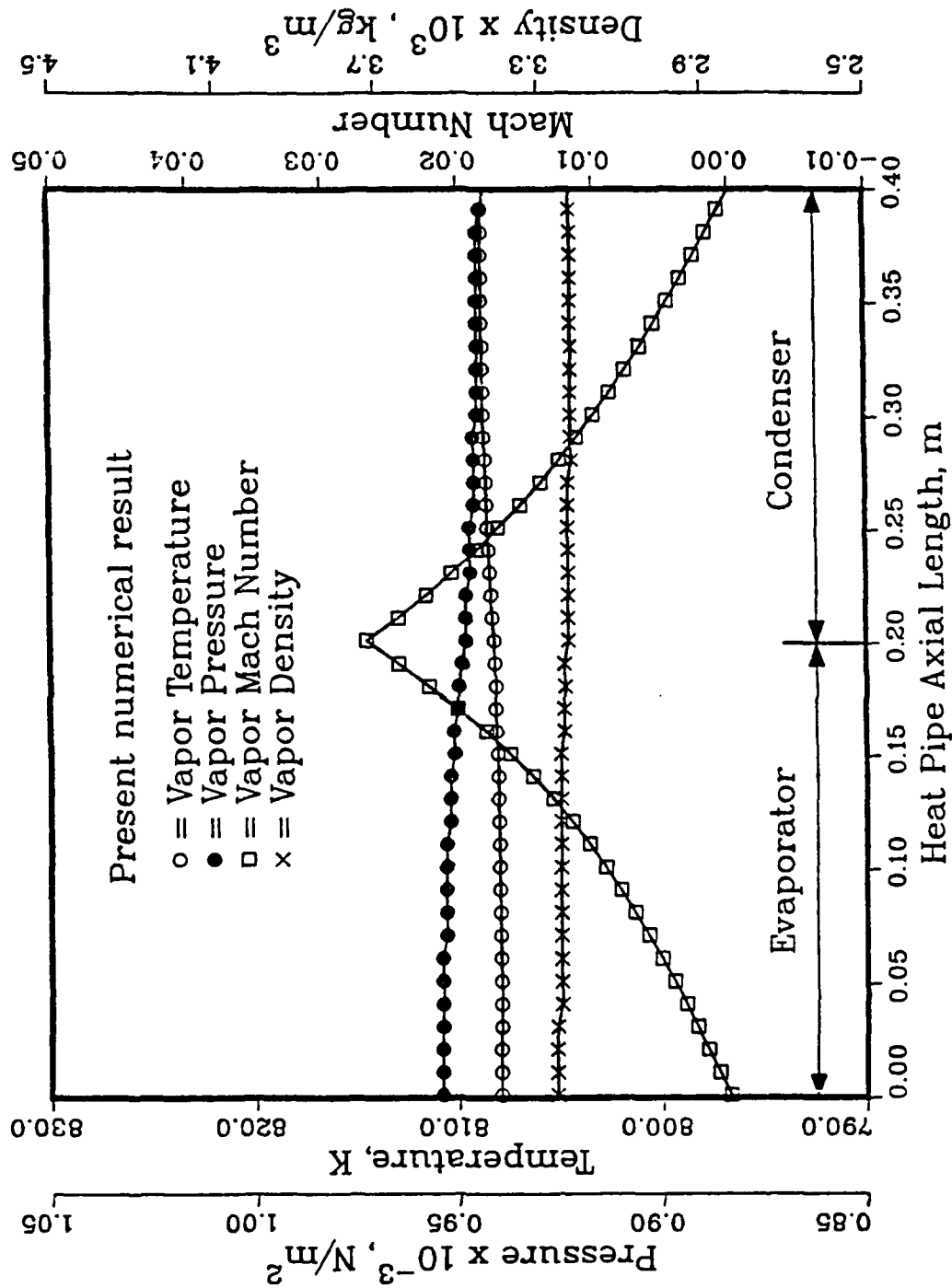


Figure 4.10. Axial variations of temperature, pressure, density and velocity for time of 0.3 second during transient continuum flow

4.8 CONCLUSIONS

The start-up process of the frozen heat pipe is described based on the experimental results. A complete mathematical model is developed to predict the start-up behavior of the heat pipe from the frozen condition. The simplified model is used to obtain the numerical results. The numerical results during the first and second periods show that the heat distributions at the outer surface of the heat pipe play an important role in successful start-up. The heat flux distributions for the evaporator and condenser should be chosen to melt the working substance in the condenser prior to vaporization occurring in the evaporator. A small amount of heat input at the condenser helps start-up and a high heat rejection at the condenser during the start-up should be avoided. The coupling of the two-dimensional transient model for the wall and wick to the one-dimensional transient model for the vapor flow is achieved when continuum flow exists in the vapor space. During the transient operation, the heat flux distribution at the interface is quite different from that at the surface. Efforts to improve the present model will continue.

Section V

A TEMPERATURE TRANSFORMING MODEL FOR PHASE-CHANGE PROBLEMS INCLUDING NATURAL CONVECTION

5.1 SUMMARY

A temperature transforming model was proposed to convert the enthalpy-based energy equation into a nonlinear equation with a single dependent variable. The model and the numerical scheme were first tested with diffusive phase-change problems. The model eliminates the time step and grid size limitations and is insensitive to the phase-change temperature ranges, proving that the model is flexible and can handle multi-dimensional phase-change problems which have large specific heat and thermal conductivity differences between the liquid and solid phases in a fixed grid system. The model was further tested against other phase-change problems including natural convection in a cavity. A comparison between the numerical solutions and the existing experimental data resulted in a good agreement.

5.2 INTRODUCTION

Heat transfer involving melting and solidification is a fertile area of research because of its great importance in applications including the start up of heat pipes from a frozen state, which was one of the motivations for the present work. Since problems of this type are inherently nonlinear due to the existence of a moving interface, whose position is not known a priori, there are relatively few analytical solutions to these so-called Stefan problems. A large number of numerical techniques have been developed which can be divided into two major groups. The first group can be called strong numerical solutions or classical solutions (Okada, 1984; Ho and Chen, 1986; Ho and Viskanta, 1984; Sparrow and Ohkubo, 1986). For this group, deformed grids or transformed coordinate systems are required to account for the positions of the phase-change fronts. They are applicable to those processes involving one or two phases in one space dimension which, with the use of complicated schemes, are being applied to two-dimensional cases as well.

The second group may be called weak numerical solutions or fixed grid solutions (Shamsundar and Sparrow, 1975; Raw and Schneider, 1985; Schneider, 1987; Voller and Cross, 1981; Voller et al., 1987; Voller and Prakash, 1987; Prakash et al., 1987; Cao et al., 1989; Morgan, 1981; Gartling, 1980; Hsiao and Chung, 1984; Hsiao, 1985). These methods remove the need to satisfy conditions at the phase-change front and can be easily extended to multi-dimensional problems. In this group, the two most important and widely-used methods are enthalpy methods and temperature-based equivalent heat capacity methods. Both methods in this group have advantages and disadvantages. Enthalpy methods are flexible and

can handle phase-change problems occurring both at a single temperature and over a temperature range. The drawback of this method is that although the predicted temperature distributions and melting fronts are reasonable, the predicted time history of the temperature at a typical grid point may have some oscillations. The temperature-based fixed grid methods have no such time history problems and are more convenient with conjugate problems involving an adjacent wall, but have to deal with the severe nonlinearity when the phase-change temperature range is small. Since the objective of this paper is to improve the temperature-based fixed-grid methods, the equivalent heat capacity model is briefly described below. The energy equation including convective terms is given by Morgan (1981) and Gartling (1980):

$$\rho c_p^* \left(\frac{\partial T^0}{\partial t} + u \frac{\partial T^0}{\partial x} + v \frac{\partial T^0}{\partial y} + w \frac{\partial T^0}{\partial z} \right) = \frac{\partial}{\partial x} \left(k \frac{\partial T^0}{\partial x} \right) + \frac{\partial}{\partial y} \left(k \frac{\partial T^0}{\partial y} \right) + \frac{\partial}{\partial z} \left(k \frac{\partial T^0}{\partial z} \right) \quad (5.1)$$

For cases without convection, eqn. (5.1) reduces to the following form as used by Hsiao and Chung (1984) and Hsiao (1985) for phase-change problems

$$\rho c_p^* \frac{\partial T^0}{\partial t} = \frac{\partial}{\partial x} \left(k \frac{\partial T^0}{\partial x} \right) + \frac{\partial}{\partial y} \left(k \frac{\partial T^0}{\partial y} \right) + \frac{\partial}{\partial z} \left(k \frac{\partial T^0}{\partial z} \right) \quad (5.2)$$

For the liquid phase and the solid phase, the properties c and k will generally have different values. To account for the latent heat effect on the liquid-solid interface, an equivalent heat capacity is introduced assuming that phase change occurs over a temperature range as shown in Fig. 5.1.

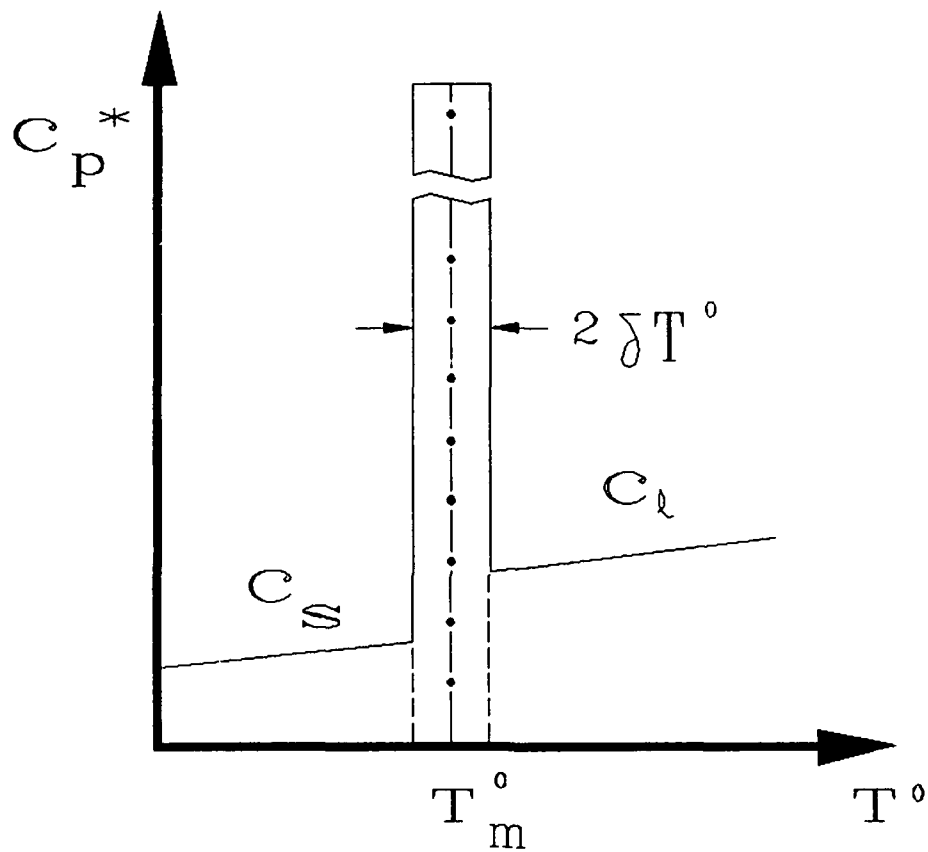


Fig. 5.1 Approximation of equivalent specific heat for melting/solidification problem.

$$c_p^* = \begin{cases} c_s & (T^0 < T_m^0 - \delta T^0) \\ \frac{L}{2\delta T^0} + \frac{c_\ell + c_s}{2} & (T_m^0 - \delta T^0 \leq T^0 \leq T_m^0 + \delta T^0) \\ c_\ell & (T^0 > T_m^0 + \delta T^0) \end{cases} \quad (5.3)$$

along with the thermal conductivity expression

$$k = \begin{cases} k_s & (T^0 < T_m^0 - \delta T^0) \\ \frac{k_\ell + k_s}{2} & (T_m^0 - \delta T^0 \leq T^0 \leq T_m^0 + \delta T^0) \\ k_\ell & (T^0 > T_m^0 + \delta T^0) \end{cases} \quad (5.4)$$

Although the equivalent heat capacity formulation has the advantage of being simple to program, many studies have revealed difficulties in the selection of the time step, mesh size and the phase-change temperature range, $2\delta T^0$. The predicted phase-change interface location advances frequently in an unrealistic oscillatory fashion and this is accompanied by distortion of the temperature profile in the region undergoing phase change (Hsiao and Chung, 1984; Hsiao, 1985). Some attempts have been made to improve this method. For example, Hsiao and Chung (1984) and Hsiao (1985) used a linear interpolation of the nodal temperatures to account for the latent heat effect. Although they claimed that the algorithm is insensitive to the phase-change temperature ranges, the time steps used are still small and the numerical results are calculated with an explicit scheme (Hsiao, 1985).

In this paper, a new temperature-based fixed-grid formulation is proposed, and the reason that the original equivalent heat capacity model

is subject to such restrictions on the time step, mesh size and the phase-change temperature range will also be discussed. In addition, the new methodology will be applied to phase-change problems including the effect of natural convection in a cavity.

5.3 NUMERICAL FORMULATION AND MODELING

The continuity, momentum, and energy equations governing three-dimensional transient laminar flows with no viscous dissipation in the Cartesian coordinate system are (Kays and Crawford, 1980)

$$\frac{\partial \rho}{\partial t} + \frac{\partial}{\partial x} (\rho u) + \frac{\partial}{\partial y} (\rho v) + \frac{\partial}{\partial z} (\rho w) = 0 \quad (5.5a)$$

$$\begin{aligned} \frac{\partial(\rho u)}{\partial t} + \frac{\partial}{\partial x} (\rho u^2) + \frac{\partial}{\partial y} (\rho uv) + \frac{\partial}{\partial z} (\rho uw) = & - \frac{\partial p}{\partial x} + \rho g_x + \frac{\partial}{\partial x} \left(\mu \frac{\partial u}{\partial x} \right) + \frac{\partial}{\partial y} \left(\mu \frac{\partial u}{\partial y} \right) \\ & + \frac{\partial}{\partial z} \left(\mu \frac{\partial u}{\partial z} \right) \end{aligned} \quad (5.5b)$$

$$\begin{aligned} \frac{\partial(\rho v)}{\partial t} + \frac{\partial}{\partial x} (\rho uv) + \frac{\partial}{\partial y} (\rho v^2) + \frac{\partial}{\partial z} (\rho vw) = & - \frac{\partial p}{\partial y} + \rho g_y + \frac{\partial}{\partial x} \left(\mu \frac{\partial v}{\partial x} \right) + \frac{\partial}{\partial y} \left(\mu \frac{\partial v}{\partial y} \right) \\ & + \frac{\partial}{\partial z} \left(\mu \frac{\partial v}{\partial z} \right) \end{aligned} \quad (5.5c)$$

$$\begin{aligned} \frac{\partial(\rho w)}{\partial t} + \frac{\partial}{\partial x} (\rho uw) + \frac{\partial}{\partial y} (\rho vw) + \frac{\partial}{\partial z} (\rho w^2) = & - \frac{\partial p}{\partial z} + \rho g_z + \frac{\partial}{\partial x} \left(\mu \frac{\partial w}{\partial x} \right) + \frac{\partial}{\partial y} \left(\mu \frac{\partial w}{\partial y} \right) \\ & + \frac{\partial}{\partial z} \left(\mu \frac{\partial w}{\partial z} \right) \end{aligned} \quad (5.5d)$$

$$\begin{aligned} \frac{\partial(\rho E)}{\partial t} + \frac{\partial}{\partial x} (\rho u E) + \frac{\partial}{\partial y} (\rho v E) + \frac{\partial}{\partial z} (\rho w E) = & \frac{\partial}{\partial x} \left(k \frac{\partial T^0}{\partial x} \right) + \frac{\partial}{\partial y} \left(k \frac{\partial T^0}{\partial y} \right) \\ & + \frac{\partial}{\partial z} \left(k \frac{\partial T^0}{\partial z} \right) \end{aligned} \quad (5.5e)$$

with the state equation

$$\frac{dE}{dT^0} = c(T^0) \quad (5.6)$$

The momentum equation should be solved in addition to the energy equation even though the focus in this study is on the energy equation.

For the phase change occurring over a temperature range as shown in Fig. 5.2, and in the case of constant specific heats for each phase, the relation between enthalpy and temperature can be expressed as

$$E(T^0) = \begin{cases} c_s (T^0 - T_m^0) + c_s \delta T^0 & T^0 - T_m^0 < -\delta T^0 \text{ (solid phase)} \\ (c_m + \frac{L}{2\delta T^0}) (T^0 - T_m^0) + c_m \delta T^0 + \frac{L}{2} & -\delta T^0 \leq T^0 - T_m^0 \leq \delta T^0 \text{ (mushy phase)} \\ c_\ell (T^0 - T_m^0) + c_s \delta T^0 + L & T^0 - T_m^0 > \delta T^0 \text{ (liquid phase)} \end{cases} \quad (5.7)$$

where T_m^0 is the melting or freezing temperature, and $\delta T^0 = (T_\ell^0 - T_s^0)/2$ is one-half of the phase-change temperature range. In the above relation, we have selected $E = 0$ to correspond to phase-change materials in the solid state at $T^0 = T_m^0 - \delta T^0$. The specific heat of the mushy phase has been taken as the average of those of the solid and liquid phases; i.e., $c_m = \frac{1}{2}(c_s + c_\ell)$.

It should be pointed out that in the above relation for the mushy region a linear change was assumed. In some real systems it may take more complicated forms, but this is outside the scope of this paper.

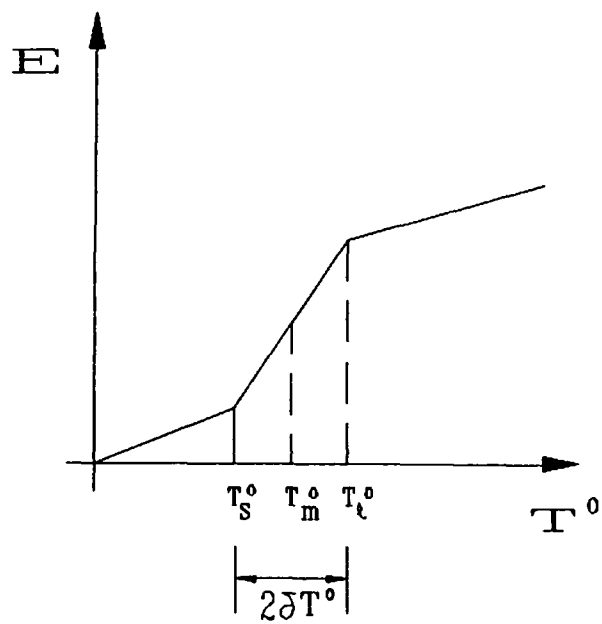


Figure 5.2 Relation between T^o and E with phase-change temperature range

Equation (5.7) can be rewritten with the scaled temperature $T^* = T^0 - T_m^0$.

$$E(T^*) = \begin{cases} c_s T^* + c_s \delta T^0 & T^* < -\delta T^0 \quad (\text{solid phase}) \\ (c_m + \frac{L}{2\delta T^0}) T^* + c_m \delta T^0 + \frac{L}{2} & -\delta T^0 \leq T^* \leq \delta T^0 \quad (\text{mushy phase}) \\ c_\ell T^* + c_s \delta T^0 + L & T^* > \delta T^0 \quad (\text{liquid phase}) \end{cases} \quad (5.8)$$

A temperature function is introduced as follows

$$E(T^*) = C^0(T^*) T^* + S^0(T^*) \quad (5.9)$$

where $C^0(T^*)$ and $S^0(T^*)$ are determined from eqn. (5.8)

$$C^0(T^*) = \begin{cases} c_s & (T^* < -\delta T^0) \\ c_m + \frac{L}{2\delta T^0} & (-\delta T^0 \leq T^* \leq \delta T^0) \\ c_\ell & (T^* > \delta T^0) \end{cases} \quad (5.10)$$

$$S^0(T^*) = \begin{cases} c_s \delta T^0 & (T^* < -\delta T^0) \\ c_m \delta T^0 + \frac{L}{2} & (-\delta T^0 \leq T^* \leq \delta T^0) \\ c_s \delta T^0 + L & (T^* > \delta T^0) \end{cases} \quad (5.11)$$

Upon substituting eqn. (5.9) into eqn. (5.5e)

$$\begin{aligned} \frac{\partial(\rho C^0 T^*)}{\partial t} + \frac{\partial}{\partial x} (\rho u C^0 T^*) + \frac{\partial}{\partial y} (\rho v C^0 T^*) + \frac{\partial}{\partial z} (\rho w C^0 T^*) &= \frac{\partial}{\partial x} (k \frac{\partial T^*}{\partial x}) \\ + \frac{\partial}{\partial y} (k \frac{\partial T^*}{\partial y}) + \frac{\partial}{\partial z} (k \frac{\partial T^*}{\partial z}) + B \end{aligned} \quad (5.12)$$

with

$$B = - \left[\frac{\partial(\rho S^0)}{\partial t} + \frac{\partial(\rho u S^0)}{\partial x} + \frac{\partial(\rho v S^0)}{\partial y} + \frac{\partial(\rho w S^0)}{\partial z} \right]$$

and $C^0 = C^0(T^*)$, $S^0 = S^0(T^*)$ given by eqns. (5.10) and (5.11), respectively.

The energy equation has now been transformed into a nonlinear equation with a single dependent variable T^* . The nonlinearity of the phase-change problem is due to the existence of the moving phase-change front. It can be shown that in the liquid and solid phase regions away from the moving front, eqn. (5.12) reduces to a linear equation when the velocity field is known.

It can be seen that eqn. (5.10) is identical to eqn. (5.3), and that when the density ρ is constant the equivalent heat capacity model is a special case of eqn. (5.12) with $B = 0$ and C^0 independent of the space variables x, y, z and time. This is why many studies using the equivalent capacity model found difficulties in selecting the time step and mesh sizes and have often encountered physically unrealistic oscillatory results. In order for $\frac{\partial(\rho C^0 T^*)}{\partial t} = C^0 \frac{\partial(\rho T^*)}{\partial t}$, and $\frac{\partial(\rho S^0)}{\partial t} = 0$, the time step must be small enough that the temperature change is so small that values of C^0 and S^0 will not change from one phase to another within the time step. Special care must also be taken for the selection of grid sizes to make C^0 and S^0 independent of the space variables. In fact, the above conditions are so severe that it is very difficult to satisfy them.

The major difference between the present model and the equivalent heat capacity model is that the present model starts from the energy equation, eqn. (5.5e), instead of eqn. (5.1). Since eqn. (5.1) is only a special case of the more general energy equation, eqn. (5.5e), the shortcoming of the equivalent heat capacity model is not surprising.

The conductivity in eqn. (5.12) is a function of T^* . With the assumption of a linear change in the mushy phase, k can be written as

$$k(T^*) = \begin{cases} k_s & (T^* < -\delta T^0) \\ k_s + (k_\ell - k_s) (T^* + \delta T^0)/2\delta T^0 & (-\delta T^0 \leq T^* \leq \delta T^0) \\ k_\ell & (T^* > \delta T^0) \end{cases} \quad (5.13)$$

5.4 NUMERICAL SCHEME FOR THE ENERGY EQUATION

Since the continuity and momentum equations are the same as those of conventional fluid flow problems, the emphasis here will be on the energy equation. In the following study, the thermophysical properties such as k and c are assumed to be constant in each phase but may differ among the solid, mushy and liquid phases, while the density is considered to be constant.

The following non-dimensionalized variables are introduced

$$X = \frac{x}{H}, \quad Y = \frac{y}{H}, \quad Z = \frac{z}{H}, \quad U = u \frac{H}{a_\ell}, \quad V = v \frac{H}{a_\ell}, \quad W = w \frac{H}{a_\ell}, \quad \tau = \frac{a_\ell}{H^2} t,$$

$$T = \frac{T^0 - T_m^0}{T_h^0 - T_c^0}, \quad C = \frac{C^0}{c_\ell}, \quad S = \frac{S^0}{c_\ell(T_h^0 - T_c^0)}, \quad K = \frac{k}{k_\ell}, \quad \delta T^* = \frac{\delta T^0}{T_h^0 - T_c^0},$$

$$St = \frac{c_\ell (T_h^0 - T_c^0)}{L}, \quad C_{s\ell} = \frac{c_s}{c_\ell}, \quad K_{s\ell} = \frac{k_s}{k_\ell} \quad (5.14)$$

It should be noted that the superscript o is used for variables that have units, while unscripted is used for dimensionless terms. The governing equation is nondimensionalized as

$$\frac{\partial(CT)}{\partial\tau} + \frac{\partial}{\partial X}(UCT) + \frac{\partial}{\partial Y}(VCT) + \frac{\partial}{\partial Z}(WCT) = \frac{\partial}{\partial X}\left(K \frac{\partial T}{\partial X}\right) + \frac{\partial}{\partial Y}\left(K \frac{\partial T}{\partial Y}\right) + \frac{\partial}{\partial Z}\left(K \frac{\partial T}{\partial Z}\right) + B^* \quad (5.15)$$

$$\text{with } B^* = - \left[\frac{\partial S}{\partial \tau} + \frac{\partial}{\partial X}(US) + \frac{\partial}{\partial Y}(VS) + \frac{\partial}{\partial Z}(WS) \right]$$

$$C(T) = \begin{cases} C_{s\ell} & (T < -\delta T^*) \\ \frac{1}{2}(1 + C_{s\ell}) + \frac{1}{2St\delta T^*} & (-\delta T^* \leq T \leq \delta T^*) \\ 1 & (T > \delta T^*) \end{cases} \quad (5.16)$$

$$S(T) = \begin{cases} C_{s\ell}\delta T^* & (T < -\delta T^*) \\ \frac{1}{2}\delta T^*(1 + C_{s\ell}) + \frac{1}{2St} & (-\delta T^* \leq T \leq \delta T^*) \\ C_{s\ell}\delta T^* + \frac{1}{St} & (T > \delta T^*) \end{cases} \quad (5.17)$$

$$K(T) = \begin{cases} K_{s\ell} & (T < -\delta T^*) \\ K_{s\ell} + (1 - K_{s\ell})(T + \delta T^*)/2\delta T^* & (-\delta T^* \leq T \leq \delta T^*) \\ 1 & (T > \delta T^*) \end{cases} \quad (5.18)$$

The discretization of the above equation employs the control-volume finite-difference approach described by Patankar (1980). In this methodology, the discretization equations are obtained by applying the

conservation laws over finite size control volumes surrounding the grid nodes and integrating the equation over the control volume, which is shown in Fig. 5.3. For the grid point P, points E and W (i.e., east and west) are its X-direction neighbors, while points N and S (i.e., north and south) are the Y-direction neighbors. The Z-direction is perpendicular to the paper. Using a fully implicit scheme, adopting upwind differencing in space and adding two more neighbors T and B (i.e., top and bottom) for the Z-direction, we can write a discretization equation based on eqn. (5.15) for multi-dimensional problems

$$a_P T_P = a_E T_E + a_W T_W + a_N T_N + a_S T_S + a_T T_T + a_B T_B + b \quad (5.19)$$

where

$$a_P = C_P \Delta X \Delta Y \Delta Z / \Delta \tau + C_P (F_e + F_w + F_n + F_s + F_t + F_b) + D_e + D_w + D_n + D_s + D_t + D_b$$

$$a_E = D_e + C_E F_e$$

$$a_W = D_w + C_W F_w$$

$$a_N = D_n + C_N F_n$$

$$a_S = D_s + C_S F_s$$

$$a_T = D_t + C_T F_t$$

$$a_B = D_b + C_B F_b$$

$$b = C'_P T'_P \Delta X \Delta Y \Delta Z / \Delta \tau + (S'_P - S_P) \Delta X \Delta Y \Delta Z / \Delta \tau - S_P (F_e + F_w + F_n + F_s + F_t + F_b) + S_E F_e + S_W F_w + S_N F_n + S_S F_s + S_T F_t + S_B F_b$$

The flow rates and conductances are defined as

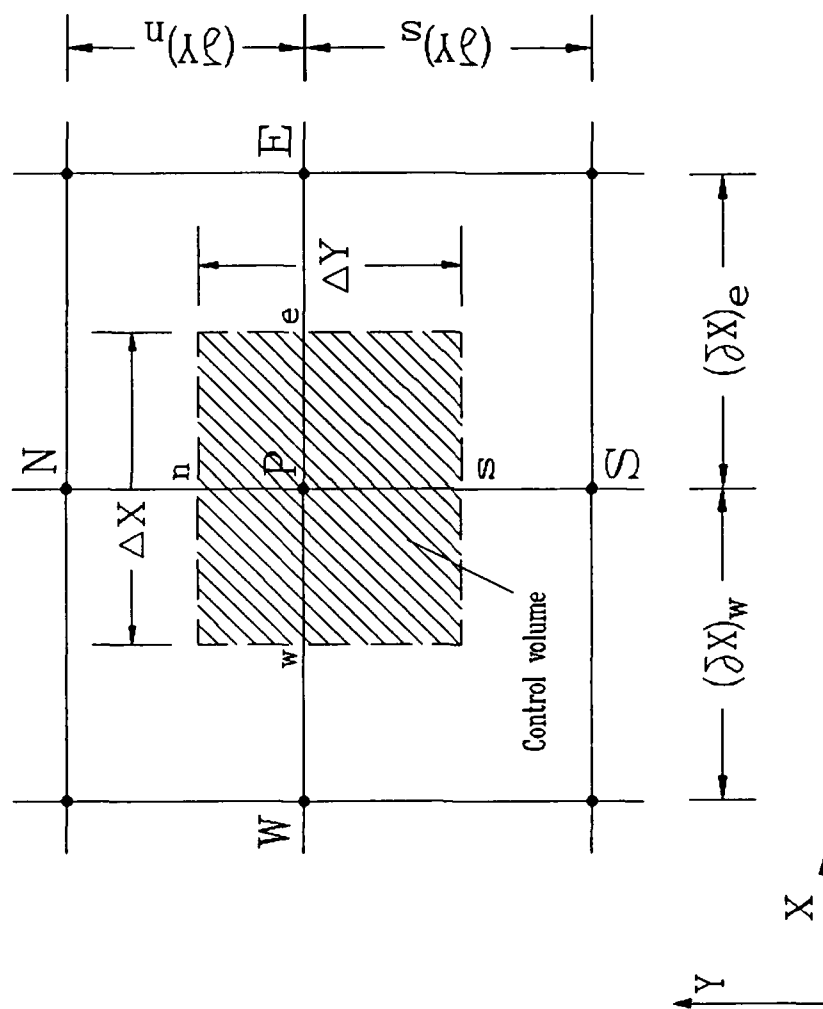


Fig. 5.3 Control Volume for the two-dimensional situation

$$F_e = \max [-U_e \Delta Y \Delta Z, 0], \quad D_e = \frac{K_e \Delta Y \Delta Z}{(\delta X)_e}$$

$$F_w = \max [U_w \Delta Y \Delta Z, 0], \quad D_w = \frac{K_w \Delta Y \Delta Z}{(\delta X)_w}$$

$$F_n = \max [-V_n \Delta Z \Delta X, 0], \quad D_n = \frac{K_n \Delta Z \Delta X}{(\delta Y)_n}$$

$$F_s = \max [V_s \Delta Z \Delta X, 0], \quad D_s = \frac{K_s \Delta Z \Delta X}{(\delta Y)_s}$$

$$F_t = \max [-W_t \Delta X \Delta Y, 0], \quad D_t = \frac{K_t \Delta X \Delta Y}{(\delta Z)_t}$$

$$F_b = \max [W_b \Delta X \Delta Y, 0], \quad D_b = \frac{K_b \Delta X \Delta Y}{(\delta Z)_b}$$

The greater of a and b is given by $\max [a, b]$, and C'_p , T'_p , and S'_p denote the old values at grid P for the last time step. The subscripts E and e, for example, denote the values at grid E and control-volume face e, respectively, for C, S, F, D, K, and the velocities.

Since eqn. (5.15) is nonlinear, iterations are needed at each time step. This procedure is as follows:

- 1) Let T^k represent the T field as it exists at the beginning of the kth iteration.

- 2) From these values, calculate tentative values of C, S and K according to their relations with T, using eqns. (5.16), (5.17) and (5.18), respectively.
- 3) Solve the nominally linear set of discretization equations to get new values of T^{k+1} .
- 4) Return to step 1 and repeat the process until further iterations cease to produce any significant change in the values of T.

For the thermal conductivity, K, it is important to use the harmonic mean described by Patankar (1980) at the faces of the control volume.

5.5 NUMERICAL RESULTS AND DISCUSSION

5.5.1 Phase change without convection

In this case, the numerical scheme in the last section is still applicable with $U = V = W = 0$. To check the validity of the present model, the one-dimensional and two-dimensional numerical results are compared to the analytical and numerical results existing in the literature.

Consider first a one-dimensional melting problem in a half-space (one-region problem). A solid at the solidification (or melting) temperature T_m^0 is confined to a half-space $x > 0$. At time $t = 0$, the temperature of the boundary surface at $x = 0$ is raised to T_h^0 , which is higher than T_m^0 and maintained at that temperature for $t > 0$. The exact solution given by Ozisik (1980) is

$$T_\ell^0(x, t) - T_h^0 = (T_m^0 - T_h^0) \operatorname{erf} [x/2(a_\ell t)^{1/2}] / \operatorname{erf}(\lambda) \quad (5.20)$$

for the liquid temperature distribution, and

$$x(t) = 2\lambda (a_\ell t)^{1/2} \quad (5.21)$$

for the solid-liquid interface position. The parameter λ is determined by the relation

$$\lambda^2 e^{\lambda^2} \operatorname{erf}(\lambda) = \frac{c (T_h^0 - T_m^0)}{L \sqrt{\pi}} \quad (5.22)$$

Figure 5.4 shows the comparison between the exact solution and the present numerical solution with a grid size $\Delta X = 0.05$ for the location of the melting front as a function of the square root of the dimensionless time τ . In order to simulate the sharp melting front, a small temperature range $\delta T^* = 0.001$ is used in the calculation and the initial temperature is set to $T = -0.001$ instead of $T = 0$. As can be seen from Fig. 5.4, the present solution is in agreement with the exact solution. The error of the numerical solution is mainly due to the boundary condition of the first kind which gives a sudden temperature rise at $\tau = 0$ and results in a nonzero melting distance at the onset of phase change. Also, with a finer grid size, the accuracy will be further increased.

The accuracy of the present model will now be tested with a two-dimensional freezing problem. Consider a liquid initially at temperature T_i^0 in a bar with a uniform square cross section and adiabatic ends as shown in Fig. 5.5a. The surface is suddenly exposed to a uniform wall temperature below the fusion temperature and freezing takes place

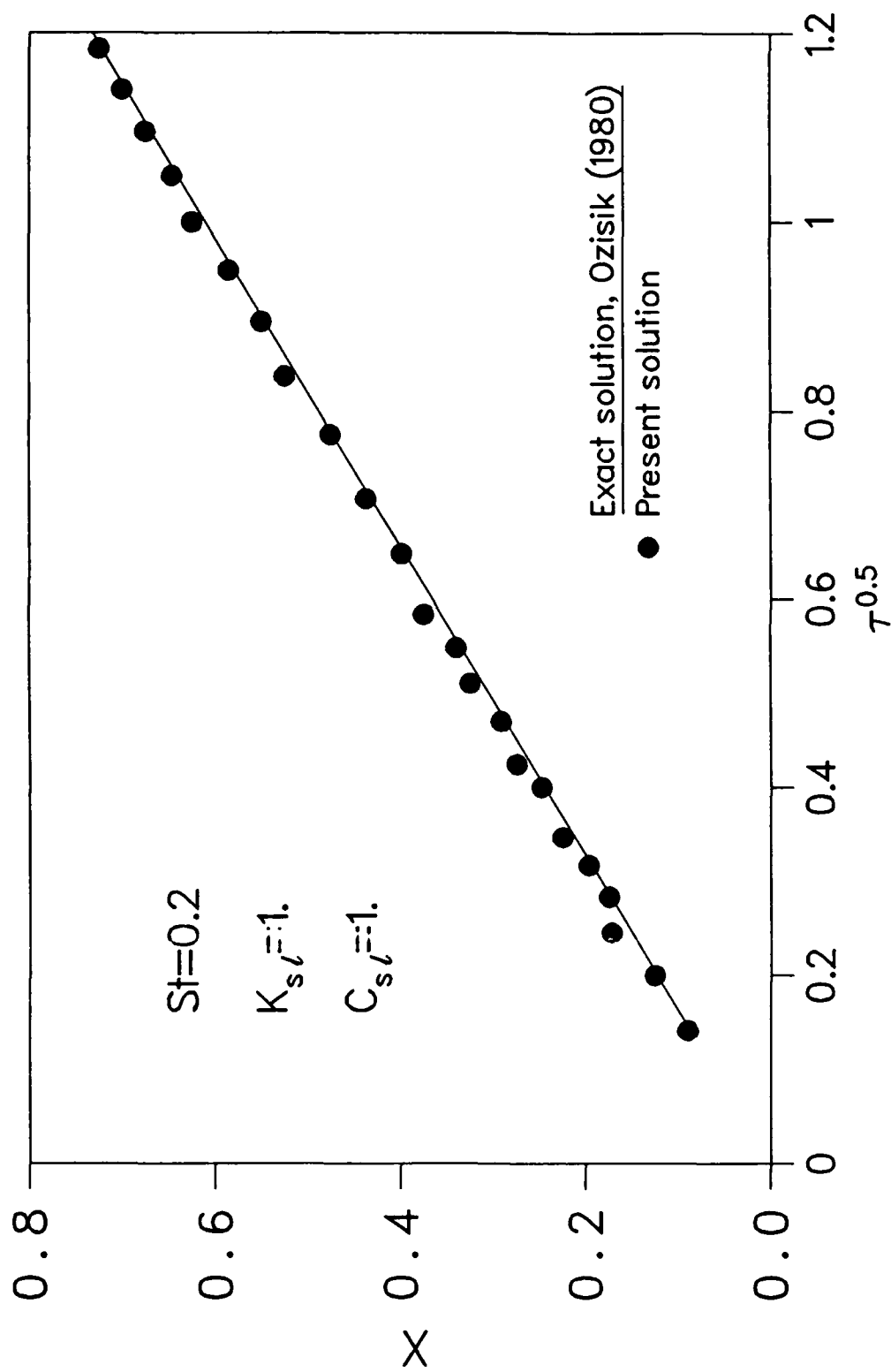
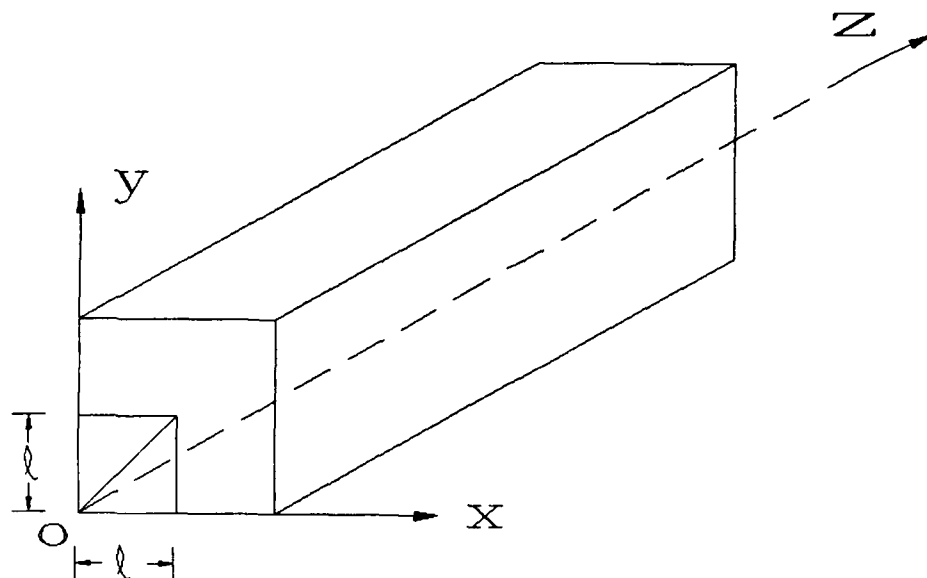
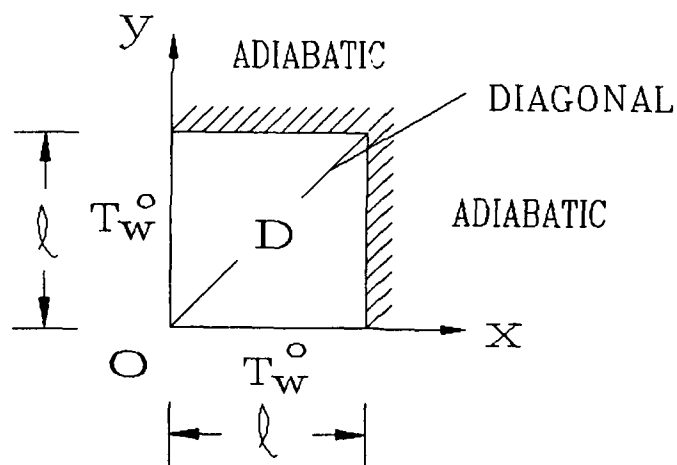


Fig. 5.4 The exact and numerical solutions of the melting front in a half-space



(a) Bar of liquid with an uniform square cross section



(b) One-quarter of the bar used for the computational domain due to the symmetry of the problem.

Figure 5.5 Description of the geometry and boundary conditions for the two-dimensional freezing problem

immediately. Because of the symmetry of the geometry, only a quarter of the bar is considered, as shown in Fig. 5.5b. The dimensionless parameters are $k_\ell/k_s = 0.9$, $a_\ell/a_s = 0.9$, $\theta_0 = (T_i^0 - T_w^0)/(T_m^0 - T_w^0) = 9/7$ and $St = c_\ell (T_m^0 - T_w^0)/L = 2$. Figure 5.6 shows the interface position as a function of dimensionless time along the diagonal with a grid size of 20×20 and a time step $\Delta\tau = 0.01$. It took about 40 seconds to run the case on a VAX 8550. Also included in Fig. 5.6 are solutions obtained by Hsiao and Chung (1984), Keung (1980), and Cao et al. (1989) using the enthalpy-transforming model. It can be seen that the present two-dimensional solution agrees well with the results of those studies.

Calculations were also made with different phase-change temperature ranges and physical property ratios between the solid and liquid phases. Figure 5.7 shows temperature distributions along the adiabatic line of the cross section in Fig. 5.5b for different values of δT^* . The initial dimensionless temperature of the liquid was set to $T_i = 0.5$ and the dimensionless surface temperature was set to $T_w = -0.5$. It can be seen that the present scheme is insensitive to the phase-change temperature range. The temperature distributions in the solid region and phase-change interfaces ($T = 0$) are almost identical with slight differences of the temperature distribution in the liquid region. It can also be seen that the curve with $\delta T^* = 0.01$ is almost the same as that with $\delta T^* = 0.001$. This means that a moderately small phase-change temperature range is enough to simulate the phase-change problem occurring at a single temperature.

Time step and grid size limits were not encountered in the above calculations. The dimensionless time step $\Delta\tau$ can be on the order of 0.1 -

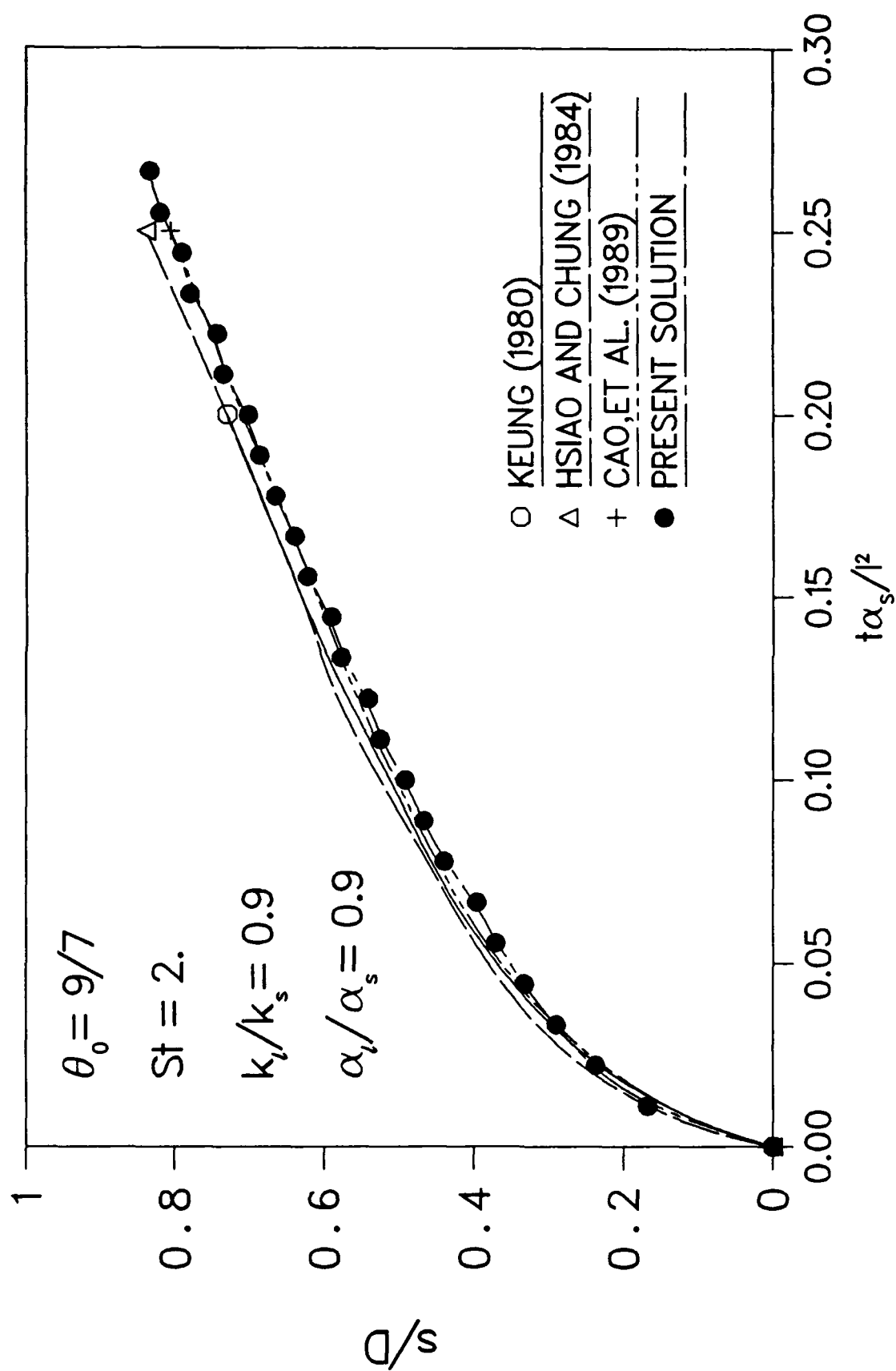


Figure 5.6 Interface position along the diagonal with prescribed boundary temperature

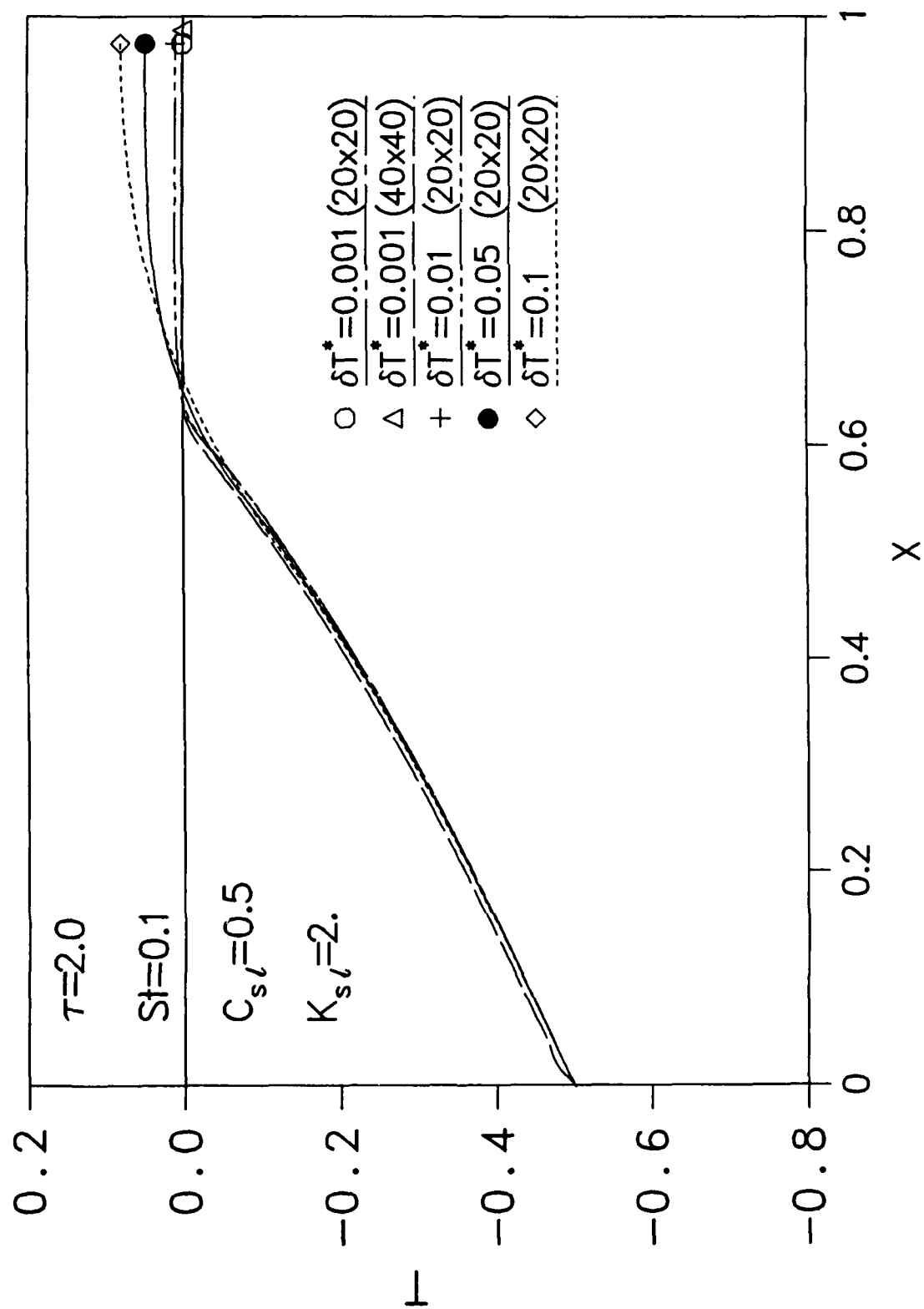


Figure 5.7 Temperature profiles along an adiabatic line for different values of δT^* and grid sizes

1.0 and the real time step Δt can be as large as several days. The model is also independent of grid sizes. The curve with a grid size of 40×40 is almost identical to that of 20×20 with the same δT^* . The CPU time for running the case with $\delta T^* = 0.1$ in Fig. 5.7 up to $\tau = 2.0$ was less than 17 seconds on the VAX 8550 with a time step of $\Delta \tau = 0.2$ and a grid size of 20×20 . The CPU time for running the case with $\delta T^* = 0.001$ in Fig. 5.7 up to $\tau = 2.0$ was about 5 minutes with a time step of $\Delta \tau = 0.2$ and a grid size of 40×40 on the same computer. The scheme can deal with phase-change problems with large specific heat and thermal conductivity differences between the solid and the liquid phases, which is often the case in many applications.

It should be pointed out that due to the severe nonlinearity of phase-changes problems, underrelaxation is needed during the iterations for C , S and K in eqn. (5.15) when δT^* is very small. The normal underrelaxation parameters are 0.1 - 0.5 for small values of δT^* . For a moderate value of δT^* , underrelaxation is not needed.

5.5.2 Phase change with natural convection

To further demonstrate the present model, the phase change with natural convection in a two-dimensional cavity as shown in Fig. 5.8 was studied. The dimensionless governing equations with parameters introduced in eqn. (5.14) and the Boussinesq approximation are as follows

$$\frac{\partial U}{\partial X} + \frac{\partial V}{\partial Y} = 0 \quad (5.23)$$

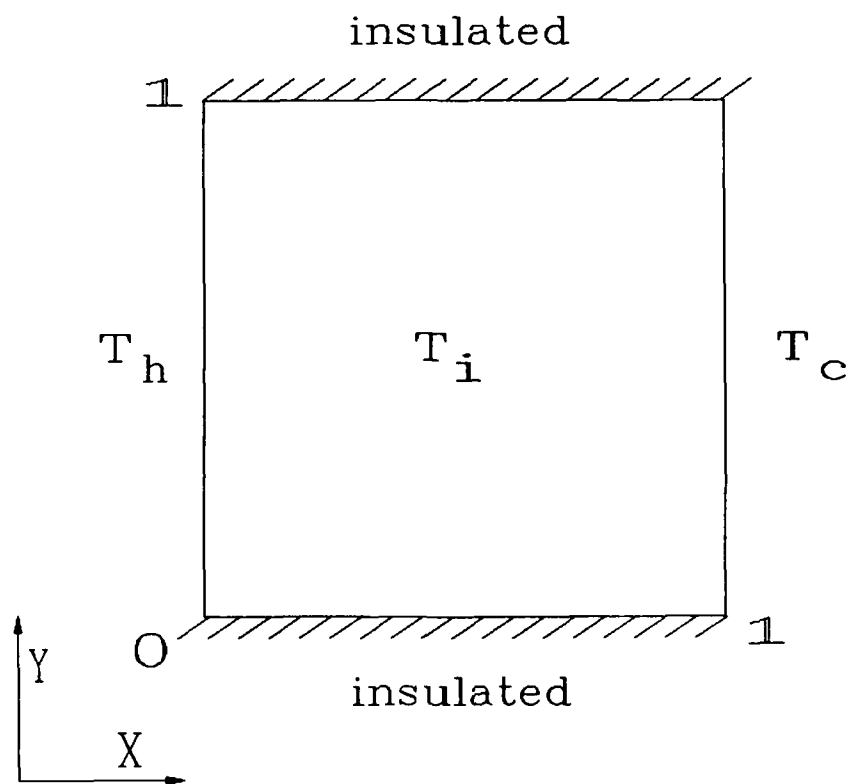


Figure 5.8 The thermal cavity configuration

$$\frac{\partial U}{\partial \tau} + \frac{\partial(U^2)}{\partial X} + \frac{\partial(UY)}{\partial Y} = - \frac{\partial P}{\partial X} + \frac{\partial}{\partial X} \left(\text{Pr} \frac{\partial U}{\partial X} \right) + \frac{\partial}{\partial Y} \left(\text{Pr} \frac{\partial V}{\partial Y} \right) \quad (5.24)$$

$$\frac{\partial V}{\partial \tau} + \frac{\partial(UV)}{\partial X} + \frac{\partial(V^2)}{\partial Y} = - \frac{\partial P}{\partial Y} + \text{Ra} \text{Pr}_\ell T + \frac{\partial}{\partial X} \left(\text{Pr} \frac{\partial V}{\partial X} \right) + \frac{\partial}{\partial Y} \left(\text{Pr} \frac{\partial V}{\partial Y} \right) \quad (5.25)$$

$$\begin{aligned} \frac{\partial(CT)}{\partial \tau} + \frac{\partial}{\partial X} (UCT) + \frac{\partial}{\partial Y} (VCT) &= \frac{\partial}{\partial X} \left(K \frac{\partial T}{\partial X} \right) + \frac{\partial}{\partial Y} \left(K \frac{\partial T}{\partial Y} \right) \\ &- \left[\frac{\partial S}{\partial \tau} + \frac{\partial}{\partial X} (US) + \frac{\partial}{\partial Y} (VS) \right] \end{aligned} \quad (5.26)$$

where $\text{Ra} = g\beta H^3 (T_h^0 - T_c^0)/\nu_\ell \alpha_\ell$, $\text{Pr}_\ell = \nu_\ell/\alpha_\ell$, $\text{Pr} = \nu/\alpha_\ell$, and C , S , and K are given by eqns. (5.16), (5.17) and (5.18), respectively. Equations (5.23 - 5.26) were solved numerically using the iterative SIMPLER algorithm (Patankar, 1980) with the numerical scheme in the previous section of this paper used for the energy equation. The SIMPLER algorithm is based on a fully-implicit discretization scheme for the unsteady terms. The discretized form of the momentum equation is very similar to eqn. (5.19). An important difference is that the grids used are "staggered" over the temperature grid. A consequence of the staggered grid approach is that care has to be taken in numerically implementing momentum sources and physical properties which depend on temperature.

At the solid-liquid interface or in the mushy region, the velocities U and V go to zero. If the momentum equations above are to be applicable in phase-change problems, this behavior must be taken into account. There are a number of alternative methods by which the behavior of the velocities in the mushy region can be modeled (Voller et al., 1987). A commonly used procedure is to prescribe a fluid viscosity which is equal to the liquid

viscosity in the liquid region and which increases gradually over the mushy zone to a large value in the solid. This representation can be used quite conveniently and was adopted in the present study because finite-difference procedures can properly handle large discontinuities in the diffusion coefficients. Therefore, the viscosity is expressed as

$$\nu = \begin{cases} \nu_\ell & (T > \delta T^*) \\ \nu_\ell + (T - \delta T^*) (\nu_\ell - N)/2\delta T^* & (-\delta T^* \leq T \leq \delta T^*) \\ N & (T < -\delta T^*) \end{cases} \quad (5.27)$$

where N takes a sufficiently large value such as 10^{10} . Notice that the term $Ra Pr_\ell T$ in eqn. (5.25) is independent of ν . Prior to the calculation of the phase-change problems, the computer program written with the SIMPLER algorithm was tested with pure natural convection in the cavity, and the results with a grid size of 25×25 were compared with those given by Raithby and Hollands (1985) with an agreement of 5 percent within the whole given Raleigh number range ($10^3 - 10^5$).

Calculations were conducted with a one-region melting problem occurring at a single temperature (Okada, 1984). The initial and boundary conditions for this problem are $T_i = 0$, $T_h = 1$, $T_c = 0$. In order to simulate the phase change having a sharp interface with the present model, δT^* was taken as 0.01 and T_i and T_c were set to -0.01 in the calculations. Figure 5.9 shows the calculated results with a 20×20 grid size compared with the experimental results given by Okada (1984). Also included in the figure are the numerical results with the coordinate transforming method and the quasi-steady assumption. It can be seen that the present results

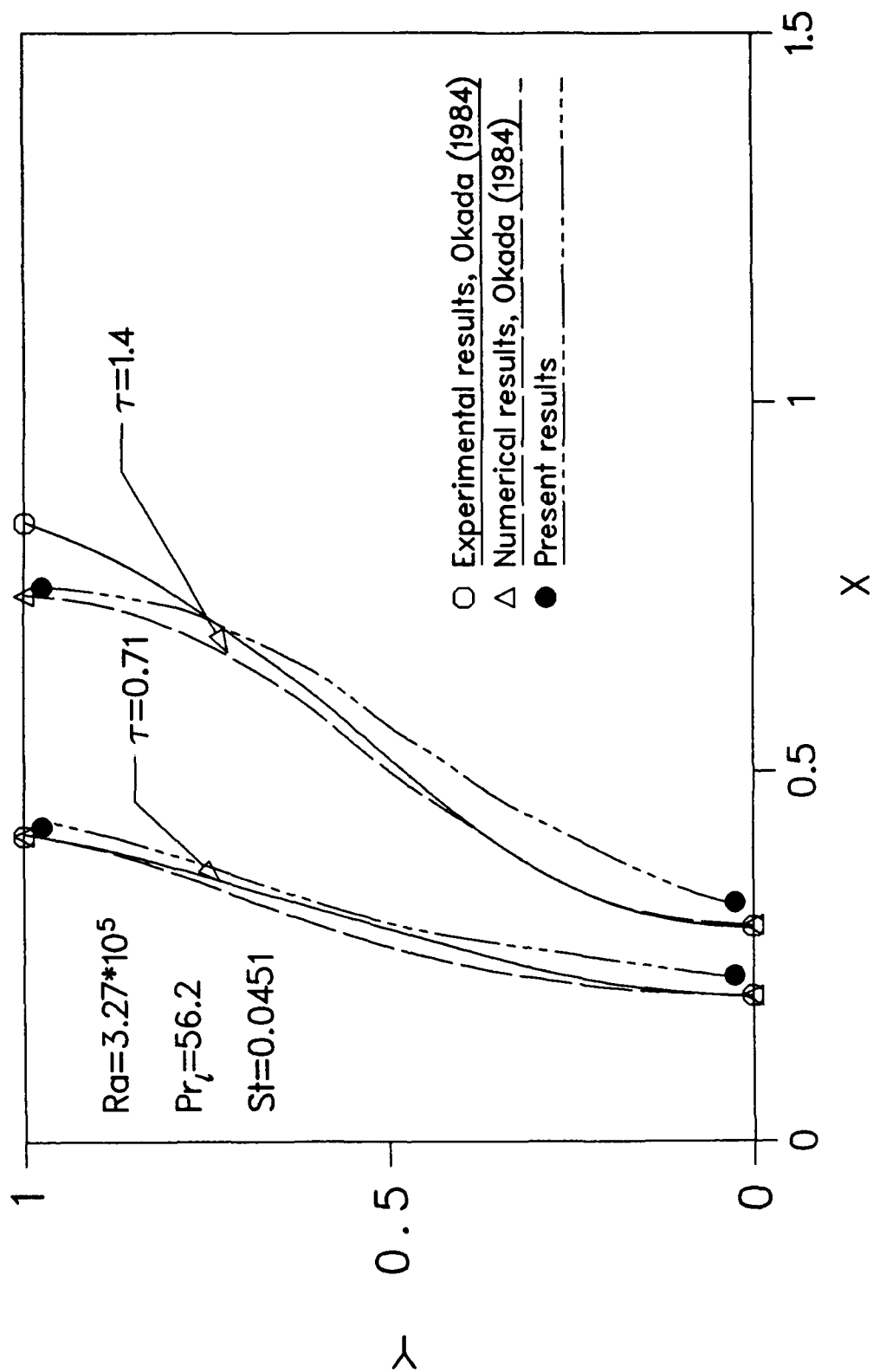


Figure 5.9 Comparison of the locations of the melting front

are in agreement with the past experimental and numerical results. The CPU time for running the case is about 3 hours on the VAX 8550, which is much higher than those of pure diffusive phase change problems.

The one-region restriction is relaxed and c and k were permitted to take different values between the liquid and solid phases. The calculation was conducted again with $T_i = 0.5$, $T_h = 0.5$, $T_c = -0.5$, $Ra = 10^4$, $Pr_\ell = 30$, $St = 0.5$, $C_{s\ell} = 0.5$, $K_{s\ell} = 1.5$, $\delta T^* = 0.01$, and a grid size of 30×30 . The numerical results for this two-region freezing problem at $\tau = 2.0$ are presented in Fig. 5.10 and Fig. 5.11 by a dimensionless temperature contour and a stream function contour, respectively.

The advantage of the present scheme is that the calculations can be made in a fixed grid system without involving complicated coordinate transforming procedures and many assumptions. The present scheme can also be applied to three-dimensional problems.

5.6 CONCLUSIONS

The temperature transforming model and the numerical scheme proposed in this paper proves to be flexible, easy to implement, and able to handle various complicated phase-change problems including those with large specific heat and thermal conductivity differences between the solid and liquid phases. For diffusion-controlled phase-change problems, the model eliminates the time step and grid size limitations which the equivalent heat capacity model usually encounters and is insensitive to phase-change temperature ranges. The model can also properly deal with convective-diffusive phase-change problems in a fixed grid system. The

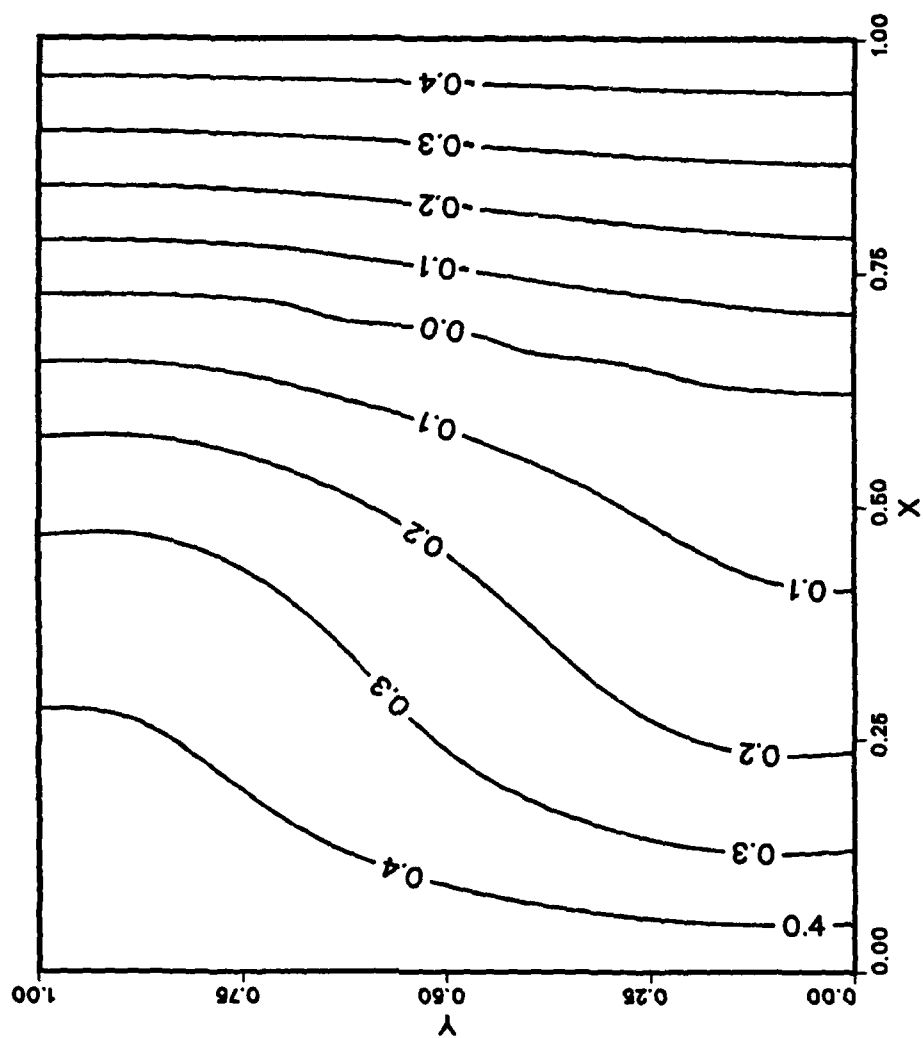


Figure 5.10 Calculated temperature contours

present solutions have been compared with previous analytical and numerical results as well as the experimental data with a good agreement. The advantage of this model is that explicit attention does not have to be given to the nature of the phase-change front and the model can be applied to three-dimensional problems without involving cumbersome mathematical schemes.

Section VI

A TRANSIENT TWO-DIMENSIONAL COMPRESSIBLE ANALYSIS FOR HIGH TEMPERATURE HEAT PIPES WITH A PULSED HEAT INPUT

6.1 SUMMARY

The transient behavior of two-dimensional heat pipes is studied numerically. The energy balance relation for the liquid-vapor interface is derived and a simplification concerning the porous wick is justified by a simple analysis. The numerical results for compressible vapor flow with high Mach numbers are compared with the experimental data in the literature. The transient responses of heat pipes to a pulsed heat input are then elaborated. The numerical results show that for transient heat pipe analysis, it is very important to include the porous wick and the wall in the numerical calculations, and to treat the entire heat pipe as a single system rather than analyze the vapor flow alone.

6.2 INTRODUCTION

The study of heat pipe dynamics is important for start-up, shut-down and operational transients such as pulsed heat loads. Most of the previous works on the transient behavior of heat pipes treat the vapor flow with one-dimensional models which incorporate friction coefficients found from two-dimensional numerical results or experiments (Ivanovskii et al., 1982; Jang et al., 1989). Heat pipes are, in general, intended for isothermal operation at a higher vapor temperature, but for the transient operation, the two-dimensional character of heat pipes is evident. Also, the friction coefficient correlations used in the one-dimensional vapor models are based on limited experimental or numerical data and their validity is not fully confirmed. Therefore, the use of empirical correlations will surely increase the uncertainty of the models.

Bowman and Hitchcock (1988) and Bowman (1987) studied the transient two-dimensional compressible flow of air in a simulated heat pipe. The experimental data for the simulated steady state heat pipe vapor flow were obtained and compared with the numerical results with a fairly good agreement. Both the experimental data and the numerical scheme are valuable to understand the flow vapor structure and pressure drops at high Mach numbers. However, the vapor flow was not actual vapor flow in a heat pipe but air flow in a porous pipe. Both the heat pipe wick and wall were also not considered in the transient numerical simulation. Because the time period of the vapor transient is very short when compared to that of the heat pipe wick and wall, the numerical results can hardly simulate the actual transient processes in a heat pipe.

Issacci et al. (1988) studied the transient behavior of the vapor flow in a rectangular heat pipe with the SIMPLE numerical scheme developed by

Patankar (1980). Flow reversal was detected in the condenser and adiabatic regions with water as the working fluid. However, only some axial and radial velocity profiles were presented in the paper, and no information concerning vapor compressibility and the transient behavior of a heat pipe was given. Also, the heat pipe wall and wick were not included in the numerical analysis.

In this paper, a liquid-vapor interface relation will be derived, and the transient and steady two-dimensional compressible vapor flow including the effects of the wick and wall will be studied numerically.

6.3 MATHEMATICAL FORMULATION AND MODELING

The heat pipe configuration and coordinate system studied in this paper is presented in Fig. 6.1. The wick is saturated with the liquid phase of the working fluid and the remaining volume of the tube contains the vapor phase. Heat applied at the evaporator causes the liquid to vaporize into the vapor space. The vapor flows to the condenser and releases the latent heat as it condenses. The released heat is rejected into the environment by convection or radiation from the outer condenser surface.

6.3.1 Governing equations

The governing equations for transient compressible laminar vapor flow with constant viscosity are as follows (Ganic et al., 1985):

$$\frac{\partial \rho}{\partial t} + \frac{1}{r} \frac{\partial}{\partial r} (\rho r v) + \frac{\partial}{\partial z} (\rho w) = 0 \quad (6.1)$$

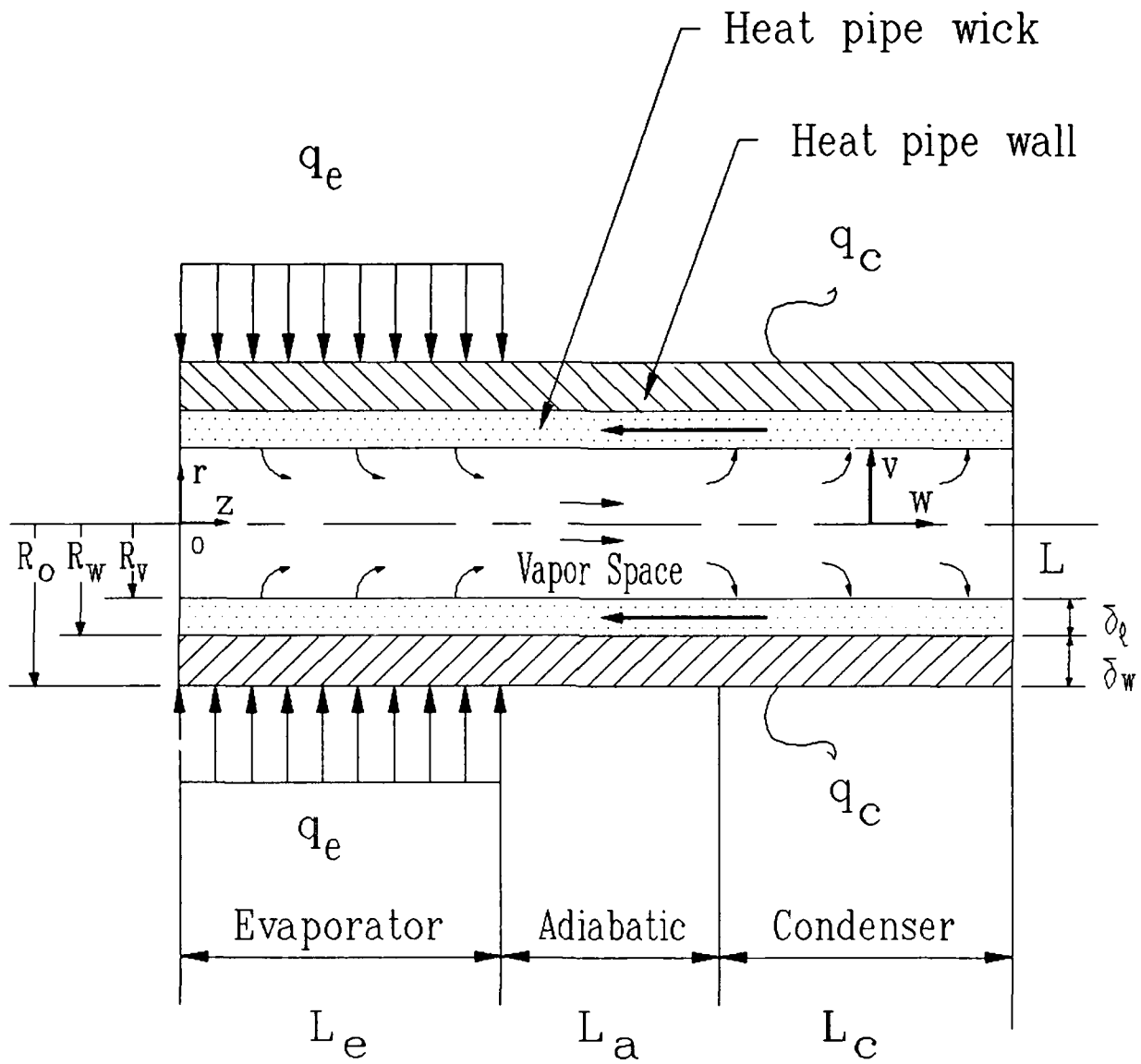


Figure 6.1 The heat pipe configuration and coordinate system

$$\begin{aligned} \frac{\partial(\rho v)}{\partial t} + \frac{1}{r} \frac{\partial}{\partial r} (\rho r v^2) + \frac{\partial}{\partial z} (\rho v w) = -\frac{\partial p}{\partial r} + \frac{4}{3} \mu \frac{1}{r} \frac{\partial}{\partial r} (r \frac{\partial v}{\partial r}) \\ + \mu \frac{\partial^2 v}{\partial z^2} + \mu (\frac{1}{3} \frac{\partial^2 w}{\partial z \partial r} - \frac{4}{3} \frac{v}{r^2}) \end{aligned} \quad (6.2)$$

$$\begin{aligned} \frac{\partial(\rho w)}{\partial t} + \frac{1}{r} \frac{\partial}{\partial r} (\rho r v w) + \frac{\partial}{\partial z} (\rho w^2) = -\frac{\partial p}{\partial z} + \frac{\mu}{r} \frac{\partial}{\partial r} (r \frac{\partial w}{\partial r}) + \frac{4}{3} \mu \frac{\partial^2 w}{\partial z^2} \\ + \frac{1}{3} \mu (\frac{1}{r} \frac{\partial v}{\partial z} + \frac{\partial^2 v}{\partial z \partial r}) \end{aligned} \quad (6.3)$$

$$\rho c_p (\frac{\partial T}{\partial t} + v \frac{\partial T}{\partial r} + w \frac{\partial T}{\partial z}) = k [\frac{1}{r} \frac{\partial}{\partial r} (r \frac{\partial T}{\partial r}) + \frac{\partial^2 T}{\partial z^2}] + \frac{Dp}{Dt} + \mu \Phi \quad (6.4)$$

where

$$\Phi = 2 [(\frac{\partial v}{\partial r})^2 + (\frac{v}{r})^2 + (\frac{\partial w}{\partial z})^2] + (\frac{\partial v}{\partial z} + \frac{\partial w}{\partial r})^2 - \frac{2}{3} [\frac{1}{r} \frac{\partial}{\partial r} (r v) + \frac{\partial w}{\partial z}]^2$$

$$\frac{Dp}{Dt} = \frac{\partial p}{\partial t} + v \frac{\partial p}{\partial r} + w \frac{\partial p}{\partial z}$$

The equation of state is given by

$$p = \rho R T \quad (6.5)$$

More effort is needed to describe the boundary conditions for the vapor flow. In fact, the most challenging problems arise from the treatment of the liquid-vapor interface and the liquid flow in the porous wick. The governing equations for the heat conduction in the wick and the pipe wall are also presented in the following section.

6.3.2 Analysis of the vapor-liquid interface

Figure 6.2 shows a control volume surrounding the vapor-liquid

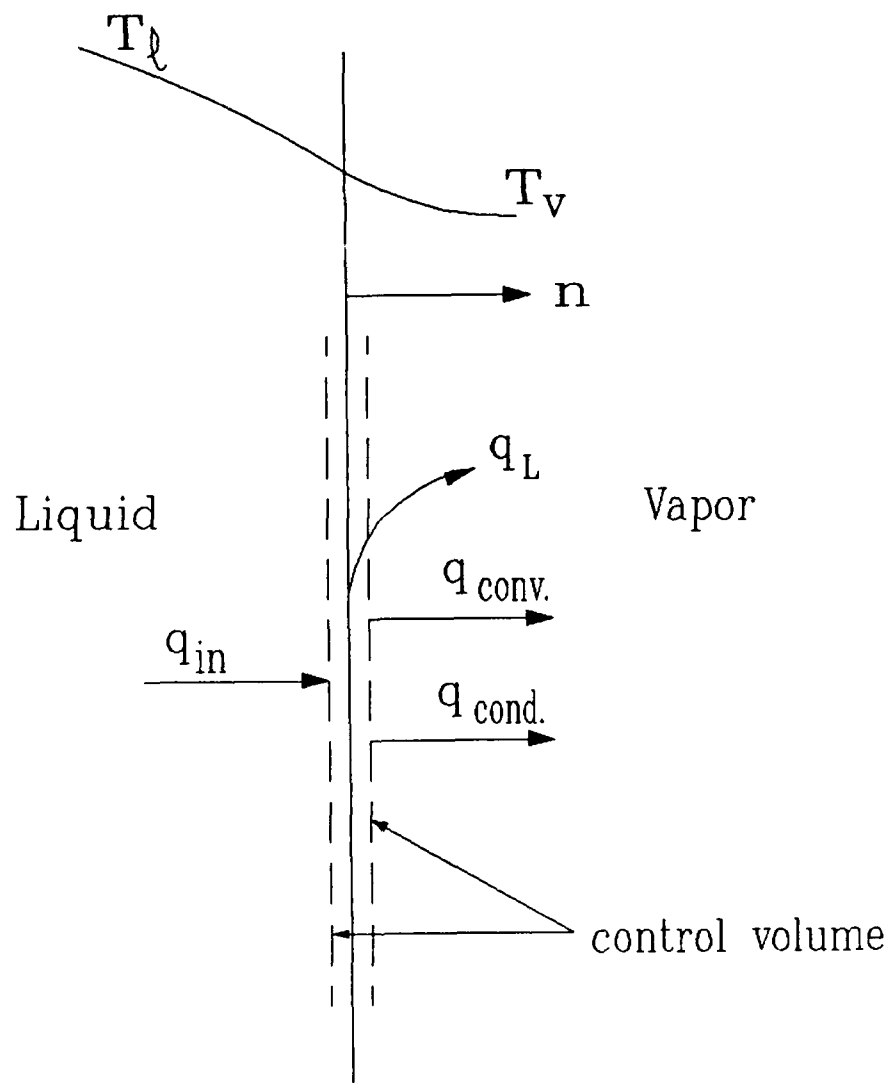


Figure 6.2 Vapor-liquid interface control volume

interface. The thickness of the control volume should be considered to be infinitesimal. In the figure, q_{in} is the heat flux from the liquid side. The convective heat flux due to the vapor velocity at the interface is

$$q_{conv} = \dot{m}_i c_{pv} T_s = \rho_i v_i c_{pv} T_s$$

The heat flux due to heat conduction into the vapor is

$$q_{cond} = -k_v \frac{\partial T_v}{\partial n}$$

where n is the normal direction of the interface. The latent heat due to phase change from the liquid phase to the vapor phase or vice versa is

$$q_L = \dot{m}_i h_{fg} = \rho_i v_i h_{fg}$$

where T_s is the saturation temperature at the interface, v_i is the radial vapor velocity at the interface, ρ_i is the interfacial vapor density, and \dot{m}_i is the corresponding mass flux.

$$v_i = \dot{m}_i / \rho_i \begin{cases} v_i > 0 & (\text{condensation}) \\ v_i < 0 & (\text{evaporation}) \\ 0 & (\text{adiabatic}) \end{cases}$$

Making an energy balance at the interface, we get

$$q_{in} = q_{conv} + q_{cond} + q_L$$

$$\text{or} \quad v_i = (q_{in} + k_v \frac{\partial T_v}{\partial n}) / (h_{fg} + c_{pv} T_s) \rho_i \quad (6.6)$$

We have neglected the kinetic energy $v_i^2/2$ in the above energy balance because the velocity at the interface is comparatively small.

The problem remains how to express q_{in} , which is composed of two parts:

$$q_{in} = q_{cond,\ell} + q_{conv,\ell} = -k_{eff} \frac{\partial T_\ell}{\partial n} + \rho_\ell v_\ell c_{pl} T_s$$

The first term on the right-hand side in the above equation is the heat conduction from the liquid side into the interface control volume, the second term is the convective heat flux due to the liquid velocity v_ℓ , where k_{eff} is the effective conductivity in the porous liquid-wick, which can be calculated with appropriate relations given by Dunn and Reay (1982).

According to the conservation of mass, we have

$$\rho_\ell v_\ell = \rho_i v_i, \quad v_\ell = \frac{\rho_i}{\rho_\ell} v_i$$

Since $\rho_i \ll \rho_\ell$, it follows that $v_\ell \ll v_i$

It should be pointed out that because v_ℓ is very small, its influence on the vapor velocities at the interface boundary is negligible. However, the term $\rho_\ell v_\ell$ may not be small because ρ_ℓ is large.

Let us now evaluate the effect of the liquid mass flow on the temperature distribution in the liquid wick. Since the porous wick is very thin (on the order of 1 mm) and the thermal conductivity of liquid metals is high, the temperature distribution in the wick could be assumed linear as shown in Fig. 6.3, where T_{iw} is the temperature at the wick-wall interface, δ_ℓ is the thickness of the wick, and T_s is the saturation

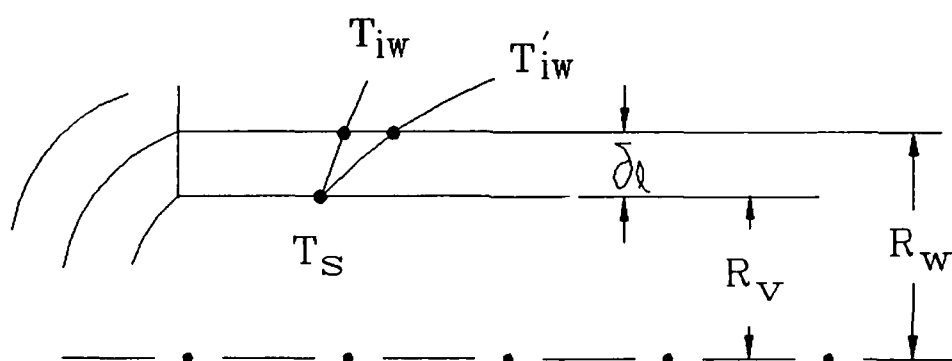


Figure 6.3 Temperature distribution in the wick

temperature at the vapor-liquid interface.

For steady state operation, we have

$$q_{\text{cond},\ell} = q_{\text{in}} - \rho_{\ell} v_{\ell} T_s c_{p\ell} = k_{\text{eff}} \frac{T_{\text{iw}} - T_s}{\delta_{\ell}}$$

$$T_{\text{iw}} = \frac{q_{\text{in}} - \rho_{\ell} v_{\ell} c_{p\ell} T_s}{k_{\text{eff}}} \delta_{\ell} + T_s$$

Now, suppose q_{in} is only attributed to heat conduction in the wick, i.e.,

$$q_{\text{in}} = -k_{\text{eff}} \frac{\partial T_{\ell}}{\partial n}$$

Then, the temperature distribution in the wick must be somewhat different. Let T'_{iw} be the wick-wall interface temperature in this situation:

$$T'_{\text{iw}} = \frac{q_{\text{in}}}{k_{\text{eff}}} \delta_{\ell} + T_s$$

Therefore, the maximum temperature difference is

$$T'_{\text{iw}} - T_{\text{iw}} = \frac{\rho_{\ell} v_{\ell} c_{p\ell} T_s}{k_{\text{eff}}} \delta_{\ell}$$

For a typical heat pipe, $\delta_{\ell} = 0.5 \text{ mm}$, $v_i = 5 \text{ m/s}$, $T_s = 818 \text{ K}$, $c_{p\ell} = 1262 \text{ J/(kg}\cdot\text{K)}$, $\rho_i = 0.461 \times 10^{-2} \text{ kg/m}^3$, $k_{\text{eff}} = 35 \text{ W/(m}\cdot\text{K)}$.

$$T'_{iw} - T_{iw} = \frac{\rho_{\ell}^v c_{p\ell} T_s}{k_{eff}} \delta_{\ell} = \frac{\rho_i^v c_{pi} T_s}{k_{eff}} \delta_{\ell} = 0.34 \text{ K}$$

It can be seen that the maximum temperature difference between these two cases is negligible. This is why many studies found that the conduction model is appropriate to describe the heat transfer in the wick for liquid metal heat pipes (Chen and Faghri, 1989). It is also worth pointing out that the above conclusion is only applicable to the working fluids that have a high thermal conductivity. For working fluids with low thermal conductivities such as water, the conduction model may need some modifications.

Based on the above analysis, we will neglect the liquid velocity in the wick and apply the conduction model to the heat transfer in the wick. This does not mean that the liquid flow in the porous wick is not important. In fact, the liquid flow in the porous wick is very important to determine the capillary limit of heat pipes. Since the major concern in this paper is the heat pipe dynamics, the porous wick is assumed to be so designed that it has enough capillary force to drive condensate to the evaporator as long as the working fluid in the wick is melted. Therefore, for the porous wick and wall, the energy equation (6.4) is still applicable with $v = w = 0$, $\frac{DP}{Dt} = \Phi = 0$ and the corresponding properties c_p , ρ , k of the wick and wall, i.e.,

$$(\rho c_p)_{eff} \frac{\partial T}{\partial t} = k_{eff} \left[\frac{1}{r} \frac{\partial}{\partial r} \left(r \frac{\partial T}{\partial r} \right) + \frac{\partial^2 T}{\partial z^2} \right] \quad (\text{for the wick}) \quad (6.7)$$

$$\rho_w c_{pw} \frac{\partial T}{\partial t} = k_w \left[\frac{1}{r} \frac{\partial}{\partial r} \left(r \frac{\partial T}{\partial r} \right) + \frac{\partial^2 T}{\partial z^2} \right] \quad (\text{for the wall}) \quad (6.8)$$

where $(\rho c_p)_{\text{eff}} = \omega \rho_\ell c_{p\ell} + (1-\omega) (\rho c_p)_m$, ω is the porosity of the wick, and $(\rho c_p)_m$ is the heat capacity of the wick structure material.

6.3.3 Boundary conditions

At both ends of the heat pipe, the no-slip condition for velocity and the adiabatic condition for temperature are applied.

$z = 0$ and L :

$$v = w = 0$$

(6.9)

$$\frac{\partial T}{\partial z} = 0$$

At the centerline, the symmetry condition implies

$r = 0$:

$$\frac{\partial w}{\partial r} = 0, \quad v = 0$$

(6.10)

$$\frac{\partial T}{\partial r} = 0$$

For the boundary conditions at the vapor-liquid interface ($r = R_v$), the evaporator, adiabatic and condenser sections are described separately. For the evaporator and adiabatic sections, the temperature at the vapor-liquid interface is assumed to be the saturation temperature corresponding to the interface pressure:

$$T_s = 1 / \left(\frac{1}{T_o} - \frac{R}{h_{fg}} \ln \frac{p_s}{p_o} \right) \quad (6.11)$$

where p_o and T_o are the reference saturation temperature and pressure.

The interface velocities following the analysis are

$$r = R_v \text{ (evaporator and adiabatic sections)}$$

$$v_i = (-k_{eff} \frac{\partial T_\ell}{\partial r} + k_v \frac{\partial T_v}{\partial r}) / (h_{fg} + c_{pv} T_s) \rho_i \quad (6.12)$$

$$w = 0$$

It is worth noting that because of the axial conduction in the wall and wick, the evaporator and adiabatic sections are not necessarily the same as those prescribed at the outer wall surface. The actual location of the adiabatic section at the interface is where the values of v_i calculated with the equation above approaches zero.

For the condenser, the interface velocity is usually described as a mass suction velocity, but this is not exactly true. The interface velocity is not only determined by the exterior factors but also by the interior flow field of the vapor. Because of the closed fluid circulation system of the heat pipe, the mass condensed at the condenser interface must be equal to that evaporated at the evaporator interface for the steady state operation. This is somewhat similar to the outflow boundary condition of a normal duct flow. Therefore, the upwind scheme is used and the diffusion is neglected at the liquid-vapor interface of the condenser section. For the velocity component w , the no-slip boundary condition is

still applicable, $w = 0$, at $r = R_v$.

At the condenser interface, vapor condenses and releases its latent heat energy. The latent heat energy, as well as the convective heat energy, is absorbed at the interface. In order to simulate this process, a heat source

$$q_s = (h_{fg} + c_{pv} T_{iv}) \rho_i v_i \quad (6.13)$$

is applied at the interface grids, where T_{iv} is the vapor temperature at the grids next to the interface on the vapor side, and v_i can be obtained by a mass balance over the grid.

Since the vapor flow is solved by using the SIMPLE algorithm (this will be described in the next section), the normal velocities at the boundaries are given and the staggered grid arrangement is used, so no information concerning p at the boundaries will be needed (Patankar, 1980).

The boundary condition at the liquid-wall interface is

$$r = R_w, \quad k_w \frac{\partial T}{\partial r} = k_{eff} \frac{\partial T}{\partial r} \quad (6.14)$$

For the outer pipe wall surface:

$$\text{evaporator} \quad k_w \frac{\partial T}{\partial r} \Big|_{r = R_o} = q_e \quad (6.15)$$

$$\text{adiabatic} \quad \frac{\partial T}{\partial r} \Big|_{r = R_o} = 0 \quad (6.16)$$

$$\text{condenser} \quad -k_w \frac{\partial T}{\partial r} \bigg|_{r=R_o} = \begin{cases} h_c(T_w - T_a) & \text{(convection)} \quad (6.17a) \\ \sigma \epsilon T_w^4 & \text{(radiation)} \quad (6.17b) \end{cases}$$

where h_c is the convective heat transfer coefficient, and T_w and T_a are the outer wall surface temperature and the environment temperature, respectively, ϵ is the emissivity and σ is the Stefan-Boltzmann constant. It should be pointed out that for the heat pipe dynamics, T_w should not be fixed, it will be allowed to change during the transient process.

6.4 NUMERICAL PROCEDURE

The governing equations along with the boundary conditions were solved by employing the control-volume finite-difference approach described by Patankar (1980, 1988). The vapor flow inside the heat pipe was solved using the SIMPLE algorithm. There are two alternatives to deal with the compressibility of the vapor flow (Patankar, 1980; Karki, 1986). One method is to use the density-correction formulation, in which the vapor density is expressed as

$$\rho = \rho^* + \rho' = \rho^* + Kp' \quad (6.18)$$

where $K = \partial \rho / \partial p$, $\rho = p/RT$ and the subsequent coefficient of the pressure correction equation consists of two terms, i.e., a diffusive term and a convective term due to density correction. The second method is to choose the pressure as a dependent variable and directly apply the state equation $\rho = p/RT$ to obtain the vapor density while iterating. Based on our numerical results, it was found that the latter is more convenient and the speed of convergence is faster when the Mach number is high. With moderate

Mach numbers ($Ma < 1$), both methods give comparable results. Therefore, the second method was selected in our numerical calculations. The sequence of numerical steps is as follows:

1. Initialize the pressure, temperature and velocity fields. The density values are obtained from the current pressure and temperature fields through the state equation.
2. Solve the momentum equations to obtain v^* and w^* .
3. Solve the p' equation and update the current pressure field.
4. Calculate v , w from their starred values using the velocity-correction formulas.
5. Solve the temperature equation.
6. Steps (1) through (6) are repeated until convergence is reached.

The discretization equations for w , v , T and p' have the general form

$$a_P \phi_P = a_E \phi_E + a_W \phi_W + a_N \phi_N + a_S \phi_S + b \quad (6.19)$$

which is described by Patankar (1980).

Since the values of the density will normally be available only at the main grid points, the interface densities need to be calculated by a closure relation. In this case, an upwind-biased density is employed as suggested by Karki (1986). The density at interface e , for instance, is calculated using the following expression

$$\rho_e = \rho_P \max [w_e/|w_e|, 0] + \rho_E \max [-w_e/|w_e|, 0] \quad (6.20)$$

A combination of the direct method (TDMA) and the Gauss-Seidel method was employed to solve the discretization equations. The converged solution was assumed to be reached when the relative change of all variables was less than 10^{-3} .

6.5 NUMERICAL RESULTS AND DISCUSSION

6.5.1 Compressible vapor flow in a simulated heat pipe

Attention will first focus on the simulated heat pipe vapor flow, and the numerical results will be compared with the experimental data of Bowman (1987) to verify the mathematical model and algorithm. The experimental data was obtained by simulating the vapor flow of a cylindrical heat pipe with a porous pipe which has an inside diameter of 1.65 m and a length of 0.61 m. The evaporator and condenser sections have equal lengths and were simulated by the injection and suction of air without phase change at the interface. Since the experiment was focused on the vapor flow, the porous wick and heat pipe wall were not considered.

Figure 6.4 shows the numerical results of the steady axial pressure profiles along the centerline compared with the corresponding experimental data by Bowman (1987). It can be seen that the agreement between the experimental data and the numerical solutions is generally good. Figure 6.5 shows the corresponding axial Mach number variations along the centerline of the simulated heat pipe. For the two subsonic cases, the axial velocity increased until it decelerated in the condenser due to mass removal. For the supersonic case, mass removal caused a further acceleration of the air in the condenser until a shock was encountered. The pressure profiles are similar to those in a converging-diverging nozzle. Kemme (1969) and Bystrov and Popov (1978) reported observing

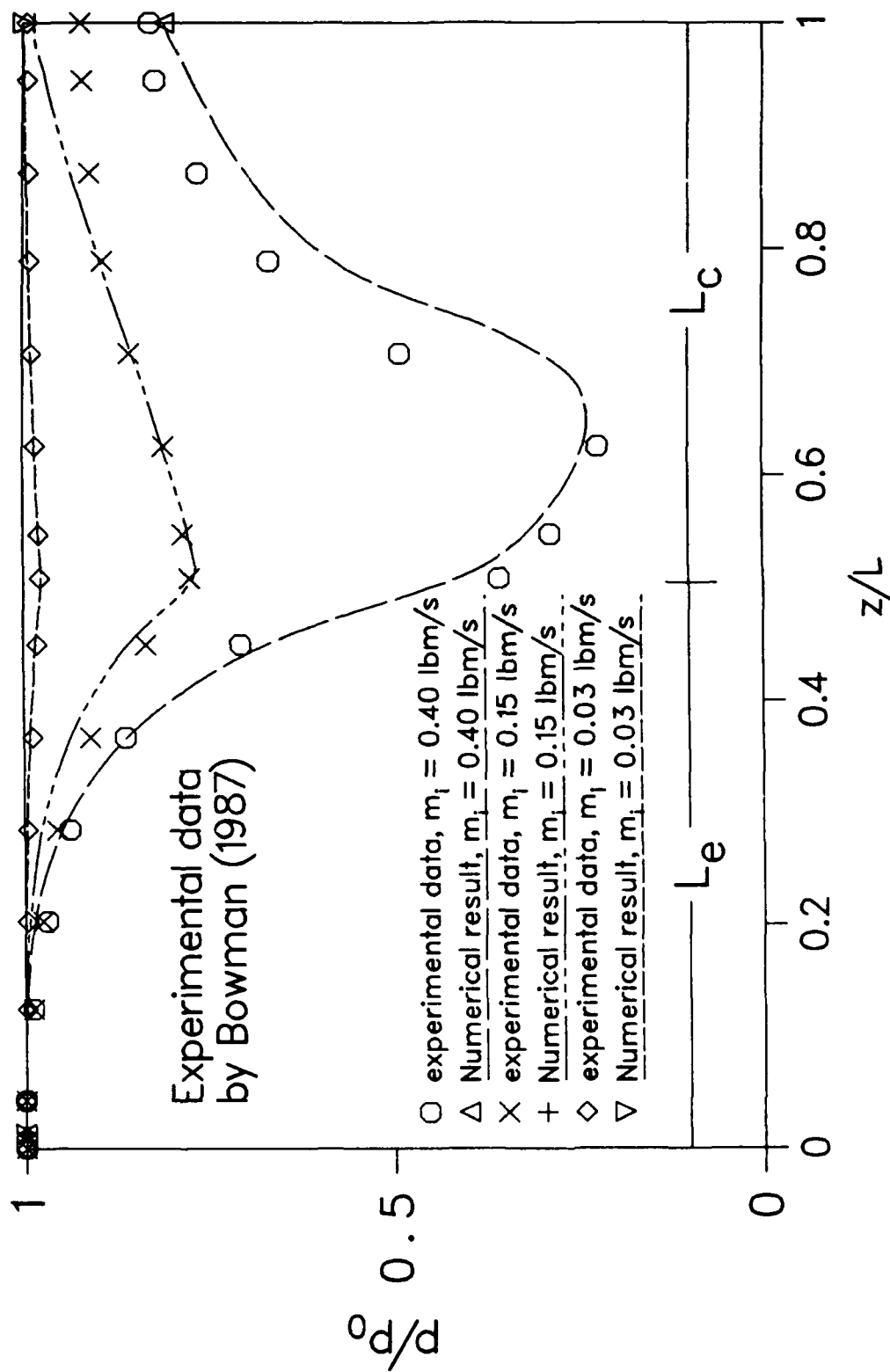


Figure 6.4 The axial pressure profile along the centerline of the simulated heat pipe for steady state

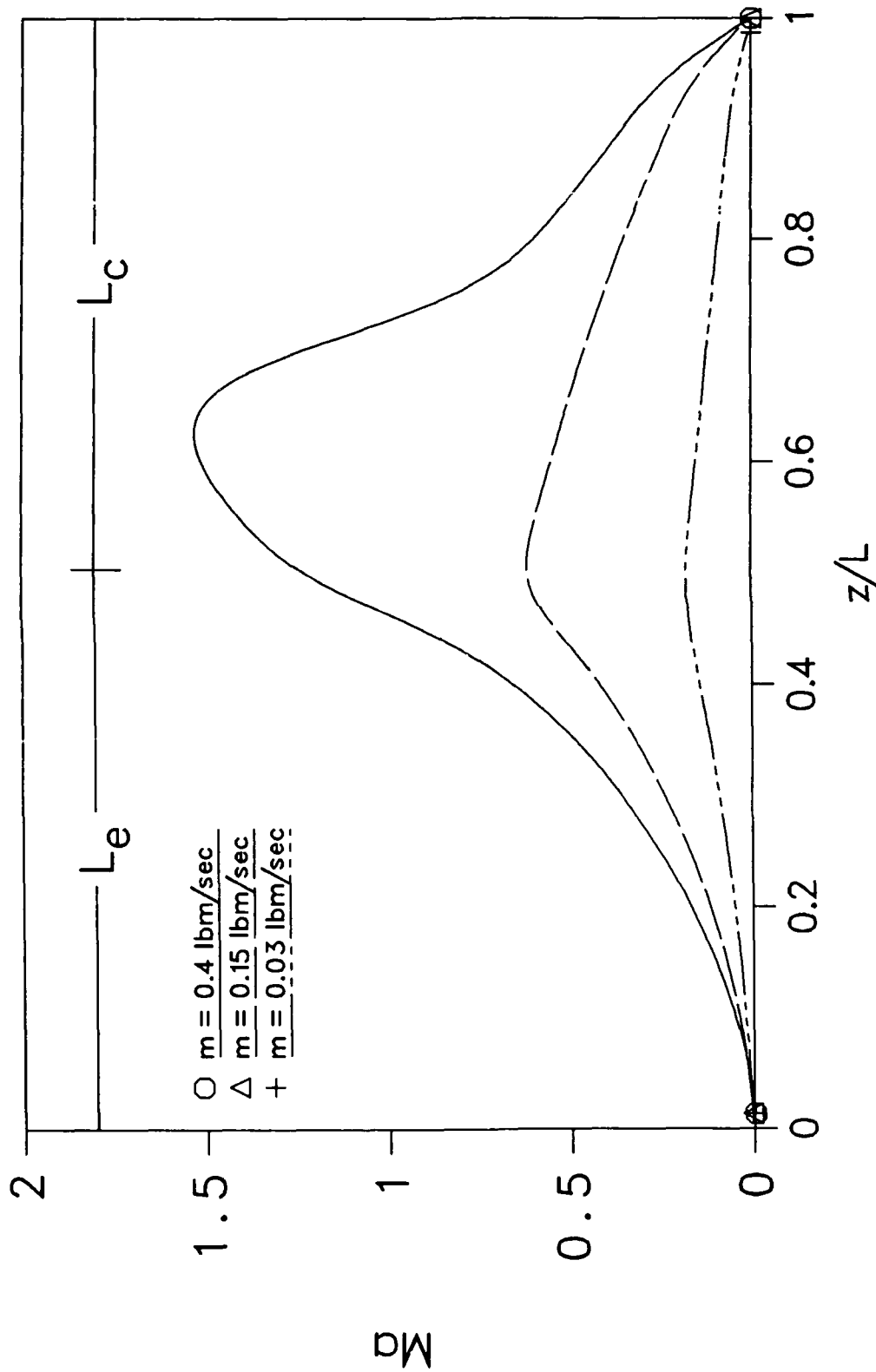


Figure 6.5 The axial Mach number profile along the centerline of the simulated heat pipe for steady state

a similar phenomenon by measuring the axial temperature variation along a sodium heat pipe. It should be pointed out that for $Ma > 1$, considerable axial temperature and pressure changes will exist and the heat pipe operation will be far from normal working conditions. This is indeed the reason that most heat pipe designs use $Ma=1$ as the sonic limit of heat pipes. Since in the experiment the uniform source and sink pressures for the blowing and suction regions were specified, the radial mass flow rate along the pipe at the interface is not uniform as indicated by Bowman (1987), so a linearized radial mass flow rate has been specified at the interface to match the experimental boundary conditions.

The above calculation has been made with a grid size of 20×60 . Different grid sizes have been used to calculate the same problem and it is found that the program is essentially independent of grid sizes for the above specifications. The steady state was assumed to be reached when the relative change of all variables was less than 0.1 percent. The CPU time for running a case from an arbitrarily guessed initial condition to the steady state is about 5-26 minutes on a VAX 6320.

6.5.2 Transient response of the heat pipe to a pulsed heat input

In this section, a heat pipe with configuration shown in Fig. 6.1 is studied. The heat pipe is treated as a single system, and the vapor flow, porous wick and the heat pipe wall are solved as a conjugated problem. The heat pipe has a stainless steel wall and sodium is the working fluid. The dimensions and properties are $L_e = 0.105$ m, $L_a = 0.0525$ m, $L_c = 0.5425$ m, $R_v = 0.007$ m, $\delta_\ell = \delta_w = 0.001$ m, $k_v = 0.0352$ W/m-K, $k_{eff} = 45$ W/m-K, $k_w = 21.7$ W/m-K, $c_{pv} = 2580$ J/kg-K, $c_{p\ell} = 1262$ J/kg-K, and $h_{fg} = 4.227 \times 10^6$ J/kg. The outer wall boundary condition at the condenser was first chosen

as a convective boundary condition (eqn. 6.17a), with the heat transfer coefficient $h_c = 39.0 \text{ W/m}^2\text{-K}$ and an environment temperature $T_a = 300 \text{ K}$. The calculation was conducted with a heat input $Q = 623 \text{ W}$ at the outer wall of the evaporator. The steady state vapor temperature at the centerline is shown in Fig. 6.6 and is labeled as $t = 0.0$. At this time, a sudden increase in heat input from $Q = 623 \text{ W}$ to $Q = 770 \text{ W}$ was imposed at the evaporator. The transient response of the vapor temperature is presented in the same figure. Since the heat transfer coefficient at the outer wall of the condenser is constant, with a larger heat input Q , the outer wall temperature at the condenser needs to be raised to reject more heat into the environment. Since the outer wall temperature is directly related to the vapor temperature in the heat pipe, the vapor temperature will increase accordingly. After about 10 minutes, the heat pipe reached another steady state as shown in the figure. It is noticeable that at a higher working temperature, the vapor temperature is more uniform along the heat pipe than that at a lower working temperature. The time step used in the above calculation was $\Delta t = 0.5$. It took about 57 minutes of CPU time on the CRAY 401R with a grid size of 20×40 .

In space applications, radiation boundary conditions are more often encountered. The calculation was conducted again for the same heat pipe with a radiative boundary condition (eqn. 17b, $\epsilon = 0.85$) at the outer wall surface. The transient vapor temperature is presented in Fig. 6.7. Like the case with the convective boundary condition, the curve labeled with $t = 0.0$ is the steady state vapor temperature with $Q = 623 \text{ W}$. At $t = 0$, the heat input is suddenly increased to $Q = 770 \text{ W}$ and remains constant afterwards. In this case, the transient time is shorter and the heat pipe reaches another steady state in about 6 minutes. Figure 6.8 shows the

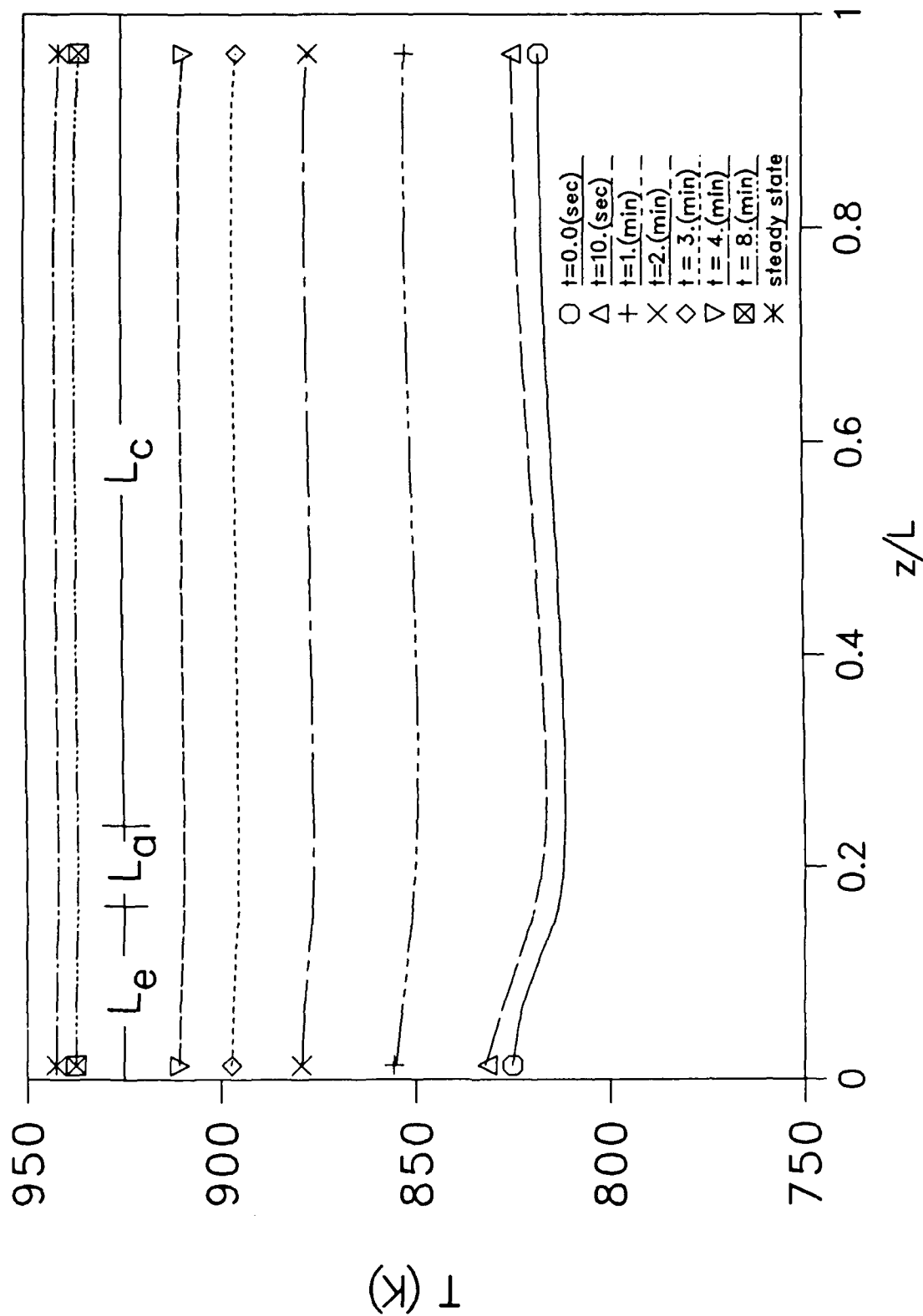


Figure 6.6 The vapor temperature along the centerline for different time periods with the convective boundary condition

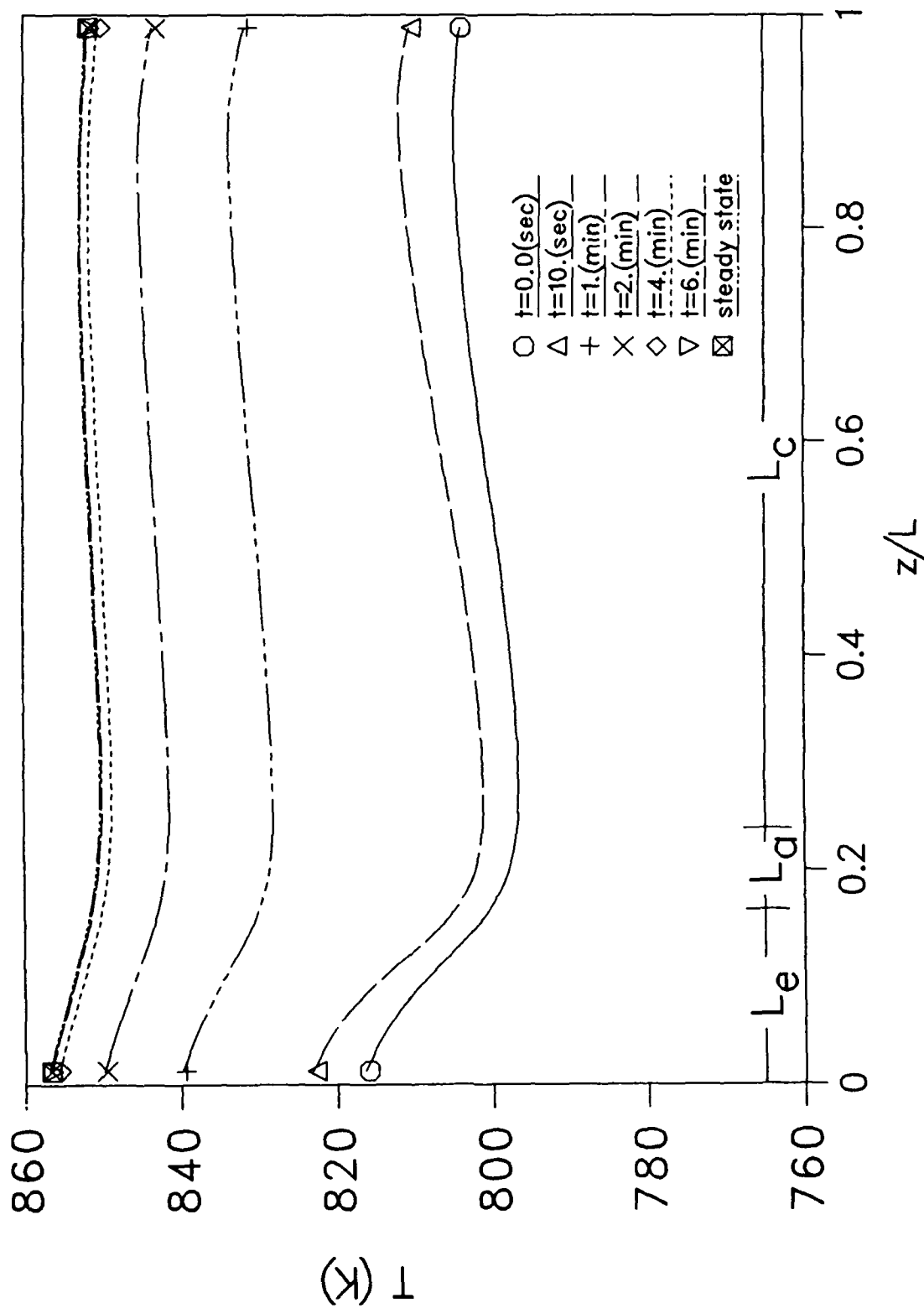


Figure 6.7 The vapor temperature along the centerline for different time periods with the radiative boundary condition

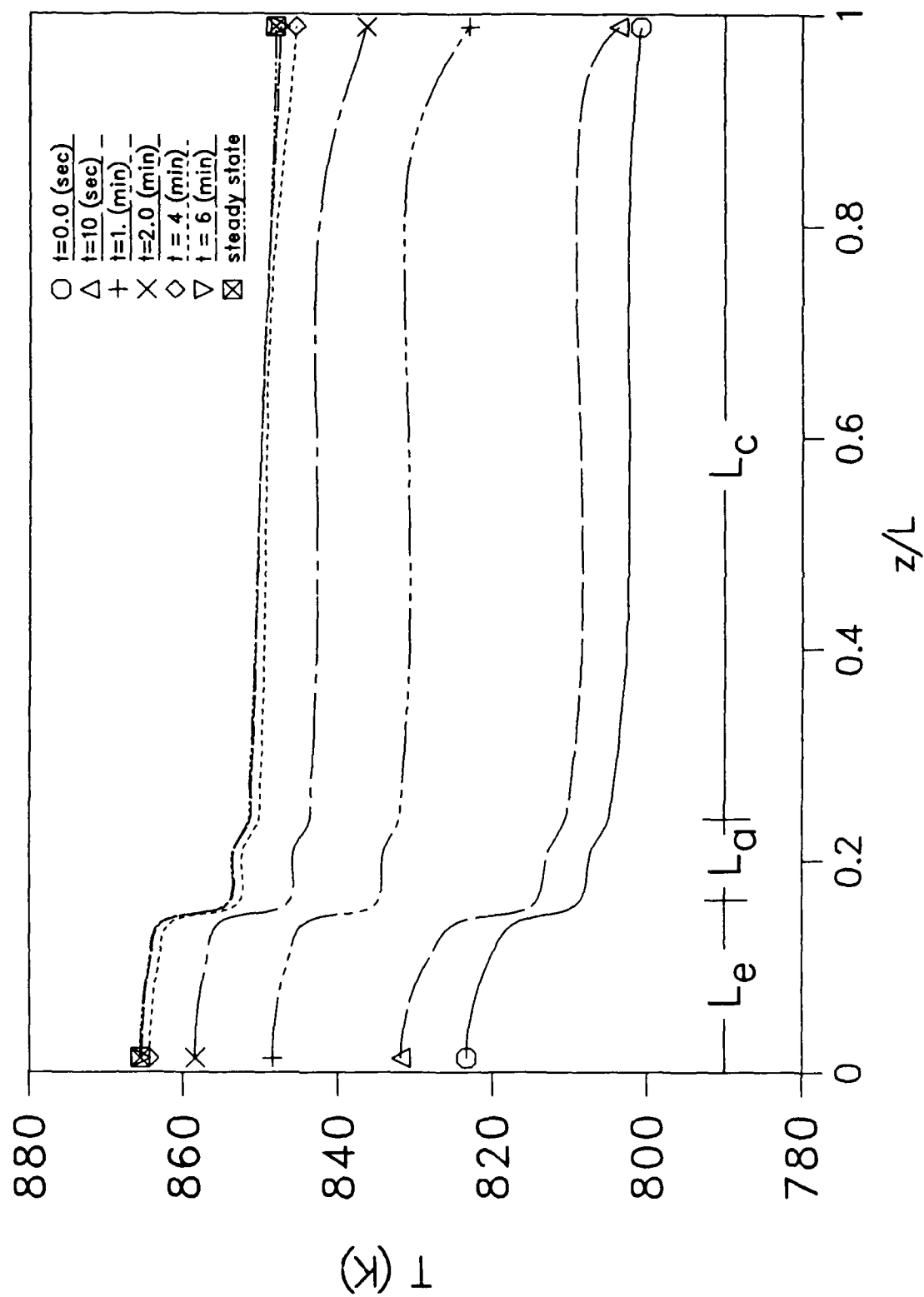


Figure 6.8 The outer wall temperature T_w of the heat pipe for different time periods with the radiative boundary condition

corresponding outer wall temperature along the heat pipe. Although the vapor temperature tends to be more uniform at a higher working temperature, its outer wall counterpart is still stepwise. This trend is reasonable and agrees with experimental observations. As will be illustrated in Fig. 6.13, since heat needs to be conducted to the vapor-liquid interface through the pipe wall and the wick, the outer wall surface temperature at the evaporator is higher than the vapor temperature, while at the condenser heat needs to be conducted from the liquid-vapor interface to the outer wall surface to dissipate into space, so the vapor temperature at the interface is higher than that of the outer wall surface.

As the heat pipe approaches the steady state, the heat rejected at the outer wall surface of the condenser must approach the input heat Q at the evaporator. This energy balance has been checked with the numerical results. At the steady state, the difference between Q and $Q_c = 2\pi r_o \int_0^{L_c} \epsilon \sigma T_w^4 dz$ is less than 1%.

The corresponding transient response of the density, pressure and axial velocity for the heat pipe with the radiation boundary conditions are presented in Figs. 6.9-6.11, respectively. It can be seen that both density and pressure increase with the pulsed heat load, while the axial velocity behaves differently. Shortly after the pulsed load is imposed, the axial velocity increased slightly and then decreased gradually to another steady state condition. Since the vapor is compressible, $m = v_i \rho_i A$, the rate at which the density increased, at some time, exceeded that of mass evaporation at the evaporator; therefore, the vapor velocity began to decrease as shown in Fig. 6.11.

Figures 6.12 and 6.13 presented the radial distributions of axial

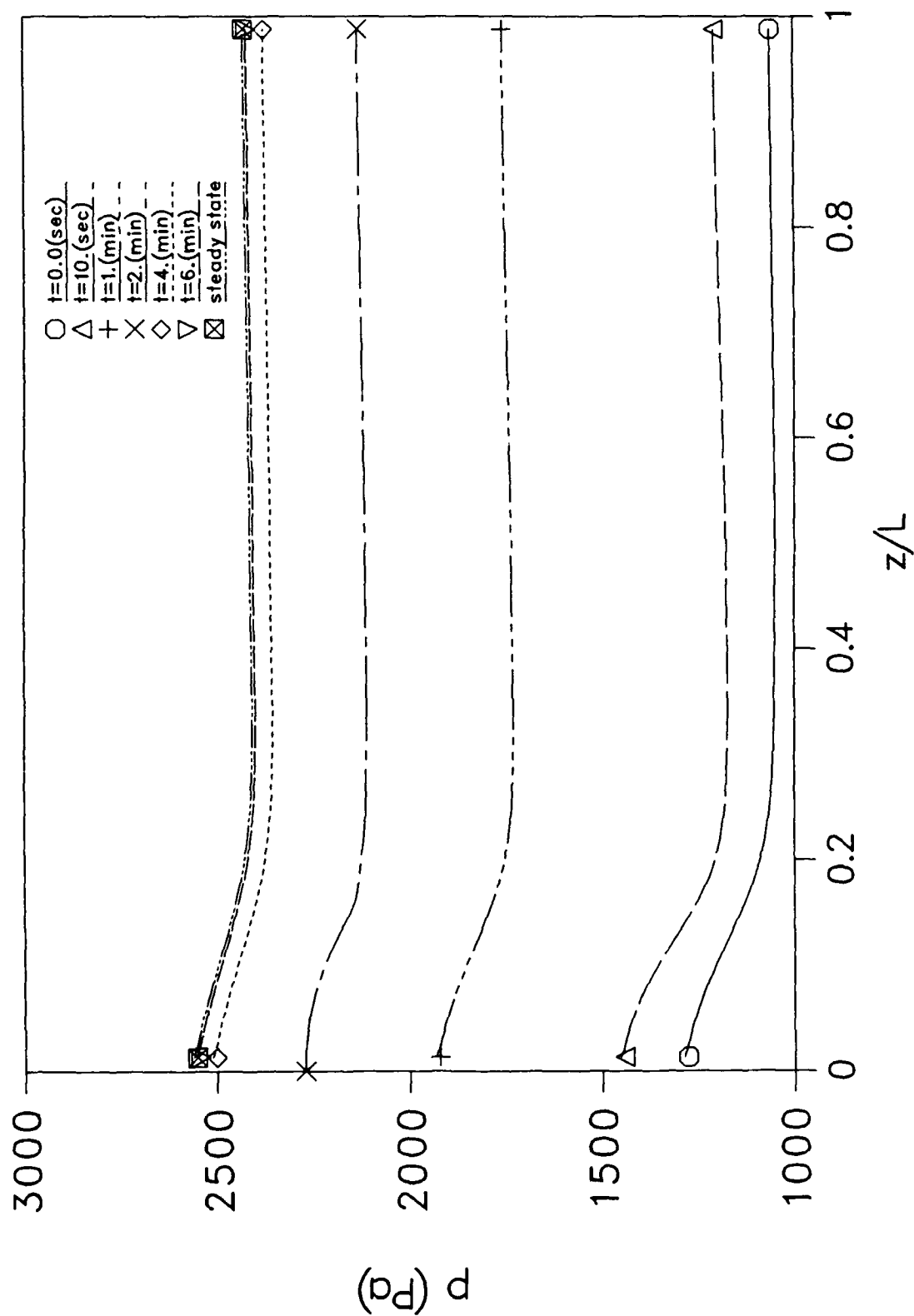


Figure 6.9 The axial pressure profile along the centerline of the heat pipe for different time periods

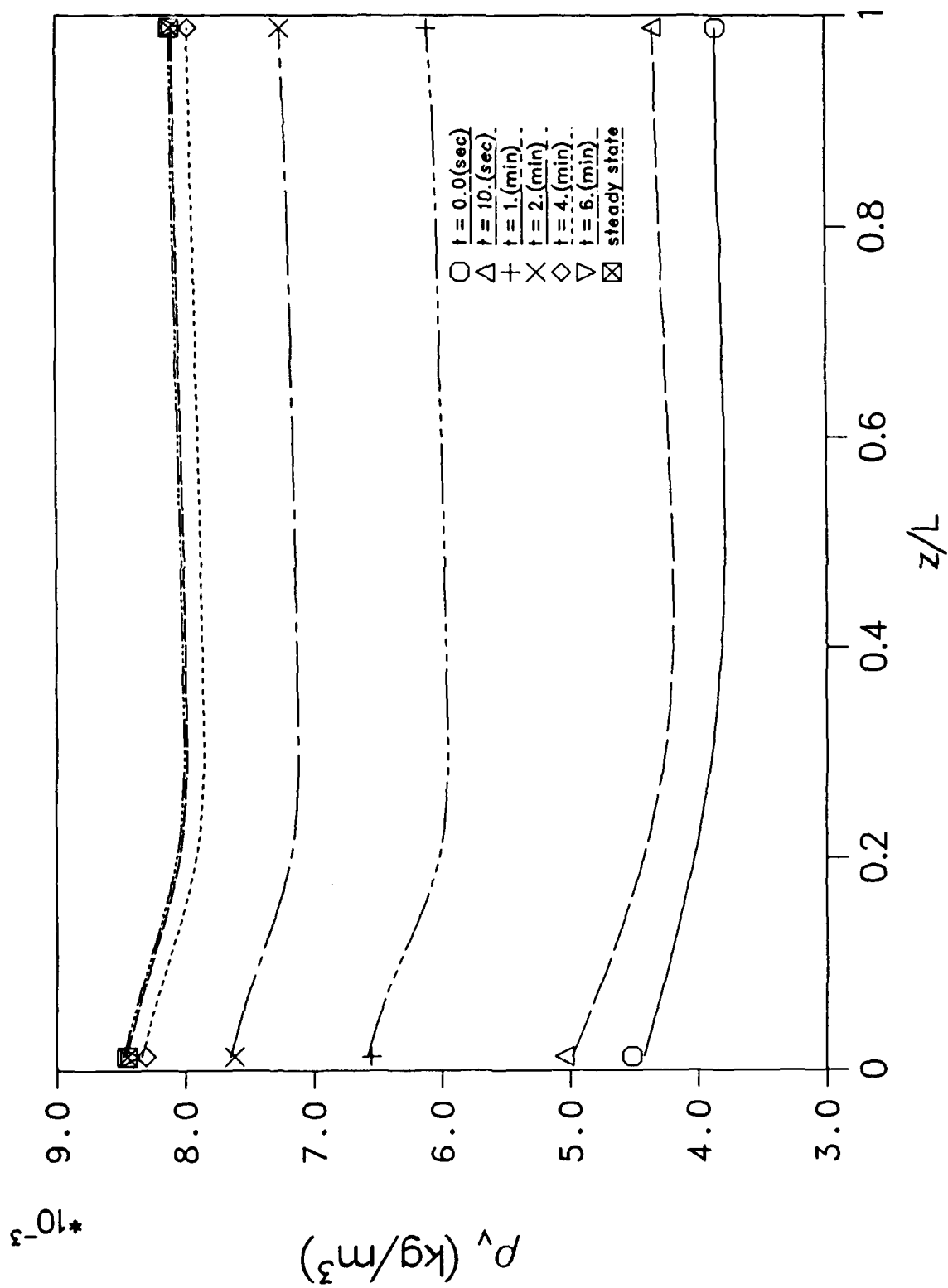


Figure 6.10 The vapor density along the centerline of the heat pipe for different time periods

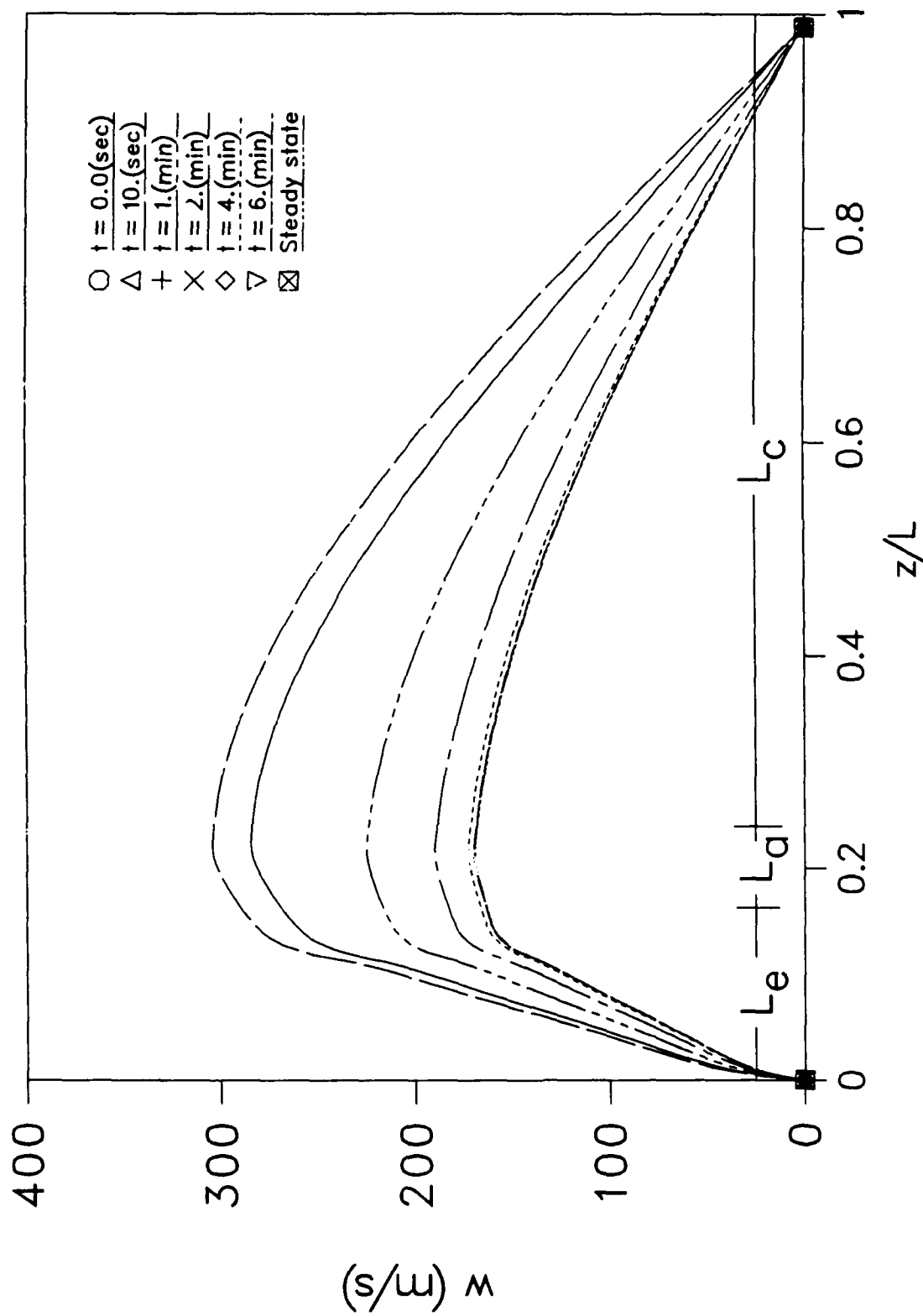


Figure 6.11 The axial velocity profile along the centerline for different time periods

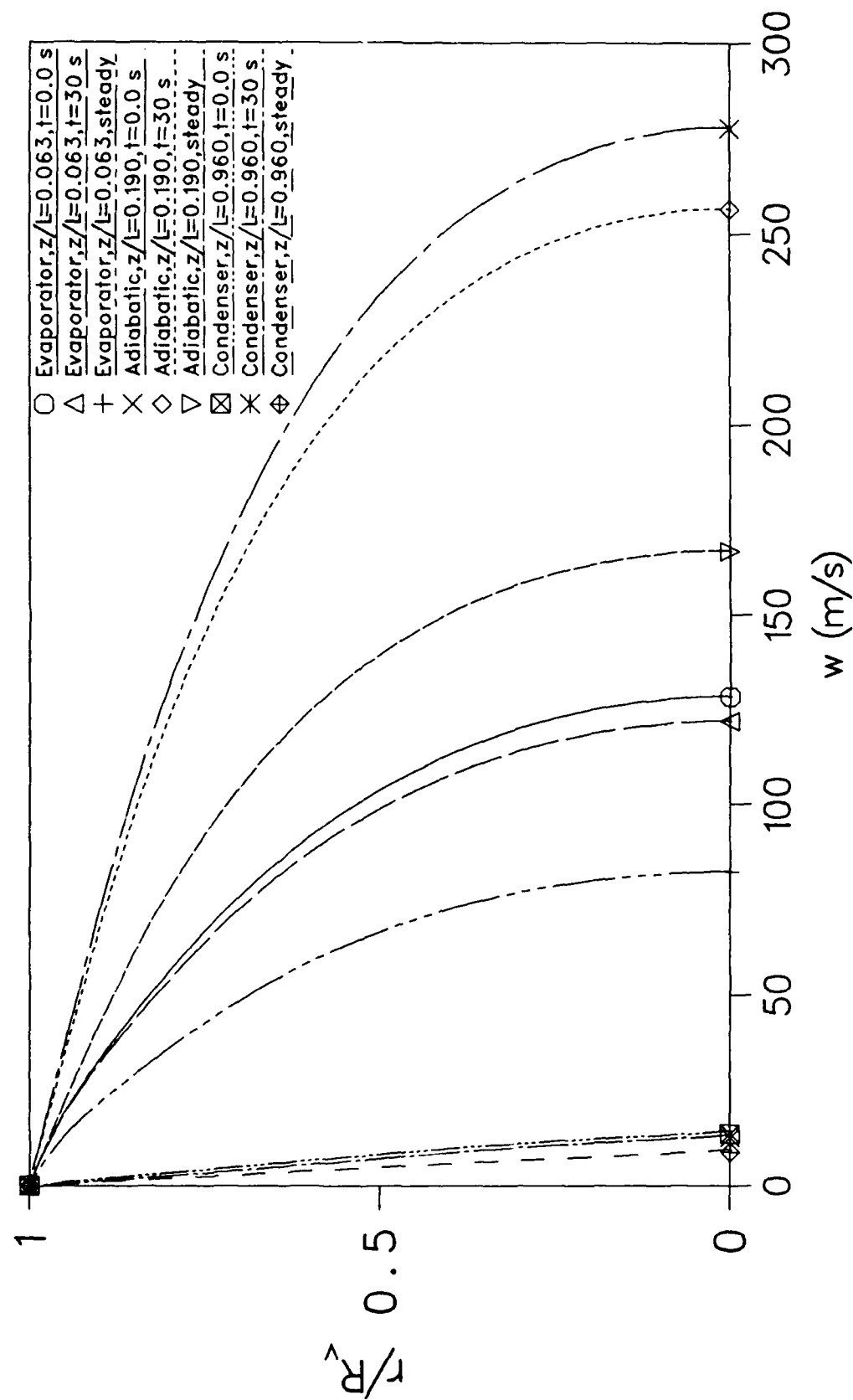


Figure 6.12. Axial velocity distributions in the radial direction at different axial locations and times

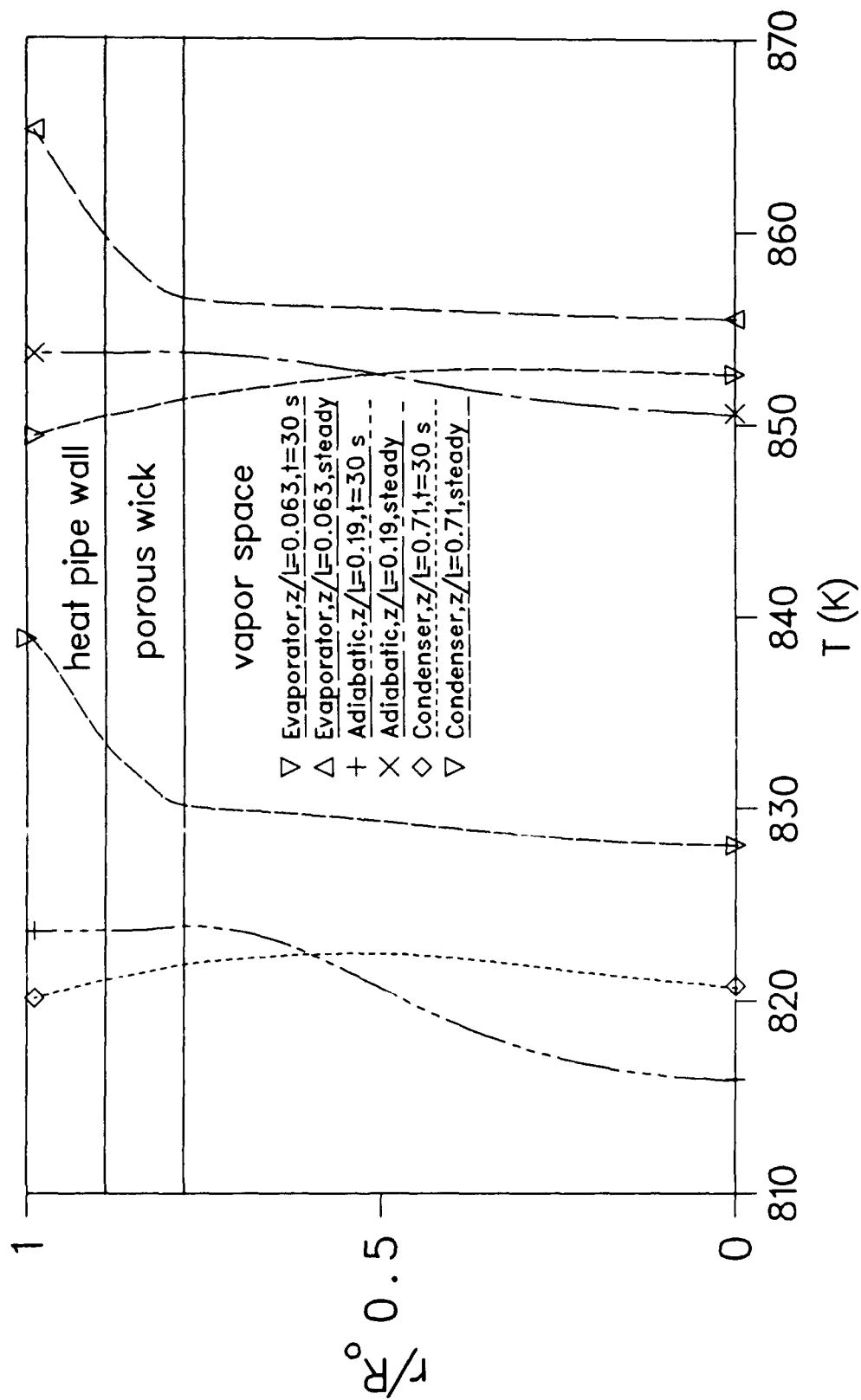


Figure 6.13 Radial temperature distribution at different axial locations and times

velocity and temperature, respectively. Different regions, namely, the vapor space, the porous wick, and the heat pipe wall are also indicated in the Fig. 6.13. As discussed concerning the outer wall temperature distributions, the temperature slope is positive in the evaporator, negative in the condenser, and zero in the adiabatic section. Also, at a higher working temperature, the vapor temperature tends to be more uniform in the radial direction, especially at the evaporator. It should be pointed out that the heat transfer mechanisms are different in different regions. In the regions of the heat pipe wall and wick, heat is transferred mainly by diffusion, while in the vapor region, heat is transferred mainly by convection.

From the numerical results presented above, it is clear that both the transient response and the steady state of a heat pipe heavily depend on the boundary conditions at the outer wall surface of the condenser. This is illustrated by comparing the numerical results in Figs. 6.6 and 6.7, where the only difference is the boundary conditions on the condenser. The temperature distributions indicate that the extent of the departure from uniform temperature along the heat pipe is determined not only by the heat load, but also by the working temperature level which is dependent on the boundary condition on the condenser.

Many of the previous numerical analyses on heat pipe dynamics were focused on the vapor flow alone, and it was found that the vapor transient periods were very short. For example, the vapor transient time without considering the wick and wall as reported by Bowman and Hitchcock (1988) and by Issacci et al., (1988) is only about $0.001 \sim 0.01$ seconds. It seems plausible that a steady-state vapor model could be used in conjunction with a transient wall model to study the heat pipe dynamics, but this is not the

case. The numerical results in this paper show that the vapor transient periods have the same magnitude of 5 ~ 10 minutes as that of the heat pipe wall. This is because the vapor and the wall are coupled through liquid-vapor interface by evaporation and condensation. Therefore, it is very important to solve them simultaneously.

The advantage of the present numerical modeling is that it is mainly based on the energy balance, so no other empirical relation or reference data from experiments is needed in the numerical calculations. The only parameter which needs to be specified, in addition to the heat pipe dimensions and the material properties, is the heat transfer coefficient or the radiation emissivity ϵ at the outer wall surface of the condenser. This, we believe, is one of the major accomplishments in the numerical analysis of heat pipe dynamics.

6.6 CONCLUSIONS

The liquid-vapor interface energy equation (6.6) is derived and the conduction model for the heat transfer in the wick proves to be a reasonable simplification for the analysis of the transient behavior of a heat pipe. For the compressibility of the vapor flow, the pressure is chosen as a dependent variable and the equation of state is directly applied during the iterations. The numerical results of the simulated vapor flow agree well with the corresponding experimental data. The numerical model and computer code can properly predict the transient process of a heat pipe. The transient response of the heat pipe to a sudden increase of the heat input shows that the wick and wall play a crucial role to the transient process of the heat pipe and it is very important to study the heat pipe as a conjugate problem.

Section VII

ANALYSIS OF THE TRANSIENT COMPRESSIBLE VAPOR FLOW IN HEAT PIPES

7.1 SUMMARY

The transient compressible one-dimensional vapor flow dynamics in a heat pipe is modeled. The numerical results are obtained by using the implicit non-iterative Beam-Warming finite difference method. The model is tested for simulated heat pipe vapor flow and actual vapor flow in cylindrical heat pipes. A good comparison of the present transient results for the simulated heat pipe vapor flow with the previous results of a two-dimensional numerical model is achieved and the steady state results are in agreement with the existing experimental data. The transient behavior of the vapor flow under subsonic, sonic, and supersonic speeds and high mass flow rates are successfully predicted. The one-dimensional model also describes the vapor flow dynamics in cylindrical heat pipes at high temperatures.

7.2 INTRODUCTION

In a heat pipe, the change of phase of the working fluid in the closed system is used instead of a large temperature gradient to transport a large amount of energy. The attention of many scientists has focused on this unique phenomenon since the concept was introduced. The vapor from the evaporator carries energy to the condenser, so the vapor flow in the core region of the heat pipe plays an important role in transferring energy from source to sink.

Many researchers have studied the steady one-dimensional compressible (Levy, 1968; Brovalsky et al., 1976; Faghri, 1989; and Jang, 1988) and the steady two-dimensional vapor flow in heat pipes (Bankston and Smith, 1972; Tien and Rohani, 1974; Ooijen and Hoogendoorn, 1979; Faghri, 1986; and Faghri and Parvani, 1988). The common cross sections of the vapor space are circular, rectangular (Jang, 1988; Ooijen and Hoogendoorn, 1979), and annular (Faghri, 1986; Faghri, 1989; and Faghri and Parvani, 1988) and are chosen based on the particular application. The heat flux distributions on the surface of the evaporator and condenser are uniform except for those presented by Jang (1988). Recently, the transient two-dimensional compressible simulated vapor flow in heat pipes (Bowman, 1987; and Bowman and Hitchcock, 1988) was solved numerically, and the experimental data for the steady state simulated heat pipe vapor flow was obtained by Bowman (1987). However, the vapor flow was not actual vapor flow in a heat pipe and the numerical and experimental data were presented only in terms of the pressure. The transient two-dimensional compressible vapor flow in a heat pipe with a rectangular cross section also was studied numerically by Issacci et al. (1988), but only the axial and radial velocity profiles were

presented. No comparison with the existing experimental data was made and the transient behavior of vapor flow in a heat pipe was not described.

During the start-up of high temperature heat pipes, the extremely small density of the vapor causes the vapor flow to attain sonic and supersonic velocities for a relatively small heat input. Thus, the correct description of the transient vapor flow is essential to predict the successful start-up and to estimate the overall performance of the entire heat pipe. The governing equations for the vapor flow as well as those for the wall and wick regions should be solved simultaneously. Also, the development of the one-dimensional transient model for the vapor flow has been suggested due to the large amount of computer time required for the two-dimensional model (Bowman, 1987; and Bowman and Hitchcock, 1988). For this purpose, a simple and efficient mathematical model is desired for each region. All previous one-dimensional models for vapor flow are for the steady state condition and the viscous dissipation was neglected, which is important for high temperature applications.

This paper describes the mathematical model and the numerical method of solution for the transient compressible one-dimensional vapor flow in the heat pipe. A comparison of the numerical results with the simulated transient two-dimensional numerical results and experimental data for the steady state given by Bowman (1987) is also presented. In addition, the numerical results from the present model for the actual vapor flow in the cylindrical high temperature heat pipe are compared with the experimental data obtained at the steady state by Ivanovskii et al. (1982).

7.3 MATHEMATICAL MODELING

The one-dimensional transient compressible vapor flow is considered to predict the vapor flow dynamics in the heat pipe. Even though a uniform velocity is used, the friction at the interface is incorporated by using the expressions for the friction coefficients which are found from the two-dimensional numerical results given by Bowman (1987). The viscous dissipation in the vapor region is included and the vapor is assumed to be a perfect gas. The governing equations for the vapor flow in the heat pipe with negligible body forces are formulated by using the principles of the conservation of mass, momentum, and energy in a control volume of cross-sectional area, $\pi D_v^2/4$, and width, dx .

The governing equations are written in a compact vectorial form as follows:

$$\frac{\partial D}{\partial t} + \frac{\partial E(D)}{\partial x} = \frac{\partial}{\partial x} F(D, D_x) + G \quad (7.1)$$

where

$$D = \begin{bmatrix} \rho \\ \rho U \\ E_t \end{bmatrix} \quad (7.2)$$

$$E(D) = \begin{bmatrix} \rho U \\ \rho U^2 + p \\ U(E_t + p) \end{bmatrix} \quad (7.3)$$

$$F(D, D_x) = \begin{bmatrix} 0 \\ \frac{4}{3} \mu \frac{\partial U}{\partial x} \\ \frac{4}{3} \mu \frac{\partial U}{\partial x} U + k \frac{\partial T}{\partial x} \end{bmatrix} \quad (7.4)$$

$$G = \begin{bmatrix} \frac{4}{D_v} \rho_o V_o(x) \\ - \frac{2\rho U^2 f}{D_v} \\ \left\{ \frac{4\rho_o V_o(x)}{D_v} \left[h_o(x) + \frac{V_o^2(x)}{2} \right] \right\} + \frac{2\rho U^2 f U}{D_v} \end{bmatrix} \quad (7.5)$$

where $V_o(x)$ refers to the velocity at the wall with a positive value for injection and a negative value for suction.

The equation of state is employed to relate the density, pressure, and temperature in the vapor space as follows:

$$p = \rho RT \quad (7.6)$$

For the simulated heat pipe vapor flow, the temperature was evaluated by using the equation of state because a change of phase was not involved. For the actual vapor flow in the cylindrical heat pipe, the Clausius-Clapeyron relationship was used to predict the saturation temperature of the vapor from the pressure as given by

$$T = \frac{1}{\frac{1}{T_c} - \frac{R}{h_{fg}} \ln \frac{p}{p_c}} \quad (7.7)$$

The known boundary conditions at the ends of the heat pipe are as

follows:

$$U = 0 \quad \text{at} \quad x = 0 \text{ and } L \quad (7.8)$$

$$\frac{\partial T}{\partial x} = 0 \quad \text{at} \quad x = 0 \text{ and } L \quad (7.9)$$

The conditions for the density and pressure at the ends of the heat pipe are unknown, so physically realistic boundary conditions should be derived. In general, near the ends of the heat pipe the mass flow rate is small, so the axial gradients of the pressure and density are small. In the region adjacent to the exit of the evaporator, the variations of the pressure and density are large. Thus, the boundary conditions for the pressure and density can be assumed as follows:

$$\frac{\partial p}{\partial x} = 0 \quad \text{at} \quad x = 0 \text{ and } L \quad (7.10)$$

$$\frac{\partial \rho}{\partial x} = 0 \quad \text{at} \quad x = 0 \text{ and } L \quad (7.11)$$

Bowman (1987) introduced a correlation between the mass flux at the wall and the pressure drop across a porous tube wall based on experimental measurements for the simulated heat pipe vapor flow. The mass flux ($\rho_o V_o$) at the wall for the simulated heat pipe vapor flow was evaluated by using this correlation:

$$\Delta(p^2) = 3.639 \times 10^9 (\rho_o V_o)^2 + 1.7015 \times 10^8 (\rho_o V_o) \quad (7.12)$$

where $\Delta(p^2)$ is the absolute value of the difference between the square of

the uniform source pressure and the square of the vapor pressure in the blowing section. In the suction section, $\Delta(p^2)$ is the absolute value of the difference between the square of the vapor pressure and the square of the uniform sink pressure. A change of phase of the working substance was not involved. The uniform source temperature of 300 K was used for his experiment, but the sink temperature was not specified. To evaluate the terms in braces {} in eqn. (7.5), the source temperature is used at the blowing section and the vapor temperature is employed at the suction section.

Since the working fluid changes phase at the vapor-liquid interface in actual heat pipes, the temperature at the interface is the saturation temperature, but the temperature in the vapor space may be quite different from the saturation temperature for high temperature heat pipes. For the one-dimensional model, the properties are the area-averaged properties so that the temperature in the vapor space is not the interface temperature but is also not the saturation temperature. The vapor temperature can be evaluated from the energy equation and the saturation temperature corresponding the vapor pressure can be obtained from the Clausius-Clapeyron relationship. However, this saturation temperature is not the actual interface temperature either. The correct estimation of the terms in braces {} in eqn. (7.5) is uncertain due to using the area-averaged properties. Since a heat pipe is a closed system, the application of the correct values of heat input and output is important. To eliminate this difficulty, terms in braces {} in eqn. (7.5) are replaced by using the heat flux applied on the surfaces of the evaporator and condenser as follows:

$$q = \rho_o V_o(x) \left[h_o(x) + \frac{V_o^2(x)}{2} \right] \quad (7.13)$$

7.4 FRICTION COEFFICIENTS

Bowman (1987) measured the turbulence intensity in the simulated heat pipe to determine the characteristics of the vapor flow. For axial Reynolds numbers up to $Re = 10^6$, laminar flow was observed in the blowing section and was retained in the suction section for axial Reynolds numbers less than $Re = 12000$. The transition from laminar to fully turbulent was predicted in the entrance region of the suction section for axial Reynolds numbers greater than $Re = 12000$. Unlike flow in impermeable tubes, laminar flow was maintained for axial Reynolds numbers greater than 2000. For the supersonic case in the suction and blowing section the flow remained laminar until a shock wave occurred and then turbulent flow abruptly appeared, which showed that no transition region existed.

Since the mathematical model is one-dimensional, proper expressions for the friction coefficient are necessary to take into account the frictional losses. Bowman (1987) carried out eleven numerical simulations by using the two-dimensional numerical model to evaluate the friction coefficients according to the characteristics of the vapor flow. The following expressions for the friction coefficients including the compressibility effect were correlated by using the friction coefficients obtained from the two-dimensional model. The friction coefficient for laminar flow in the condenser or evaporator is

$$f = \frac{16}{Re} (1.2337 - 0.2337e^{-0.0363Re_o})e^{1.2M^2} \quad (7.14)$$

The absolute value of the radial Reynolds number at the wall, Re_o , is used in the evaporator and condenser. For the adiabatic section where the wall radial Reynolds number is zero, eqn. (7.14) is identical to that for the impermeable circular tube. For fully-developed turbulent flow in the condenser, the friction coefficient is

$$f_t = \frac{0.046}{Re^{0.2}} \left[1 + 55Re^{0.1} \left[\frac{V_o(x)}{U} \right]^{0.9} \left[\frac{2L_c}{D_v} \right]^{0.1} e^{1.2M^2} \right] \quad (7.15)$$

For transition flow in the condenser entrance region, the friction coefficient is defined as

$$f = f_t + (f_e - f_t) e^{-0.412\bar{x}^2} \quad (7.16)$$

For the one-dimensional numerical model presented in this paper, the vapor flow in the evaporator and adiabatic sections is assumed to be laminar. In the condenser, laminar flow is assumed for the axial Reynolds numbers below $Re = 12000$ at the entrance of the condenser and for supersonic flow. When the axial Reynolds number is greater than $Re = 12000$, transition and turbulent flows are considered in the condenser. Also, after a shock wave turbulent flow is assumed in the condenser. Equation (7.14) is used to evaluate the friction coefficients in the evaporator and adiabatic sections and is also employed in the condenser when the axial Reynolds number at the entrance of the condenser is less than $Re = 12000$ and the vapor flow is supersonic. When the axial Reynolds number is larger than $Re = 12000$, eqn. (7.16) is applied to the transition region, which is assumed to exist from the entrance of the condenser to

about 60 percent of the condenser length based on the experimental data shown in Fig. 3.8 given by Bowman (1987). Equation (7.15) is used for the turbulent flow in the condenser. The initial location of the transition region, $x_{t,i}$, is equal to the location at the entrance of the condenser, and from Fig. 7.3.8 given by Bowman (1987), $x_{\Gamma} = 3/4$ and $x_{\Gamma} = 1/4$ were estimated to be 0.7 and 0.6, respectively.

7.5 NUMERICAL FORMULATION

From the many schemes (Anderson et al., 1984) available for the solution of the compressible flow problem, the Beam-Warming finite difference scheme is chosen to transform the governing equation (7.1) to the finite difference formulation. This scheme is a non-iterative implicit method and is similar to ADI for multidimensional flow problems by using the factorization which retains the tridiagonal block matrix.

The spatial derivatives are approximated by using the three-point second-order accurate central difference approximation for the interior points and the one-sided second-order accurate difference approximation for the boundary nodes. After the approximation operators are applied, the system of equations becomes

$$[J_{i-1}] \delta^n D_{i-1} + [K_i] \delta^n D_i + [L_{i+1}] \delta^n D_{i+1} = [RHS]_i^n \quad i = 2, \dots, I_{\max}-1 \quad (7.17)$$

where

$$\delta^n D = D^{n+1} - D^n$$

$$\begin{aligned}
[J_{i-1}] &= - \frac{\theta_1 \delta t}{1 + \theta_2} \left[\frac{1}{2\delta x} ([A]^n - [P]^n + [R_x]^n) + \frac{1}{\delta x^2} [R]^n \right]_{i-1} \\
[K_i] &= [I] - \frac{\theta_1 \delta t}{1 + \theta_2} \left[[S]^n_i - \frac{2}{\delta x^2} [R]^n \right]_i \\
[L_{i+1}] &= \frac{\theta_1 \delta t}{1 + \theta_2} \left[\frac{1}{2\delta x} ([A]^n - [P]^n + [R_x]^n) - \frac{1}{\delta x^2} [R]^n \right]_{i+1} \\
[RHS]_i^n &= \frac{\delta t}{1 + \theta_2} \left[\frac{1}{2\delta x} (- E_{i+1}^n + E_{i-1}^n + F_{i+1}^n - F_{i-1}^n) + G_i^n \right] + \\
&\quad \frac{\theta_2}{1 + \theta_2} \delta^{n-1} D_i - \epsilon (D_{i+2}^n - 4D_{i+1}^n + 6D_i^n - 4D_{i-1}^n + D_{i-2}^n)
\end{aligned}$$

where $[I]$ is the unit matrix, $[A]$, $[P]$, $[R]$ and $[S]$ are the Jacobian matrices, and ϵ is the coefficient of the dissipative term to damp the oscillation.

This time difference formula reproduces many different schemes with the appropriate choice of θ_1 and θ_2 . The scheme is second-order accurate in time when $\theta_1 = 1/2 + \theta_2$ and first-order accurate otherwise. For $\theta_1 = 1$ and $\theta_2 = 1/2$, the formula becomes second-order accurate in time over three grid points. The system of equations, (7.17), has the following block tridiagonal structure:

$$[JKL] \{ \delta^n D_i \} = \{ RHS_i^n \} \quad (7.18)$$

where $[JKL]$ represents the banded coefficient matrix of which components are 3×3 matrices for one-dimensional vapor flow, and $\{ \delta^n D_i \}$ and $\{ RHS_i^n \}$ are column vectors. The tridiagonal block matrix size is now $(3 \times I_{\max-2}) \times (3 \times I_{\max-2})$ where I_{\max} is the number of nodal points. This system of equations can be solved using the conventional methods for solving block

tridiagonal systems of equations. The vector of unknowns at $n + 1$ time step is then determined by simply adding $\delta^n D$ to the value of D^n at n step. The primitive variables (ρ , U , p , T) can be obtained from D^{n+1} .

A total of 80 nodes, which is the minimum number of nodes to obtain accurate results, are evenly spaced in the axial direction and a time step of 0.1×10^{-3} s is used for the simulated heat pipe vapor flow. Since the heat flux at the wall in the evaporator is different from that in the condenser due to the different lengths for the cylindrical heat pipe, the coarse nodal system presented some difficulty to reach the steady state. For the cylindrical heat pipe, 200 evenly-spaced nodes are used in the axial direction and a time step of 0.1×10^{-3} s is employed.

7.6 RESULTS AND DISCUSSION

7.6.1 Comparison with the simulated heat pipe vapor flow

A comparison of the numerical results with the experimental data given by Bowman (1987) is desired to verify the mathematical model and algorithm. However, the existing experimental data was obtained by simulating the vapor flow of a cylindrical heat pipe with a porous pipe which has an inside diameter of 1.65 cm and a length of 0.61 m as shown in Fig. 7.1. The blowing and suction sections have equal lengths and were simulated by the injection and suction of air without phase change at the interface. Also, uniform source and sink pressures for the blowing and suction regions are specified instead of the radial mass flow rate. Thus, to simulate the experiment eqn. (7.12) is used to obtain the radial mass flux with the known source and sink pressures.

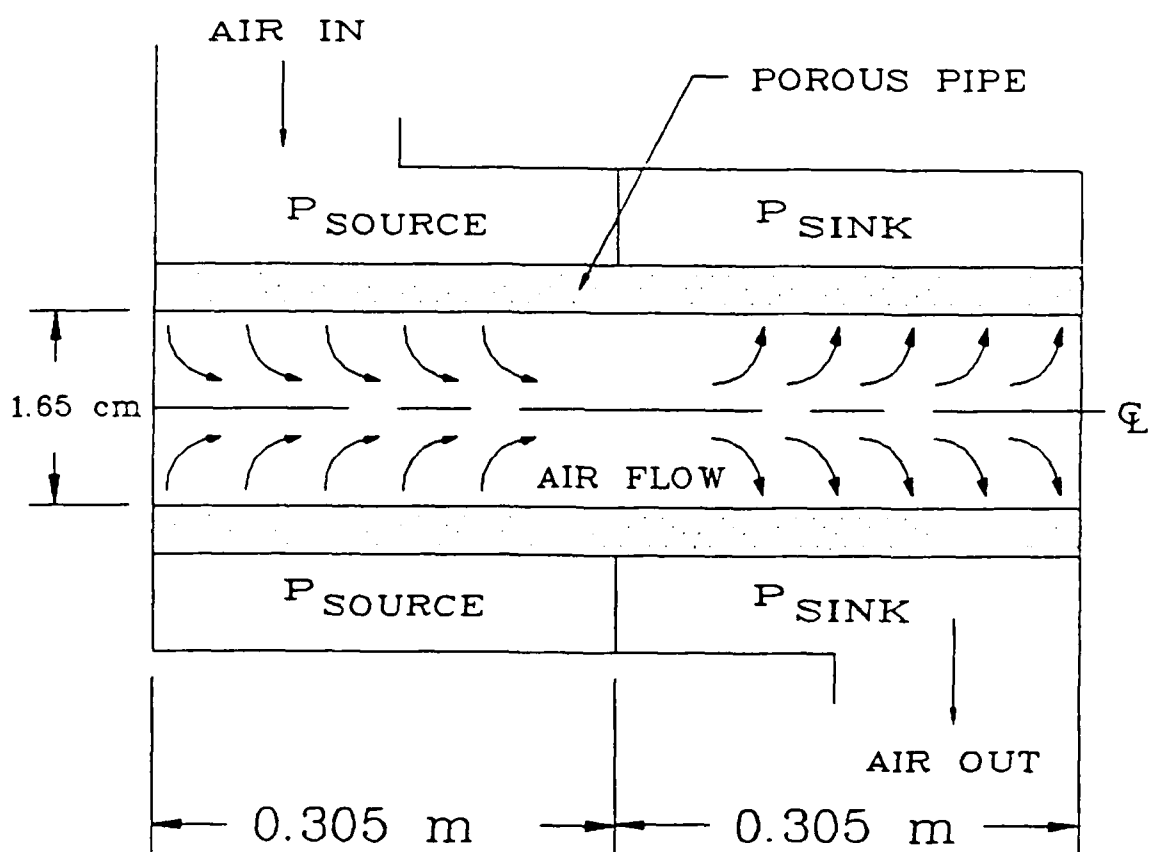


Figure 7.1. Schematic diagram of model for air flow in the porous pipe

7.6.1.1 Transient results

The existing experimental data was obtained at the steady state so the present transient numerical results can only be compared with the transient numerical results for the two-dimensional model (Bowman, 1987). For this purpose, the same geometry and physical conditions are used such as the source pressure of $2.06 \times 10^5 \text{ N/m}^2$ (30 psia) and the sink pressure of $1.03 \times 10^5 \text{ N/m}^2$ (15 psia) corresponding to case B.1.

Initially, the velocity of the vapor is zero and the pressure and temperature are the same as the source pressure and temperature, respectively. To simulate the transient flow, the sink pressure is suddenly lowered to $1.03 \times 10^5 \text{ N/m}^2$ (15 psia), while the source pressure remains the same as the initial pressure. This difference between the source and sink pressures initiates the air flow from the blowing section to the suction section. The pressures at the inlet of the blowing section, the center of the pipe, and the end of the suction section are plotted to compare with the numerical results for the two-dimensional model as shown in Fig. 7.2.

Figure 7.2 shows the following transient behavior of the air flow in the porous pipe. Since the sink pressure is abruptly changed from the initial pressure to $1.03 \times 10^5 \text{ N/m}^2$ (15 psia) along the entire suction section, the pressures at the center and last nodes decrease immediately due to the evacuation of air. For this period, the blowing section pressures adjacent to the suction section start to decrease due to the flow of mass from the blowing section to the suction section, but the pressure near the beginning of the blowing section remains constant. Also, the mass

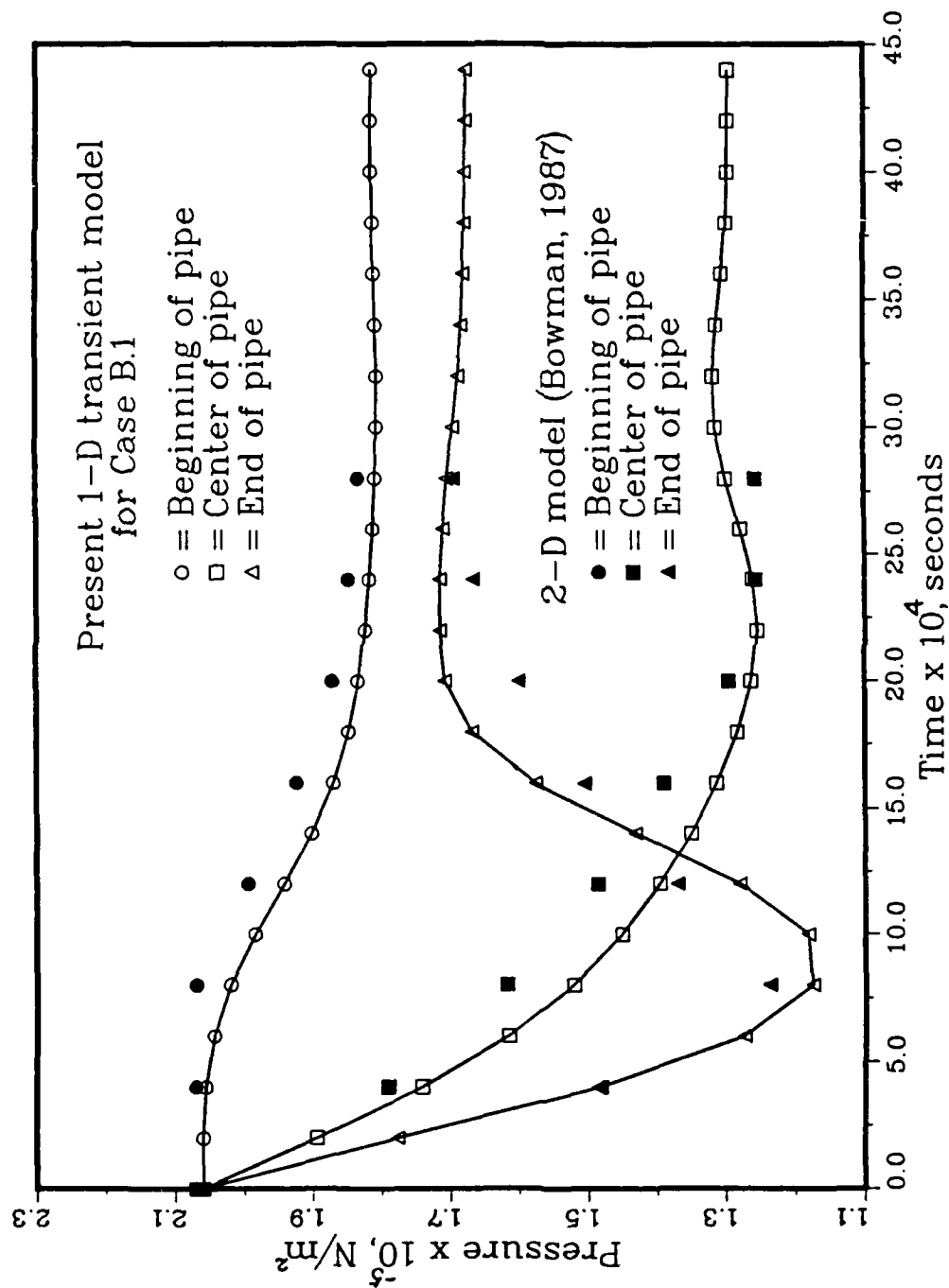


Figure 7.2. Comparison of the present numerical results with Bowman's 2-d model for pressure variations with time at three locations of the porous pipe: Case B.1

flow rate from the blowing section to the suction section is not sufficient to influence the end of the suction section so that the pressure at this point decreases faster than that at the center of pipe.

At about $0.8 - 1.0 \times 10^{-3}$ s, the pressure at the end of the suction section reaches the minimum value and then starts to increase while the pressure at the center of pipe keeps decreasing due to the frictional loss and the acceleration of the flow. At this time, the pressures over the entire blowing section become less than the initial pressure so that the mass flow rate is sufficient to influence the end of suction section. As the pressure in the blowing section decreases and the source pressure remains constant, the mass flow rate from the blowing section to the suction section increases. Thus, the pressure at the center node keeps decreasing and the pressure at the end of the suction section rises due to the contribution of the mass from the blowing section.

At about 3.5×10^{-3} s, the pressures at all three points reach the steady state. As expected, the pressure at the end of the suction section does not recover completely due to the frictional loss at the pipe wall. Figure 7.2 shows that the present results and numerical results for the two-dimensional model (Bowman, 1987) are in agreement.

7.6.1.2 Steady state results

When the present numerical results reach the steady state, those results are compared with the experimental data given by Bowman (1987). Numerical calculations are conducted for four different sets (i.e., cases B.2, B.3, B.4, and B.5) of the source and sink pressures by using eqns.

(7.14 - 7.16) for the friction coefficient. The cases examined are as follows:

Case B.2: $P_{so} = 1.39 \times 10^5$ and $P_{sk} = 1.21 \times 10^5 \text{ N/m}^2$

Case B.3: $P_{so} = 2.09 \times 10^5$ and $P_{sk} = 1.57 \times 10^5 \text{ N/m}^2$

Case B.4: $P_{so} = 2.68 \times 10^5$ and $P_{sk} = 1.69 \times 10^5 \text{ N/m}^2$

Case B.5: $P_{so} = 5.30 \times 10^5$ and $P_{sk} = 1.06 \times 10^5 \text{ N/m}^2$

Figure 7.3 shows the comparison of the pressure distributions along the axial direction. The top three lines in Fig. 7.3 show the pressure distributions for the low mass flow rates. The pressures in the blowing section decrease due to friction and the acceleration of the flow caused by mass injection, but the pressures in the suction section increase owing to the deceleration of the flow by the extraction of mass. However, the pressures at the end of the suction section are less than those at the beginning of the blowing section because of the loss due to friction. In these three cases, the pressure distributions at the steady state correspond well to those for low temperature heat pipes and are in agreement with the experimental data.

The fourth data profile (case B.5) shows the pressure variation in the axial direction for the high mass flow rate. Unlike the previous three cases, the pressure drop in the blowing section is very large. The pressure ratio at the exit of the blowing section is about 0.4 and this ratio corresponds to a Mach number of $M = 1$. After the pressure decreases in the blowing section, the pressure keeps decreasing in the entrance region of the suction section due to the expansion of air even though mass

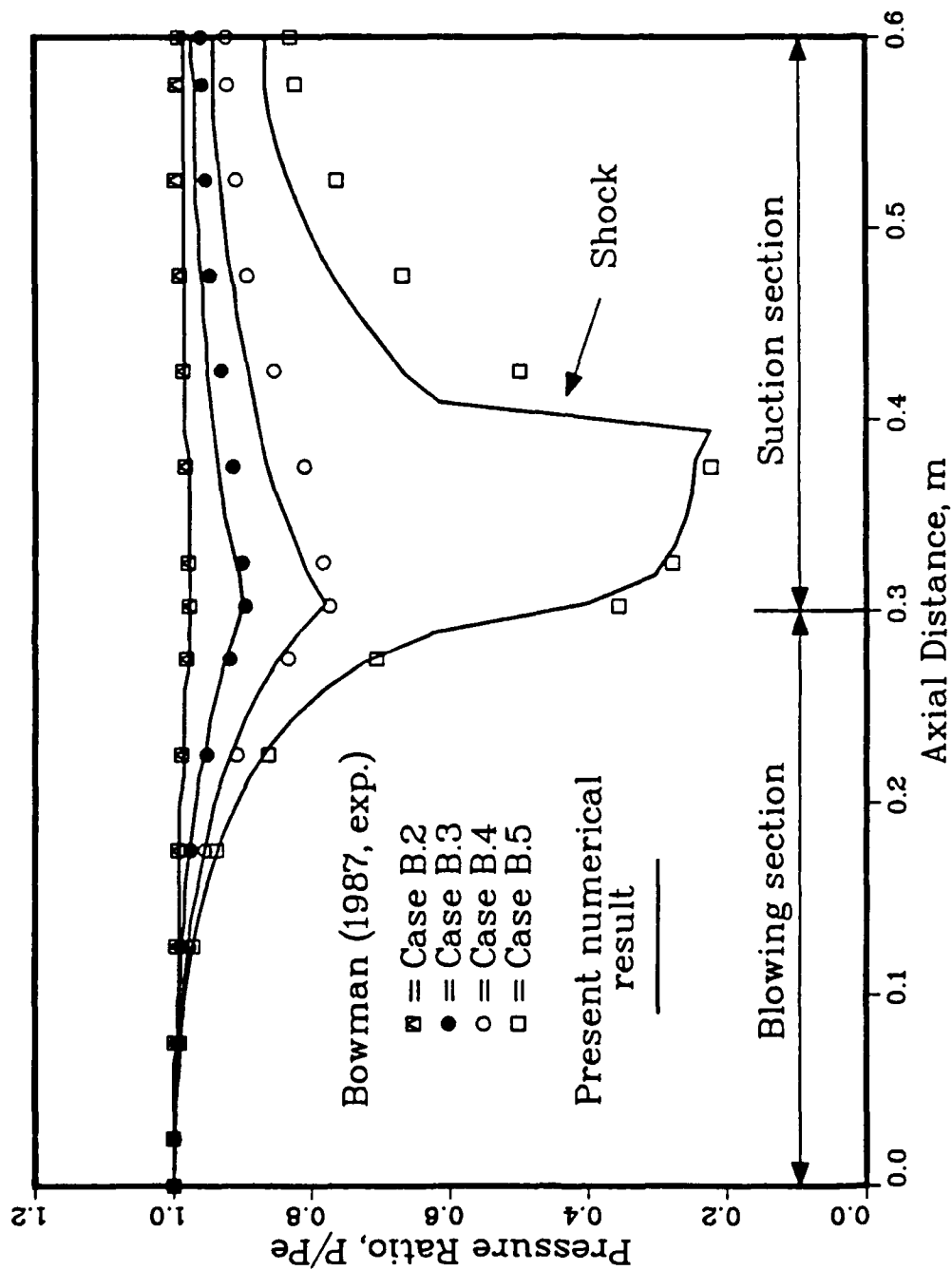


Figure 7.3. Comparison of the present numerical results with the experimental pressure variations (Bowman, 1987) in the porous pipe

removal occurs. Then, the pressure suddenly increases and then continues to increase as the flow slows down. This implies that a shock wave occurs at the place where the pressure changes abruptly. When a shock wave does not exist in the suction section, the pressure is supposed to decrease along the suction section. The one-dimensional model predicts the supersonic flow and shock wave in the suction section and the comparison of the numerical results and experimental data shows a good agreement except for the region immediately after the shock wave.

The variations of the pressure, temperature, velocity and density at the steady state corresponding to cases B.4 and B.5 are shown in Figs. 7.4 and 7.5, respectively. For the low mass flow rate, the temperature and density in the blowing section decrease corresponding to the decrease in pressure and the velocity increases due to the mass injection as shown in Fig. 7.4. The Mach number, however, is less than $M = 1$ at the exit of the blowing section, so the velocity in the suction section decreases because of the extraction of mass. Also, the temperature and density increase in the suction section. Figure 7.5 shows the axial variations of the temperature, pressure, velocity and density for the high mass flow rate. After the sonic velocity is reached at the exit of the blowing section, the velocity keeps increasing in the suction section until a shock wave occurs. Then, the velocity decreases to $U = 0$ at the end of the pipe. As shown by the density profile, the air expands near the entrance region of the suction section and then the density suddenly increases after the shock wave.

The most interesting aspect in Figs. 7.4 and 7.5 is the variation of

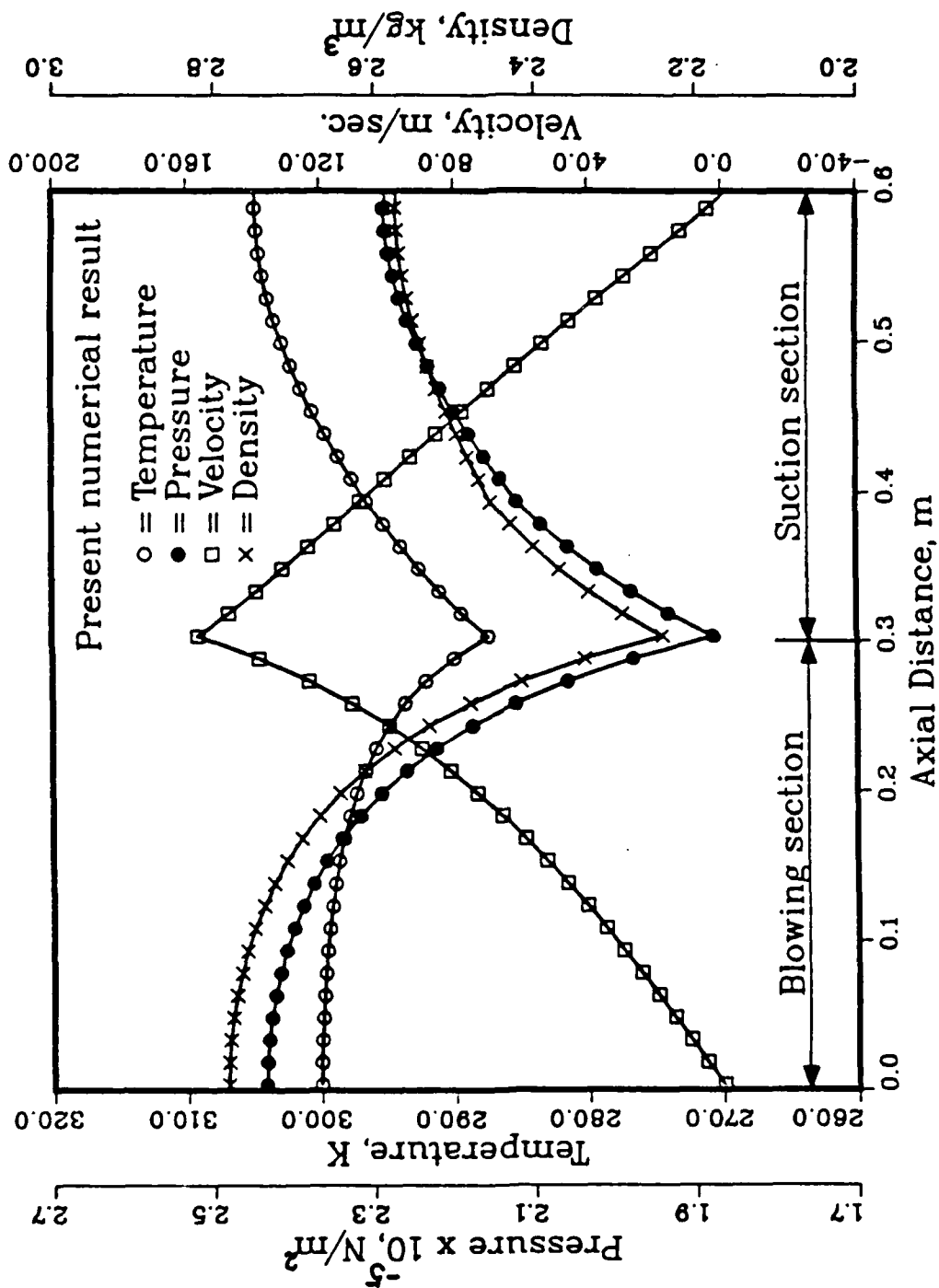


Figure 7.4. Axial variations of temperature, pressure, velocity, and density for Case B.4

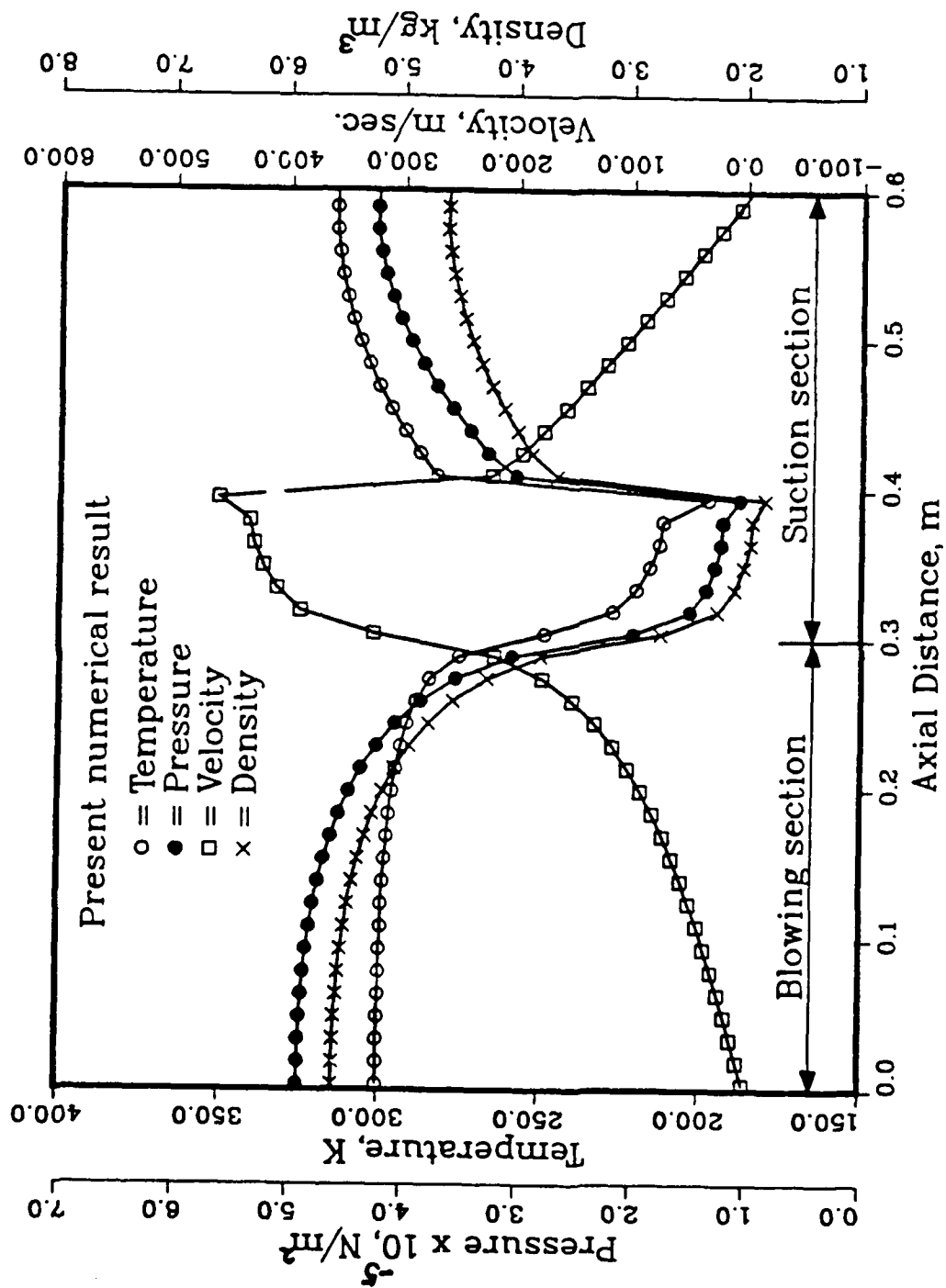


Figure 7.5. Axial variations of temperature, pressure, velocity, and density for Case B.5

temperature. The temperature at the end of the suction section is greater than that at the beginning of the blowing section. In the present model viscous dissipation is included. The Mach number at the entrance of suction section is about $M=0.5$ for case B.4. Since the present model is one-dimensional, the derivative of the axial velocity with respect to the radius is zero, but the friction effect at the interface between the wall and the vapor is included by using eqns. (7.14 - 7.16) for the friction factor. This effect corresponds to viscous dissipation due to the axial velocity derivative with respect to the radius. The increase in temperature is due to viscous dissipation.

7.6.2 Comparison with actual vapor flow in cylindrical heat pipes

The model was tested for the actual vapor flow in a sodium heat pipe corresponding to the experiment given by Ivanovskii et al. (1982) as shown in Fig. 7.6. The lengths of the evaporator, adiabatic, and condenser sections are 0.1, 0.05, and 0.35 m, respectively. The diameter of the vapor space is 0.014 m. The experimental data (Ivanovskii et al., 1982) represents only the saturation temperature and heat transfer rate ($Q = 560$ W) at the steady state. The initial conditions and actual boundary conditions applied on the surface of the evaporator and condenser are unknown. The present numerical model is transient, however, so the initial conditions and history of heat input and output in the evaporator and condenser sections are needed.

For the numerical calculations, the uniform initial temperature of 810 K is used and the vapor is assumed to be saturated at the initial temperature. Initially, the velocity of the vapor is zero. The same

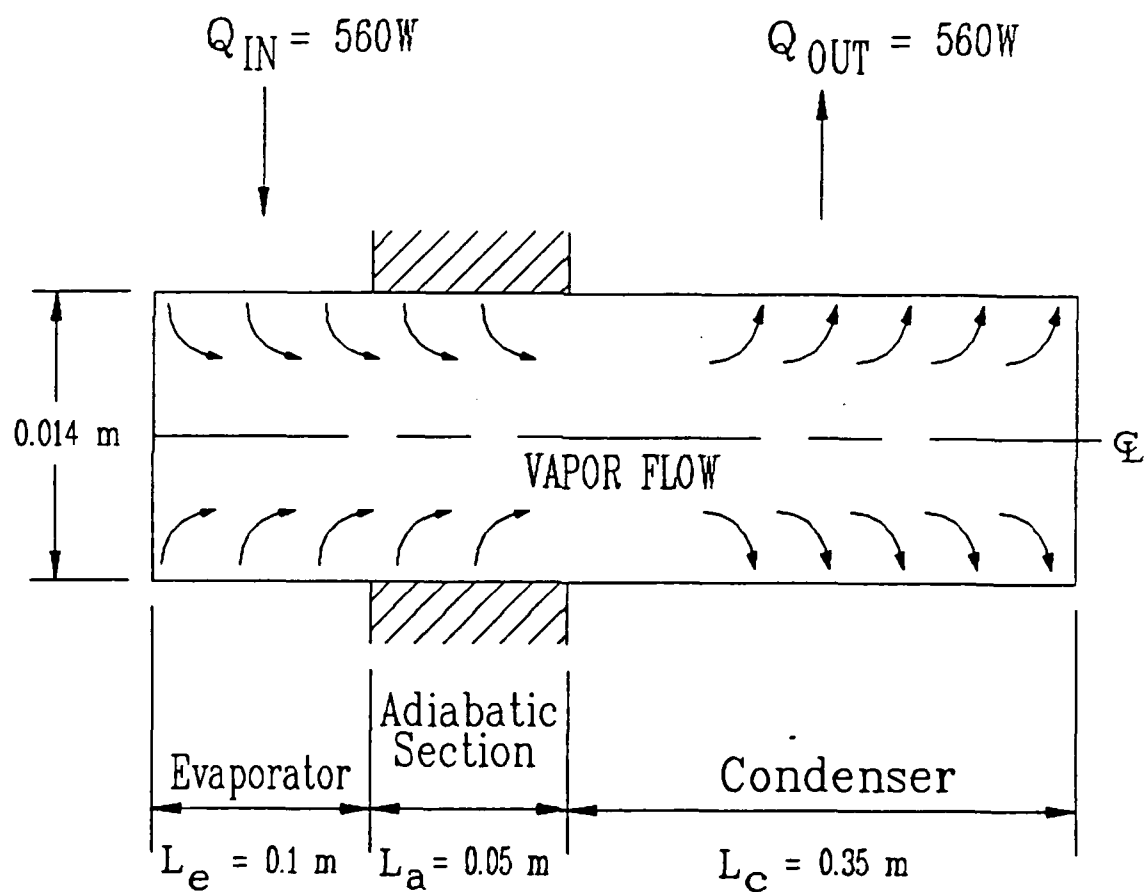


Figure 7.6. Schematic diagram of model for sodium vapor flow in the heat pipe

amount of heat ($Q = 560 \text{ W}$) is uniformly applied on the surface of the evaporator and the convective boundary condition is used on the surface of the condenser. The reference temperature of 300 K for the convective boundary condition is employed and the heat transfer coefficient is determined by iteration. At first, an arbitrary initial heat transfer coefficient is guessed. When the numerical results reach the steady state, the saturation temperature at the end cap of the evaporator is compared with the experimental data at the same location. This procedure is repeated until the same temperature is obtained at the steady state. For this test, the heat transfer coefficient of $69.1 \text{ W/m}^2 \cdot \text{K}$ is used.

Figure 7.7 shows the axial variation of the saturation and vapor temperatures, pressure, velocity and density obtained from the present numerical model and the experimentally measured saturation temperature distribution (Ivanovskii et al., 1982). The pressure, temperature and density in the evaporator decrease and the velocity increases due to the injection of mass and the effect of friction. In the adiabatic section, the vapor temperature increases because of viscous dissipation and the pressure decreases owing to friction at the interface. The density also decreases while the velocity continues to increase. The vapor temperature in the condenser continues to increase due to viscous dissipation so that the vapor temperature at the end cap of the evaporator is less than that at the end cap of the condenser. The pressure recovery in the condenser is almost negligible. This may result from dominant friction effect at the interface of the condenser compared to the effect of mass extraction in this long condenser. In the adiabatic section a difference between the calculated and measured saturation temperatures is observed, but the trend

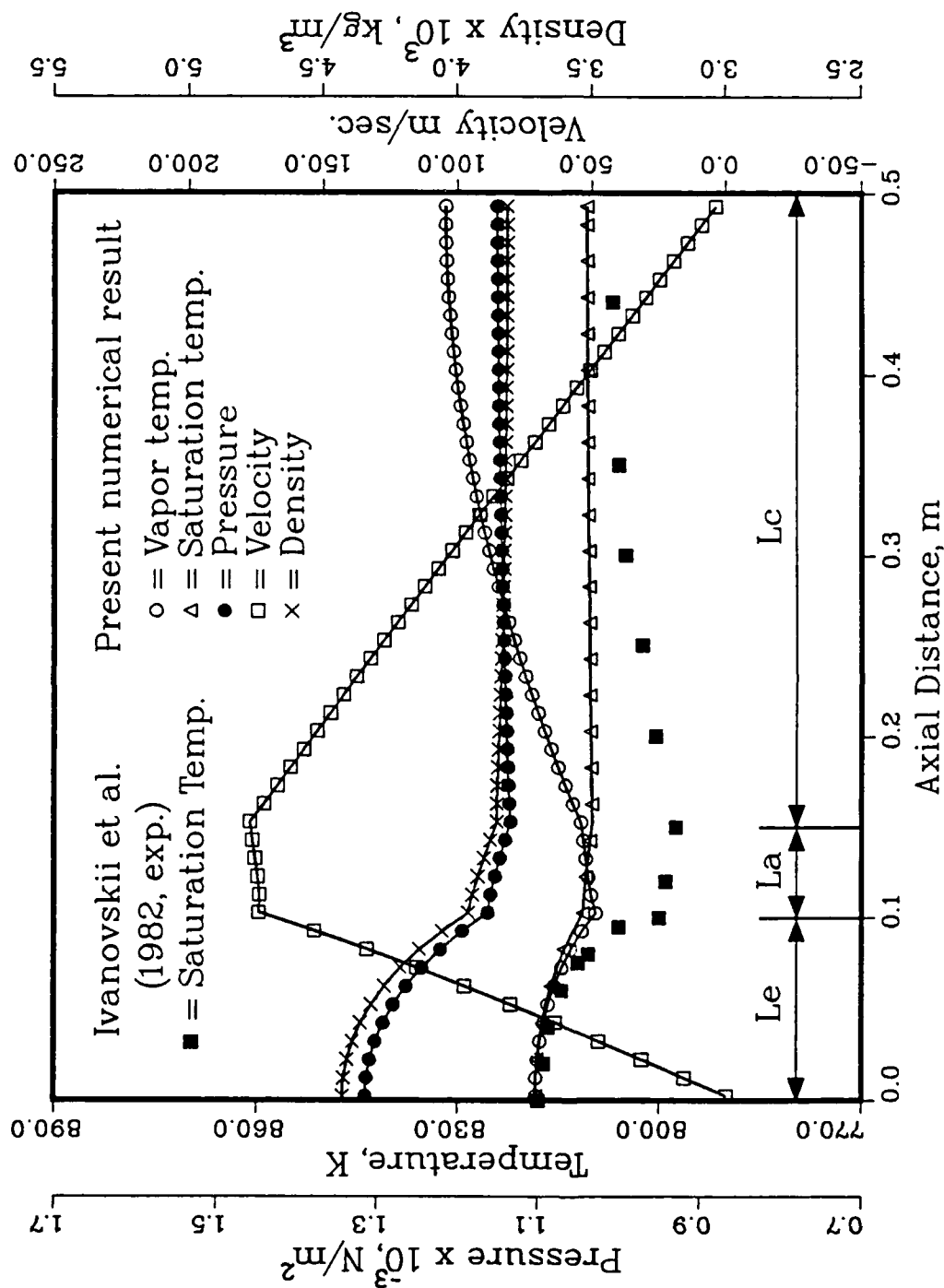


Figure 7.7. Axial variations of temperature, pressure, velocity, and density of the sodium heat pipe at steady state

of the saturation temperature variation is the same. The trend of the vapor temperature in the condenser is quite different from that of the saturation temperature in the same region, so the saturation temperature may not be assumed to be the vapor temperature in the condenser for the one-dimensional model.

The effect of viscous dissipation in the vapor flow for the high temperature heat pipe is investigated as shown in Fig. 7.8. The vapor temperature at the end cap of the evaporator with viscous dissipation is less than that at the end cap of the condenser. However, the vapor temperature at the end cap of the evaporator without viscous dissipation is almost the same as that at the end cap of the condenser. In the adiabatic section, the vapor temperature with viscous dissipation increases while that without viscous dissipation does not change. Therefore, the viscous dissipation should be taken into account in the energy equation for the high temperature heat pipe.

7.7 CONCLUSIONS

A model for the transient one-dimensional compressible vapor flow in the cylindrical heat pipe is developed. This model predicts the vapor flow in cylindrical heat pipes as well as simulated heat pipes for the subsonic, sonic, and supersonic flows under transient and steady state conditions. The vapor flow quickly reaches the steady state condition. The distributions of the temperature and pressure during the transient state are quite different from those for the steady state. The viscous dissipation terms play an important role in the energy equation and have to be taken into account. The one-dimensional compressible model predicts the

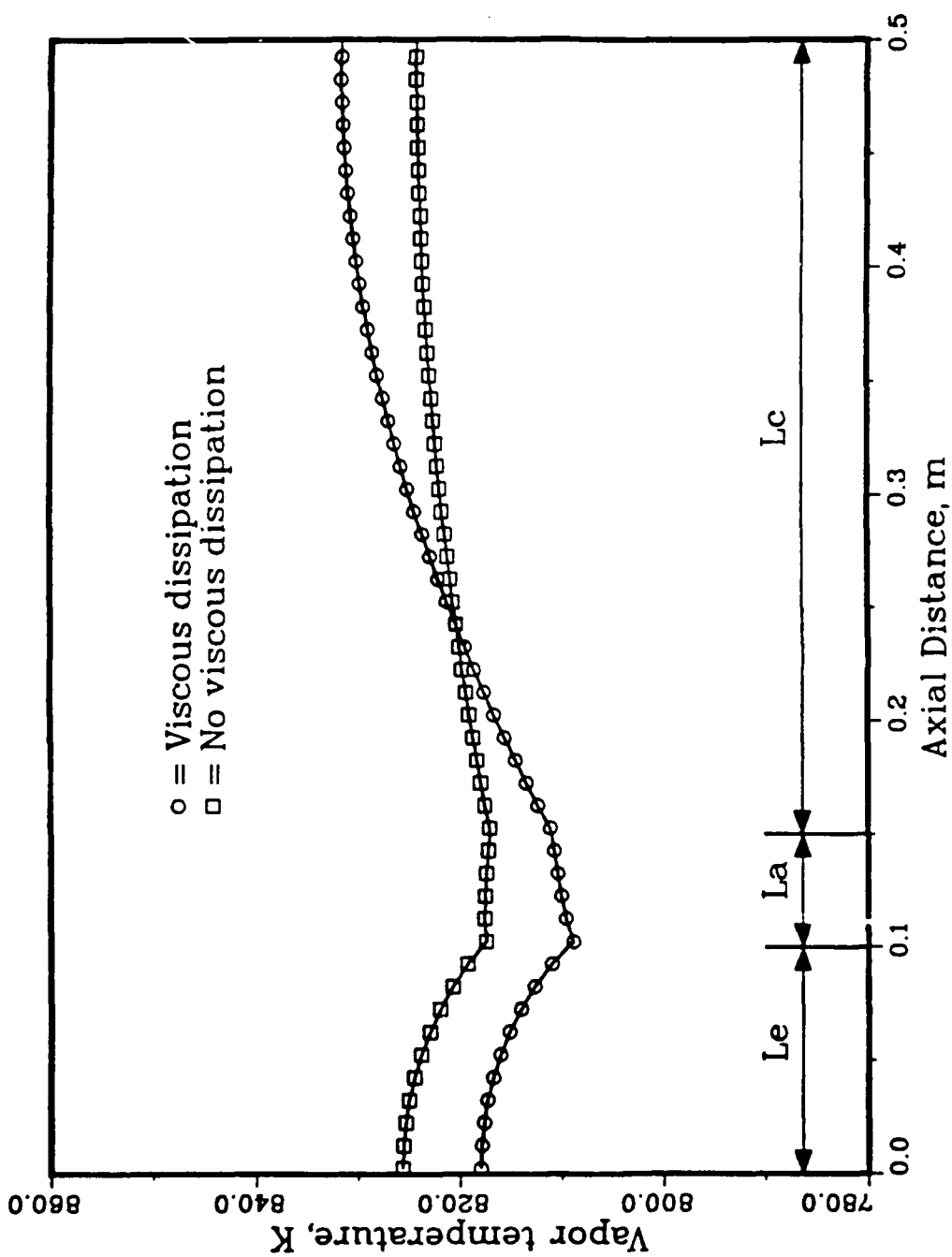


Figure 7.8. Comparison of the temperature variations with and without viscous dissipation for actual vapor flow

experimental data well for the cylindrical heat pipe and the simulated heat pipe at the steady state. The experimental data for the transient state are needed to understand clearly the transient behavior of the vapor flow in the heat pipe both at low and high temperatures. The one-dimensional model can reduce the computational effort needed to solve the vapor flow problem.

REFERENCES

Anderson, D.A., Tannehill, J.C., and Pletcher, R.H., 1984, Computational Fluid Mechanics and Heat Transfer, Hemisphere Pub. Co., New York.

Bachmat, Y., and Bear, J., 1986, "Macroscopic Modeling of Transport Phenomena in a Porous Media," Parts 1 and 2, Transport in Porous Media, Vol. 1, pp. 213-269.

Bankston, C.A., and Smith, H.J., 1972, "Incompressible Laminar Vapor Flow in Cylindrical Heat Pipes," ASME Paper No. 71-WA/HT-15.

Bienert, W.B., Ducao, A.S., Trimmer, D.S., 1977, "Development of a Jet Pump-Assisted Arterial Heat Pipe," Final report, Dynatherm Corp., Cockeysville, MD.

Boehm, R.F., and Kamyab, D., 1977, "Analysis of Established Natural Convection Due to Stripwise Heating on a Horizontal Surface," J. Heat Transfer, Vol. 99, No. 2, pp. 294-299.

Bowman, W.J., 1987, "Simulated Heat Pipe Vapor Dynamics," Ph.D. Dissertation, Air Force Institute of Technology.

Bowman, W.J., and Hitchcock, J., 1988, "Transient Compressible Heat-Pipe Vapor Dynamics," Proc. 25th ASME National Heat Transfer Conf., Vol. 1, pp. 329-337.

Brovalsky, Y.M., Bystrov, P.I., and Melkinov, M.V., 1976, "The Method of Calculation and Investigation of High-Temperature Heat Pipe Characteristics Taking into Account the Vapor Flow Compressibility, Friction, and Velocity Profile," Proc. 2nd Int. Heat Pipe Conf., pp. 113 - 122.

Busse, C.A., 1987, "Subsonic Pressure Recovery in Cylindrical Condensers," personal communication.

Bystrov, P.I. and Popov, A.N., 1978, "The Supersonic Flow of Vapor in the Condensation Zone of High Temperature Heat Pipes," Third Int. Heat Pipe Conf., pp. 21-26.

Camarda, C.J., 1977, "Analysis and Radiant Heating Tests of a Heat-Pipe-Cooled Leading Edge," NASA TN-8486.

Cao, Y., and Faghri, A., 1989, "A Temperature Transforming Model With a Fixed Grid Numerical Methodology for Phase-Change Problems Including Natural Convection," Proc. 1989 ASME National Heat Transfer Conf., HTD-Vol. 109, pp. 45-53. Also to appear in ASME Journal of Heat Transfer.

Cao, Y., Faghri, A., and Chang, W.S., 1989a, "A Numerical Analysis of Stefan Problems for Generalized Multi-Dimensional Phase-Change Structures Using the Enthalpy Transforming Model," Int. J. Heat and Mass Transfer, Vol. 32, No. 7, pp. 1289-1298.

References (continued)

Cao, Y., Faghri, A., and Mahefkey, E.T., 1989b, "The Thermal Performance of Heat Pipes with Localized Heat Input," Int. J. Heat Mass Transfer, Vol. 32, No. 7, pp. 1279-1287.

Cao, Y., Faghri, A., 1990, "Thermal Protection For Intense Localized Moving Heat Fluxes Using Phase-Change Materials," Int. J. Heat Mass Transfer, Vol. 33, No. 1, pp. 127-138.

Catton, I., Ayyaswamy, P.S., and Clever, R.M., 1974, "Natural Convection Flow in a Finite, Rectangular Slot Arbitrarily Oriented with Respect to the Gravity Vector," Int. J. Heat Mass Transfer, Vol. 17, No. 2, pp. 173-184.

Chang, W.S., 1987, "Effective Thermal Conductivity of Wire Screens," Fundamentals of Conduction and Recent Developments in Contact Resistance, HTD-Vol. 69, pp. 64-75.

Chen, M.-M., and Faghri, A., 1989, "An Analysis of the Vapor Flow and the Heat Conduction Through the Liquid-Wick and Pipe Wall in a Heat Pipe with Single or Multiple Heat Sources," Proc. 26th ASME National Heat Transfer Conf., ASME Paper 89-HT-12. Also to appear in International Journal of Heat and Mass Transfer.

Chi, S.W., "Heat Pipe Theory and Practice," Hemisphere Publishing Corporation, 1976.

Colwell, G.T., Jang, J.H., and Camarda, C.J., 1987, "Modeling of Startup from the Frozen State," Proc. 6th Int. Heat Pipe Conf., France, Vol. 1, pp. 165-170.

Cotter, T.P., 1967, "Heat Pipe Startup Dynamics," Proc. IEEE Thermionic Conversion Specialist Conf., Palo Alto Calif., pp. 344-348.

Deverall, J.E., Kemme, J.E., and Florschuetz, L.W., 1970, "Sonic Limitations and Startup Problems of Heat Pipes," LA-4518.

Dunn, P.D., and Reay, D.A., 1982, Heat Pipes, 3rd Ed., Pergamon Press, Oxford.

Faghri, A., 1986, "Vapor Flow Analysis in a Double-Walled Concentric Heat Pipe," Numerical Heat Transfer, Vol. 10, No. 6, pp. 583 - 595.

Faghri, A., 1989, "Performance Characteristics of a Concentric Annular Heat Pipe, Part II: Vapor Flow Analysis," ASME J. Heat Transfer, Vol. 111, No. 4, pp. 851-857.

Faghri, A., and Parvani, S., 1988, "Numerical Analysis of Laminar Flow in a Double-Walled Annular Heat Pipe," J. Thermophysics and Heat Transfer, Vol. 2, No. 3, pp. 165 - 171.

References (continued)

Faghri, A., and Thomas, S., 1989, "Performance Characteristics of a Concentric Annular Heat Pipe, Part I: Experimental Prediction and Analysis of the Capillary Limit", ASME J. Heat Transfer, Vol. 111, No. 4, pp. 884-850.

Faghri, A., and Chen, M.M., 1989, "Numerical Analysis of the Effects of Conjugate Heat Transfer, Vapor Compressibility and Viscous Dissipation in Heat Pipes," Numerical Heat Transfer, Part A, Vol. 16, pp. 389-405.

Ganic, E.N., Hartnett, J.P., and Rohsenow, W.M., 1985, "Basic Concepts of Heat Transfer," in Handbook of Heat Transfer Fundamentals (Edited by W.M. Rohsenow et al.), McGraw-Hill Book Company.

Gartling, D.K., 1980, "Finite Element Analysis of Convective Heat Transfer Problems with Change of Phase," in Computer Methods in Fluids (Edited by K. Morgan et al.), pp. 257-284, Pentech, London.

Gernert, N.J., 1986, "Analysis and Performance Evaluation of Heat Pipes with Multiple Heat Sources," AIAA/ASME 4th Joint Thermophysics and Heat Transfer Conf.

Grover, G.M., Cotter, T.P., and Erikson, G.F., 1964, "Structures of Very High Thermal Conductance, J. Applied Physics, Vol. 6, pp. 1990-1991.

Holman, J.P., 1981, Heat Transfer, 5th Ed., McGraw-Hill Book Co., New York.

Hong, J.T., Tien, C.L., and Kaviany, M., 1985, "Non-Darcian Effects on Vertical-Plate Natural Convection in Porous Media with High Porosities," Int. J. Heat Mass Transfer, Vol. 28, pp. 2149-2157.

Ho, C.J., and Chen, S., 1986, "Numerical Simulation of Melting of Ice Around a Horizontal Cylinder," Int. J. Heat Mass Transfer, Vol. 29, No. 9, pp. 1359-1368.

Ho, C.J., and Viskanta, R., 1984, "Heat Transfer During Melting From an Isothermal Vertical Wall," J. Heat Transfer, Vol. 106, pp. 12-19.

Hsiao, J.S., 1985, "An Efficient Algorithm for Finite-Difference Analysis of Heat Transfer with Melting and Solidification," Numerical Heat Transfer, Vol. 8, pp. 653-666.

Hsiao, J.S., and Chung, B.T.F., 1984, "An Efficient Algorithm for Finite Element Solution to Two-Dimensional Heat Transfer with Melting and Freezing," ASME paper no. 84-HT-2.

Issacci, F., Catton, I., Heiss, A., and Ghoniem, N.M., 1988, "Analysis of Heat Pipe Vapor Dynamics," Proc. 25th ASME National Heat Transfer Conf., Vol. 1, pp. 361-365.

References (continued)

Ivanovskii, M.N., Sorokin, V.P., and Yagodkin, I.V., 1982, The Physical Principles of Heat Pipes, Clarendon Press, Oxford.

Jang, J.H., 1988, "An Analysis of Startup from the Frozen State and Transient Performance of Heat Pipes," Ph.D. Dissertation, Georgia Institute of Technology.

Jang, J.H., Faghri, A., and Chang, W.S., 1989a, "Analysis of the Transient Compressible Vapor Flow in Heat Pipes," Proc. 26th ASME National Heat Transfer Conf., submitted to J. Heat Transfer.

Jang, J.H., Faghri, A., Chang, W.S., and Mahefkey, E.T., 1989b, "Mathematical Modeling and Analysis of Heat Pipe Start-Up From the Frozen State," Proc. 25th ASME National Heat Transfer Conf., HTD-Vol. 114, pp. 11-20. Also to appear in ASME J. Heat Transfer.

Karki, K.C., 1986, "A Calculation Procedure for Viscous Flows at all Speeds in Complex Geometries," Ph.D. Dissertation, The University of Minnesota.

Kays, W.M., and Crawford, M.E., 1980, Convective Heat and Mass Transfer, Second Edition, McGraw-Hill Book Company.

Kemme, J.E., 1969, "Ultimate Heat-Pipe Performance," IEEE Transactions on Electronic Devices, Vol. ED16, No. 8, pp. 717-723.

Keung, C.S., 1980, "The Use of Source and Sink in Solving Two-Dimensional Heat Conduction Problems with Change of Phase in Arbitrary Domains," Ph.D. dissertation, Columbia University.

Levy, E.K., 1968, "Theoretical Investigation of Heat Pipes Operating at Low Vapor Pressures," J. Eng. for Industry, Vol. 90, pp. 547-552.

McDonough, J.M., and Catton, I., 1982, "A Mixed Finite Difference - Galerkin Procedure for Two-Dimensional Convection in a Square Box," Int. J. Heat Mass Transfer, Vol. 25, No. 8, pp. 1137-1146.

Merrigan, M.A., Keddy, E.S., and Sena, J.T., 1985, "Transient Heat Pipe Investigations for Space Power Systems," LA-UR-85-3341.

Merrigan, M.A., Keddy, E.S., and Sena, J.T., 1986, "Transient Performance Investigation of a Space Power System Heat Pipe," AIAA Paper No. AIAA-86-1273.

Morgan, K., 1981, "A Numerical Analysis of Freezing and Melting With Convection," Computer Methods in Applied Mechanics and Engineering, Vol. 28, No. 3, pp. 275-284.

Neal, L.G., 1967, "An Analysis and Experimental Study of Heat Pipes," TRW System Rept. No. 99900-6114-R000.

References (continued)

Okada, M., 1984, "Analysis of Heat Transfer During Melting from a Vertical Wall," Int. J. Heat Mass Transfer, Vol. 27, No. 11, pp. 2057-2066.

Ooijen, H.V., and Hoogendoorn, C.J., 1979, "Vapor Flow Calculations in Flat-Plate Heat Pipe," AIAA J., Vol. 17, No. 11, pp. 1251 - 1259.

Ozisik, M.N., 1980, Heat Conduction, John Wiley and Sons.

Patankar, S.V., 1980, Numerical Heat Transfer and Fluid Flow, McGraw-Hill, New York.

Patankar, S.V., 1988, "Elliptic Systems: Finite-Difference Method I" in Handbook of Numerical Heat Transfer, Edited by W.J. Minkowycz, et al., John Wiley and Sons, Inc.

Prakash, C., Samonds, M., and Singhal, A.K., 1987, "A Fixed Grid Numerical Methodology for Phase Change Problems Involving a Moving Heat Source," Int. J. Heat Mass Transfer, Vol. 30, No. 12, pp. 2690-2694.

Prasad, V., and Kulacki, F.A., 1987, "Natural Convection in Horizontal Porous Layers with Localized Heating from Below," J. Heat Transfer, Vol. 109, No. 3, pp. 795-798.

Raithby, G.D., and Hollands, K.G.T., 1985, "Natural Convection," in Handbook of Heat Transfer Fundamentals (Edited by W.M. Rohsenow et al.), McGraw-Hill Book Company.

Rathjen, K.A., and Jiji, L.M., 1971, "Heat Conduction with Melting or Freezing in a Corner," J. Heat Transfer, Vol. 93, pp. 101-109.

Raw, M.J. and Schneider, G.E., 1985, "A New Implicit Solution Procedure for Multi-Dimensional Finite-Difference Modeling of the Stefan Problem," Numerical Heat Transfer, Vol. 8, pp. 559-571.

Reed, C.B., 1987, "Convective Heat Transfer in Liquid Metals," in Handbook of Single-Phase Convective Heat Transfer (Edited by S. Kakac, et al.), Ch. 8, pp. 1-30, John Wiley & Sons.

Schneider, G.E., 1987, "Computation of Heat Transfer with Solid/Liquid Phase Change Including Free Convection," J. Thermophysics and Heat Transfer, Vol. 1, No. 2, pp. 136-145.

Shamsundar, N., and Sparrow, E.M., 1975, "Analysis of Multidimensional Conduction Phase Change via the Enthalpy Model," J. Heat Transfer, Vol. 97, No. 3, pp. 333-340.

Shlosinger, A.P., 1968, "Heat Pipe Devices for Space Suit Temperature Control," TRW System Rept. No. 06462-6005-R0-00.

References (continued)

Solomon, A.D., Morris, M.D., Martin, J., and Olszewski, M., 1986, "The Development of a Simulation Code for a Latent Heat Thermal Energy Storage System in a Space Station," Technical Report ORNL-6213.

Spalding, D.B., 1980, "Mathematical Modeling of Fluid-Mechanics," Heat Transfer and Chemical-Reaction Process, a lecture course, CFDU Report HTS/80/1, Imperial College, London.

Sparrow, E.M., and Ohkuho, Y., 1986, "Numerical Analysis of Two-Dimensional Transient Freezing Including Solid-Phase and Tube-Wall Conduction and Liquid-Phase Natural Convection," Numerical Heat Transfer, Vol. 9, No. 1, pp. 59-77.

Stovall, T.K., Arimilli, R.V., 1988, "Transient Thermal Analysis of Three Fast-Changing Latent Heat Storage Configuration for a Space-Based Power System," Proc. 23rd Intersociety Energy Conversion Engineering Conference, pp. 171-177.

Subbotin, V.I., Sorokin, D.M., Ovechkin, D.M., and Kudryavtsev, A.P., 1972, "Heat Transfer in Boiling Liquid Metals by Natural Convection," English Trans. by U.S. Atomic Energy Commission and the National Science Foundation, Washington, D.C.

Takenaka, N., Murata, T., Takahashi, O., and Michiyoshi, I., 1983, "Boiling Heat Transfer from a Horizontal Plane Heater to a Potassium Layer," Int. J. Heat Mass Transfer, Vol. 26, No. 1, pp. 154-156.

Tien, C.L., and Rohani, A.R., 1974, "Analysis of the Effects of Vapor Pressure Drop on Heat Pipe Performance," Int. J. Heat Mass Transfer, Vol. 17, No. 1, pp. 61 - 67.

Tolubinsky, V.I., Shevchuk, E.N., and Stambrovsky, V.D., 1978, "Study of Liquid-Metal Heat Pipes Characteristics at Start-up and Operation under Gravitation," Proc. of 3rd Int. Heat Pipe Conf., pp. 274-282.

Voller, V.R., and Cross, M., 1981, "Estimating the Solidification/Melting Times of Cylindrically Symmetric Regions," Int. J. Heat Mass Transfer, Vol. 24, No. 9, pp. 1457-1461.

Voller, V.R., Cross, M., and Markatos, N.C., 1987, "An Enthalpy Method for Convection/Diffusion Phase Change," Int. J. for Numerical Methods in Engineering, Vol. 24, No. 1, pp. 271-284.

Voller, V.R., and Prakash, C., 1987, "A Fixed Grid Numerical Modelling Methodology for Convection-Diffusion Mushy Region Phase-Change Problems," Int. J. Heat Mass Transfer, Vol. 30, No. 8, pp. 1709-1718.

Yang, K.T., 1987, "Natural Convection in Enclosures," in Handbook of Single-Phase Convective Heat Transfer (Edited by S. Kakac et al.), Ch. 13, pp. 1-51, John Wiley & Sons.